R-1353
CU-365
NEVIS-259

Nevis Laboratories
Columbia University
Physics Department
Irvington-on-Hudson
New York

A STUDY OF WRONG SIGN MUON AND TRIMUON EVENTS IN NEUTRINO-NUCLEON SCATTERING

Sanjib Ratan Mishra

Submitted in partial fulfillment of
the requirements for the degree
of Doctor of Philosophy in the
Graduate School of Arts and Sciences,
Columbia University

1986

AAB1990

A STUDY OF WRONG SIGN MUON AND TRIMUON EVENTS IN NEUTRINO-NUCLEON SCATTERING*†

Sanjib Ratan Mishra
Columbia University, New York, N.Y.

---

*Research supported by the National Science Foundation

†Submitted in partial fulfillment of the requirements for the degree of Doctor of Philosophy in the Graduate School of Arts and Sciences, Columbia University.

Abstract

Wrong sign muon events in neutrino-nucleon scattering are characterized by a single muon in the final state carrying lepton number different from that of the incident neutrino. A search for such events in two experiments employing the Fermilab Narrow Band Neutrino beam is reported here. We derive an upper limit of 3.1×10^{-4} on the rate of production of these events. Limits on the intrinsic charm content of the sea ($<.02$), flavour changing neutral current ($<.0085$), and lepton number violating processes (rate $< 7.1 \times 10^{-5}$) have also been derived. Further, if the lepton number violation is brought about by a massless Majorana neutrino with a non-zero right handed coupling, then these data set the upper limits on the mass of the right handed gauge boson ($>$ 849 GeV) and its mixing angle with the ordinary boson ($<.009$). The rate and kinematical properties of wrong sign events are compared with those of the neutrino induced dimuon events. Finally we report on a set of 12 neutrino initiated trimuons, with muon momentum $>$ 4.5 GeV. We conclude that the trimuon events could be understood in terms of the hadronic and the radiative production of an extra dimuon pair in a charged current event.

Contents

Chapter 6. Results and Conclusion 51

Chapter 1

Introduction and Motivation for Studying WSM

§1.1 Introduction

This thesis concerns neutrino-nucleon scattering experiments carried out by CCFRR collaboration at Fermi National Laboratory. A neutral, massless spin-1/2 and left-handed lepton, the neutrino is known to participate in weak-interactions only. It is sterile as far as electromagnetic and strong interactions are concerned. At present three flavours of leptons have been seen; these are the electron (e), the muon (μ) and the tau (τ). With each lepton flavour is associated a neutrino type. (Similarly there are three types of antineutrinos corresponding to three antileptons). Of the three proposed neutrino flavours, only the electron-neutrino (ν_e), and the muon-neutrino (ν_μ) have been observed, while the tau-neutrino (ν_τ) is actively being sought. Neutrinos may couple only to their corresponding lepton parterns by emitting a left-handed vector boson of appropriate charge, e.g. a muon-neutrino (ν_μ) may couple only to a muon and not any other lepton or antilepton and emit a W^+ (See Fig. 1.1a). This is known as lepton number conservation. It is this empirical rule which motivates the pairing of the lepton and neutrino. Each particle of the pair carries a unit lepton-flavour-number. The corresponding antilepton possesses a unit of negative lepton number for its particular flavour. The lepton flavour number conservation law implies that a reactions in which a lepton might be converted to an antilepton is forbidden.

A "charge current" (CC) interaction of a neutrino with a nucleon is one in which a negative muon is an end product (Fig. 1.1a).

$$\nu_\mu + N \rightarrow \mu^- + X$$

One notices that the muon lepton number is +1 before and after the interaction. However, the reaction such as :

$$\nu_\mu + N \rightarrow \mu^+ + X$$

appears to violate lepton number conservation. Such events, called Wrong Sign Muons' (WSM), with a positive muon in the final state have been observed and are the subject of this thesis (see Fig. 1.1d).

Other known neutrino interactions are :

Neutral Current (NC) (Fig. 1.1b), with a neutrino and hadron shower as end products, (the emergent neutrino remains unobserved) :

$$\nu_\mu + N \rightarrow \nu_\mu + X$$

Opposite Sign Dimuons (OSDM), (Fig. 1.1c), in which a μ^-, a μ^+ and hadron shower are the end products :

$$\nu_\mu + N \rightarrow \mu^- + \mu^+ + X$$

Like Sign Dimuons (LSDM) (ig. 1.1e), two negative muons with hadron shower appear in the final state :

$$\nu_\mu + N \rightarrow \mu^- + \mu^- + X$$

Trimuons, (Fig. 1.1f), three muons, typically two negative muons and a positive muon, and a hadron shower in the final state :

$$\nu_\mu + N \rightarrow \mu^- + \mu^+ + \mu^- + X$$

There are two prominent backgrounds which mimick a WSM event. (a) A background contamination of antineutrinos in the neutnrino beam would produce a μ^+ after interacting with the nucleon due to lepton number conservation, (b) Dilepton backgrounds : various OSDM-like interactions may produce a μ^+ without a μ^-. These backgrounds have been discussed in Chapter 5 and 6.

The CCFRR experiments at FNAL employed a beam of muon-neutrinos. The beam ν_μ were decay products of a beam of positive pions and kaons. These mesons were produced by impinging 400 GeV protons on a berillium target. Symbolically :

$$P + Be \rightarrow \pi^+ + K^+ + X$$

such that π^+/K-> $\mu^+ + \nu_\mu$. There is also a three body decay mode of kaons producing ν_μ, referred to as $K_{\mu 3}$. However the branching ratio for the $K_{\mu 3}$ is smaller by a factor of 18 compared to the two body decay. The neutrino source and beam will be discussed in detail in the following chapter.

Prevailing theories of elementary particles conserve lepton numbers. Therefore, an unequivocal experimental signature violating this rule would compel a modification of the present understanding of forces of nature. The study of WSM provides a means of examining this issue.

§1.2 The need for an extension of the "Standard Model"

The unified theory of electromagnetism and weak interactions [1] along with the colour interaction (QCD) [2], commonly known as the standard model, has been remarkably successful in explaining an ever-widening range of experiments conducted over the past decade. The underlying ideas of a local, non-abelian gauge symmetry, spontaneous symmetry breaking [3] and asymptotic freedom [4] form an elegant and consistent scheme. Not only does the model propose a unified theory of electromagnetism and weak interactions, it can also provide meaningful corrections to processes at all orders of perturbation theory. The standard model is based on the gauge group $SU(3) \times SU(2) \times U(1)$. This is referred to as the minimal version of the standard model. It contains three generations of fermions (e, ν_e, u, d), (μ, ν_μ, c,s) and (τ, ν_τ, t,b), 12 gauge bosons (γ, W, W, Z, and 8 gluons) and one scalar field, ϕ, the Higgs field. Inspite of its breakthroughs the standard model has been found lacking in many aspects, primarily theoretical [5]. To begin with, the number of free parameters in the minimal standard model is 19. Even a simple extension of the minimal version, for example addition of massive neutrinos, may inflate this number to 26. Thus it violates the basic tenets of a 'good' theory – simplicity and brevity. Furthermore it provides no answer or intimation to the generation puzzle. After thirty six years, Rabi's question, "Who ordered the muon?", remains unanswered. In the same vein the standard model does not furnish , beyond anomaly cancellation, any deeper connection between quarks and leptons, for example relations of their electric charges. Another dissatisfying aspect of the theory involves the CP-violating interactions. There are provisions for such interactions, but there are no explanations for them within the model. If indeed the standard model is the correct theory and the new physics occurs on the scale of Planck-mass , then the "fine tuning problem" is a serious theoretical hurdle to be overcome within its context. This, perhaps, is the gravest lacuna of the present theory [5]. Any alleviation of this problem would imply the existence of new physics beyond standard model. The experimental motivations to modify the standard model are less pressing. At present there is no definitive experimental result that contradicts the standard model. Signatures of events such as the $\zeta(8.3)$ [95] and the CERN "zoo-events" [6,97,98,99,100,101,102and103] which could have provided a reason to extend the standard model, have vanished. Other searches for instance proton-decay, massive neutrinos and neutrino oscillation have not discovered any phenomenon contradicting the standard model. In the deep-inelastic neutrino scattering experiments two types of events have been found which exist around 2σ level above respective backgrounds. These events, if proven to exist beyond backgrounds would force an extension of the standard model, are Like-Sign Dimuons (LSDM) and Wrong Sing Single Muons (WSM). LSDM in Neutrino interactions[7] have been known to exist for past eight years. Even though the signal for such events has been meager, most expalnations within the stantard model, have failed to explain LSDM. WSM on the other hand have not been reported so far to exist beyond background. Other neutrino interactions, which are well understood and mentioned earlier, are Charged Current (CC), Neutral Current (NC) and Opposite Sign Dimuons (OSDM). The relative rates of all these interactions with respect to CC are:

CC	*NC*	*OSDM*	*LSDM*	*WSM*	3μ
1.	.307	$(9. \pm .8) \times 10^{-3}$	$(1. \pm .7) \times 10^{-4}$	$(1.8 \pm .8) \times 10^{-4}$	$(5.5 \pm 1.8) \times 10^{-5}$

Relative rates of ν-induced interactions.

(The Feynman diagrams for these interactions, as pointed out in Sec. 1.1, are presented in Fig. 1.1a, 1.1b and 1.1c respectively. Fig. 1.1d and 1.1e illustrate schematically WSM and LSDM.) It should be noted that the rates of production of both of the exotic interactions are small $\approx 1.0 \times 10^{-4}$, and at present, since only a handful of these events are available, there is no clear indication of their existence beyond backgrounds. It is impressive that experimental signatures which refuted the standard model have proven to be either erroneous or mere fluctuations. One is inclined to conclude that the present theory is, at least, a very good approximation at low energy. However the theoretical problems confronting the standard model encourage the belief that new physics beyond the prevaling theory is inevitable and imminent.

§1.3 Two theoretical models

It is interesting to note that there are at least two theoretical models that explain the LSDM, CERN "zoo-events" or (Z -> e^+ e^- γ or Z -> μ^+ μ^- γ) and WSM. The rates of LSDM and WSM are quite similar, and there may exist a deep connection between these two exotic events. The CERN events have been disavowed as backgrounds or statistical fluctuations, consequently weakening the claims of these models. A short description of these models is given below, with particular attention to relevant Feynman diagrams of WSM and LSDM production within the theory. The first of these models is due to Veltman [8]. The theory postulates the existence of a new interaction which enables the electroweak intermediate bosons to form a composite. The bond is expected to have a strength of the order of strong interaction. This composite may decay to leptons and quarks. Fig. 1.2a and Fig. 1.2b show the Feynman diagrams for the production of WSM and LSDM in a neutrino interaction. The second model [9] assumes that quarks, leptons and the intermediate vector bosons are composites. The model treats the weak interaction at present experimental energies as the residual interaction of a more fundamental colour interaction, just as the strong force, binding the nucleons, is understood to be a residual 'Van der Waals' interaction of QCD. The model also predicts the existence of another heavy neutral boson, Y. One can derive, in the low energy approximation, the Weinberg-Salam lagrangian from this theory. Within the interactions permitted in this model are LSDM, WSM as well as the "zoo-events" Fig. 1.3a and Fig. 1.3b show schematically the production of WSM and LSDM in a neutrino interaction. In Chapter 6 a comparison between the two interactions, their kinematical characteristics and rates will be discussed. However, the poor statistics of the data for both LSDM and WSM prevent one from forming quantitative conclusions.

§1.4 WSM events and outline of presentation

If it were actually neutrinos (not antineutrinos) which produce WSM and these events were found to exist beyond dilepton backgrounds such that the μ^+ originated at the lepton vertex, then such interactions would violate lepton-number conservation. Therefore searches of such interactions primarily depend upon the purity of the incident neutrino beam. Furthermore, since the rate of such interactions is quite small, only high statistics neutrino experiments will be able to detect such events. The present thesis reports a search for WSM in the two experiments, E616 and E701, conducted at FNAL by CCFRR collaboration (see Appendix A). The experiment E616 was primarily aimed at measuring the ν_μ-N cross-section, the nucleon stucture-functions and the Wienberg angle ($sin^2\theta_W$). The experiment E701 was conducted to search for neutrino-oscillations. The data from the two experiments were also used to study OSDM and LSDM. The search for WSM was another off-shoot from the cumulative data. This search was conducted in the neutrino-nucleon scattering event sample with 337,407 charge current events. After the background subtraction an excess of WSM at 2σ level survived. An overall review of various neutrino interactions, including LSDM, has been presented in a report by Fisk and Sciulli [10]. Six other disertations have been made on the data accumulated by the two experiments. The topics encompassed by them are neutrino-nucleon cross-section [11], nucleon structure functions [12,13], neutrino oscillation [14,15] and dimuons [16]. The thesis is organised as follows. Chapter 2 deals with the narrow band neutrino beam and the antineutrino contamination. The station for the neutrino-detector is called Lab-E. Fig. 2.1 shows the location of Lab-E with respect to the accelerator and the neutrino-beam. Chapter 3 briefly describes the neutrino detector at Lab-E. Chapter 4 contains the selection and properties of WSM. Chapter 5 presents various backgrounds and their estimates. Chapter 6 contains the results and discusses a few ramifications of the data. The last chapter, Chapter 7, concerns a study of 23 trimuons events observed in the two experiments. Having dealt with the backgrounds for trimuons, various models of trimuon-production have been discussed. We measure the raw rate (without applying acceptance correction), relative to CC events, of production of trimuons to be $(5.5 \pm 1.8) \times 10^{-5}$.

Chapter 2

Neutrino Source and the Narrow Band Beam

The study of WSM in a neutrino experiment is possible only if the beam contains neutrinos or antineutrinos with as little contaminant of the other as possible. Precise measurement of the neutrino-nucleon cross-section and $sin^2\theta_W$ depend crucially upon this factor as well. The ideal neutrino beam for all these purposes would be produced from a hadron beam of pions and kaons, which is both sign-selected and monoenergetic. A close approximation to such a beam has been achieved in the narrow band neutrino beam at FNAL. There are numerous advantages to a narrow band neutrino beam. By means of a steep targeting angle and sharp bends in the horizontal plane the dichromatic magnet train is able, to a great extent, to sweep hadrons of the wrong charge and wrong momentum out of the beam (see Fig. 2.3 and the discussions in the subsequent sections). If the beam were tuned to select high energy secondaries the resulting energy spectrum of the neutrinos at the experimental apparatus would peak at high energy. In contrast, the energy spectrum of the secondary particles produced at the target peaks at low energy.

Some of these secondary hadrons decay before being swept out of the beam, forming a diffused source of low energy neutrinos and antineutrinos called Wide-band background (WBB). The clustering of narrow band neutrino events at high energy contrast sharply with motley energied WBB events. Furthermore the monoenergetic nature of the beam implies that the radius of the event-vertex and the neutrino-energy will be correlated (see Fig. 2.7) at Lab-E; this provides a check on the total energy measurement and a way of accounting for any appreciable missing energy. The neutrino beam line, its overall design, focusing elements and monitoring devices have been discussed extensively in references [11, 17, 18 ,19 ,20]. Therefore in this chapter the presentation of only the salient features of the production and transportation of the secondary beam will be attempted. After a brief discussion of the focusing and bending of the hadrons emerging from the BeO target, the dumping of the primary protons, which have not interacted, is addressed. The monitoring of the primary and secondary beams is then presented. The chapter concludes with a description of neutrino flux at Lab-E from various sources and their relative abundance.

§2.1 Production and the focusing of secondary particles

Fig. 2.1 gives an overview of the Fermilab neutrino beam. The protons, approximately 3×10^{13}, were accelerated to 400. GeV by Fermilab's synchrotron. The acceleration and extraction of the proton beam is shown vs time in Fig. 2.2, where the times are referenced with the machine generated time T1. During E616 running the beam was extracted in two modes: between T5 and T6 there was a long extraction of 1 second, called slow spill, and right after T6 there was a short extraction of approximately a millisecond, referred to as fast spill. In E701 the slow spill extraction was replaced by a series of mini fast spills known as pings. This was done to minimize the cosmic ray background in the slow spill data.

In each extraction, roughly 10^{13} protons impinged upon a 304 mm Beryllium oxide (BeO) target. The incident proton beam was at an angle of 11.96 mrad in the horizontal direction and 1.13 mrad in the vertical direction with respect to the axis coincident with the detector axis and taken to be the z-direction (Fig. 2.3b). This "twisted configuration" helped to reduce the WBB enormously. The beam design was poineered by Sciulli and associates. Ref [17] gives details of the design and comparision with other beam configurations.

The secondaries produced in the P-Be collisions were subjected to a series of beam elements,magnets and collimators, which transported particles of given sign and specified momentum (± roughly 10%). Particle selection and transport using magnets is analogous to the extraction of a ray of light of specified wavelength from a white source with the aid of prisms and lenses. Fig. 2.3a depicts a simple schematic of the narrow band focusing system. A detailed illustration of the train layout is shown in Fig. 2.3b. The accompanying Fig. 2.3c shows the various beam elements and the access stations along the dichromatic train. The target was placed at the focus of the vertical and horizontal quadrupole doublets. The first quadrupole focused in the horizontal direction and defocused in the vertical direction; the second quadrupole did the opposite. The focusing system thus provided point-to-parallel focusing. The first bending magnet, a dipole, introduced lateral dispersion in the momentum of each particle. The momentum defining slit then passed rays with momenta within the given momentum acceptance ($P \pm \Delta P$). The dipoles stationed at the tail of the train recombined the rays with varying momenta and directed them to the decay pipe. It follows that for positive settings the positive secondaries were bent down and into the beam whereas the negative secondaries were bent up and out of the beam. With the secondaries there were primary protons which had not interacted in the BeO target. These protons had to be dumped and subsequently removed from the particles (protons,pions and kaons) within the desired momentum bite. These primaries, at 400 GeV, were dumped into the inserts placed along the beam line. The dumping position changed with the beam setting. Also the angle at which the primaries were dumped varied from energy setting to energy setting (see Table 5.5). Chapter 5 describes some of these individual cases in detail. Most of the bending occurred in the horizontal direction. As stated in preceding paragraphs, there was a tiny bend in the vertical direction as well. As a result, the secondary beam of hadrons followed a helical trajectory around the central axis until it arrived at the last bending magnet. Up to this point it had never pointed in the direction of the neutrino apparatus. This helical twist of the beam minimized the number of the neutrinos (intercepting Lab-E) coming from the premature decays of the hadrons or from hadrons of wrong signs. The production of the secondaries and their relative abundances have been measured by Atherton et.al. [21]. Table 2.1 summarizes some of the characteristic parameters of the dichromatic beam.

§2.2 Monitoring of the primary and the secondary beams

To calculate the flux from the WBB one needs the total number of protons on the target. The proton beam was monitored from the targetting station called Neuhall. An inductive pickup toroid, through which the primary protons passed, measured the incident proton flux and a signal from it provided a gate, indicating the presence of beam, to be used by Lab-E. The readout and gating of the primary flux toroid is sketched in Fig. 2.5. The incident neutrino flux was measured through the following steps : First using ionization chambers and a tuned RF cavity the total intensity of the secondary beam in the decay pipe was measured. Relative number of pions kaons and protons were obtained by using a Cerenkov counter. With these two sets of measurements as the normalization, a Monte Carlo program was used to simulate the flux of neutrinos per secondary particle incident at Lab-E. The relative positions of various monitors in the beam line is shown in Fig. 2.4. In the preceding few lines the barest essentials of the flux measurement have been sketched. More details of the measurement of the secondary flux may be found in ref. [18]. However the details of secondary flux measurement are of little importance in the studies of WSM. The steering of the secondary beam is of interest since a cut on secondary beam steering was made in order to normalise the WSM data to the total charged current sample. The position of the primary beam near the BeO target was measured by a set of Segmented Wire Ionization Chamber (SWICs). The position of the secondary beam was also monitored through SWICs and by split plate ionization chambers positioned at two stations , the Expansion Port and the Target Manhole, along the decay pipe. These two stations are situated 136.m and 290.m from the beginning of the decay region. SWIC profiles in X and Y views gave the orientation of the secondary beam. Fig. 2.6a shows the SWIC profiles of the secondaries in the two stations. The split plate ionization chambers had two circular read out electrodes, the electrodes being split in half – right and left, top and bottom. The differences in the accumulated charges on the two halves quantified beam's deviation from its normal direction. Further details concerning steering cuts are described in Chapter 4. A schematic diagram of the ion chamber is presented in Fig. 2.6b.

§2.3 Beam Monte Carlo Program

In order to calculate the WBB component of the WSM events a beam Monte Carlo was used. It was essentially a program for tracing particle rays through beam elements. The production of the secondary particle at the target was simulated by using the measurements made by Atherton et al. [21]. This measurement and the subsequent parametrization for the invariant cross section of secondary production has been described in Appendix D. The surveyed positions of the various beam elements and the measured magnet currents were used in the particle ray tracing program, call the DECAY TURTLE. (Fig. 2.3 gives the location of various beam element in the N0 train.) The program is capable of tracing arbitrary number of particles through the beam elements. Each paricle is specified by five parameters in its phase sapce, $(x,y,\theta_x,\theta_y,p)$. The WBB Monte Carlo computation using this program is discussed in Chapter 5.

§2.4 Neutrino fluxes from various sources

Fig. 2.8 sketches the neutrino flux at the neutrino detector from two-body pion decays, two-body kaon decays and three-body kaon decays. The correct sign WBB is also shown. The WBB was measured by closing the momentum defining slit and preventing secondaries from entering the decay pipe. The neutrinos that reached Lab-E could have originated from upstream sources only. The closed slit data, however, was statistically inadequate to provide a good measurement of wrong sign WBB. Therefore a detailed WBB Monte Carlo calculation had to be performed to assay this background. In Chapter 5 the calculation of the WBB for WSM has been discussed at length. The difference in mass of the pion and the kaon cause the neutrinos to have a dichromatic spectrum. The Fig. 2.7 illustrates the energy versus radius correlation. These scatterplots show the separation of neutrino events caused by pion and kaon neutrinos. This separation is explained by simple kinematic considerations discussed in Appendix B. The subsequent calculation yields an expression for the neutrino energy in terms of the pion or kaon energy and the decay angle.

$$E_\nu = \frac{E(max)}{(1 + \gamma^2_{\pi,K} \times \theta^2)}$$

where $\theta = R/L$, R = Event radius at the detector, L=Longitudinal distance of the vertex from the point of decay of the meson, $\gamma_{\pi,K} = \frac{m_{\pi,K}}{E_{\pi,K}}$ and,

$$E(max) = E_{\pi,K} \times (1 - (\frac{m_\mu}{m_{\pi,K}})^2)$$

From the transverse event vertex in Lab-E one may, using the above expression, deduce the neutrino energy and compare it with the total energy visible in the apparatus. This gives a measure of the missing energy. The missing energy for reqular charge-current events must be zero. Chapter 5 discusses the missing energy calculation in detail.

Chapter 3

The Neutrino Detector and the Two Experiments

The salient features of the neutrino detector at Lab-E are recapitulated in this chapter. A table of apparatus summary is presented. Finally a synopsis of each of the two experiments, E616 and E701, follows, indicating the main differences between them.

§3.1 The neutrino detector

The ensemble of various instruments used in the neutrino detector is shown in Fig. 3.1. The apparatus consisted of a 690 ton target with scintillation counters for calorimetry and spark chambers for muon-tracking. A 310 ton toroidal muon spectrometer, also instrumented with counters and chambers, followed the target. The instrumented target was a made up of six conseqtutive approximately cubic carts (four for E701). Each cart, containing seven units of two steel plates, two counters and one chamber, could be independently moved transverse to the neutrino-beam axis. A target cart is shown in Fig. 3.2.

Similarly the spectrometer had three instrumented movable carts. Table 3.1 lists some of the relevant statistics for the target and the spectrometer.

3.1.1 Calorimetry

The measurement of hadron energy was accomplished by recording the pulse heights from light produced from the hadron shower in the counters. Each counter was a 3 m X 3 m X 2.5 cm tank of plexiglas containing a mixture of scintillator and wavelengh shifter chemicals in mineral oil base. These chemicals shifted the UV light produced by the scintillator to blue light to facillitate transmission to the phototubes. The four photomultiplier tubes, located at the four corners of the counter, received the light from wavelength shifter bars. These shifter bars which ran along the edges of the counter, separated optically by an air gap, shifted the blue light to green and passed it on to the photomultiplier tubes. An individual counter yielded approximately 10-15 photoelectrons per minimum ionizing particle and thus provided a means to record the passage of a single muon. In a charged current or neutral current event the few counters downstream of the vertex exhibited large pulse heights caused by the hadron shower. The first counter downstream of the vertex provided the longitudinal vertex position, called 'Place' in subsequent chapters. The hadron shower subsided after a few steel plates and the following counters displayed a constant pulse height indicating the passage of the muon. The pulse heights recorded from the photomultiplier tubes are then subjected to various corrections. To mention a few important ones : (a) pedestals were subtracted (b) the shifts in the counter gains were corrected and (c) the attenuation in the counters was estimated. The corrected pulse heights were then converted to energy by first expressing them as the number of equivalent minimum ionizing particles. The calculated energy deposited by the muon in the shower region was subtracted from this. The resulting number is directly proportional to the hadron energy. The calibration factor was measured in a calibration run. During this run a hadron beam of well defined momentum was injected into the apparatus, the pulse heights were converted into the number of equivalent minimum ionizing particles and finally the calibration constant was obtained. The measured hadron energy, E_H, had a fractional error of $\frac{.89}{\sqrt{E_H}}$. The relevant details of a target counter are shown in Fig. 3.3.

3.1.2 Muon momentum

Muons were tracked in the detector by means of 3.2m X 3.2m spark chambers with magnetostrictive readout. The spark chambers provided the horizontal and vertical coordinates of the muons every 20 cm of steel. The spatial resolution of these chambers was found to be approximately 0.5 mm. The chamber resolution and the spacing in steel results in the following approximate angualr resolution of the muon,

$$\frac{35}{P_\mu} = \delta\theta_\mu \text{ (in mrad)}$$

where the muon's position was measured in chambers beginning at the vertex. In practice the hadron shower masked the (x,y) measurement at the first few chambers, thereby exacerbating the muon angle resolution by a factor of two. For efficient reconstruction of muon tracks, the event vertex was required to occur at least twenty steel plates (seventeen for E701) upstream of the toroid.

The muon momentum was measured in the spectrometer downstream of the detector. Each toroid cart contained acrylic scintillators, for calorimetry and triggering, and spark chambers, to track the bending of the muons. The total muon energy (or, equivalently, the muon energy at the vertex) is the sum of the muon's energy as measured in the spectrometer and the muon's energy loss (dE/dx) in the target. The error in the muon's momentum for traversing the full length of the spectrometer was 11 %- 12 %. Fig. 3.4 sketches the various instruments in the target and toroid.

Table 3.2 summarises the calorimetric and muon-momentum resolutions in the detector.

§3.2 Muon triggers

Two muon triggers were used for this analysis : (1) the Muon trigger, where the muon was required to be momentum reconstructed in the toroid and (2) the Penetration trigger which selected charged current events with hadron energy above a certain minimum, however, the muon failed to get momentum reconstructed in the toroid.

The muon trigger, also called Trigger1, was designed to record the CC events for which the muon was produced in the foward direction and hence of high energy. The trigger demanded a recorded pulse height in a counter, known as T2, between the first and the second toroid carts, and hits in at least two counter of the four counter stationed upstream or downstream in the toroid. Fig. 3.5a shows the logic diagram for the muon trigger and Fig. 3.5b a regular muon trigger event with the wrong sign.

The penetration trigger on the other hand is designed to accept CC events where the muon did not reach the spectrometer, either because it ranged out in the target or because it emerged at a steep angle and exited the sides of the detector. The trigger thus takes events over a larger range of muon energy than the muon trigger. (Many penetration events are also muon trigger events.) The trigger required that the muon penetrate at least sixteen steel plates and the energy of the hadron shower be $>$ 4 GeV. Fig. 3.6a and Fig. 3.6b show the logic diagram for this trigger and a penetration trigger event.

§3.3 E616 and E701

The FNAL experiment E616 is the first of the above two experiments. The data for E616 were acquired from June 1979 to January 1980. The second experiment, primarily a search for neutrino-oscillations, ran from January of 1982 to June of 1982. The Lab-E apparatus was curtailed in tonnage to instrument another neutrino detector stationed upstream of Lab-E. The main differences in the detectors for the two experiments are listed in Table 3.3. Fig. 3.7 shows the detector configuration as used in E701.

Chapter 4

Selection and Analysis of Wrong Sign Muon Events

The data accumulated during neutrino running can be separated into two groups : (1) neutrino induced interactions and (2) interactions from other sources. The events, discerned to have originated from deep inelastic scattering of neutrinos off the nucleon may be further classified as charged current, neutral current, opposite sign dimuon and like sign dimuon events. The like sign dimuon events are the least understood of all the above four, as mentioned earlier.

The events from the other source are almost completely due to cosmic rays.

The wrong sign muon events form an extremely small fraction of the data, with a rate comparable to that for the like sign dimuons. The final data set of WSM was found after imposing a set of loose fiducial cuts on the original sample, visually scanning the events , reconstructing the candidate WSM events interactively and imposing a final set of cuts. This chapter deals with these steps in detail. Distributions of interesting kinematical quantities of WSM and regular CC events are also presented.

§4.1 Data analysis

The anlysis of the neutrino data was broken down into three stages. (a) The raw data tapes were compressed and many of the data acquisition details summarised. This was done by a program called the 'Stripper'. (b) The event reconstruction followed next. The hadron energy and the energy of the muon were calculated as outlined in the preceding chapter. This was accomplished by a program called the 'Cruncher'. (c) Finally all the relevant quantities concerning the event were written onto data summary tapes (DST) for physics analysis. The sample of WSM was extracted from the crunched data.

4.1.1 Preliminary cuts

Preliminary cuts were imposed on the original full data set to distinguish the candidates for WSM. These cuts were essentially fiducial cuts. They were :

1. Proper gate

The different types of gatings for each of the two experiments, E616 and E701, have been mentioned in Chapter 2. Events to be accepted, had to fall in one of the three categories :

a. a. Fast Spill : Both E616 and E701

b. b. Slow Spill : E616 only

c. c. Pings : E701 only

ii. Trigger cut

Since the muons of interest were defocused by the magnetic field it was imperative that the events be adequately momentum analysed. Therefore the bit representing the muon hardware trigger, the requirement for which has been stated in Chapter 2, in principle, had to be set. Since the resulting events were to be visually scanned, this trigger requirement was relaxed by allowing either the muon trigger bit or the penetration trigger bit to be set.

iii. PLACE cuts

The 'PLACE cut' restricts the event vertex to be within the legitimate longitudinal dimension of the apparatus. As described in Chapter 3, 'PLACE' represents the z-location of the vertex. The downstream or lower PLACE cut ensures efficient track reconstruction while the upstream or the higher cut eliminates straight through muons and cosmic rays. The PLACE cuts were –

$$E616 : 20 < PLACE < 80$$

$$E701 : 17 < PLACE < 54$$

iv. Number of tracks

A cut requiring that atleast one track in either view, (x or y),in the target be found, was imposed.

v. Vertex cut

The vertex cut delineates the fiducial area of the neutrino apparatus. It excludes most of the cosmic rays, which abound at the edges of the detector. To acertain the vertex-cut, a scatter plot of X-position vs Y-position of cosmic ray events was examined. One noticed the edge of the fiducial area emerging at around ±54 inches. The fiducial area was chosen to be :

$$-54.in < X - position < 54.in$$

$$-54.in < Y - position < 54.in$$

vi. Hole cut

The toroid has a central hole, 5 inches in radius, within which the magnetic field is zero. A muon track which spends more than a certain fraction of its time within the hole may not be properly reconstructed. The 'hole cut' was imposed to remove these muons from the sample. It was required that the fraction of the muon track spent inside the hole be less than .2.

vii. Toroid cuts

The 'Toroid cuts' ensure that the muon track is sufficiently within the dimensions of the spectrometer to be momentum reconstructed. Two cuts were imposed to insure this. The first cut demanded that the radius of the projected track of the muon at the toroid be less than 69 inches and the second that the projected track intersects the trigger counter,T2, behind the first toroid. As pointed out in Chapter 2, the toroid has a radial dimension of 69 inches. The T2 counter was a square extending to ±60 inches in X and Y. To put these cuts into symbols:

$$\rho_t < 69in.$$

$$-58in. < X_{T2} < 58in.and - 58in. < Y_{T2} < 58in.$$

where ρ_t is the radious of the muon at upstream end of the toroid and (X_{T2}, Y_{T2}) are the projected coordinates at the T2 counter.

viii. Momentum of the muon

To extract the wrong sign muon events it is finally required that the muon be defocused by the magnet or in other words the reconstructed momentum of the muon be negative.

ix. Evis cut

This cut was imposed on the slow spill events (E616 only) to reduce the enormous cosmic ray backgound, which is immanent in the slow spill, to a manageable level. An examination of the histogram of total visible energy of cosmic ray events revealed that above Evis of 20. GeV there were few cosmic rays. The cut was accordingly chosen to be Evis $>$ 20. GeV.

Tables 4.1a through 4.1e show the reduction of the initial data set due to the cuts described above for all the energy settings of the two experiments. Further cuts were imposed upon the obtained set of events. This is treated in Sec 4.4.

§4.2 Scanning and interactive reconstruction of WSM

The above cuts yielded a total of (753) events for E616, including fast and slow spills, and (843) events for E701, including fast and ping. The events that obviously did not contain defocused muons were weeded out. Such events could fall into one of the following : (1) regular charged current events which could not be properly reconstructed by the program or (2) multimuon events such as dimuons or trimuons, or (3) "zoo events" implying events that defied any classification. Some of the events in the sample appeared to be cosmic ray events, with characteristic low hadron energy. The vertex cut eliminated most of the cosmic rays that entered the apparatus through the target, but those entering the through the toroids could have escaped this cut. These cosmic rays, called 'Backwards going cosmic rays', comprise a small fraction of the data populating the low energy bins. An effort was made to develop an algorithm to eliminate the backward going cosmic rays. Some success was attained in recognizing these events statistically, but establishing quantitative criteria to pick them out event by event turned to be a formidable task. Since these events were in the low energy tail of the spectrum and were not too numerous, it was felt adequate to subtract out the cosmic ray background statistically. This subtraction is described in the following chapter.

After selecting candidate events by scanning, the events were reconstructed by hand. A conspectus of general features of event reconstruction has been presented in the preceding chapter. At this stage only two features of event reconstruction were evoked (a) finding the right track and (b) calculating the muon momentum. The hadron energy computation was unaltered. It should be mentioned that the scanning for WSM candidates was done twice to ensure that no event has been omitted. The efficiency was found to be better than 99%.

The candidate WSM events were examined on a high resolution graphics terminal. An interactive display and fitting program was used that enabled one to add or delete sparks as required. A certain pattern emerged for the events for which the track finding algorithm had not succeeded. The failure was attributed to one of the following snags : (1) spark chamber inefficiency, (2) too many hits in the toroid chambers (this was particularly the case for E701 events where the voltages of the toroid chambers were raised to increase the efficiencies), (3) large multiple scattering in the toroid chambers and occasionally in the target chambers, (4) track too close to the hole in the toroid, (5) backward going cosmic rays, (6) low energy focused muons weaving around the hole. An effort was made to keep the χ^2 per degree of freedom less than 2.0. Occasinally this could not be achieved. However none of the final candidate WSM events had the χ^2 above 5.0. Fig. 4.1a presents the histogram of χ^2 for WSM events.

4.2.1 Ambiguous events

Ambiguous events were those for which either the track finding routine could not determine a sign or the error on the momentum was computed to be very large, owing to the small deflection the muon underwent in the toroid. In spite of repeated efforts these events defied momentum reconstruction. Tables 4.2a and 4.2b list these events for E616 and E701 respectively. The third and the fourth columns of the tables contain the reconstructed momenta of these muons and the radius at the front face of the toroid. By "default" momentum is meant that no sign could be assigned to the muon-momentum. One common feature of them was that the radius at the upstream end of the toroid (ρ_t) is greater than 65. inches. This motivated the imposition of a more stringent cut requiring ρ_t be less than 65. inches instead of 69. inches.

§4.3 Flux monitoring cuts

In addition to the above cuts a monitor cut was imposed on the data, on a spill-by-spill basis, to ensure that the primary proton beam and the secondary hadron beam were properly directed. As described in the Chapter 2, this was called the 'Steering cut'. The reason for imposing the steering cut was the following : To calculate the WBB for WSM events the total number of protons delivered on the target was required. If the proton beam direction were changed from spill to spill the WBB would be altered in a time-dependent manner and thereby making it impossible to estimate the WBB content of WSM. As mentioned in Chapter 2, the beam steering was managed with the aid of SWICs and split-plate ion chambers situated in two stations in the neutrino beam line (see Fig. 2.3c), the expansion port and the target-manhole. The difference over the sum of the two halves of the split-plate ion chamber was used as a quantitative steering parameter. A marked asymmetry in the signals from the two halves indicated missteered beam. The steering cut, then, amounts to demanding a symmetric output of the split-plates, which corresponds to beam pointing to within ± 1.4 inches of the centre of Lab-E detector. The split-plates at both the stations were required to satisfy this cut. The proper steering was quantified as follows :

$$\frac{(LEFT - RIGHT)}{(LEFT + RIGHT)} < .1$$

$$\frac{(TOP - BOTTOM)}{(TOP + BOTTOM)} < .1$$

Roughly 10 %of the total WSM data were eliminated due to the steering cut.

§4.4 Final cuts and Wrong Sign Muon data

Having hand selected the WSM events and examined in some detail their kinematical distributions a set of final cuts was chosen. This included the nine previous cuts with the new toroid cut of $\rho_t < 65$ inches, to remove ambiguous events. The steering cut along with five additional cuts, listed below, were imposed on the final sample.

x. θ_μ cut

The polar angle of the muon, with the Lab-E axis as the z-axis, was required to be less than 200 milliradians. This cut ensured that the event had a reasonable geometrical acceptance. Fig. 4.1a shows the θ_μ distribution.

xi. P_μ cut

In order to be properly reconstructed in the toroid the muon must have an energy above a certain minimum. Due to the PLACE cut, the muon must traverse through a minimum of 2.m of steel (1.7m for E701), and therefore must have enough energy to overcome the energy loss in the target before it reached the toroid. The minimum momentum cut is chosen to be 7 GeV.

xii. X cut

X is the scale parameter of deep inelastic scattering. In order to have a legitimate deep inelastic scattering X must be between 0. and 1 (See Appendix B and C).

xiii. Y cut

Y is the inelasticity of the interaction. It was also required to be between 0. and 1. (See Appendix B and C).

xiv. **Q^2 cut**

The Q^2 of the event was demanded to be within 0. and 999. This cut is intended to throw away any spurious event in the regular data set. For WSM The above two cuts did not eliminate any event.

§4.5 Distributions of some kinematical variables of WSM

Fig. 6.1a, Fig. 6.2a, and Fig. 6.3a display histograms of the total visible energy(Evis), momentum of the muon (P_μ) and the hadron energy (E_H) for the entire sample of WSM. The entries with error bars represent data and the solid lines are the computed backgrounds (see Chapter 5). Since WBB constituted one of the largest backgrounds the data were also examined under an additional cut requiring $Y > .5$. Below and in subsequent chapters, WSM, CC or backgrounds with this additional Y cut, will be referred to as Group Y. In contrast, the events (WSM, CC or background) with no Y cut belong to Group X. Fig. 6.1b, Fig. 6.2b and Fig. 6.3b show distributions of Evis, P_μ and E_H. Fig. 4.2 shows a histogram of the geometrical weights associated with WSM events of E616. However, the acceptance of any event can be calculated only if the mechanism of its production is known. If, indeed, WSM exist beyond backgrounds then the acceptance calculation mentioned above is moot. This issue is discussed in greater detail in Chapter 6. Fig. 6.5a and Fig. 6.6a depict the x and y distributions for WSM. The same distributions for WSM, Group Y, is shown in Fig. 6.5b and Fig. 6.7b. It should be noted that the total visible energy, muon energy and the hadron energy distributions are on the log scale.

4.5.1 Missing energy

The dichromatic structure of the beam provided a means of measuring any missing energy in the neutrino interaction. This has been discussed in Chapters 2 and 3. In a regular charged current event there should not be any missing energy. Fig. 4.3 shows the distribution of the measured missing energy for CC events. The analogous distributions for WSM, Group X and Group Y, are presented in Fig. 6.4a and Fig. 6.4b. The graph shows a few events with missing energy greater than 20 GeV. These are in concordance with the expectation, since one of the backgrounds for WSM is NC induced dileptons. The leading lepton in this reaction is a neutrino and hence the large missing energy.

§4.6 Equivalent charged current sample

The CC events corresponding to the sample of WSM are needed to obtain the relative rate of the latter. The CC data of E616 and E701 were made to pass through the identical set of fourteen cuts along with the steering cut, except that the muon momentum was required to be positive.

The characteristics of the CC events, obtained through the steps outlined above, is shown in Table 6.3. The number of CC events along with the WSM events in two energy bins of Evis, Evis $<$ 100 GeV and Evis $>$ 100 GeV, are listed in Tables 6.1a and 6.1b for two Y cuts. The average values of certain kinematical quantities of WSM are presented in Tables 6.2a-6.2d for various cuts, whereas Tables 6.9 and 6.10 collate these events with other multimuon events. This comparision will be discussed in detail in Chapter 6.

Chapter 5

Background

The backgrounds for Wrong Sign Muons can be broadly classified into two categories :

1. Wide Band Background

   Pions and kaons that decay before the momentum selection in the dichromatic train (see Fig. 2.8) constitute a source of diffused low energy neutrinos and antineutrinos which are referred to as the wide band background (WBB). WBB illuminates the detector uniformly. The modeling of this background is rather difficult since its production depends upon the various beam line elements and details of beam dumping. Indeed, any scraping of the beam or any collimator along the beam line could be a potential source of the WBB. As mentioned earlier, to estimate this background, events were recorded with protons on target but with momentum defining collimator closed. Such events could then be used to subtract out the WBB content of the open-slit data. However, at positive energy settings the WBB is not as large with respect to WSM as it is for negative energy setting. This necessitated a Monte Carlo calculation of the WBB. In reference to WSM the main sources of WBB are two :

a. The production and decays of π^-/K^- at the BeO Target

b. The production and decays of π^-/K^- at the Primary Dump

In addition to the above, we have estimated the WBB $\overline{\nu_\mu}$ from three other sources:

c. WBB $\overline{\nu_\mu}$ from μ^+ decays in the decay region

d. WBB $\overline{\nu_\mu}$ from the interactions of the secondary particles (p, π^+, K^+) in the Secondary Dump which was stationed at the end of the decay region

e. WBB $\overline{\nu_\mu}$ from the interactions of the secondary particles with the material of the monitoring devices at the Expansion Port and Target Manhole

The first two sources of WBB antineutrinos will be referred to as target WBB and dump WBB respectively. The contribution to the WSM sample from the three latter sources, discussed in Appendix H, constitutes less than 2%of the amount due to the first two. Fig. 5.0a shows, schematically the production of WSM due to this background. In the sections which follow, we sketch the Monte Carlo computations of WBB from these two sources. The Monte Carlo reproduced the low energy tail of the WSM data satisfactorily. It was also consistent with the meager data accumulated during close-slit running.

ii. Dilepton Background

Neutrino interactions could produce dileptons ($l^- \mu^+$), where the leading lepton (l^-)

is not observed, and such a reaction would mimick a WSM. There are three prominent interactions which contribute to the dilepton background.

a. Missing μ^- in a regular dimuon event. See Fig. 5.0b for the Feynman diagram of this interacition.

b. Neutral current induced production and decay of π^+/K^+. Fig. 5.0c contains the Feyman diagram depicting WSM production from this source.

c. K_{e3} induced $e^-\mu^+$: By K_{e3} is meant the three body decay mode of Kaons which produces an electron neutrino,a positron and a π^0. The decay is expressed as (Refer to Fig. 5.0d):

$$K^+ \longrightarrow e^+\pi^0\nu_e$$

The ν_e spectrum at the apparatus is shown in Fig. 2.8.

In the discussion that follows estimates of the above backgrounds and of the cosmic ray background are presented. The comparison with the data is tabulated at the end of this chapter. Without the Y (inelasticity) cut signal for WSM at two sigma is barely visible. However the excess of WSM events becomes more prominent after one imposes that Y be greater thatn .5.

§5.1 Wide Band Background

5.1.1 Closed slit data

A first estimate of WBB was provided by WSM from the closed slit data. Closed slit data were accumulated to measure WBB contamination of the regular CC events. The measurement of this background was made by letting the dichromatic train operate normally, but with the momentum defining slit closed. This prevented any pion or kaon from entering the decay pipe. Consequenlty neutrinos reaching the apparatus originated from the upstream decays of the mesons and provided a measure of WBB.

WSM events constituted a small fraction of the closed slit data. These data were extracted with cuts identical to those described in Chapter 4. After imposing the priliminary fiducial cuts, the events were scanned and interactively reconstructed. Tables 5.2a and 5.2b list these events from the close-slit data of E616 and E701 respectively. The tables also contain the Evis and Y of the events. The number of events at an individual setting is too small to draw any tangible conclusion about this background. It was assumed that the wide band background for antineutrinos in a positive setting is independent of the energy setting of the secondary beam. This assumption was confirmed by the Monte Carlo calculation. Fig. 5.1 shows the number of interactions in Lab-E detector from WBB-antineutrinos versus the five energy settings. The WBB antineutrinos originating at the primary target were found to be completely independent of energy setting. However their production at the primary dump rose slightly as the secondary energy went up. This does not impugn the assumption above since the the dump production was a small fraction of that at the primary target.

The data from the closed slit was then normalised to the total number of protons on the target for open stit running. Before carrying out this normalization cosmic ray background of the WSM close-slit data was estimated. This was accomplished by extracting cosmic rays (see section 5.3), and normalising the cosmic ray live-time to the live-time of the apparatus while the close-slit data was taken. For both the normalizations one needs the number of protons impinging upon the BeO target for all the spills that pass the steering cut as well as the live times. These numbers are presented in Tables 5.1a, 5.1b and 5.1c. The former two contain the incident flux information while 5.1c provides the live-time information during close-slit running. The corresponding informations, for open-slit running, are furnished in Tables 5.3a and 5.3b, and 5.4a and 5.4b. Tables 5.4a and 5.4b also contain the total secondary flux information which is used in estimating K_{e3}-induced dilepton background of WSM (see Sec. 5.2.3).

Even when all the settings are lumped together the paucity of events made the precise determination of WBB spectrum intractable. The closed slit data did, nonetheless, provide a broad outline of the energy spectrum of the WBB events and a check on the Monte Carlo computation.

5.1.2 Estimation of WBB originating at the target

The neutrino beam line and the beam Monte Carlo have been described briefly in Chapter 2 [23,24]. The beam Monte Carlo was employed to compute the target WBB. The salient features of the calculation are as follows :

The production of the secondary particles was simulated following Atherton et al. [21]. The momentum spectrum of the π^- and its "P_t" distribution are discussed in Appendix D. The secondary π^- and K^- were traced through the beam elements till they were swept out of the beam. Almost all of the rays of π^- and K^- were focussed out of the beam by the time they reached the third beam element. Out of 100,000 secondary π^-, the number of surviving π^- at various longitudinal distances is shown in Table 5.5. A weight was assigned to each π^-/K^- quantifying the probability of its decay during the flight. Finally the probability of the acceptance of the resultant anti-neutrino by the Lab-E apparatus was computed. Fig. 5.2 shows the target WBB antineutrino energy spectrum at Lab-E from π^- and K^- normalized to the total number of protons incident on the target for both the experiments.

5.1.3 Estimation of WBB originating at the primary dump

The function of the primary dump, which was actually an aluminium insert in the beam line, was to absorb principally the 400. GeV protons that passed through the BeO target without interacting. The angle of dumping and the z-location of the collimator varied from energy setting to energy setting. Table 5.6 gives the angles and the z-locations of the collimators for three energy setting – 250, 200, and 165 GeV. The dumping angles for the 140 and 120 settings were roughly the same as that for 165. GeV.

Estimation of antineutrino flux from proton interactions in the dump is similar to the procedure described in the preceding section. The details of the dump simulation followed along the lines of references [25, 26 and 27]. We checked our calculations against the measurement and the calculations performed by CDHS and CHARM [28 and 29]. The first few interaction lengths of the dump were composed of aluminium. Consequently a correction [22] has to be applied to Atherton's data which was obtained for Proton-Be interaction. The Atherton data were corrected for the difference of production rates in Be and Al by multiplying by $(A(Cu)/A(Be))^{.7}$.

Fig. 5.2 shows the energy distribution of the antineutrinos at Lab-E, produced by 5.55×10^{18} protons, the entire proton flux for E616 and E701, for positive settings, interacting in the dump. The factor of three excess of antineutrinos from the former source is apparent from the figure.

5.1.4 Acceptance of μ^+ produced by WBB$\overline{\nu}_\mu$ in Lab-E

In order to calculate the number of WSM from WBB the acceptance of the neutrino detector must be folded into the ν_μ spectrum. A Monte Carlo, which simulated the neutrino detector, was used for this purpose. Fig. 5.3a plots the acceptance of WSM coming from WBB nueutrino versus energy. This plot pertains to E701 apparatus. The acceptance for E616 apparatus was somewhat lower at low energies since the spectrometer subtended a smaller solid angle for events with larger PLACE. To cut down the WBB one may impose cut in Y of .5. The acceptance of WBB events with Y>.5 is plotted against total visible energy in Fig. 5.3b

After determining the acceptance the total contibution of WBB ν_μ to WSM may be computed. The cross-section for $\overline{\nu}_\mu$ interaction is assumed to be:

$$\sigma_{\overline{\nu}-N} = .34 \times E_{\overline{\nu}} \times 10^{-38}$$

which yields $.95 \times E_{\bar{\nu}} \times 10^{-11}$ interactions per incident antineutrino for the stated fiducial volume of the E616 apparatus. The latter number for the E701 apparatus is $.60 \times E_{\bar{\nu}} \times 10^{-11}$. Fig. 5.4a is a histogram of the total visible energy of the WBB events from the two sources. Table 6.1a compares the number of events in this background with the number in other dilepton backgrounds and the WSM data. Fig. 5.4b and Table 6.1b depict the same for Group Y events.

§5.2 Dilepton Backgrounds

The dilepton interactions which mimick WSM events cannot be identified on an event by event basis. This is chiefly due to the high density of the neutrino detector. Instead, the number of these interactions has to be estimated statistically. For instance, OSDM events where the leading muon, μ^-, remains unobserved, constitute one of the dilepton backgrounds. A simple extrapolation of the dimuon data[16] intimates that the contribution of this background to WSM sample is $\approx$ 5 to 6 events which is in fair agreement with the number (6.9 ± 1.5; see Table 6.1a) furnished by the detailed Monte Carlo calculation. The main component of this calculation is a Monte Carlo program which simulates dimuon production in the Lab-E apparatus. The Monte Carlo has been described in detail in ref [16], therefore only the salient features of this program are given below.

5.2.1 Dimuon Monte Carlo Program

A neutrino interaction with two muons in the final state is called a dimuon interaction. Symbolically:

$$\nu_\mu + N \longrightarrow \mu^- + \mu^+ + X$$

Whereas the sources of like-sign dimuon events are not well known, the opposite sign dimuon interactions, their sources, and their kinematical properties can be explained and modelled within the context of standard model. The dominant source of opposite sign dimuon events is the production and semileptonic decay of D-mesons [30,31,32,33] in ν-N interactions as confirmed by Bubble Chamber and Emulsion experiments [34,35,36,37,38]. According to the prevaling phenomenology of hadron production, the D-meson comes about through the fragmentation of a charm quark produced in the neutrino-nucleon scattering. Infact opposite sign dileptons in neutrino-nucleon scattering offerred the first experimental evidence for open charm [39]. The program simulates the dimuon production, following ref. [48], in the following steps:

a. Deep-inelastic production of the charm quark

The dimuon Monte Carlo program takes as input the single muon CC events. These events are generated by the single muon CC Monte Carlo described in Appendix E. The rate of production of charm quark is proportional to

$$d(x) \cdot sin^2\theta_c + s(x) \cdot cos^2\theta_c$$

where d(x) and s(x) denote the valence and the sea quark distributions respectively. In the program the distributions measured by CCFRR have been used. Since the mass of the charm quark is significant, it cannot be ignored in the expression for the scaling variable x. The mass-corrected scaling variable is often reffered to as 'slow scaling variable' or x' where

$$x' = \frac{(Q^2 + M_c^2)}{(2 \cdot M_P \cdot E_H)} = x + \frac{M_c^2}{2 \cdot M_P \cdot E_H}$$

Here M_c is the charm quark mass, Q^2 is the square of the momentum transfer and E_H is the energy of the hadron (see Fig. 5.0.b). The differential cross section for the production of charm quarks may be written as:

$$\frac{d^2\sigma}{dx\,dy} = \frac{G_F^2 \cdot M_P \cdot E_\nu}{\pi} \left(x'\, d(x')\, sin^2\theta_c + x'\, s(x')\, cos^2\theta_c\right) \left(\frac{1}{1 + \frac{M_c^2}{Q^2}} \right)$$

where E_ν is the energy of the incident neutrino and G_F is the Fermi constant. It should be noted that the last factor is essentially that for the production of a heavy quark.

b. Fragmentation of the charm quark

Fragmentation of quarks into hadrons is one of the least understood processes confronting QCD. The fragmentation of the charm quark into D-meson therefore has been handled phenomenologically in the Monte Carlo. Fragmentation is described through the scaling variable z, where

$$z = \frac{E_D}{E_c} \approx \frac{E_D}{\nu}$$

i.e. z is the fraction of energy taken by the charmed meson in the W-nucleon centre of mass system. Charm being a heavy quark is expected to display hard fragmentation i.e. the fragmentation function should peak at higher values of z [41,42]. The fragmentation itself is parametrized following Peterson et.al. [43]. If D(z) were the fragmentation function then

$$D(z) = \frac{1}{z \times (1 - \frac{1}{z} - \frac{\epsilon}{1-z})^2}$$

where ϵ was treated as a free parameter. A measurement by the Argus collaboration [95] yields the best value for ϵ at $0.19 \pm .04$. The D-meson was given a P_T distribution (following LEBC EHS result [44]) as follows:

$$f(P_T) = e^{-a P_T^2}$$

where the constant a = 1.1.

c. Semileptonic decay of the charmed meson

Finally the fragmented charmed meson was made to decay semileptonically. The square of the decay-amplitude was parametrized following Barger and Phillips and Gottschalk [46,47,48]. If M represents the decay amplitude then

$$|M|^2 = (2P_D \cdot P_l) \cdot (2P_D \cdot P_\nu) - (M_D^2 - 2M_X^2) \times (2P_\nu \cdot P_l)$$

where P_α refers to the four momentum of the particle α and M_X is treated as a free parameter with the dimension of mass. Its value, .65 GeV, was chosen to provide a good fit to the inclusive production of electrons from D-decays which was measured at $\psi''(3772)$ by DELCO [46,47]. The smileptonic branching ratio was assumed to be $(10.9 \pm 1.4)\%$.

There is one other source of opposite sign dimuon. In a regular neutrino induced CC event, the hadron shower may produce a π^+ or a K^+ which then may decay to a μ^+.

This source of dimuons, far smaller than the previous source and subsequently treated as a background, is described briefly in the section below. The kinematical distribution of background subtracted dimuon data agreed well with the charm Monte Carlo program. Figs. 5.7 show certain relevant comparisions between the two [16].

5.2.2 Dimuon events with missing μ^-

A dimuon event in which the leading muon, μ^-, is unobserved would appear to be a WSM. There are two ways in which the μ^-, might evade detection. Either it could escape out the sides of detector, or it could range out in the target, before or right after the hadron shower. For calculational purposes following selection rule was chosen : if the μ^- (the leading muon) succeeded in penetrating enough steel beyond the end of the shower so as to show up in three spark chambers, the event was rejected as a dimuon. This amounted to demanding that the leading muon should traverse through 60. cm of steel beyond the end of the hadron shower in either case.

The dimuon Monte Carlo program was employed to estimate this background. Once the dimuon was produced the criterion discussed above was applied. The penetration of hadron shower of a given energy in the detector was simulated by using the data of the test run of E744 and E652 accumulated during May-June 1984 [49]. The test run and the experimental set up is discussed briefly in Appendix I. The integral probability for the shower penetration for various hadron energy is shown in Table 5.7. Fig. 5.5 shows the probability vs length of shower penetration in the Lab-E detector for various hadron energies.

The candidates for WSM were selected and normalised to the single muon charged current event sample for each setting. Fig. 5.6 shows the total visible energy distribution from such events normalised to the total charged current sample of the two experiments. Table 6.1a compares this background with all of the others as well as the data. Most of these events had Y>.5. The corresponding comparision, for Group Y events, is presented in Table 6.1b.

5.2.3 Neutral current induced π^+/K^+ production and decay

In a neutral current interaction a μ^+ might be generated at the hadron vertex. This muon would be a decay product of a π^+ or a K^+ produced in the hadron shower. Such a neutral current interaction would look like a WSM. This background is, for WSM, analogous to the background for opposite sign dimuons. The calculation for this background aims at answering the following question : given the hadron energy of an event, what is the probability of producing a μ^+ at the hadron vertex such that the event satisfies all the cuts on WSM mentioned in the earlier chapter? For a given event the program took two inputs, the hadron energy and the scaling variable X. The program was equipped with the BEBC Nu-Ne and EMC (μ-P) hadron production and multiplicity data (see ref [16 and 50]). The production of μ^+ from the subsequent interactions and decays of these hadrons was computed using the prompt and non-prompt muon production by hadrons measured by E379 [51]. The P_T or the angle of the generated muon was computed from the fits made to the transverse momenta of hadrons in EMC μ-P data. Fig. 5.6 shows the histograms of total visible energy for these events. The plots have been normalised to the charged current sample for the two experiments. Table 6.1a lists this background along with the others and with the WSM data.

5.2.4 K_{e3} induced $e^-\mu^+$

The dimuon-like interaction of the ν_e in the neutrino detector, where ν_e arises from the three body decay of a kaon, induces the third background for WSM. In this case the leading lepton, e^-, would be absorbed in the hadron calorimeter and the μ^+ produced from the semileptonic decay of the D-meson would appear like a WSM. In chapter 2 the relative flux of ν_e from K_{e3} decay was shown. As mentioned in the Sec 5.1.1, Tables 5.4a and 5.4b show the total number of secondaries for the two experiments. The accompanying Table 5.4c lists the fraction of kaons in the secondary beam for each setting. To calculate this background, the ν_e flux at Lab-E from K_{e3} decay, was computed and the flux was used to generate events in the apparatus. These events were used as input to the dimuon Monte Carlo described above and the dileptons subsequently were generated. Since the neutrino detector at Lab-E cannot distinguish between the electromagnetic and hadronic showers, the leading lepton, e^-, was merged with the hadrons. The resultant distribution of background events is presented in Fig 5.6 which contains the Evis histograms for such events. Table 6.1a compares this background with the others.

Fig. 5.2 offers a comparision of the three dilepton backgrounds. One notices that the first two backgrounds, OSDM with the leading μ^- undetected and NC induced π^+/K^+ decays, have similar magnitudes as well as shape. Both are slightly larger than the K_{e3} background. Table 6.1a and 6.1b match these magnitudes more candidly. After the Y cut was imposed the magnitude of these backgrounds diminishes only slightly ($\approx$ 7%), however, the shape of the distributions remain virtually unchanged.

Finally Fig. 5.4a illustrates the total dilepton background contribution to WSM. The histogram has been normalized to the total CC event sample. From the figure 5.4a, it is evident that the WBB background is the dominant one below 150 GeV. Dilepton backgrounds are the major contributor to WSM after 150 GeV. The situation is some what different for WSM where a $Y > .5$ cut has been imposed. The distribution is presented in Fig. 5.4b. WSM events with $Y > .5$,from WBB and dileptons, have been separately histogrammed in this figure. Above 100 GeV, one notices, that the dilepton contribution completely dominates the WBB events. Further details and ramifications of this comparison are discussed in the Chapter 6.

§5.3 Cosmic Ray Background

Cosmic rays constituted a small background at the low energy tail of the WSM data. As pointed in the earlier chapter the cosmic ray content in the slow spill data was almost eliminated by making a cut on the total visible energy. The estimate of this background is outlined below.

A hundred cosmic ray events were extracted from each experiment. The extraction of these events was identical to that of WSM. These events were visually scanned and interactively reconstructed. Finally the set of final cuts, identical to the data and other backgrounds, were imposed. The resulting set of cosmic ray events were renormalised to the live-time of the data. Tables 5.3a, 5.3b, 5.4a and 5.4b show the live times for the event-gates and cosmic-ray-gates for the two experiments. The contribution of this background to WSM open as well as close-slit data was computed. None of the cosmic ray backgrounds survived the Evis or Y cut.

Chapter 6

Results and Conclusion

The backgrounds producing WSM do not account for the entire observed data sample. A possible signal of WSM at the 2σ level emerges after imposing a cut of 100 GeV on the total measured energy. This effect becomes more pronounced by an additional cut on the inelasticity, Y, of the events. These two cuts eliminate most of the WBB contribution to the WSM sample. The Evis cut diminishes the dilepton backgrounds by half, however, the Y-cut does not alter its contribution significantly. This chapter will examine these backgrounds closely (Sec. 6.1), compare their kinematical distributions with the data (Sec. 6.2), and endeavor to arrive at a limit on the rate of production of WSM (Sec. 6.3). This limit is the best answer to the question: whether WSM exist as distinct phenomenon.

Next (Sec. 6.4) the rate and kinematical properties of WSM are compared with those of opposite-sign dimuons and like-sign dimuons. The contention, whether WSM events constitute the "neutral current analog" of OSDM and LSDM, will be addressed.

If one could proclaim a signal for WSM, one might entertain the possibility, within the standard model, that a higher order process accounts for the occurrence of such events. For instance, the intrinsic charm of the nucleon sea might produce a WSM in a neutral current interaction. Then, based on the limit of the production of the WSM, one can place limits on the intrinsic charm content of the nucleon sea. This limit, with 90 %confidence level, has been found to be,

$$\eta_C = \frac{C}{U} < .02$$

The calculation and the limit will be presented below (Sec. 6.4.2.2).

In the same speculative vein, one may conjure an extention of Weinberg-Salam theory to explain WSM by means of a small, flavour-changing, neutral current coupling. Assuming such a mechanism for the production of WSM, we will derive an upper limit on the rate of flavour changing NC interactions (Sec. 6.4.2.1). The result, with 90 %confidence level, could be expressed as follows,

$$\frac{\sigma(\text{flavour changing NC})}{\sigma(NC)} < .0085$$

The study of WSM and their related backgrounds offers a venue to explore the right-handed couplings in the weak interaction within specific assumption. This topic will be dealt with in Sec. 6.5.

§6.1 Wrong Sign Muons and the backgrounds

We first turn to the question,"Is there a WSM signal?". The table below includes the observed WSM data and the computed backgrounds with and without the Y cut.

	$Y < 0$			$Y > .5$
	$Evis < 100$	$Evis > 100$	$Evis < 100$	$Evis > 100$
DATA	400 ± 20	43 ± 6.6	58 ± 7.6	24 ± 4.9
BACKGROUND				
Total	397 ± 79	22.4 ± 4.5	47.7 ± 9.5	11.2 ± 2.2
WBB Closed Slit	375 ± 85.9	0 ± 19.7	19.7 ± 19.7	0 ± 19.7
WBB MC	389	14.0	40.2	3.0
Dilepton	8.5	8.55	7.5	8.2

WSM: Data and backgrounds.

One notices that the background estimate of the low energy WSM agrees well with the observed data. This lends credence to the modeling of WBB. As discussed earlier, parametrizing this background is rather difficult. There are grave uncertainties, (for example possibility of beam-scraping, holes in the primary dump and interactions of the primary protons even before it is transported to the BeO target), which may jeopardise the credibility of the Monte Carlo calculations. The agreement of the predicted number of WSM with the data for Evis $<$ 100 GeV is therefore reassuring. One may then venture to trust that the calculation yields the number of WSM above 100 GeV reliably. Still, the uncertainty due to possible holes in the primary dump persists, since this could cause the high energy WBB component of the background to go up without appreciably affecting the low energy content. However, above 100 GeV the contribution to WSM sample from the primary dump is ≈ 1.5 events. Even if this contribution were to be increased by a factor of five, a 2 standard deviation effect of WSM would persist.

To further curtail the WBB background, $Y > .5$ requirement is imposed. A scatter plot of Evis vs Y (see Fig. 6.8) reveals a clustering of events with $Evis > 100$ GeV and $Y > .5$. A band in the scatter plot where very few events occur is marked. This plot motivated a detailed investigation of WSM with $Y > .5$. The table above indicates that the WBB component in the WSM sample, above 100 GeV consists of only three events. Apart from the uncertainties of the WBB Monte Carlo, this estimate depends upon knowledge of the antiquark distribution in the nucleon. From the published results on the structure functions, F_2 and xF_3 the error on the antiquark distribution is 9.67 Mean values of X and Q^2 of the WSM sample were used to estimate this error. The error associated with the background estimation is assumed to be ≈ 20%. Therefore in calculating the WBB component of the background one is not limited by the uncertainty in the structure functions. On a note of circumspection, one might further assume that all of the WSM events above 100 GeV with no Y cut, arise from the backgrounds. This would imply a total of 34.5 WBB induced events (as against 14 indicated in the table). The assumption, when carried over to the sample with $Y > .5$, causes the WBB component of the background to increase from 3 events to 7.4 events. Thus the total background for WSM with $Evis > 100$ GeV and $Y > .5$, would be 15.4 events. If the errors were added in quadrature, there are still (9 ± 5.4) excess wrong sign muons. Hence the effect continues to manifest itself at the 2 standard deviation level. The preceding table and discussions demonstrate, if one insists on conservative punctiliousness, that the observed WSM events constitute a signal beyond one standard deviation and within two standard devaition of the background estimates.

Next, the detailed comparison between the data and the background will be carried out. Table 6.1a presents the WSM events along with the four backgrounds,in two energy bins, below and above 100 GeV. Table 6.1b shows the same with the additional cut of $Y > .5$. One notices that the events exceed the backgrounds by roughly a factor of 2 in both cases.

With no cut on Y there were 43 WSM events and $22.3 + 4.6$ background events. The corresponding numbers with $Y > .5$ cut were (24 ± 4.6) and (11.2 ± 2.2). The error on the background is assumed to be 20 If the errors were added in quadratures, this would imply an excess of 20.6 ± 7.9 and 12.8 ± 5.4 events for the two cases. A summary of kinematical properties of these 24 events is given in Appendix F.

Fig. 6.1a and 6.1b are the plots of the total visible energy distribution of WSM and the backgrounds for the two cases. The excess of data is noticeable particularly at higher energies.

§6.2 Kinematical Distributions

This section aims at bringing out differences in the shapes of various kinematical distributions between the data and cumulative background. The kinematical quantities of the data and the backgrounds which have been considered here are total visible energy

(Evis), momentum of the μ^+ (P_μ), hadron energy (E_H), missing energy, X, Y and Q^2. Tables 6.2a-6.2d list the mean values of these kinematical quantities of WSM from data and computed backgrounds. The four classes of events being considered are (a) no cuts imposed on Y or total visible energy Evis, (b) Y $>$ .5 and no cut on Evis, (c) no cut on Y and Evis $>$ 100 GeV and (d) Y $>$ .5 and Evis $>$ 100 GeV. The last class shows the largest excess of number of events over the background events. Further, the mean values of the kinematical quantities for the data lie between the WBB and the dilepton backgrounds. Table 6.2d reveals a marked difference in the average values of missing energy, X and Q^2 for WBB and dilepton backgrounds. Making further cuts on missing energy, x and Q^2 failed to diminish the backgrounds or bring about a better understanding of the excess of the data, primarily due to lack of statistics.

A similar table, Table 6.3, shows the mean values of the corresponding kinematical quantities for single muon charge current events. These events were culled from the original data set with cuts similar to WSM (see Chapter 3) and were used in the subsequent normalization of the dilepton backgrounds to the data. The numbers mentioned in the tables above represent "raw" data, meaning that the events were not corrected for acceptance in the neutrino detector. The acceptance correction applied to CC events, as well as to the backgrounds of WSM, is discussed in the section below.

Figures 6.2a-6.7a compare the following distributions for data and the cumulative background : muon momentum, hadron energy, missing energy, X, Y and Q^2. Figures 6.2b-6.7b carry out the same collation for the class of events – data and cumulative background, with Y $>$ .5 and Evis $>$ 100 GeV. No sharp disagreement in the shape of any of the above kinematical quantity between the data and the cumulative background is observed. From the figures it appears that the background reproduces the shapes of the various distributions.

§6.3 Rate for WSM events

To quote a limit on the rate of production of WSM it is necessary to correct for the geometric acceptance of such events in the Lab-E detector. Only an acceptance-corrected rate may be compared with measurements of similar events in other detectors. However the calculation of such acceptance is feasible only if the mechanism of production of WSM is known. The arguments presented in Sec. 6.1 suggest that the number of WSM cannot be entirely accounted for by invoking the various backgrounds. Further complexity arises from the vastly different detection efficiencies for the four backgrounds in the Lab-E detector. Therefore, to attempt a calculation for the acceptance correction for WSM and thereby to arrive at a limit on the rate of WSM production, it was assumed that the excess of data originated from the backgrounds. Each background was considered separately. For example, first it was assumed that the excess of WSM (20.7 events when no Y cut was imposed) were WBB antineutrinos and their acceptance was computed accordingly (the acceptance corrected number was then 21.27). The same steps were repeated for each of the other three backgrounds. Table 6.4 lists the acceptance-corrected number of excess WSM corresponding to each model.

The group of WSM with $Y > .5$ was treated in similar fashion. Table 6.4 also presents the acceptance-corrected numbers for $Y > .5$ group. It should be noted that, for this group, the cumulative dilepton model and WBB model yield very similar numbers of WSM after the acceptance correction. This table also contains the raw and acceptance-corrected numbers of single muon charged current events.

Table 6.5 presents the resulting rates of production of WSM for each of the various models. Assuming a 20%error in the background estimation, for $Y > .5$ and Evis > 100, the raw number of background events was 11.2 ± 2.2. The corresponding raw number for data was 24 ± 4.9. Adding the errors in quadrature, this yielded an excess of 12.8 ± 5.4 events. This implies that the raw rate of production of WSM is $< 1.3 \times 10^{-4}$, with 90 The corresponding acceptance-corrected number is 3.1×10^{-4}. Table 6.6 presents these rates for the two cases of Y cuts.

§6.4 Comparision of WSM with multimuon events

It is interesting to compare the hadful of WSM events with the other multimuon events. Motivated by the fact that there could be an effect causing WSM, this comparision has been carried out in this section. Various ramifications based on the limit of rate of production of WSM have been discussed.

6.4.1 WSM versus LSDM

The two types of anamolous events of neutrino interaction, Wrong Sign muons and Like Sign dimuons, have very similar rate of production: 1.8×10^{-4} for WSM and 1.4×10^{-4} for LSDM. The conjecture that they might arise from similar sources was discussed in Chapter 1. One question worth investigating is whether WSM are the neutral current counterparts of the same mechanism which produces LSDM in CC interactions. In the abscence of exotic processes giving rise to LSDM, the current inclination is that the origin of these events are related to origin and production of charm. This charm production is different from flavour changing currents which would give rise to the opposite sign dimuon. LSDM requires that there be an anticharm in the final state hadronic system. The mechanism would also furnish (e.g. char-anticharm production) a charm which susquently could explain the WSM events. It should be pointed out, however, that the first estimates of such mechanism involving perturbative QCD techniques, give rates for LSDM production which an order of magnitude lower than the ovserved value. In spite of the unclarity of the LSDM situation, one would like to investigate the connection between the $\mu^- \mu^-$ and WSM events. This question will be addressed in this section.

In order to investigate the proposed similarity between WSM and LSDM, the entire analysis, that is , the extracting of WSM and CC data and background calculations, was carried out with LSDM cuts. These cuts differed from those previously mentioned in that (a) a cut on hadron energy $>$ 2. GeV was applied; (b) the event transverse vertex position was constrained to lie within a square of $\pm$50"; (c) the hole-cut was loosened: (d) the momentum of the muon was required to be greater than 9 GeV; (e) the cut on the angle of the muon was loosened. These differences are tabulated in Table 6.7.

Table 6.8a and Table 6.8b present the WSM data and backgrounds with LSDM cuts. The tables also contain the mean values of the various kinematical distribution. Two additional cuts of Evis $>$ 100 GeV and Y $>$ .5 have been imposed on the entries of

Table 6.8b because of the following reason. In Table 6.8a one observes that most of the data with Evis below 100 GeV are due to the backgrounds. Out of a total of 305 WSM events, the 272 below Evis of 100 GeV, are almost entirely WBB antineutrinos. However, above Evis of 100 GeV, the ratio of data to background is 2. To reduce further the WBB contibution to the data, the cut $Y > .5$ was imposed. This brought down the number of WSM events with Evis > 100 GeV from 33 to 20. To compare WSM with multimuon events these 20 WSM are considered.

The collation with LSDM is carried out next. The leading muon in a LSDM event is treated as neutrino and consequently unobservable. The nonleading muon becomes the leading lepton and is used in calculating the scaling variables X and Y and Q^2. The mean Evis drops from 151 GeV to 93 GeV and the average missing energy goes up by the same amount. Similarily $<Y>$ changes significantly (where $< >$ represent the average value). Upon this sample the cuts of Evis > 100 GeV and $Y > .5$ are imposed. The resultant set of events are the "neutral current" analog of LSDM. This is compared to WSM sample with identical cuts. Table 6.10 summarises the analyses of LSDM and the "neutral current" analogue of LSDM. After background subtraction there are 7.8 ± 4.3 LSDM and 15.2 ± 6.8 WSM above Evis of 100 GeV. The average values of all of the kinematical quantities agree, within errors, for the two classes of events. The paucity of events in both types of events hinders from drawing a quantitative conclusion about rates, in paticular, one cannot discern whether the WSM rate equals one third of the LSDM rate, as one would naively expect. A point of importance in the above comparision is to acertain whether the μ^+ in a WSM event originates at the lepton or hadron vertex. Unfortunately, from the existing data, one cannot infer that the μ^+ in WSM originated from the hadron vertex, nor measure the transverse momentum of the muon with respect to the hadron shower direction.

6.4.2 WSM versus OSDM

A further possibility is that WSM are neutral current analogs of Opposite Sign Dimuons. There are two ways in which this might come to pass.

The first is by way of a flavour changing neutral current coupling, for example the neutrino might interact with an up quark and produce a charm quark in the final state via neutral current coupling. This would produce a WSM as shown in Fig. 6.9a. Symbolically:

$$\nu_\mu + u \Rightarrow \nu_\mu + c$$

The kinematical distributions of such WSM would be quite similar to those of OSDM with the leading muon missing. The ramification of such an interaction is discussed in 6.4.2.1

The second mechanism, considering WSM as the neutral current anolog of OSDM, is by the dint of intrisic charm quark in the nucleon $q\overline{q}$ sea. Once again this process is not unlike OSDM production. An event is portrayed in Fig. 6.9b and this reaction can be described as:

$$\nu_\mu + c_{intrinsic} \Rightarrow \nu_\mu + c$$

The subsection below, 6.4.2.2, treats this possibility in some detail and arrives at a limit on the charm content of the sea quarks.

Table 6.9 contains the number of OSDM and the mean values of certain relevant kinematical quantities. To model the neutral current analog of OSDM, the leading muon is treated as neutrino. The nonleading μ^+ of the OSDM becomes the leading muon and is used in calculating the kinematical variables. As a result of the above rearrangement the mean Evis drops to 88.9 GeV from 151.5 GeV and the mean missing-energy goes up by the same amount. Similarily $< Y >$ changes significantly ($< >$ denotes the mean value). The third column of the table contains the corresponding WSM value. One notices that the mean values of Evis, Emis, hadron energy and the inelasticity, Y, agree within the errors for the two classes of events. It should be noted that the neutral current interaction of neutrinos has a somewhat different Y distribution (difference of $\approx$ 7%for up quark), arising from Z-couplings to right handed quarks, compared to the CC interaction. It is interesting to note that the ratio of the total numbers of WSM and NC analog of OSDM is $.214 \pm .147$, quite consistent with the ratio of NC to CC.

6.4.2.1 Flavour changing Neutral Current as source of WSM

The experimental result on the suppression of strangeness changing neutral current in the decays of kaons necessitated the existence of a new flavour and thus played a pivotal role in formulating the prevaling theory of weak interactions [39,52]. The postulated new quark, the charm quark, in the milieu of the electroweak interaction based on the non-abelian gauge group SU(2) X U(1), explained the above suppression quite successfully. Furthermore, the theory forbade any flavour changing neutral current. Assuming that the WSM arises due to flavour changing NC coupling, where an up quark is converted to a charm quark by the intermidiate Z boson, one may naively impose a limit on such an interaction as follows :

$$\frac{\sigma(\text{flavour changing NC}\rightarrow\mu^{+})}{\sigma(NC)} = \frac{N(\mu^{+})}{N(NC)\times Br(semileptonic)}$$

where, N(μ^{+}) is the number of acceptance corrected excess of WSM, Br is the semileptonic branching ratio of the D-meson (10.4 ± 1.5)%and N(NC) is the acceptance corrected number of neutral current events. From the rates WSM production quoted above, the desired limit on the flavour changing neutral currents, with 90 %confidence level is:

$$\frac{\sigma(\text{flavour changing NC})}{\sigma(NC)} < .0085$$

It should be noted that the corresponding limit on the flavour-changing neutral current decays of the bottom quark, shown in Fig. 6.10 , is < .34%at 90%confidence level [53].

6.4.2.2 Intrinsic charm content of the nucleon sea as source of WSM

Various experiments in hadron scattering have reported the observation of charm production [54,55,56and57], which amounts to ≈ 1% of the total cross section. These observations motivated the idea of an intrinsic charm component of the hadronic sea [58,59]. From the quark-gluon coupling one expects a small but non-zero number of charm and anticharm quarks in the neucleon sea. Naively, for $q\bar{q}$ configurations the vaccum polarization mechanism of Fig. 6.11 suggests a scaling regarding the number of a given flavour of quark with respect to its mass:

$$\frac{n_c}{n_q} = \frac{m_q^2}{m_c^2}$$

i.e., the ratio of the number of charm quarks in the sea to the number of up or down quarks will be roughly .44%. This idea of virtual gluon exchange followed by vacuum-polarization was employed within the context of the bag-model, (where all coloured particles are assumed to be confined by some effective QCD potential [60,61] by Donoghue and Golowich [62]. They estimated the probability of finding a five-quark state within the nucleon bag, |uudcc>, to be of the order of 1-2 %. In terms of the ratio discussed in the preceding paragraph this estimate would imply the average ratio of charmed to up quark to be .4 to .8 %. Brodsky et al. [58,59] have analysed this idea in detail. They have computed the contribution of the intrinsic charm to the structure functin F_2 to be:

$$F_2^{ic} = (\frac{2}{3})^2\, \xi\, [c(\xi) + \bar{c}(\xi)]$$

where $c(\xi)$ is the fractional momentum distribution of the intrinsic charm quark which is given by:

$$c(\xi) = \frac{1}{2} N_c\, \xi^2\, [\frac{1}{3}(1-\xi)(1+10\,\xi+\xi^5) - 2\,\xi^5\,(1-\xi)\,ln\,\xi^{-1}]$$

where $N_c \approx 3600$ and, ξ, the fractional momentum of the intrinsic c-quark is:

$$\xi = \frac{Q^2 + M_c^2}{2\,M_P\,\nu}$$

The mass of the charm quark is assumed to be 1.5 GeV. The probability of observing such a quark would be, from the expression above :

$$\int_{\xi_{min}}^{1} c(\xi)\, d\xi \approx \lambda$$

Brodsky et. al. assumed this probability to be ≈ 1% in order to account for the hadron production cross section for charm. As mentioned above, the WSM may provide a clue to the charm content of the nucleon sea. This is accomplished by considering the ratio of the WSM to OSDM and comparing it to the theoretical prediction. The steps to compute this quantity from the WSM rate are outlined below.

The differential cross-section of the neutral current scattering of a neutrino by an up-quark, in an isoscalar target, is given by :

$$\frac{d\sigma(\nu_\mu + u = \nu_\mu + u)}{dy} = \frac{2\, G_F^2\, M_P\, E_\nu}{\pi} [|C_L^u|^2 + |C_R^u|^2\, (1-y)^2 - \frac{1}{2} (\overline{C}_R^u\, C_L^u + \overline{C}_L^u\, C_R^u)\, \frac{M_P}{E_\nu}] \times \frac{(U+D)}{2}$$

where

$$C_L^u = t_3^u - Q_u^2\, sin^2\theta_W = .34$$

and

$$C_R^u = -Q_u^2\, sin^2\theta_W = -.16$$

and other terms have their usual meaning.

The value of $Sin^2\theta_W$ has been measured in E616 [63] to be .24 ± .012. The interference term is much smaller than the other two terms and will be neglected. Inserting this value and integrating over Y yields, for the up-quark:

$$\sigma(\nu_\mu + u = \nu_\mu + u) = \frac{2\, G_F^2\, M_p\, E_\nu}{\pi} \times (.124) \times \int_0^1 u(x)\, dx = \frac{2\, G_F^2\, M_p\, E_\nu}{\pi} \times (.124) \times U$$

The neutral current scattering off a charm quark will be given by an identical expression for the cross-section except that U is replaced by C, where C denotes the intrinsic charm content of the nucleon sea. One may further assume that

$$C = \eta_c U$$

So the cross-section of $\nu_\mu + c \rightarrow \nu_\mu + c$ is:

$$\sigma(\nu_\mu + c = \nu_\mu + c) = \frac{2\, G_F^2\, M_p\, E_\nu}{pi} \times (.124) \times \int_{\xi_{min}}^{1} c(x)\, dx = \frac{2\, G_F^2\, M_p\, E_\nu}{pi} \times (.124) \times C$$

The struck charm quark then fragments into a D-meson, which subsequently decays semileptonically into a μ^+. If D(z) represent the fragmentation function, B(semileptonic) the branching ratio for semileptonic decay of the D-meson, the cross-section for producing a μ^+ from a charm neutral current interaction will be :

$$\sigma(\nu_\mu + N = \mu^+ + X) = \sigma(\nu_\mu + c \rightarrow \nu_\mu + c) \times \int_{z_{min}}^{1} D(z)\, dz \times B(\text{Semileptonic decay of D-meson})$$

The cross-section for producing an opposite sign dimuon is quite similar (see Chapter 5). Here too, the charm-quark fragments into the D-meson which decays semileptonically to give a μ^+. Symbolically:

$$\sigma(\nu_\mu + N \rightarrow \mu^- + \mu^+ x) = \sigma(\nu_\mu + s or d) \times \int_{z_{min}}^{1} D(z)\, dz \times B(\text{Semileptonic decay of D-meson})$$

The ratio of the two expressions is:

$$\frac{\sigma(\nu_\mu + N = \mu^+ + X)}{\sigma(\nu_\mu + N = \nu_\mu + X)} = \frac{.124\, \eta_c\, U}{[U\, sin^2\theta_c + S\, cos^2\theta_c]}$$

where $sin^2\theta_c = .058$, $cos^2\theta_c = .942$, D = U and $S = .128 \times U$. The last quantity, the strange-sea content has been measured from studies of OSDM to be

$$\eta_s = \frac{2S}{(U+D)} = .068 \pm .016$$

The detection efficiency (or the acceptance) for the two reactions is expected to be very similar and can be cancelled. The rate of OSDM production is $(9.0 \pm .8) \times 10^{-3}$. If the rate of production of WSM is taken to be $< 3.1 \times 10^{-4}$, with 90 then

$$\eta_c < .02 \text{with } 90\% \text{confidence level}$$

The limit on the rate of production of WSM enables one to impose an upper limit on the charm content of the nucleon sea to be $.02 \times U$, with 90 Assuming that only half of the nucleon momentum is carried by valence quark, the above limit implies that the probability of observing an intrisic charm is less than .50 %with 90%confidence level. It is interesting to compare this limit with that proposed by the EMC collaboration [64]. They impose an upper limit on the probability of observing an intrinsic charm to be .59%with 90%confidence level. These experimetal results are quite consistent. Furthermore they are not in violent discordace with the proposed theoretical estimates.

§6.5 Limit on the right-handed coupling of neutrinos

An extension of Weinberg-Salam model considered by many authors [65,66,67,68and69] is a left-right symmetric theory. The gauge group of such a theory is postulated to be $SU(2) \times SU(2) \times U(1)$. The presence of the additional SU(2) gauge group implies the existence of right-handed coupling mediated by right-handed gauge bosons W_R. Since almost all the processes interacting weakly follow the V-A theory, it appears that the predicted right-handed boson must be significantly heavier than the left-handed boson at the present energies. This mass difference might be negligible at the Planck scale. Several experimental searches on such right-handed coupling in muon, pion and kaon decays have been made. Whereas the limit on the right-handedness in muon decays has been measured to be less than .41%with 90%confidence, the corresponding number for kaon decays is known to 5%only [70,71,72,73,74,75and76]. The present analysis on search for WSM in high statistics neutrino interaction offers an opportunity to impose a limit on the right-handed coupling of neutrino interaction, provided lepton number violating amplitude is non zero.

The angular momentum conservation constrains the Y distrubution to be proportional to $(1-Y)^2$ in such a reaction. Therefore we concentrate on the WSM sample with Y $< .5$. This condition eliminates the dilepton background. The table below presents the data and the calculated background for this sample.

	$Y < .5$	
	Evis < 100	*Evis* > 100
DATA	342 ± 18.5	19 ± 4.4
BACKGROUND		
Total	349.3 ± 70	11.2 ± 2.2
WBB Closed Slit	$355.3 \pm 86.$	0 ± 19.7
WBB MC	348	11.0
Dilepton	1.0	.2

WSM: Data and backgrounds with $Y < .5$

One notices that below 100 GeV, most of the WSM events comes from WBB. To delineate the WSM sample over and above the backgrounds, the only events considered are with Evis $>$ 100 GeV. The remaining WSM events after background subtraction are (7.5 ± 4.9). Thus with 90%confidence level the upper limit on such right handed coupling of neutrinos is (9.5×10^{-5}). The above rate is without the acceptance correction. After the acceptace correction the upper limit one obtains is (7.9×10^{-5}).

In the left-right symmetric theory mentioned above, the physical gauge bosons mediating the weak interaction, might be considered as an admixture of the left and the right gauge bosons. If W_L and W_R are the vector bosons corresponding to $SU_L(2)$ and $SU_R(2)$, then the bosons participating in the weak interactions, W_1 and W_2 could be represented as:

$$W_1 = W_L \cos\varsigma + W_R \sin\varsigma$$

and

$$W_2 = -W_L \sin\varsigma + W_R \cos\varsigma$$

where ς is the mixing angle between the right and the left handed bosons. The limit imposed on the right-handed coupling of the neutrino obtained above enables one to impose a limit on the mass of the right-handed boson. One uses the fact that the cross section is inversely proportional to the fourth power of the mass of the mediating boson, i.e.

$$\frac{\sigma(W_R)}{\sigma(W_L)} = (\frac{M_{W_R}}{M_{W_L}})^{-4}$$

If the the mixing angle is assumed to be zero, the limit on WSM production enables the limit, $M_{W_R} > 849$ GeV with 90%confidence level. Equivalently the mixing angle $\varsigma < .009$ if $M_{W_R} \rightarrow$ infinity.

§6.6 Conclusion and outlook

Wrong Sign Muons are interesting because they pose a threat to the standard model. The rate of production of WSM is similar to that of LSDM. However we have not found a deeper connection between the two in these studies. There are several experimental venues by which one might improve the measurements of WSM. To begin with, one might attempt to understand, measure, and eliminate WBB to a better degree than was achieved in the two experiments discussed here. It is difficut to model WBB and, inspite of the good agreement between data and background in the low energy region, the uncertainty at the high energy end of the spectrum remains. One means of eliminating the WBB as well as the Ke3 background to a large extent would be by "tagging" neutrinos thus acertaining the flavour of the incident neutrino. However in a tagged neutrino experiment statistics prove the greatest limiting factor. (see ref [77] for details).

An important quantity to measure in WSM is its P_T with respect to the hadron shower. This might tell us whether the events originate at the hadron vertex. Unfortunately it is difficult to measure the hadron shower direction in a high density neutrino detector. Some hope of accomplishing this arises from the use of fast analog to digital converters [96] that may provide some information about hadron shower direction. These are being currently studied and tested by the CCFR collaboration. A deeper motivation to study WSM might come from the unequivocal observation of LSDM beyond backgrounds. A high statistics experiment, E744, has recently been conducted at FNAL with the Lab-E detector substantially improved. The analysis of this experiment may shed more light upon LSDM and possibly on WSM.

Chapter 7

Trimuons

Trimuon events are characterized by three muons in the final state of a neutrino-nucleon scattering. Trimuon events were briefly mentioned in Chapter 1. Fig. 1.1f schematically depicts the production of trimuons in a neutrino-nucleon interaction. This chapter will endeavour to present a comprehensive study of trimuons observed in the two experiments, E616 and E701. Neutrino induced trimuons were first observed by the present experimental group in 1976 [78] and by another group at FNAL [79] early 1977. Since then two other experiments have reported the observations of trimuons in neutrino interactions, [80,81]. These initial observations [78,79,80] of trimuons refuted explanations based upon either multiple decays of pions and kaons in the hadron shower or a dimuon event accompanied by an extra muon originating from the hadron shower. It was conjectured that trimuons were related to "exotic" processes permitted by the standard model such as diffractive production of heavy quark pairs [82,83], heavy quark cascade [84], or the production and decay of a Higgs boson [85]. Other, more conventional and perhaps less exciting, suggested sources were the radiative or trident production of muon pairs [87,88,89] and the production and decay of vector mesons, such as ρ, ω, ϕ or J/ψ in the hadron shower [81,90].

Further, mechanisms beyond the standard model were put forward. These models predicted the existence of heavy neutral lepton with or without heavy quark production [91,92]. Some of these mechanisms have been summarised in ref. [88]. Since neutrino induced opposite sign dimuons were caused, predominantly, by decays of charmed hadrons, the question arose could the trimuons be harbingers of some new heavy particle?

Experimental results on trimuons, [see ref. 81] ruled out most of the forementioned exotic possibilities. The observed rates and kinematical properties of trimuons were found to be consistent with the two conventional mechanisms already mentioned, the hadronic and radiative production of trimuons. The hadronic production of trimuon purports the idea that the dimuons ($\mu^+\mu^-$) in a neutrino-induced trimuon events come from the decays of vector mesons such as ρ, ω, ϕ or J/ψ as well as from the continuum (Fig. 7.26). The radiative production implies that some of the dimuons may come from the trident production by the leading muon or interacting quarks (Fig. 7.27a, 7.27b and 7.27c). In the subsequent sections the two models will be referred to as Model 1 and Model 2 respectively.

We report here 24 trimuon events observed in a total of 163,900 neutrino charge current events. The backgrounds and the two conventional mechanisms of trimuon production have been simulated. A detailed comparision of the various kinematical properties of these trimuons with those of the two mechanisms has been carried out. Our conclusion supports the present understanding of neutrino induced trimuons as primarily originating from vector meson decays and trident production.

§7.1 Data

Candidates for trimuons were culled from the neutrino data accumulated during the running of experiments, E616 and E701. The neutrino beam and the apparatus employed to record the neutrino-nucleon scattering have been described in Chapter 2 and 3. (Chapter 3 has also pointed out the essential differences in the apparatus configuration during E701 from that of E616.) The preliminary cuts imposed on the crunched data set were roughly the same as those for WSM. The main differences were as follows :

a. Place cut : For the E616 sample the lower place cut was loosened to 17 from 20.

b. Cut on the number of "computer found" tracks : It was required that the track finding algorithm should detect at least two tracks. The resulting sample comprised almost all dimuon as well as trimuon events. This sample was scanned for trimuon candidates. Two criteria were adopted :

i. At least three tracks should be noticed converging to a common longitudinal as well as transverse vertex.

ii. Counter pulse heights following the end of the hadron shower should display pulse heights corresponding to an average of three minimum ionizing particles per counter.

The final set of events were reconstructed interactively on a high resolution graphics terminal. The details of the reconstruction have been outlined in Chapter 4. Here only those reconstruction features pertaining to trimuons need be presented. The track reconstruction for any given muon commenced in the first or second spark chamber immediately upstream of the end of the hadron shower. It was required that at least one of the three muons be momentum reconstructed in the toroids and that all three muons have momenta greater than 2.5 GeV. Of the 27 surviving candidates only 4 events had all three muons reconstructed in the toroid, 11 events had two and the remaining 12 events had one. The muon tracks (interactively chosen) were projected backwards to the vertex. The longitudinal position of the vertex was determined by the scintillation counters. The reconstructed trimuon event candidates were required to converge to a common transverse vertex to within ±4 inches. The track parameters were determined by a least square fit.

7.1.1 The errors on the track parameters of trimuon events

24 trimuon events comprised the sample after reconstruction and the imposition of the set of final cuts (see Chapter 4). Since the spectrometer was the most upstream part of the detector, only four of the 24 events had all momenta reconstructed in the toroid. The other events had muons ranging out in the target. Only one of the trimuons appeared to have a muon escaping the detector.

The fractional error on the hadron energy determination was the same as pointed out in Chapter 4, being equal to $\frac{.89}{\sqrt{E_H}}$, where E_H is the hadron energy. The error on the muon energy was, in general, better in the trimuon sample than in the WSM sample. This is because the only source of error on muon momentum for the trimuon events was multiple scattering in the target, since most of them did not traverse the toroids. This error also depends upon the sampling frequency and the amount of steel the muon goes through. In our detector the momentum of such "range-out" muons can be determined to .4 GeV.

The resolution of muon angle depends in general on the momentum as well as the hadron energy. The muon's momentum determines the error in the angle due to multiple scattering. On the other hand, generally a large hadron energy would imply more hits in the chambers and consequently a greater probability of assigning a wrong spark to the muon track. Table 7.1 shows the error in the angle measurements in momentum and hadron energy bins. The uncertainty in the longitudinal position is the spacing between the counters which is 4 inches or 10.2 cm. For most trimuon events, two tracks converged to a transverse vertex within half an inch. Events where this convergence was worse than 4 inches were rejected.

7.1.2 Loss of trimuon events

The loss of a trimuon event may occur if a muon escapes before being recorded in the chambers beyond the end of the hadron shower. This loss will depend upon the azimuthal angle of the muon and the transeverse vertex position. For the sample of trimuons under consideration the detection efficiency (obtained by azimuthal rotation) was approximately 90 %. The efficiency was 100 %for all the events occuring at radii less than 30 inches and diminished to 45

Overlapping of tracks might be another cause for the loss of trimuons. Tracks that are within half an inch of each other will not be distinguished by the spark chambers in the target. However, the multiple scattering of muons in the steel enables the tracks to open up. The smaller the momentum of the muon, the greater will be the opening due to multiple scattering. For examle, two parallel muons of 20 GeV each will be resolved by this effect after traversing through 4 chambers. An inspection of the counter pulse heights as well as the amount of steel the muon traversed through for all the trimuon events revealed that probability for such losses is negligible.

7.1.3 The trimuon events

A list of pertinent kinematical quantities for each of the twenty four trimuon events, such as Evis, various momenta and angles, invariant masses etc, has been presented in Appendix G. The computer drawn pictures of these twenty four events have also been presented in Figs. G.1 - G.23.

For the reliable estimation of the background (see Sec. 7.2) and simulation of various mechanisms for trimuon production, it was considered important to impose a more stringent cut of 4.5 GeV on the muon momentum. Eleven trimuon events survived this cut.

§7.2 Background estimation for trimuons

The major background for trimuons is an opposite sign dimuon event with an additional muon emerging from the hadron shower. This muon may come from the decay of either a kaon or a pion. The resulting background is quite similar in concept to the background for opposite sign dimuons which comes from the normal charge current events. The estimation of this background proceeded as follows : The entire dimuon sample was subjected to the trimuon cuts described above. The hadron energy and X distribution of the surviving dimuons were used to predict a rate for producing an extra muon from the hadron shower. The resultant trimuon background from the dimuons was :

	$\mu^-\mu^+\mu^-$	$\mu^-\mu^+\mu^+$
DATA	10 ± 3.2	1 ± 1
BACKGROUND	$.6 \pm .12$	$.74 \pm .15$

Trimuons: Data and background

One expects a slightly higher rate of muon production from the hadronic showers of dimuons than that from the showers in regular CC events. This is due to an enhancement of the kaon fraction in dimuon events, the kaons coming from the decays of the D mesons. To compensate for this relatively greater content of kaons the above rate for the trimuon background was increased by 10 %[81].

Among the trimuons for which all three momenta were reconstructed in the toroid, only one event was of the configuration $\mu^-\mu^+\mu^+$. It appeared to be consistent with the background. In the subsequent section this event has been dropped from the sample. Fig. 7.1a shows the distribution of total visible energy for the remaining 10 events (after 4.5 GeV momentum cut), and the corresponding background distribution for events of the type, - + -. (The background has been normalized to 10 events).

The second source of background for trimuon will be discussed below. If the vertex of a regular CC event were to overlap with that of a dimuon event, it would appear to be a trimuon. The likelihood of this was considered to be miniscule since the corresponding background for like sign dimuons has been estimated to be < .1 event. It follows, given that the dimuons comprise one percent of the total CC sample, no such background for trimuons would be observed in the present sample.

§7.3 Rate of production for trimuons

The raw rate of production of trimuons with respect to CC events is given below. The trimuon event with the configuration, $\mu^{-}\mu^{+}\mu^{+}$, has been removed from the sample for this purpose. The dimuon background of the type $\mu^{-}\mu^{+}\mu^{-}$ has been subtracted from the remaining sample.

$$Rate(\frac{3\,\mu}{1\,\mu}) = (5.7 \pm 1.9) \times 10^{-5}$$

It should be noted that the mean total visible energy of the 10 trimuon events. is 149 GeV, whereas the corresponding average value for CC events is 120 GeV.

§7.4 Characteristic kinematical quantities of trimuons

This section discusses in detail various kinematical variables associated with the observed trimuon sample. All such variables have been compared to the predictions of the two trimuon production models considered here. Details of these models will be discussed in the next section. A summary of various mean kinematical properties of the trimuons has been presented in Table 7.2. Table 7.2 also lists the average values of kinematical quantities that these models predicts for the trimuons.

7.4.1 The definition of the leading muon

As pointed out earlier, the only events being considered are of the configuration, $\mu^-\mu^+\mu^-$. The positive muon (or the one being focussed) offers no ambiguity and will be referred to as the "third" muon. The distinction between the other two muons (having same sign) is a subtle one. A simple criterion would be to call the muon with the larger momentum, the "leading" muon. However, in view of the models of trimuon production and an examination of the distributions of the azimuthal angles of the muons from the data, the above definition is found to be inappropriate. The following criterion was applied to the two negative muons : For the three muons the momentum perpendicular to the hadron shower direction was computed. Let these perpendicular momenta be called P_T^1, P_T^2 and P_T^3, where the assignments "1" and "2" have been made arbitrarily. If $(P_T^2+P_T^3)$ $>$ $(P_T^1+P_T^3)$, the second muon was called the "leading" or "1" muon. Unfortunately, in the present sample there were very few events where muon polarities could be distinguished and consequently the ambiguity (between "1" and "2") mentioned above could not be resloved for all the events. For such events, the muon with larger of the two momenta was called "leading".

7.4.2 Evis, hadron energy and muon momenta

Figs. 7.1b, 7.1c and 7.2a depict the histograms of the total visible energy, the hadron energy and the momentum of the leading muon (P_μ^1) of the data. The momenta of the nonleading muons (P_μ^2 and P_μ^3) are shown in Fig. 7.2b and 7.2c. One notices that $<P_\mu^2>$ is equal to $<P_\mu^3>$ ($=$ 11 GeV) within errors and this value is roughly a factor of six smaller than $<P_\mu^1>$ ($=$ 70 GeV), the average value of the momentum of the leading muon. ($< >$ denotes the average value). This vast difference in the momenta of the leading and the nonleading muon suggests a deep kinematical disparity between the leading muon and the two nonleading ones. Qualitatively, this can be seen in P_μ^2 vs P_μ^1 and P_μ^3 vs P_μ^1 scatter plots (see Fig. 7.3b and 7.4a respectively). The accompanying scatter plots, 7.3b, 7.4b, 7.3c and 7.4c simulate the same quantities for the two aforementioned models of trimuon production, 1 and 2. A quantity which sheds some light on the symmetric production of the two non leading muons, is the "momentum asymmetry" associated with them. It is defined as follows :

$$\eta = \frac{P_\mu^2 - P_\mu^3}{P_\mu^2 + P_\mu^3}$$

Fig. 7.5 illustrate the momentum asymmetry distribution for the trimuon sample. It is consistent with zero. The large values of η do not appear in the figure, presumably because of the enegy cut. This cut would tend to eliminate vastly asymmetric events because one of the muons might fail to pass the cut.

The discussions in the preceding paragraphs as well as in those which follow, point out a good deal of similarity between the non leading muons. Where as the leading muon appears to be distinctly different. The distribution of η (Fig. 7.5) lends support to be the intuition that the non leading muons are emitted as a symmetric pair. In the figures mentioned above, the simulation of the two models of trimuon production reproduces these conclusions successfully.

7.4.3 The scaling variables

It is instructive to explore the scaling variable normally associated with CC events. The muon pair (+ -) can be emitted from the hadron vertex in two ways, (a) the production and decay of vector mesons, which is Model 1 and (b) trident production by the interacting quarks, which constitutes a part of the total trimuon production via the mechanism of Model 2. In either case the muon pair derives its energy from the total hadronic energy and there by shifting the scaling variable Y, the inelasticity, to a lower value. (See below for the definition of Y).

Similarily P_{μ}^{1} will be lower in value should the trident production occur at the lepton vertex, which comprises the other means of radiative production of trimuons. Consequently, the scaling variable X appears to have a smaller value.

We define and plot (see Figs. 7.7 and 7.8) the following variables:

$$X_{vis} = \frac{Q^2}{2\,M_P\,E_H}$$

$$X = \frac{Q^2}{2\,M_P\,(E_H + P_\mu^2 + P_\mu^3)}$$

$$Y_{vis} = \frac{E_H}{E_\nu}$$

$$Y = \frac{(E_H + P_\mu^2 + P_\mu^3)}{E_\nu}$$

The peaking of the Yvis distribution at lower value than that of the Y distribution, supports the idea that the dimuons (+ -) might be originating from the hadron shower. The actual pattern depicted by the Monte Carlo simulations (Fig. 7.7 and 7.8) upholds this observation. Another interesting variable to explore is the ratio of the sum of the energies of the two muons to the total hadronic energy; symbolically :

$$X_F = \frac{P_\mu^2 + P_\mu^3}{E_H + P_\mu^2 + P_\mu^3}$$

This is the Feyman's X_F which will be used in simulating the production of vector mesons. Fig. 7.9 histograms this variable. One notices that Model 1 reproduces the high Xf behaviour well.

7.4.4 Invariant masses

The momenta and the angles of the three muons offer an opportunity to investigate the dimuon and trimuon invariant masses. One hopes that these invariant masses may provide a clue to the dynamics of trimuon production. First the rate of change in the dimuon invariant masses, M_{12}, M_{13} and M_{23} with an increase in the trimuon mass M_{123} is studied. This has been accomplished in the scatter plots of Fig. 7.14a, 7.15a and 7.16a. Even for the handful of trimuons one notices a linear increase in M_{12} and M_{13} with the trimuon mass M_{123}. The behaviour of M_{23} vs M_{123} is different. Most of the events in Fig. 7.16a cluster below M_{23} value of 1 GeV. From the (M_{12} vs M_{123}) and (M_{13} vs M_{123}) graphs one might draw the following conclusion : for given energies P^1_μ, P^2_μ and P^3_μ, larger values of the dimuon mass would imply larger angle between the two muons. Since M_{123} appears to be proportional to M_{12} and M_{13} at once, the production of the pair "23" must be related to the direction of W boson.

The third graph states that the invariant dimuon mass of the non leading muons is confined to values below 1 GeV. This observation encourages one to look at the mass projections of these invariant masses. These have been shown in Fig. 7.10 - 7.13. If the dimuons (+ -) were originating from the decays of vector mesons (Model 1) , one should see a peak in M_{23} corresponding to the mass of the parent meson. No such prominence is seen in any of these histograms. This is due to poor mass resolution of the neutrino detector. Fig. 7.12c illustrates the effect of smearing on the invariant mass M_{23}. Here the simulation of Model 1 was employed to produce this curve. It is interesting to note that the resolution of the invariant mass has the following dependence upon the angles of the muons in our detector:

$$\Delta M_{23} \approx \frac{M_{23}}{2}\sqrt{2\left(\frac{\delta P}{P}\right)^2 + 16\left(\frac{\theta\,\delta\theta\,cos(\frac{\phi_2-\phi_3}{2})}{\theta^2_{23}}\right)^2}$$

where it was assumed that $P_2=P_3=$P and $\frac{\delta P}{P} \approx .11$.

The above expression implies that the resolution is completely dominated by the angle of the pair, "2 and 3", for small values of θ_{23}. Fig. 7.12a shows (dashed line) the unsmeared M_{23} obtained after simulating Model 1 and 2. Here one can see the continuum as well as the ρ-ω peak. But after smearing M_{23} (Fig. 7.12b) no such peak is observed.

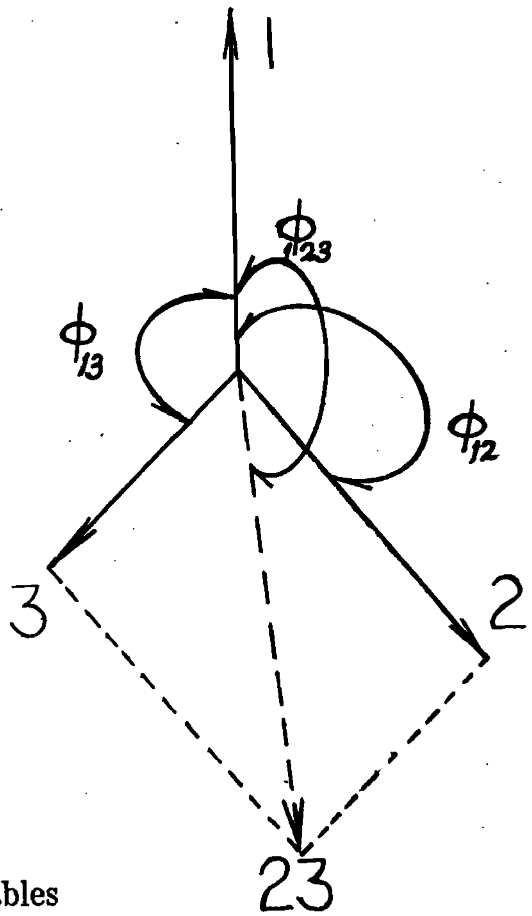

7.4.5 The ϕ variables

A further insight into trimuons comes from examining the momenta of the muons in the plane transverse to the direction of incident neutrino. The azimuthal angles between muons may support or refute the two models under consideration. The ϕ angle is defined below:

If ϕ_{123} peaks at 180^0, it means that the dimuons probably originate from the hadron shower. On the other hand should it peak at zero, the implication would be that the (+ -) originated at the lepton vertex. Figs. 7.18, 7.19 and 7.20 are the histograms of ϕ_{12}, ϕ_{13} and ϕ_{123}. These histograms are very suggestive and one might even try to infer how many dimuons of the entire sample of trimuons originated from the hadron or lepton vertex. The typical behaviour of all these histogram is as follows : the azimuthal angle peaks at 180^0, goes through a mimimum at 90^0 and finally rises again to have a local maximum at zero degrees. By examining Fig. 7.20 one might crudely guess that 67 %of the dimuons originate at the hadron vertex and the rest at the lepton vertex. (One counts the number of events with $\phi_{123} > 90^0$ and divides it by the total number). Futhermore from these figures it appears that the Monte Carlo reproduces the shape of the curves satisfactorily.

Based upon these arguments it is expected that for higher values of P^2_μ, ϕ_{12} would peak at 180^0 (similarly for ϕ_{13} vs P^3_μ). It is difficut to observe this trend in the data (Fig. 7.21a and 7.21b) owing to the poor statistics. However, events from Model 1 reproduce this behaviour while Model 2 does the opposite, as one would expect. The corresponding scatter plots for these models are shown in Fig. 7.21b, 7.22b and Fig. 7.21c and 7.22c.

For the sake of completion, the P_T distributions of the dimuons are studied. The average values of P^2_T and P^3_T are approximately .5 GeV/c and are reproduced by the subsequent Monte Carlo calculations. The distributions of P^2_T, P^3_T and $(P^2_T+P^3_T)$ appear in Figs. 7.23, 7.24 and 7.25.

§7.5 Production mechanisms for trimuons

The two production models mentioned in the introduction will be discussed in this section. The possibility of observing the trimuons from a charmed vector meson will be entertained. A brief subsection on exotic possibilities concludes this section.

7.5.1 Hadronic production of trimuons : Model 1

The production of vector mesons in hadron-hadron collision has been studied [90]. Some of these mesons might decay and produce dimuons. Beam-dump experiments have seen, after measuring dimuons, the mass peaks of these meson [13]. These experiments have also seen and parametrized the continuum contribution to the dimuon sample. In a neutrino CC event, one may expect similar production of a $\mu^+\mu^-$ pair, originating from the interaction of the virtual W boson and the nucleon. One tacitly assumes that the latter interaction may produce vector bosons, after the fashion of the ones found in the beam-dump experiments and the continuum components (producing dimuons) are similar.

The preceding argument induces one to express the hadronic component of neurino induced trimuon production in a factorized form, as follows:

$$\frac{d\sigma^{\nu_\mu N -> \mu^-\mu^+\mu^- X}}{dx\, dy\, d^3P\, dm} = \frac{d\sigma^{\nu_\mu N -> \mu^- X}}{dx\, dy} \cdot \frac{\lambda}{\sigma_{tot}(\pi N)} \cdot \frac{d\sigma^{\pi N -> \mu^+\mu^- X}}{d^3p\, dm}$$

where $\sigma(\pi N)$ is the cross section evaluated at the centre of mass energy $W^2 = (M^2 - Q^2 + 2M\nu)$, which is the hadronic mass of the neutrino interaction. The process quantified above has been schematically presented in Fig. 7.26. In the following $\sigma(\pi N)$ is assumed to be 25 mb and the factor λ is assumed to be of the order 1 [88]. To simulate the production of the vector mesons, the data by Anderson et al. [90] has been used. They have parametrized the inclusive muon pair production from ρ, ω, ϕ and J/ψ mesons.

The X-Fenyman distribution is parametrized as:

$$\frac{d\sigma}{dX_F} = A \cdot (1 - X_F)^c$$

Whereas the Pt distribution is fitted according to :

$$\frac{d\sigma}{dp_T} = constant \times e^{-b\,p_T}$$

The parameters A, b and c are obtained via fits to the data for the various mesons considered here. Table 7.3 contains these fitted parameters for inclusive muon pair production from various sources. To estimate the continuum component, the dependence of the differential cross section on the invariant dimuon was assumed to have the form,

$$\frac{d\sigma}{dm_{\mu^+\mu^-}} \approx e^{-\alpha\, m_{\mu^+\mu^-}}$$

where Anderson et al. have found the parameter α to be 5. The table 7.3 also lists the fitted parameters A, b and c for the continuum. From the values in table above one can naively estimate (without any cuts on X_F or the muon momentum) the hadronic component of trimuon production from ρ-ω alone to be $\approx 5.7 \times 10^{-5}$. The measurement and the fitted values for dimuon production from the vector mesons reported above was incorporated in the our CC Monte Carlo program. The simulation of this mechanism yielded a total of (11.4 ± 2.3) trimuon events, when normalized to the entire CC sample. The contibution of the vector mesons alone was calculated to be $(3.88 \pm .8)$. (This CC sample was obtained by applying "trimuon-cuts" on the original sample). Thus the rate of the hadronic componet of trimuon production in our apparatus is calculated to be :

$$Rate(\frac{3\,\mu}{1\,\mu}) = (6.9 \pm 1.4) \times 10^{-5}$$

The distributions of various kinematical variables of the trimuons produced via this mechanism has been shown in Fig. 7.1-7.26. In this comparison, the total number of trimuons predicted by this mechanism has been normalised to the data. Many of the features of the data are well reproduced by this model, particularly the distributions of the azimuthal angles. It would have been of some interest to see mass peaks for the various sources, however, as discussed earlier the poor mass resolution of the detector prevents one from doing so.

7.5.2 Radiative or Trident production of 3μ : Model 2

A virtual photon radiated by the μ^- or by the interacting quarks may produce muon pairs. This is a non negligible effect. It has been discussed by various authors (see the introduction). The simulation of this model has been carried out following Barnett et al. and Barger et al. [for ref. see above].

Fig. 7.27a shows trident production off the muon. The corresponding production off the quarks cannot be ignored, since the former alone is not gauge invariant. Furthermore, in Feynman Gauge , there are large cancellations between the square of 7.27a and the its interference with the terms representing the other two processes. Radiations off the spectator quarks as well as the W boson may be ignored. The differential cross section $d\sigma_{3\mu}$ for radiative production of trimuons can be written as :

$$d\sigma_{3\mu}^{rad} = \frac{1}{4ME} \cdot \Sigma_{i,f} \, |M|^2 \, \Pi_{i=1}^{3} \frac{d^3k_i}{2E_i} \frac{d^3p_x}{2E_x} \, dM_x^2 \, \frac{2xF_2(x)}{2M\nu x} \, \delta^4(p+q-p_x)$$

Here $k_1, k_2, k_3 and E_1, E_2, E_3$ are the muon momenta and energies.The variables k,E represent the beam momentum and energy respectively; p_x, M_x are the momentum and mass of outgoing hadrons; M is the proton-mass; and ν is the transferred energy.

In the expression above the effect due to Fermi-Dirac statistics, which is known to be small, has been neglected [87]. Barnett et al. have found the above differential cross section to be insensitive to the details of choice of the stucture function $F_2(x)$. The total rate of trimuon production with respect to CC events is given by :

$$\sigma_{3\mu} = \frac{1}{4ME} \int \frac{1}{2} \Sigma_{i,f} \, |M|^2 \, \Pi_{i=1}^{3} \frac{d^3k_i}{2E_i} \frac{F_2(x)}{4M\nu x^2} \, \theta(p_x^0 - M) \, \theta(p_x^2 - M_x^2)$$

The trident production rate was found to be by the authors mentioned above :

$$Rate(\frac{3\mu}{1\mu}) \approx 2 \times 10^{-5}$$

To simulate this process in our detector, we have used a parametrization of the above expression due to Barger et al., which is

$$Rate(\frac{3\mu}{1\mu}) = \alpha^2 \cdot [.035\,(lnE)^2 - .19]$$

Where α is the fine stucture constant. This expression gives a similar rate of production as quoted above. Furthermore it can be calculated that the relative contributions of the three diagrams 7.27a, 7.27b and 7.27c are :

$$|M_\mu| : |M_u| : |M_d| = 1 : .41 : .1$$

It is interesting to observe that the above ratios are very close to that of the charges of the photon emitting particles.

The formalism, adapted to our apparatus and with the cuts identical to those for the data trimuons, estimated $(1.5 \pm .30)$ trimuons. Thus, the rate of the radiative component of trimuons was found to be :

$$Rate(\frac{3\,\mu}{1\,\mu}) = (.91 \pm .18) \times 10^{-5}$$

One interesting feature of the trimuons produced via this mechanism is that the azimuthal angle peaks at zero degrees with respect to the leading muon, provided the photon was emitted by the lepton.

7.5.3 Charmed meson contribution to trimuons

Dimuon production from charmed meson has been seen in the beam dump experiments. Could it be observed in the neutrino induced trimuons? An estimate of such a production can be arrived at by using the measurements by Anderson et al. mentioned above. This yields a rate of dimuon production from cc pairs in a neutrino CC interaction to be $.49 \times 10^{-6}$. This rate is considerably lower than both the observed rate for trimuons and the rates furnished by the two model considered earlier. B. Young et al. [95] have estimated this rate via perturbative QCD consideration to be less than $< 10^{-6}$, which is consistent with value stated above.

7.5.4 Exotic sources of neutrino induced trimuons

In the late seventies, many exotic sources of trimuons were proposed. Some of them are easily eliminated due to improved limits on the masses of various conjectured particles, for example mass of the top quark, neutral heavy lepton , Higg's boson etc. It would be of interest to investigate consequences of some exotic models :

a. Production of a heavy muon

Compositeness of leptons (and quarks) is a natural extension of the prevaling ideas concening the building blocks of elementary particles. One does question, along the lines of Rutherford's α-scattering and SLAC deep inelastic scattering experiments, the indivisibility of these fermions. Furthermore, compositeness may alleviate some of the problems confronting the standard model. One such composite model by Lee postulates production of a heavy lepton, a muon for example, in a high energy interaction, which then decays into a regular muon and a hard photon. Decays such as this would reveal an internal structure of the muons and are to be distinguished from the case of photon emitted in brensstrahlung. One may incorporate this speculation in the ν_μ-trimuon production as follows : In a neutrino nucleon scattering a heavy muon may get produced, which might then decay into a negative muon and a hard photon. The process can be described as (Fig. 7.28) :

$$\nu_\mu + N \longrightarrow M^- + X$$

such that,

$$M^- \longrightarrow \mu^- + \gamma \longrightarrow \mu^- + \mu^+ + \mu^-$$

Such a mechanism would predict a flat behaviour in the azimuthal plots (see Fig. 7.18 - 7.20). Reversing the argument, by studying the azimuthal behaviour of the muons one can deduce a limit on the produciton cross section and the mass of such heavy muons. Unfortunately, our sample is too small to go into such deductions, which must be deferred till the measurements of E744 may become available.

b. Quark cascade

A trimuon event might come about through the following cascade reaction [Fig. 7.29]

:

$$\begin{tikzcd}
\nu_\mu N \arrow[r] & \mu^- X t \arrow[dr] & & & \\
& & b X' \arrow[dr] & & \\
& & & c \mu^- \bar{\nu}_\mu \arrow[dr] & \\
& & & & s \mu^+ \nu_\mu
\end{tikzcd}$$

Such a mechanism has been considered by Hansl et al. and they have concluded it to be inconsistent with the data.

c. Production of a neutral heavy lepton

In the hadron shower a neutral heavy lepton, if produced, might give rise to dimuons. The reaction is assumed to proceed as follows :

$$\begin{tikzcd}
\nu_\mu N \arrow[r] & M^0 b X \arrow[dr] \arrow[ddr] & \\
& & c \mu^- \bar{\nu}_\mu \\
& & \mu^+ \mu^- \nu_\mu
\end{tikzcd}$$

This event would have a large M_{23}. However, there exist rather stringent limits on the production of such particles from beam dump experiments, e^+e^- experiments.

We do not have enough events to quantitatively test the hypotheses mentioned above. The present data seems to be consistent with the two conventional sources of trimuon production, hadronic and radiative. The prediction of the total number of trimuons using these models is consistent with the observed data.

Appendix A

CCFRR Collaboration

Y.K. Chu, D.B. MacFarlane[1], R.L. Messner[2],
D.B. Novikoff[3], M.V. Purohit[4]
California Institute of Technology, Pasadena, CA 91125

P. Auchincloss, R. Blair, C. Haber[5], S. Mishra,
M. Ruiz[6], E. Oltman, F.J. Sciulli, M.H. Shaevitz,
W. Smith, R.Zhu[7]
Columbia University, New York, NY 10027

R. Coleman, H.E. Fisk, Y. Fukushima[8], Q. Kerns,
B.N. Jin[7], D. Levinthal[9], D.D. Jovanovič,
T. Kondo[8], W. Marsh, P.A. Rapidis, S.L. Segler,
R.J. Stefanski, D.E. Theriot, H. B. White

Fermilab, Batavia, IL 60510

D. Garfinkle, F. S. Merritt, M. Oreglia, P. Reutens

I. E. Stockdale[11], K. Lang

University of Chicago, Chicago, Ill 60637

A. Bodek, F. Borcherding[4], N.Giokaris[10],

I. E. Stockdale[11], K. Lang

University of Rochester, Rochester, NY 14627

O.D. Fackler, K.A. Jenkins

Rockefeller University, New York, NY 10021

---

[1] Now at University of Toronto, Canada.

[2] Now at SLAC, Stanford, CA 94305.

[3] Now at Hughes Aircraft Co., El Segundo, CA 90245.

[4] Now at Fermilab, Batavia, IL 60510.

[5] Now at LBL, Berkeley, CA 94720.

[6] Now at University of Florida, Gainsville, FL, 32611.

[7] Now at the Institute for High Energy Physics, Peking, P.R. China.

[8] Now at the National Laboratory for High Energy Physics, Tsukuba-gun, Ibaraki-ken 305, Japan.

9. Now at the Florida State University, Tallahassee, FL 32306.

10. Now at University of Notre Dame, Notre Dame, IN 46556.

11. Now at University of Illinois, Urbana, Il 60510.

Appendix B

Beam and ν_μ-N Event Kinematics

The kinematics for the two body π/K decay and that for the deep inelastic ν_μ-nucleon scattering is discussed below. In particular, we derive the expression for the scaling variables, X and Y, and show their relation to the momentum-transfer and centre of mass energy.

§B.1 Beam Kinematics

The Narrow Band Beam allows one to select the secondary mesons of a specified sign and momentum. The neutrino obtained from the decay of these mesons appear at the apparatus in two distinct band characterizing their origin from either a pion decay or a kaon decay. This occurs due to the energy-radius correlation of the NBB ν. We present the derivation of this energy-radius correlation and discuss some relevant aspects of NBB neutrinos in this section.

Very briefly, the two body decay kinematics of the mesons ($\pi \rightarrow \mu\nu_\mu$, and $K \rightarrow \mu\nu_\mu$) initmates the energy of the ν_μ,

$$E_{\nu_\mu} = \frac{E_{max}}{1 + \gamma^2 \frac{R^2}{L^2}}$$

R refers to the transverse vertex of the event at the detector and L to the longitudinal distance of the event from the decay point. The quantity E_{max} refers to the maximum attainable energy of the decay neutrino and is given by the expression,

$$E_{max} = E_{\pi,K} \times \left[1 - \frac{m_\mu^2}{m_{\pi,k}^2}\right]$$

The factor $\left[1 - \frac{m_\mu^2}{m_{\pi,k}^2}\right]$ is .427 for π's and .954 for K's, which shows the disparity in energies of the pion and kaon neutrinos. The rest of the symbols have their ususal meaning.

In reality, there are slight deviations form the monoenrgetic and dispersion free meson beam considered above. To begin with the meson beam has a beam dispersion of .1 to .2 milliradians. This affects the energy-radius correlation – particularly affecting the pion-neutrinos. The kaon neutrinos are relatively insensitive to the beam divergence of the secondary beam owing to their large decay angles. Secondly, the momentum spread of $\pm 10\%$ in the secondary beam causes a further smearing of the ν-flux. Thirdly, the decay of the meson occurs over the entire length of the decay region (=350m). As a result, the uncertainity in the decay coordinate of the meson directly gets translated into the derived ν energy for the case when the decay is assumed to have occured at the mid point of the decay region. Lastly, there are three body decays of the kaons which have been

discussed in Chapter 2 and Chapter 5. These cause further exacerbation the distinction of the pion-neutrinos from the kaon-neutrinos.

It should be pointed out that the analysis of the WSM events is not drastically dependent upon the deviations form the ideal condition of the ν_μ production. We have employed the dichromatic feature of the data only to compute any missing energy in the event and as a consistency check on the overall analysis. A through discussion of some of these features is presented by Purohit [12].

§B.2 Event Kinematics

Consider the following Feynman diagram,

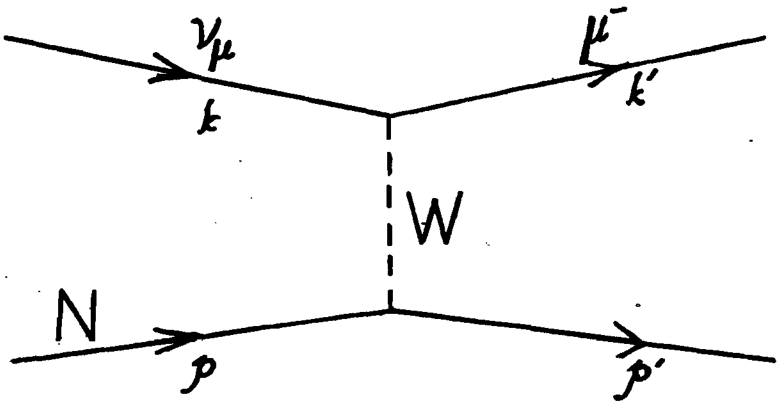

Let the 4-momentum of the incident neutrino be k and that of the outgoing muon, k'. The target nucleon, initially at rest, is assumed to have a four momentum p, and the final hadron shower is represented by a particle carrying a 4-momentum p'.

$$\left.\begin{aligned} & k=(E_\nu,0,0,E_\nu) \\ & k'=(E_\mu,\mathbf{p}_\mu\sin\theta_\mu\cos\phi_\mu,\mathbf{p}_\mu\sin\theta_\mu\sin\phi_\mu,\mathbf{p}_\mu\cos\theta_\mu) \\ & p=(m_p,0,0,0) \\ \Rightarrow\quad & p'=(m_p+E_\nu-E_\mu,-\mathbf{p}_\mu\sin\theta_\mu\cos\phi_\mu,-\mathbf{p}_\mu\sin\theta_\mu\sin\phi_\mu,E_\nu-\mathbf{p}_\mu\cos\theta_\mu) \\ & \quad=(E_h,\mathbf{p}_h\sin\theta_h\cos\phi_h,\mathbf{p}_h\sin\theta_h\sin\phi_h,\mathbf{p}_h\cos\theta_h) \end{aligned}\right\} \tag{B.1}$$

The square of the centre of mass energy, s, in ν_μ-N frame is:

$$s=(p+k)^2=m_p^2+2m_pE_\nu\approx 2m_pE_\nu \tag{B.2}$$

The energy transferred to the hadronic system, conventionally denoted as ν, could be expressed in terms of the above quantities,

$$\nu\equiv p\cdot(k-k')=m_p(E_\nu-E_\mu)=m_p(E_h-m_p) \tag{B.3}$$

The square of the 4-momentum transfer to the hadronic system, Q^2, is expressed as:

$$\begin{aligned} Q^2 &\equiv -(k-k')^2=2E_\mu E_\nu-2E_\nu|\mathbf{p}_\mu|\cos\theta_\mu-m_\mu^2\approx 2E_\nu E_\mu(1-\cos\theta_\mu) \\ &= 4E_\mu E_\nu\sin^2\frac{\theta_\mu}{2}\approx E_\mu E_\nu\theta_\mu^2 \end{aligned} \tag{B.4}$$

We could now give an expression for the inelasticity variable, y, in a Lorentz-invariant fashion:

$$y\equiv\frac{\nu}{p\cdot k}=\frac{m_p(E_h-m_p)}{m_pE_\nu}\approx\frac{E_h}{E\nu}\approx 1-\frac{E_\mu}{E_\nu} \tag{B.5}$$

Since the nucleon mass $m_p << Q^2$, the mass of the initial quark (approximately a fraction of the nucleon mass) could be neglected. However, it is entirely possible that the final state quark has a non-negligible mass, e.g. production of charm quark ($m_{q=c}$=1.5 GeV; for details see Chapter 5). If x refers to the fraction of the initial quark momentum, then one can obtain an expression for the variable x by balancing the 4-momenta:

$$(q+xp)^2 = m_q^2$$

$$or, \qquad -Q^2 + 2xq\cdot p + x^2 m_p^2 = m_q^2 \cdot$$

$$\text{Neglect } x^2 m_p^2 \text{ to give} \qquad x \approx \frac{Q^2 + m_q^2}{2q\cdot p} = \frac{Q^2 + m_q^2}{2m_p(E_h - m_p)} \cdot \tag{B.6}$$

Traditionally, the above expression for x, is referred to as "slow scaling variable" discussed in Chapter 5.

$$\text{Neglecting } m_q, m_p \text{ gives} \qquad x \approx \frac{Q^2}{2m_p E_h} \tag{B.7}$$

$$\text{or} \qquad Q^2 \approx sxy \tag{B.8}$$

One could also derive the expression of the angles of the scattered hadron from (B.1),

$$\begin{aligned} \cos\theta_h &= \frac{E_\nu - p_\mu \cos\theta_\mu}{\sqrt{E_\nu^2 + |\mathbf{p}_\mu|^2 - 2E_\nu |\mathbf{p}_\mu| \cos\theta_\mu}} \\ \Rightarrow \qquad \sin\theta_h &= \frac{|\mathbf{p}_\mu| \sin\theta_\mu}{\sqrt{E_\nu^2 + |\mathbf{p}_\mu|^2 - 2E_\nu |\mathbf{p}_\mu| \cos\theta_\mu}} \end{aligned} \tag{B.9}$$

Thus,

$$\sin\theta_h = \frac{|\mathbf{p}_\mu|}{|\mathbf{p}_h|} \sin\theta_\mu \approx \frac{1-y}{y} \sin\theta_\mu \cdot \tag{B.10}$$

The inelasticity variable, y, could be linked with the angle, θ^*, in the centre of mass system:

$$(1-y) = \frac{(1+cos\theta^*)}{2}.$$

This follows if we assume that all centre-of-mass energies are equal to ϵ and all particles are massless. If γ were the boost from the centre-of-mass to the lab frame,

$$\begin{aligned} E_\mu &= \gamma\epsilon + \gamma\epsilon\cos\theta^* \\ E_\nu &= \gamma\epsilon + \gamma\epsilon, \end{aligned} \tag{B.11}$$

which intimates the above result.

It should be noted that the deep inelastic variables, x, y and Q^2, even though expressed in terms of the measured quantity, $E_\nu, E_\mu, \theta_\mu and E_H$, are Lorentz-invariant quantities.

Appendix C

ν_μ-N Differential Cross Section

The expressions for the differential cross sections for neutrino and antineutrino are given in the following paragraphs. First the quark-parton phenomenology motivated derivation is presented. Next, the same expression is derived within some very general assumptions.

§C.1 Quark-parton phenomenological arguments

From purely dimensional arguments and without regards to the spin considerations for neutrinos or quarks, the total corss section of a neutrino scattering off a point particle is given by,

$$\sigma \alpha G_F^2 \times s$$

or more exactly,

$$\sigma = \frac{2 \cdot G_F^2 \cdot s}{2\pi}$$

If the point particle were a quark, a spin 1/2 particle, carrying a fractional momentum x of the nucleon such that the probability of finding the quark with x is q(x), then the above expression can be cast into a diffrential form:

$$\frac{d\sigma^{\nu q}}{dx\, dy} = \frac{G_F^2\, s}{2\pi} \cdot x\, q(x)$$

It should be noted that the square of centre of mass energy, s, has been replaced by sx, the c.m. energy in the neutrino-quark reference frame. Furthermore the first expression has be multiplied by 1/2 because only the left handed quarks participate in the interaction.

The differential cross section of the neutrino-antiquark collision is likewise given by,

$$\frac{d\sigma^{\nu\overline{q}}}{dx\, dy} = \frac{G_F^2\, s}{2\pi} \cdot \overline{xq(x)} \cdot (1-y)^2$$

The additional factor of $(1-y)^2$ appears due to spin consideration shown in Fig. C.1.

Thus, in terms of quark-antiquark momentum distribution in the nucleon, the neutrino-nucleon inelastic cross section can be written as

$$\frac{d\sigma^{\nu_\mu N}}{dx\, dy} = \frac{G_F^2\, s}{2\pi} \cdot (x\, q(x) + \overline{xq(x)}\,(1-y)^2)$$

The corresponding expression for the antineutrino-nucleon cross section is,

$$\frac{d\sigma^{\overline{\nu_\mu} N}}{dx\, dy} = \frac{G_F^2\, s}{2\pi} \cdot (x\, q(x)\,(1-y)^2 + \overline{xq(x)})$$

A fanciful way of writing the above expressions in terms of the nucleon structure functions is

$$\frac{d\sigma^{\nu_\mu N}}{dx\,dy} = \frac{G_F^2\,s}{2\pi} \cdot \left[(1-y)\,F_2^{\nu\overline{\nu}}(x) + \frac{y^2}{2}\,2\,x\,F_1^{\nu\overline{\nu}} + y\,(1-\frac{y}{2})\,x\,F^{\nu\overline{\nu}}\right]$$

where the following substitutions have been made:

$$F_2^{\nu\overline{\nu}}(x) = q(x) + \overline{q(x)}$$

$$2\,x\,F_1^{\nu\overline{\nu}}(x) = F_2^{\nu\overline{\nu}}(x)$$

$$x\,F_3^{\nu\overline{\nu}}(x) = q(x) - \overline{q(x)}$$

A more exact expression within the context of Quantum Chromodynamics predicts the formula below for the differential cross section for $\nu_\mu(\overline{\nu_\mu})$-N scattering:

$$\frac{d\sigma^{\nu_\mu\overline{\nu_\mu},N}}{dx\,dy} = \frac{G_F^2\,s}{2\pi} \cdot \left[(1-y-\frac{M_N\,x\,y}{2\,E_\nu})\,F_2^{\nu\overline{\nu}}(x) + \frac{y^2}{2}\,2\,x\,F_1^{\nu\overline{\nu}} \pm y\,(1-\frac{y}{2})\,x\,F^{\nu\overline{\nu}}\right] \tag{C.1}$$

In the above the spin-zero constituents of the nucleon contribute to the cross section. The relevant quantity, R is,

$$R = \frac{\sigma_L}{\sigma_T}$$

R can be expressed in terms of the structure function F_1 and F_2,

$$R = \frac{F_2(x)}{2\,x\,F_1(x)} - 1$$

For the case when R = 0 i.e. $F_2(x) = 2\,x\,F_1(x)$ we obtain the expression derived from simple parton-phenomenology.

§C.2 General derivation of the differential cross section

The expression (C.1) could be derived within quantum field theoretica frame work, invoking rather general assumptions of locality, Lorentz invariance, CP conservations and the fact that the muon mass could be neglected. In particular no reference to the spin structure of nucleon constituents or the quark-parton picture of the nucleon is needed to arrive at C.1.

One begins with the general expression of differential cross section, assuming that there are "n" final hadronic states as well as an emergent muon.

$$d\sigma = \frac{|M|^2}{4\,[(k.p)^2 - m_\nu^2\, m^2]^{\frac{1}{2}}} \times dL_{ips}$$

, where dL_{ips} refers to the Lorentz invariant phase space for the final states. The process is schematically shown below.

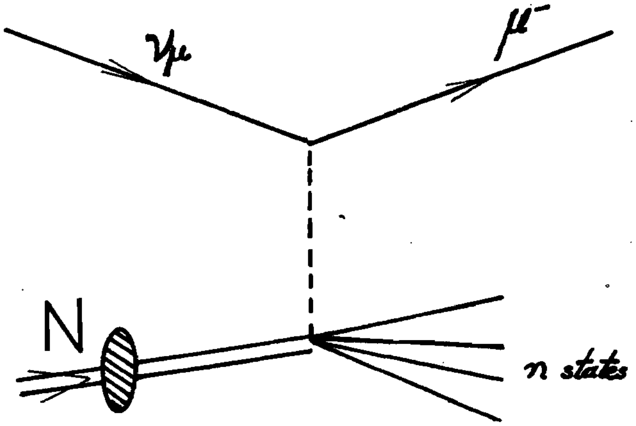

Upon substituting the expression for the Lorenz invariant phase space the above expression becomes:

$$d\sigma = \frac{|M|^2}{4\,[(k.p)^2 - m_\nu^2\, m^2]^{\frac{1}{2}}} \cdot (2\pi)^4\, \delta^4(P_{final} - P_{initial}) \cdot \frac{d^3k'}{(2\pi)^3\, 2\,E'} \cdot \Pi_{i=1}^{n} \frac{d^3p_i}{(2\pi)^3\, 2\,E_i}$$

where the energy and momentum variables are adopted from the figure shown above. The quantity M is the invariant amlitude for ν_μ-N scattering. M could be expressed in terms of the lepton and hadron currents and let the invariant amplitude be,

$$M = \frac{G_F}{\sqrt{2}} \cdot j^{\mu}_{lepton} \cdot J_{\mu,hadron}$$

where G_F is the Fermi constant of weak interaction. The initial nucleon and the final muon states are averaged over their respective spins. It follows,

$$|M|^2 = \frac{G_F^2}{2} \cdot L^{\mu\nu} \cdot W_{\mu\nu}$$

The lepton tensor, $L^{\mu\nu}$, is assumed to follow V-A and, thus, is calculable in terms of the neutrino and muon 4-momenta:

$$L^{\mu\nu} = 8\,[k'^{\mu} k^{\nu} + k'^{\nu} k^{\mu} + g^{\mu\nu}\,\frac{q^2 - m_\mu^2}{2} + i\,\epsilon^{\mu\nu\alpha\beta}\, k'_\alpha\, k_\beta]$$

where the 4-momentum transfer is $q = k - k'$.

The hadronic tensor, $W_{\mu\nu}$, is an unknown quantity. The most general form it could assume is:

$$\begin{aligned} W_{\mu\nu} = -W_1\, g_{\mu\nu} &+ \frac{W_2}{m^2}\, p_\mu\, p_\nu - i\,\frac{W_3}{2\,m^2}\, \epsilon_{\mu\nu\alpha\beta}\, p^\alpha\, q^\beta \\ &+ \frac{W_4}{m^2}\, q_\mu\, q_\nu + \frac{W_5}{m^2}\,(p_\mu\, q_\nu + q_\mu\, p_\nu) \\ &+ \frac{W_6}{m^2}(q_\mu\, p_\nu - q_\nu\, p_\mu) \end{aligned}$$

where the form factors (or structure functions) W_i are dimensionless functions of two of the three lorentz invariant quantities that could be constructed out of the 4-momenta q and p, i.e.

$$W_i = W_i(p.q, p^2)$$
$$\text{or } W_i = W_i(p.q, p^2)$$

Symmetries are invoked to eliminate some of the structure functions. CP invariance or equivalently T invariance dictates that W_6 be zero. Furthermore, to invoke the electromagnetic interaction type of gauge symmetry,

$$q_\mu \cdot L^{\mu\nu} = q_\nu \cdot L^{\mu\nu} = 0$$

one assumes that $m_\mu = 0$. This assumption is justified in the light of extreme high energy of the incident ν and that of the emergent μ. As a result two more structure functions, W_4 and W_5 could be dropped. There are three remaining form factors in the hadronic tensor.

Contracting the two tensors and rearranging some of the terms in the expression of the differential cross section, one arrives at:

$$\frac{d\sigma^{\nu,\bar{\nu}}}{dE'\,d\Omega'} = \frac{G_F^2}{2(2\pi)^2} \times \frac{E'}{E} \times \left[2W_1 Q^2 + W_2(4EE' - Q^2) \mp W_3 Q^2 \frac{E+E'}{m}\right] \quad \text{(C.2)}$$

Lastly, expressing the kinematical quantities in terms of the scaling variables, x and y, and redefining the structure functions as:

$$mW_1 = F_1$$
$$\nu W_2 = F_2$$
$$\text{and } \nu W_3 = F_3$$

one derives the expression C.1.

Appendix D

Production of Secondary Mesons in P-Be Collision

The invariant cross section of high-energy hadron colllision follows a scaling law proposed by Feynman [104]. It scales with a variable, X_F, which is defined as

$$X_F = \frac{P_{\text{secondary particle}}}{P_{\text{primary particle}}}$$

The invariant cross section can then written in a factorized form: a factor containing the X_F distribution and another the P_T behaviour of the secondary particles. This could be stated as:

$$E \cdot \frac{d^3N}{d^3P} = E \times \frac{d^3N}{P^2\, dP\, d\Omega} = f(P_T) \times g(X_F)$$

where f(P_T) is some function of P_T of the secondaries and "g(X_F)" expresses the distribution of the scaling variable.

§D.1 Measurement of Particle Production at CERN

Atherton et. al. have measured the composition of secondary $\pi^+, \pi^-, K^+, K^-, P$ and $\overline{P}$ in a 400 GeV P-Be collision at CERN. They have also measured the absolute production cross section. Measurements were made on the positives and negative secondaries at four momenta (60, 120, 200 and 300 GeV/c), two transverse momenta (0 and 500 MeV/c), and for three target lengths (100, 300 and 500 mm of Be).

The measured X_F and P_T of each of the secondary particles were fitted to the following form for the invariant cross section:

$$\frac{d^2N}{dP\,d\Omega} = A \cdot \left[\frac{B}{P_0} e^{-B \cdot \frac{P}{P_0}} \right] \cdot \left[\frac{2CP^2}{2\pi} e^{-C(P\theta)^2} \right]$$

where the variable P_0 denotes the initial momentum of the proton (400 GeV) and the parameters A, B and C depend upon the type of secondary paritcles . One notices that the above formula for the invariant cross section scales with $X_F = P/P_0$. The table below present the fitted values of these parameters for the various secondaries.

Particles	*A*	*B*	*C*
π^+	1.2	9.5	5.0
π^-	0.8	11.5	5.0
K^+	0.16	8.5	3.0
K^-	0.10	13.0	3.5
P	0.06	16.0	3.0

Atherton: Secondary Production in P-Be Collision

There is another fit made to the same data due to Malensek [105]. Malensek has made a four parameter fit to Atherton's data. The form for the invariant cross section assumed here is:

$$d^2\sigma/dP\,d\Omega = B X_F \frac{(1-X_F)^A\,(1+5\,e^{-DX_F})}{(1+\frac{P_T^2}{M^2})}$$

The table below shows the best fit values for the parameters A, B, M^2 and D.

Particles	*A*	*B*	M^2	*D*
π^+	3.598	177.2	.7077	27.00
π^-	4.122	70.60	.8932	11.29
K^+	2.924	14.15	1.164	19.89
K^-	6.107	12.33	1.098	17.78
P	7.990	5.81	1.116	14.25

Malensek: Secondary Production in P-Be Collision

The secondary production for the CCFRR NBB was simulated using both the fits. When folded against the dichromatic train acceptance, both yeilded very similar results. In our results presented in this dissertation we have employed the fit due to Atherton et. al. Fig. D.1 shows the momentum distributions of the secondary negative pions and kaons for a fixed number of 400 Gev protons.

Appendix E

Error Estimates for the WSM Monte Carlo Calculations

The errors incurred in the various monte carlo computation employed in this thesis have been discussed in this appendix.

§E.1 Error in WBB Monte Carlo

The systematic error in estimating the WBB component of WSM occur in the following three stages,

a. Production of the secondary particles

Atherton et. al. (see Appendix D) have estimated their measurement errors as follows :

i. Error on the primary flux ≈ 5%

ii. Error in the beam optics ≈ 4%

iii. Collimator opening uncertainty $\approx$ 1%- 4%

iv. All other corrections are of the order 1%

When added in quadrature the above errors yeild an error of $\approx$ 8%. However the data at P_T's of 300 Mev or 500 Mev is rather poor and the agreement between the data and the value given by the formula (see Appendix D) is only marginally good. We estimate this to contribute an addition of 6%error. Thus the overall error form the particle production is of the order $\approx$ 10%.

b. Errors in simulating the hadron beam

We have used the program Decay Turtle to simulate transportation of the secondary beam. The errors in the turtle calcuations have been discussed in detail in [15,23,24]. The error so incurred is estimated to be $\approx$ 10%- 15%. The error depends rather critically on the P_T-dependence of the secondry production as well as the proton spot-size on the target. The latter is a poorly measured quantity being equal to $\approx$ $(.5 \pm .2)$mm X 1mm.

c. Errors in simulating antineutrino inetractions in the detector

The critical factor here is the precision to which the antiquark distribution is known. In the text we have extimated this to be of the order of 8%- 9%. In addition to the above, the WBB contibution form the primary dump has large errors. The error is of the order of 50%when the various assumptions are employed to estimate this contribution. However, the background due to this source is an order of magnitude lower than the corresponding background arising at the primary target at high energies. Therefore this large error is not a detrimental factor in the WBB estimations.

The overall errors in WBB computation is assumed to be, ≈ 20%.

§E.2 Dilepton Monte Carlo Calculations

The three dilepton background estimations use essentially the same dimuon Monte Carlo with little variation. We estimate the error to be 20%following Lang [16]. The simulation of charm production in ν-N interaction as well as the parametrization of π/K production and decay in the ν-initiated hadron shower uses data from other experiments, e.g. BEBC, EMC, E379 etc., as well as theoretical assumptions. The errors in the input data and the uncertainties in the theoretical parameters contribute to the systematic errors in our calculations enumerated below:

a. The errors in the fragmentation functions used to generate the hadronic states in ν-N scattering lent an uncertainty of ±15%in the probability of muon production. This came about because the Lund Monte Carlo fragmentation function was considered to be target-invariant. This assumption is refuted by the EMC measurement.

b. The uncertainty in the Lund Monte Carlo parameter, λ, caused an error of ±6%in the μ^+ production estimation.

c. The uncertainty of ±2%in the decay probability and interaction lengths of π/K led to a ±1%systematic error in the dimuon Monte Carlo.

d. The simulation of multiple interactions of the secondary mesons was not exact and an inherent uncertainty of ±20%in this parameter caused an error of ±10%in the muon production.

e. The final muon rates were computed to an accuracy of ±5%.

The overall systematic uncertainty incurred in the dimuon Monte Carlo, ±20%, was obtained after adding the above errors in quadrature.

Appendix F

24 WSM Events with Evis > 100 GeV and Y > .5

Kinematical quantities associated with the 24 WSM events have been summarized in this appendix.

```
  SMOM     200  RUN      1633  EVENT     695  PLACE        23  IGATE       2  RINT     59.77
  EVIS  113.69  EMIS    32.20  PTOT1   -8.26  EHAD   105.4250  VERTX   25.89  VERTY    53.87
 THETA    .087  PHI     2.162  XVIS      .04  YVIS       .927  QSQ      7.13

  SMOM     200  RUN      1763  EVENT    1968  PLACE        57  IGATE       2  RINT     61.25
  EVIS  117.83  EMIS    23.71  PTOT1  -29.08  EHAD    88.7479  VERTX   47.44  VERTY   -38.75
 THETA    .043  PHI     3.109  XVIS      .04  YVIS       .753  QSQ      6.21

  SMOM     250  RUN      1349  EVENT    4269  PLACE        39  IGATE       2  RINT     26.18
  EVIS  145.78  EMIS    70.19  PTOT1  -12.04  EHAD   133.7453  VERTX  -17.09  VERTY    19.83
 THETA    .081  PHI     2.596  XVIS      .05  YVIS       .917  QSQ     11.61

  SMOM     250  RUN      1383  EVENT     187  PLACE        20  IGATE       2  RINT     35.83
  EVIS  108.80  EMIS    84.52  PTOT1  -53.37  EHAD    55.4309  VERTX  -12.94  VERTY   -33.41
 THETA    .011  PHI     2.477  XVIS      .01  YVIS       .509  QSQ       .73

  SMOM     250  RUN      1582  EVENT    6194  PLACE        25  IGATE       2  RINT     19.92
  EVIS  136.11  EMIS    81.35  PTOT1  -12.75  EHAD   123.3629  VERTX   -3.25  VERTY   -19.66
 THETA    .086  PHI     2.053  XVIS      .06  YVIS       .906  QSQ     12.86

  SMOM     250  RUN      1803  EVENT    1752  PLACE        44  IGATE       2  RINT     58.97
  EVIS  159.58  EMIS     5.18  PTOT1  -18.54  EHAD   141.0318  VERTX   34.42  VERTY    47.88
 THETA    .056  PHI     3.037  XVIS      .04  YVIS       .884  QSQ      9.39

  SMOM     250  RUN      1968  EVENT    1363  PLACE        73  IGATE       2  RINT     58.73
  EVIS  125.79  EMIS    37.62  PTOT1  -47.42  EHAD    78.3758  VERTX   53.20  VERTY    24.89
 THETA    .056  PHI     2.559  XVIS      .13  YVIS       .623  QSQ     18.92

  SMOM     250  RUN      2007  EVENT    4762  PLACE        23  IGATE       2  RINT     27.64
  EVIS  161.12  EMIS    50.09  PTOT1  -15.03  EHAD   146.0934  VERTX   26.12  VERTY    -9.02
 THETA    .067  PHI      .949  XVIS      .04  YVIS       .907  QSQ     10.97

  SMOM     140  RUN      1524  EVENT    6911  PLACE        27  IGATE       1  RINT     50.90
  EVIS  120.60  EMIS      .36  PTOT1  -30.43  EHAD    90.1688  VERTX  -41.38  VERTY    29.64
 THETA    .017  PHI     1.601  XVIS      .01  YVIS       .748  QSQ      1.00

  SMOM     165  RUN      1732  EVENT    4093  PLACE        36  IGATE       1  RINT     37.52
  EVIS  122.58  EMIS    24.87  PTOT1  -19.87  EHAD   102.7175  VERTX  -22.82  VERTY    29.78
 THETA    .022  PHI     2.746  XVIS      .01  YVIS       .838  QSQ      1.21

  SMOM     200  RUN      1755  EVENT    3236  PLACE        56  IGATE       1  RINT     42.78
  EVIS  231.46  EMIS   -68.12  PTOT1  -80.66  EHAD   150.7982  VERTX   37.14  VERTY   -21.23
 THETA    .062  PHI     2.779  XVIS      .26  YVIS       .652  QSQ     72.35

  SMOM     250  RUN      1850  EVENT    2846  PLACE        36  IGATE       1  RINT     16.85
  EVIS  148.64  EMIS    72.71  PTOT1  -40.70  EHAD   107.9413  VERTX    1.08  VERTY   -16.82
 THETA    .069  PHI     2.013  XVIS      .14  YVIS       .726  QSQ     28.82

  SMOM     250  RUN      1988  EVENT    7090  PLACE        29  IGATE       1  RINT     23.10
  EVIS  129.43  EMIS   -61.14  PTOT1  -45.17  EHAD    84.2579  VERTX   -5.87  VERTY    22.35
 THETA    .067  PHI      .117  XVIS      .17  YVIS       .651  QSQ     26.60
```

```
 SMOM     165  RUN      372  EVENT    1828  PLACE       34  IGATE       2  RINT     31.34
 EVIS  128.20  EMIS   23.02  PTOT1  -29.82  EHAD   98.3719  VERTX   24.67  VERTY   -19.33
THETA    .016  PHI    1.622  XVIS      .00  YVIS      .767  QSQ       .92

 SMOM     250  RUN      436  EVENT   10820  PLACE       45  IGATE       2  RINT     45.38
 EVIS  140.78  EMIS   48.05  PTOT1  -58.99  EHAD   81.7875  VERTX   15.24  VERTY    42.74
THETA    .075  PHI    2.531  XVIS      .30  YVIS      .581  QSQ     46.57

 SMOM     250  RUN      443  EVENT    1332  PLACE       23  IGATE       2  RINT     28.57
 EVIS  187.98  EMIS   20.75  PTOT1  -59.18  EHAD  128.7933  VERTX   24.16  VERTY   -15.25
THETA    .013  PHI     .719  XVIS      .01  YVIS      .685  QSQ      1.81

 SMOM     250  RUN      460  EVENT    5372  PLACE       24  IGATE       2  RINT     42.94
 EVIS  176.73  EMIS    4.30  PTOT1  -73.76  EHAD  102.9751  VERTX  -11.40  VERTY   -41.40
THETA    .045  PHI    2.445  XVIS      .14  YVIS      .583  QSQ     26.95

 SMOM     250  RUN      461  EVENT    1016  PLACE       20  IGATE       2  RINT     17.68
 EVIS  220.16  EMIS     .09  PTOT1  -64.43  EHAD  155.7240  VERTX   -8.24  VERTY   -15.64
THETA    .001  PHI     .695  XVIS      .00  YVIS      .707  QSQ       .01

 SMOM     250  RUN      478  EVENT      53  PLACE       30  IGATE       2  RINT     40.79
 EVIS  176.25  EMIS   14.71  PTOT1  -11.36  EHAD  164.8874  VERTX  -37.97  VERTY    14.90
THETA    .030  PHI     .444  XVIS      .01  YVIS      .936  QSQ      1.83

 SMOM     200  RUN      619  EVENT    1564  PLACE       19  IGATE       2  RINT     20.44
 EVIS  113 26  EMIS  -49.16  PTOT1  -12.60  EHAD  100.6611  VERTX   17.76  VERTY    10.13
THETA    .025  PHI    3.085  XVIS      .00  YVIS      .889  QSQ       .87

 SMOM     140  RUN      684  EVENT    2150  PLACE       32  IGATE       2  RINT     32.04
 EVIS  118.30  EMIS   10.93  PTOT1  -18.47  EHAD   99.8349  VERTX  -14.60  VERTY   -28.52
THETA    .038  PHI     .881  XVIS      .02  YVIS      .844  QSQ      3.21

 SMOM     250  RUN      837  EVENT     930  PLACE       22  IGATE       2  RINT     50.26
 EVIS  132.56  EMIS   45.30  PTOT1  -19.06  EHAD  113.4993  VERTX  -28.84  VERTY    41.17
THETA    .012  PHI     .809  XVIS      .00  YVIS      .856  QSQ       .36

 SMOM     200  RUN      545  EVENT    4552  PLACE       31  IGATE       3  RINT     31.79
 EVIS  110.10  EMIS   61.39  PTOT1   -7.78  EHAD  102.3153  VERTX  -22.40  VERTY   -22.55
THETA    .064  PHI    1.259  XVIS      .02  YVIS      .929  QSQ      3.46

 SMOM     200  RUN      727  EVENT    1964  PLACE       52  IGATE       3  RINT     50.97
 EVIS  110.70  EMIS   40.52  PTOT1  -17.82  EHAD   92.8801  VERTX  -50.95  VERTY    -1.37
THETA    .060  PHI     .706  XVIS      .04  YVIS      .839  QSQ      7.07
06.43.42.UCLP, GC, TA10,       0.174KLNS.          ** END OF LISTING **
```

Appendix G

23 Trimuon Events

Kinematical quantities pertaining to 23 trimuon events are presented below. The computed generated event-schematics are shown in Fig. G.1-G.23.

```
RUN, EVENT, EVIS, EHAD, PMU1, PMU2, PMU3       354     4373    147.30   121.60     3.90    10.90    10.90
PT1, PT2,   PT3,  M12,  M13,  M23,  M123       .14     1.50      1.50      .20      .75      .75     1.05
TH1, TH2,   TH3,  PHI1, PHI2, PHI3,PHI23      .036     .138      .138  170.684  206.723  206.723  206.723
                  PHT1, PHT2, PHT3,                                      -.145   -1.225   -1.225

RUN, EVENT, EVIS, EHAD, PMU1, PMU2, PMU3       365     4505    137.60    86.00    25.30    16.50     9.80
PT1, PT2,   PT3,  M12,  M13,  M23,  M123       .94      .61       .43      .20      .34      .30      .44
TH1, TH2,   TH3,  PHI1, PHI2, PHI3,PHI23      .037     .037      .044  312.778  312.778  336.269  322.473
                  PHT1, PHT2, PHT3,                                     -1.211    -.790    -.502

RUN, EVENT, EVIS, EHAD, PMU1, PMU2, PMU3       371       67    156.40    65.60    32.40    54.30     4.10
PT1, PT2,   PT3,  M12,  M13,  M23,  M123      2.14     3.53       .36      .20     2.27     1.76     2.87
TH1, TH2,   TH3,  PHI1, PHI2, PHI3,PHI23      .066     .065      .087  263.905  263.905   95.799  262.581
                  PHT1, PHT2, PHT3,                                     -3.189   -5.290     .215

RUN, EVENT, EVIS, EHAD, PMU1, PMU2, PMU3       416     5662    176.40    37.40    90.40    31.70    16.90
PT1, PT2,   PT3,  M12,  M13,  M23,  M123      1.90      .63       .56      .52      .52      .50      .86
TH1, TH2,   TH3,  PHI1, PHI2, PHI3,PHI23      .021     .020      .033  341.540  316.388  350.765  332.441
                  PHT1, PHT2, PHT3,                                     -6.481   -2.181   -1.407

RUN, EVENT, EVIS, EHAD, PMU1, PMU2, PMU3       478     1631    200.20    45.10   137.90     3.50    12.40
PT1, PT2,   PT3,  M12,  M13,  M23,  M123      1.10      .62       .78     2.93     4.47     1.75     5.62
TH1, TH2,   TH3,  PHI1, PHI2, PHI3,PHI23      .008     .179      .063  300.975  256.055  125.019  176.694
                  PHT1, PHT2, PHT3,                                     -4.476    -.525     .476

RUN, EVENT, EVIS, EHAD, PMU1, PMU2, PMU3       478     9194    202.00    74.60   104.40    16.40     6.60
PT1, PT2,   PT3,  M12,  M13,  M23,  M123      2.92      .39       .46      .74     2.17      .96     2.48
TH1, TH2,   TH3,  PHI1, PHI2, PHI3,PHI23      .028     .024      .069   31.799   69.786  282.354  -17.859
                  PHT1, PHT2, PHT3,                                     -7.008    -.952    -.107

RUN, EVENT, EVIS, EHAD, PMU1, PMU2, PMU3       542       47    219.10   170.50    21.60     5.40    21.60
PT1, PT2,   PT3,  M12,  M13,  M23,  M123       .58      .93       .41      .85     2.09     1.97     2.99
TH1, TH2,   TH3,  PHI1, PHI2, PHI3,PHI23      .027     .173      .019  141.864  276.853   30.596  -56.974
                  PHT1, PHT2, PHT3,                                      -.657     .639     .075

RUN, EVENT, EVIS, EHAD, PMU1, PMU2, PMU3       569     3241     88.20    43.50    31.10     8.50     5.10
PT1, PT2,   PT3,  M12,  M13,  M23,  M123      3.94      .66       .16     3.08     1.63      .72     3.54
TH1, TH2,   TH3,  PHI1, PHI2, PHI3,PHI23      .127     .078      .032  328.477  101.586  243.908  112.180
                  PHT1, PHT2, PHT3,                                     -6.713    -.316    -.476

RUN, EVENT, EVIS, EHAD, PMU1, PMU2, PMU3       671     1592     49.30    18.30    14.10    11.30     5.60
PT1, PT2,   PT3,  M12,  M13,  M23,  M123       .79      .10       .51      .73      .66      .70     1.18
TH1, TH2,   TH3,  PHI1, PHI2, PHI3,PHI23      .056     .009      .091   42.342  125.535   93.220   98.442
                  PHT1, PHT2, PHT3,                                     -1.395    -.499    -.561

RUN, EVENT, EVIS, EHAD, PMU1, PMU2, PMU3       674     2164    124.90    53.40    65.20     3.60     2.70
PT1, PT2,   PT3,  M12,  M13,  M23,  M123      2.02      .31       .09     1.46      .66      .43     1.64
TH1, TH2,   TH3,  PHI1, PHI2, PHI3,PHI23      .031     .087      .035    2.521  269.119   92.418  267.693
                  PHT1, PHT2, PHT3,                                     -4.485    -.117    -.102
```

```
RUN, EVENT, EVIS, EHAD, PMU1, PMU2, PMU3        1834      6175     88.07     28.81     52.85      3.51      2.91
PT1, PT2,   PT3,  M12,  M13,  M23,  M123        1.59       .26       .24      1.15      1.25       .23      1.69
TH1, TH2,   TH3,  PHI1, PHI2, PHI3,PHI23        .030      .075      .081   289.860    24.523    49.504    36.310
                  PHT1, PHT2, PHT3,                                         -4.489     -.171     -.043

RUN, EVENT, EVIS, EHAD, PMU1, PMU2, PMU3        1859      2333    195.49    186.83      2.21      2.21      4.25
PT1, PT2,   PT3,  M12,  M13,  M23,  M123         .56       .56       .12       .75       .41       .73      1.09
TH1, TH2,   TH3,  PHI1, PHI2, PHI3,PHI23        .258      .258      .029    53.572    90.470    93.564    91.026
                  PHT1, PHT2, PHT3,                                          -.569     -.456     -.107

RUN, EVENT, EVIS, EHAD, PMU1, PMU2, PMU3        1614       434    220.68    127.47     75.06      7.37     10.77
PT1, PT2,   PT3,  M12,  M13,  M23,  M123        1.65       .51       .37      1.58      2.10       .38      2.64
TH1, TH2,   TH3,  PHI1, PHI2, PHI3,PHI23        .022      .069      .034   104.508   314.783   303.954   310.249
                  PHT1, PHT2, PHT3,                                         -2.623      .343      .206

RUN, EVENT, EVIS, EHAD, PMU1, PMU2, PMU3        1782       550     72.50     62.94      4.23      2.84      2.49
PT1, PT2,   PT3,  M12,  M13,  M23,  M123         .95       .47       .29      1.22       .43       .65      1.42
TH1, TH2,   TH3,  PHI1, PHI2, PHI3,PHI23        .227      .166      .116   132.468   256.342   146.448   220.215
                  PHT1, PHT2, PHT3,                                         -1.015      .219     -.317

RUN, EVENT, EVIS, EHAD, PMU1, PMU2, PMU3        1713      2702    121.72     39.95     68.39      5.40      7.98
PT1, PT2,   PT3,  M12,  M13,  M23,  M123        4.10       .32       .34      2.24      2.30       .29      3.21
TH1, TH2,   TH3,  PHI1, PHI2, PHI3,PHI23        .060      .060      .042    12.032   180.539   149.771   164.878
                  PHT1, PHT2, PHT3,                                        -11.074     -.237     -.571

RUN, EVENT, EVIS, EHAD, PMU1, PMU2, PMU3        1343      3220    143.47       .16    134.50      5.57      3.23
PT1, PT2,   PT3,  M12,  M13,  M23,  M123        5.51       .64      1.04      4.24      7.60       .93      8.75
TH1, TH2,   TH3,  PHI1, PHI2, PHI3,PHI23        .041      .115      .329    59.874   259.321   264.420   262.483
                  PHT1, PHT2, PHT3,                                         -8.036    -1.157    -1.252

RUN, EVENT, EVIS, EHAD, PMU1, PMU2, PMU3        1800      1109    140.75     66.50     65.31      5.54      3.40
PT1, PT2,   PT3,  M12,  M13,  M23,  M123        1.70       .39       .66      1.05      2.86       .66      3.11
TH1, TH2,   TH3,  PHI1, PHI2, PHI3,PHI23        .026      .071      .196   345.952    26.471    63.713    50.001
                  PHT1, PHT2, PHT3,                                         -3.364     -.440     -.225

RUN, EVENT, EVIS, EHAD, PMU1, PMU2, PMU3        1839       393    133.66     76.15     48.47      6.49      2.55
PT1, PT2,   PT3,  M12,  M13,  M23,  M123         .15      1.60       .18      4.46       .84       .85      4.61
TH1, TH2,   TH3,  PHI1, PHI2, PHI3,PHI23        .003      .249      .071   227.808    52.655    10.084    48.613
                  PHT1, PHT2, PHT3,                                          -.238     1.582      .138

RUN, EVENT, EVIS, EHAD, PMU1, PMU2, PMU3        1780      3364    142.50       .16    126.04      9.46      6.84
PT1, PT2,   PT3,  M12,  M13,  M23,  M123        4.41       .26       .54      1.94      3.03       .47      3.62
TH1, TH2,   TH3,  PHI1, PHI2, PHI3,PHI23        .035      .027      .079   331.972   101.414    95.913    97.679
                  PHT1, PHT2, PHT3,                                        -78.552    -6.270    -4.662

RUN, EVENT, EVIS, EHAD, PMU1, PMU2, PMU3        1541       123     54.00     41.96      3.38      4.33      4.33
PT1, PT2,   PT3,  M12,  M13,  M23,  M123         .25       .68       .68       .20       .45       .45       .61
TH1, TH2,   TH3,  PHI1, PHI2, PHI3,PHI23        .074      .157      .157     5.500    39.248    39.248    39.248
                  PHT1, PHT2, PHT3,                                          -.270     -.588     -.588
```

```
RUN, EVENT, EVIS, EHAD, PMU1, PMU2, PMU3         674      2625    130.50     18.00    102.70      4.90      4.90
PT1, PT2,   PT3,  M12,  M13,  M23,  M123        2.67       .56       .35      3.13      1.99       .40      3.72
TH1, TH2,   TH3,  PHI1, PHI2, PHI3,PHI23        .026      .115      .072   296.219   138.541   175.153   152.509
                  PHT1, PHT2, PHT3,                                        -17.813     -.205     -.542

RUN, EVENT, EVIS, EHAD, PMU1, PMU2, PMU3         700      1836     37.80       .80     17.10      2.80     17.10
PT'  PT2,   PT3,  M12,  M13,  M23,  M123        1.20       .77       .50       .95      1.65      1.96      2.72
T    TH2,   TH3,  PHI1, PHI2, PHI3,PHI23        .070      .279      .029     4.354    51.624   317.763    17.778
                  PHT1, PHT2, PHT3,                                        -17.100    -2.724   -17.070

RUN, EVENT, EVIS, EHAD, PMU1, PMU2, PMU3         717      2289    119.70     85.10     15.10      4.40     15.10
PT1, PT2,   PT3,  M12,  M13,  M23,  M123        1.61       .78       .11      1.52       .88      1.43      2.25
TH1, TH2,   TH3,  PHI1, PHI2, PHI3,PHI23        .107      .179      .007   123.644    91.788   122.900    95.364
                  PHT1, PHT2, PHT3,                                         -1.897     -.747     -.392
```

Appendix I

The E744/E652 Test Run

To study the calorimetric response to hadrons of well defined energy for calibration purposes as well as to measure the muon-production from the hadronic interactions, a vital measurement for the LSDM/OSDM background estimation, CCFR collaboration conducted a test run in May-June 1984 using the improved Lab-E detector. The data from this test run was employed in one of the background estimation for the WSM events. This test run is briefly described below.

The hadrons of momenta 15, 25, 50, 100, 200 and 300 GeV were transported to the Lab-E apparatus through the NTW (neutrino test west) line of Fermilab. Primary 800 GeV protons form the tevatron were targetted at an aliminum target. The beam line transported the secondary hadrons, produced between 0 and 10 milliradians, to the detector. The secondary hadrons, mostly positively charged particles, could be momentum analysed using the spectrometer at the upstream end of the detector. This spectrometer, consisting of four multi-wire proportional chambers, two magnets and one drift chamber, had a momentum resolution from 7%at 10 GeV to 2%at 100 GeV and higher. A small scintillation counter located at the aperture of the magnet provided the timing information. The beam line and the various components of the hadron spectrometer are shown in Fig. I.1.

The Lab-E apparatus was essentially the one discussed in Chapter 3. The primary modification entailed the replacement of the spark chambers by drift chambers with new data acquisition system. The drift chambers had an active area of 3m X 3m with 24 horizontal and 24 vertical cells. Each cell was 12.7 cm wide by 1.9 cm high by 3m long. Each cell was equipped with three wires, two wires constituting the readout sense wires (.03mm diameter) facilitating the resolution of left-right ambiguity within the cell and the third wire was the field wire (.13 mm diameter). Hits from each sense wire was buffered into multi-hit TDCs and read out for each event. The hadron energy information was measured from the counter pulse heights. Three carts of the neutrino-detector were involved in this test.

The event trigger used in the analysis was the coincidence between the incident beam signal from the small timing counter and an energy deposition signal from the calorimeter. The data used in the analysis was with the beam of low intensity. This yields a cleaner sample of unbiased hadronic interactions. Furthermore, the selected events had a single hadron showering in the calorimeter. This was achieved by demanding that not more than one hit be observed in the X and the Y view of the upstream most drift chamber. There was some electron contamination in the beam. At high energy (> 100 GeV) this didnot pose a problem since the E.M. shower has a smaller penetration and consequently the ratio of the shower energy measured in the first three counters to the total energy peaks at one. For hadrons, the typical penetration is a lot longer (see Table 5.7). For the low energy setting, a 10 cm lead 'filter' was positioned in the beam line ahead of the upstream of the magnetic spectrometer to eliminate the electron background.

The analysis of the events proceeded along the lines discussed earlier. The pentration depth, shown in Table 5.7 and used in the analysis, was the calculated in terms of the downstream most counter with energy greater than 25%of a minimum ionizing particle. Details of the analysis are presented in Ref. [49].

References

[1] S.Weinberg, Phy. Rev. Lett. 19, 1264(1967). A. Salam and J.C. Ward, Nuovo Cimento 11, 568(1959), Phy. Lett 13, 168(1964). A. Salam in "Proceedings of the Eighth Nobel Symposium, ed. N. Svartholm (New York, Wiley Interscience, 1968).

[2] O. Klein, in "New Theories in Physics " (International School of Intellectual Cooperation, League of Nations, 77-93(1938). C. N. Yang and F. Mills, Phy. Rev. 96, 191(1954).

[3] Y. Nambu, Phy. Rev. Lett. 4, 380(1960). J. Goldstone, Nuovo Cimento 19, 154(1961); P. W. Higgs, Phy. Lett. 12, 132(1964); Phy. Rev. Lett. 13, 508(1964), and Phy. Rev. 145, 1156(1966); F. Englert and R. Brout, Phy. Rev. Lett. 13, 321(1964); G. S. Guralnik, C. R. Hagen and T. W. B. Kibble, Phy. Rev. Lett. 13, 585(1964); T. W. B. Kibble, Phy. Rev. 155, 1554(1967).

[4] D. Gross and F. Wilczek, Phy. Rev. Lett. 30, 1343(1973); H. D. Politzer, Phy. Rev. Lett. 30, 1346(1973).

[5] H. Harari, "Weak Interactions of Quarks and Leptons", Lectures presented at the twelfth annual SLAC Summer Institute on Particle Physics, Stanford, July 1984.

[6] C. Rubbia, Lectures presented at the twelfth annual SLAC summer institute on Particle Physics (Stanford, July 1984).

[7] M. Holder et al. Phy. Lett. 70B, 396(1977). A. Benvenuti et.al. , Phy. Rev. Lett. 41, 725(1978). J. G. H. de Groot et al.,Phy. Lett. 86B, 103(1979); T. Trinko et al., Phy. Rev. D23, 1889(1981); K. Nishikawa et al., Phy. Rev. Lett. 46, 1555(1981); K. Nishikawa et al., Phy. Rev. Lett. 54, 1336(1985).

[8] M. Veltman, UM 83-22 (1983), (university of Michigan).

[9] D. Schildknecht in XIX Rencontre de Moriond, La Plagne, February 1984.

[10] G. Fisk and F. Sciulli , Ann. Rev. Part. Sci. 32, 499(1982).

[11] R. E. Blair, Ph. D. thesis, Caltech (1982).

[12] M. V. Purohit, Ph. D. thesis, Caltech (1983).

[13] D. B. MacFarlane, Ph. D. thesis, Caltech (1983).

[14] I. Stockdale, Ph. D. thesis, University of Rochester, (1984).

[15] C. Haber, Ph. D. thesis, Columbia University, (1984).

[16] C. Lang, Ph. D. thesis, University of Rochester, (1985).

[17] D. A. Edwards and F. J. Sciulli, Fermilab T.M.-660, 2972.000.

[18] R. Blair et al., Nuc. Inst. and Meth., 226, 281(1984).

[19] P. Limon et al., Nuc. Inst. and Meth., 116, 317(1974).

[20] F. Merritt, Ph. D. thesis, Caltech (1977).

[21] H. W. Atherton et al., CERN 80-07, Super Proton Synchroton Division, 22 August 1980.

[22] T. Eichten et al., Nucl. Phy. B44, 333(1972).

[23] K. L. Brown et al., "Decay Turtle", CERN 74-2, 5 Feb, 1974.

[24] D. Carey, "turtle", NAL-64, 2041.000.

[25] C. H. Albright et al., "Signal for Tau neutrino events in a Beam Dump experiment", Fermilab-conf-79/36-THY, May 1979.

[26] S. Mori, "Estimated Tay Neutrino Flux From a Beam Dump at 400 Gev and 1000 Gev", TM-848, 2251.0, January, 1979.

[27] S. Mori, "Estimated Event Rates For Beam Dump Experiments", TM-774,2251.0,March, 1978.

[28] H. Abramowicz et al., "Prompt Neutrino Production In A Proton Beam-Dump Experiment", CERN-EP/82-17, 16 Feb, 1982.

[29] H. Wachsmuth, "Neutrino and Muon Fluxes In The CERN 400 Gev Proton Beam Dump Experiment", CERN-EP/79-125, 1979.

[30] M. J. Murtagh, Proc. 1979 Int. Symp. on Lepton and Photon Interactions at high energies, Fermilab, 1979, ed. T.B.W. Kirk and H.D.I. Abarbanel.

[31] B. C. Barish et al., Phy. Rev. Lett. 36, 939(1976).

[32] A. Benvenuti et al., Phy. Rev. Lett. 41, 1204(1978) and Phy. Rev. Lett. 42, 149(1979).

[33] M. Holder et al., Phy. Lett. 69B, 377(1977).

[34] C. Baltay et al., Columbia Univ. Preprint, 1984.

[35] H. C. Ballagh et al., Phy. Rev. Lett. 24, 7(1981).

[36] C. Baltay et al., Phy. Rev. Lett. 39, 62(1977).

[37] J. Blietschau et al., Phy. Lett. 60B, 207(1976).

[38] H. Deden et al., Phy. Lett. 58B, 361(1975).

[39] S. L. Glashow, J. Iliopoulos and L. Maiani, Phy. Rev. D2, 1285(1970).

[41] J. D. Bjorken, Phy. Rev. D17, 171(1978).

[42] M. Suzuki, Phy. Lett. B71, 139(1977).

[43] C. Peterson et al., Phy. Rev. D27, 105(1983).

[44] M. Aguilar-Benitez et al., Phy. Lett., 123B, 98(1984).

[45] M. Aguilar-Benitez et al., Phy. Lett., 123B, 103(1984).

[46] V. Barger et al., Phy. Rev. D14, 80(1976).

[47] V. Barger et al., Phy. Rev. D16, 746(1977).

[48] B. J. Edwards and T. D. Gottschalk, Nucl. Phy. B186, 309(1981).

[49] F. S. Merritt et al., "Hadron Shower Punchthrough for Incident Hadron of Momentum 15, 25, 50, 100, 200 and 300 Gev/c", Workshop on Muon Identification and Momentum Measurement at SSC and LHC Energies, Univ. Of Wisconsin, April 1985.

[50] M. Arneodo et al., Phy. Lett. 150B, 458(1985).

[51] A. Bodek, "Punchthrough in Hadronic Shower Cascade, Muon Identification and Scaling Laws for Different Absorbers", Univ. of Rochester preprint, ER13065-412, and Internal group memos.

[52] M. Kobayashoi and T. Maskawa, Prog. Theor. Phys. 49, 652(1973).

[53] P. Avery et al., Phy. Rev. Lett. 53, 1309(1984).

[54] D. Drijard et al., Phys. Lett. 81B, 250(1979).

[55] K. L, Giboni et al., Phy. Lett. 85B, 437(1979).

[56] W. Lockmacn et al., Phy. lett. 85B, 443(1979).

[57] D. Drijard et al. Phy. Lett. 85B, 452(1979).

[58] S. Brodsky et al., Phy. Lett. 93B, 451(1980).

[59] S. Brodsky wt. al., Phy. Rev. D23, 2745(1981).

[60] A. Chodos et al., Phy. Rev. D9, 3471(1974).

[61] W. A. Bardeen et al. Phy. Rev. D11, 1094(1975).

[62] J. F. Donoghue adn E. Golowich, Phy. Rev. D15, 3421(1977).

[63] P. Reutens et al., Phy. Lett. 152B, 404(1985).

[64] J. J. Aubert et al., Phy. Lett. 110B, 73(1982).

[65] J. C. Pati and A. Salam, Phy. Rev. Lett. 31, 661(1973).

[66] J. C. Pati and A. Salam, Phy. Rev. D10, 275(1974).

[67] R. N. Mohapatra and J. C. Pati, Phy. Rev. D11, 566(1975).

[68] R. N. Mohapatra et al., Phy. Rev. D11, 2588(1975).

[69] M. A. B. Beg et al., Phy. Rev. Lett. 38, 1252(1977).

[70] J. Carr et al., Phy. Rev. Lett. 51, 627(1983).

[71] R. S. Hayano et al., Phy. Rev. Lett. 52, 329(1984).

[72] H. Abramowicz et al., Z. Phy. C12, 225(1982).

[73] T. Yamanaka, Ph. D. Thesis, University of Tokyo, UT-HE-85/02.

[74] V. V. Akhmanov et al., Sov. J. Nucl. Phys. 6, 230(1968).

[75] C. A. Coombes et al., Phy. Rev. 108, 1348(1957).

[76] D. Cutts et al., Phy. Rev. 138, 969(1965).

[77] P. Auchincloss et al., Columbia University preprint, June 1985.

[78] B.C. Barish et al., Phy. Rev. Lett., 38, 577(1977).

[79] A. Benvenuti et al., Phy. Rev. Lett. 38, 1110(1977) ; A. Benvenuti et al., Phy. Rev. Lett. 38, 1183(1977).

[80] M. Holder et al., Phy. Lett. 70B, 393(1977).

[81] T. Hansl et al., Nucl. Phy. B142, 381(1978).

[82] F. Bletzacker, H. T. Nieh and A. Soni, Phy. Rev. Lett. 38, 1241(1977)

[83] H. Goldberg, Phy. Rev. Lett. 39, 1598(1977)

[84] A. Soni, Phy. Lett. 71B, 435(1977).

[85] R. Godbole, Stony Brook preprint ITP-SB-77-70.

[86] C. H. Albright, J. Smith and J. A. M. Vermaseren, Fermilab-Pub -78/14-THY, January 1978.

[87] R. M. Barnett et.al., Phy. Rev. D 17, 2266(1978).

[88] V. Barger et al., Phy. Rev. D 17, 2284(1978); Phy. Lett. 76B, 494(1978).

[89] J. Smith and J. A. M. Vermaseren, Phy. Rev. D17, 2288(1978).

[90] K. F. Anderson et al., Phy. Rev. Lett 37, 799(1976) and the following article in the same issue.

[91] R. M. Barnett and L. N. Chang, Phy. Lett, 72B, 233(1977).

[92] V. Barger, T. Gottschalk and R. J. N. Philips, Phy. Lett. 70B, 243(1977).

[93] S. Brodsky and S. Ting, Phy. Rev. 145, 1018(1966).

[94] J. J. Russell et al., Phy. Rev. Lett. 26, 46(1971).

[95] B. Young et al., Phy. Lett. 74B, 111(1978)

[96] P. Auchincloss et al., "Hadron Shower Profile and Direction Measurement in a Segmented Calorimeter", Proceedings of Gas Calorimetry Workshop, Batavia, 1982. Also on-going studies on FADC that were used during the experiment E744.

[97] C. Peck et. at., DESY/SLAC preprint (1984).

[98] UA1 Collaboration, G. Arnison et al., Phy. Lett., 139B, 115(1984).

[99] UA2 Collaboration, P. Bagnaia et al., Phy. Lett. 139B, 105(1984).

[100] UA1 Collaboration, G. Arnison et al., Phy. Lett. 135B, 250(1984).

[101] UA2 Collaboration, P. Bagnaia et al., Phy. Lett. 129B, 130(1983).

[102] J. Ellis, Talk at Fourth Workshop on Proton Antiproton Collider Physics, Bern, March 1984, Editors H. Hanni and J. Schacher, CERN Geneva, 1984.

[103] L. J. Hall, R. L. Jaffe and J. L. Rosner, Phy. Report, 125, No. 3, 103(1985).

[104] R. P. Feynman, Phy. Rev. Lett., 23, Number 24 (1969)

[105] A. J. Malensek, FNAL Technical Memo,, FN-341, 2941.000.

Acknowledgements

A native from a village in the foothills of the Himalayas, I always thought the mountains were easy of access, their peaks beckoning. But as one approaches them difficulties appear; the higher one goes the more steep becomes the climb; the peaks recede into the clouds. My five years journey through graduate studies in Physics was in some ways like those mountains. But the journey was worth while. And now I have the pleasant task of thanking my teachers and friends who lent a helping hand along the way, who fostered an exciting atmosphere in which to do research, and who instilled in me the joy of doing physics.

I am deeply indebted to my advisior, Professor Frank Sciulli, for his encouragement and support through these years. I shall cherish his insight in all facets of experimental high energy physics; his ability to state the problem with a rare clarity. I am thankful to Dr. Drasko Jovanovic for sharing his enthusiasm on Wrong Sign events with me and offering full support for my work at Fermilab. To Professor Mike Shaevitz, I extend my heartfelt thanks for numerous discussions and for his characteristic good cheer when I needed it most.

I offer my special appreciation to Professor Wesley Smith for his infectious enthusiasm and 'a sense of humour that never goes awry'. To Professor Robert Blair I owe my gratitude for his great patience, for his deligent analysis of any problem I was confronted with and for his friendship. As a measure of my regard for him I can honestly say that I never had a discussion with him without learning something.

The experiments E616 and E701 represent a splendid accomplishment of the CCFRR collaboration. Each member of the collaboration has my appreciation for his contribution to the group. In particular, I would like to thank Gene Fisk, Arie Bodek, Frank Merritt, Petros Rapidis, Mark Oreglia, Fred Bocherding and Nikos Giokaris as my mentors. I should like to thank my predecessors Bob Blair, Milind Purohit and Dave MacFarlane for their herculean analysis efforts. The same applies to my colleagues Carl Haber, Ian Stockdale, Carol Lang, Patrik Reutens, Ed Oltman and Priscilla Auchincloss. It was a pleasure to learn the intricacies of analyzing a problem with Milind. I could not have done the wide band background calculation quite so speedily without the help of Carl Haber. I consider it a privilege to have had the opportunity to work in CCFRR collaboration.

Nevis, which at times does appear to be the queerest lab besides Alice in Wonderland, provided a superb environment to grow and work in. I wish to thank Anne Therrian, who, ever since my first year, freely offered her friendship, and helped me in many a fix. I am greateful to Mr. Bill Sippach, Mr. Herb Cunitz and Mr. Yin Au for helping me to be aware of the hidden architecture behind an experiment and for teaching me many technical details over the years I worked with them. I thank Dr. Bruce Knapp for sharing his vast knowledge and meticulous reflections on many aspects of high energy physics. My tenure at Nevis would not have been so pleasant and productive without my friends Kurt Bachman, Willis Sakamoto, Paul Quintas, Costas Foudas, Wing Cheong Leung, Ed Oltman and Priscilla Auchincloss. To Ed (an American Indian indeed!) and Priscilla, my longest companions, I wish many successes and productive years. I express my thanks to my dear friends Dr. Yi Xie Xu, Dr. Nilotpal Mitra and Dr. Subhash Gupta for their affectionate support throughout these years.

I thank Priscilla Auchincloss for critically reading this thesis and often smiling at a particular paragraph only to tell me it was not my elucidation but the spelling which amused her.

Finally, I think with gratitude of my teachers who have inspired me, shared with me their joy of learning and chiselled me into a better physicst: my teachers at Palamau, at St. Xavier's College, at B.I.T.S. Pilani, and at Columbia University. It is to them I humbly dedicate my thesis.

Table Captions

Table 2.1a: Characteristic Parameters of N0 Dichromatic train. The numbers refer to, for most cases, measurements made during E616 running.

Table 2.1b: Mean momenta and angular divergences of secondary beam. The angular divergences θ_x and θ_y are fractional changes in x and y with respect to change in z i.e.

$$\theta_x = \frac{\Delta_x}{\Delta_z}$$

$$\theta_y = \frac{\Delta_y}{\Delta_z}$$

The numbers are taken from E616 measurements.

Table 3.1: The parameters of the neutrino-detector at Lab-E. E616 had 6 target carts whereas E701 had 4.

Table 3.2: Muon momentum and hadron energy resolution.

Table 3.3: The table points out the differences in the apparatus for the two experiments.

Table 4.1: Reduction of the initial data through the WSM cuts mentioned in Sec. 4.2, for the five energy settings (4.1a through 4.1e). The number of μ^+, shown as the last entry of the tables, represent the sample to be visually scanned before interactive reconstruction. These scanned and reconstructed events, along with the regular CC events μ^-, were subjected to the final set of WSM cuts.

Table 4.2: Ambiguous events in E616(4.2a) and E701(4.2b). Default momentum refers to the lack of sign determination of the muons in the spectrometer. "Rtore" is the radius of the projected muon track at the front face of the toroid. Almost all of the ambiguous events had ρ_t greater than 65 inches.

Table 5.1: Incident primary proton flux and live-time for E616(5.1a) and E701(5.1b), during close-slit running. The number of incident protons per setting is in the units of 10^{17} protons. The units of live-times are different for fast and slow spills. However the corresponding units for fast spill live time and fast spill cosmic ray live time are equal. Same is the case for slow spill live time and slow spill cosmic ray live time.

Table 5.1c: Cosmic Ray live time for close-slit events.

Table	5.2:	WSM events from clos-slit data for E616(5.2a) and E701(5.2b). This data has to be normalized to the total number of protons incident during the open slit running. The nomalization factor is 19.7. Only one close-slit WSM event has Y $>$ .5 and none of these events has Evis $>$ 100 GeV.
Table	5.3:	Flux of the primary protons and the corresponding live times for five energy setting for E616(5.3a) and E701(5.3b). Once again the units of the live times are different for fast and slow spills.
Table	5.4:	Flux of the secondary particles and cosmic ray live times are listed for the five settings, for each of the two experiments respectively (E616:54.a and E701:5.4b). Fast spill cosmic ray live time has the same units as the fast spill live time tabulated in the previous table.
Table	5.4c:	Particle fractions of the secondary beam. The table has been compiled from E616 data. The data from E701 is currently under investigation. As pointed in Chapter 2; the particle fractions are measured employing the Cerenkov counter.
Table	5.5:	Number of secondary particles versus the distance-traversed from BeO target before being swept of the dichromatic train. The distances quoted in the table are in the units of feet.
Table	5.6:	Coordinates of the primary dump for various energy setting. The

logitudinal distance, Z, is in meters.

Table 5.7: The probability of penetration by a hadron shower of a given energy versus the depth of penetration. The depth of penetration has been represented in terms of counter number. The separation between two counters represent approximately 11 cm of steel (see Chapter 4). The table presents the probability of penetration vs depth for 15, 25 and 50 GeV in "2 cart" configuration. By "2 cart" configuration is meant that the corresponding data, during the test run, was recorded with two instrumented carts. The table lists the penetration probability for higher energies with "3 cart" configuration as well.

Table 6.1: Data and all backgrounds in two energy bins : Evis $<$100 and Evis $>$100 GeV. The table 6.1b refers to the data and background with Y $>$ .5. and Evis $>$ 100.

Table 6.2: Tables list the averages of various kinematical quantities, namely total visible energy, muon momentum, hadron energy, missing energy, Xvis, Yvis and Q^2. They also present the number of events in the tow energy bins. The four tables, a-d, represent four set of cuts : (a) Yvis $>$ 0., Evis $>$ 0., (b) Yvis $>$ .5 and Evis $>$ 0 (c) Yvis $>$ 0. and Evis $>$ 100, and finally, (d) Y $>$ .5 and Evis $>$ 100. Cosmic ray contamination have been subtracted. In both the cases, Y greater of less than .5, the same CC current

data has been employed to normalize the background.

Table 6.3: Shows the mean values of CC events as welll the total number of CC evet, used to calculate the relevant background.

Table 6.4: Acceptance correction for CC and WSM evets. The acceptance for WSM was obtained by making various assumption regarding its production mechanism. The acceptance corrected numbers are shown with and without the Y cuts.

Table 6.5: Acceptance corrected rates of WSM for various models. The cumulative model, assuming WBB and dilepton background jointly giving reise to WSM, yields approximately the same rate for the two cuts.

Table 6.6: Limits (upper and lower) on the rates of WSM. Only those events with Evis $>$ 100 GeV have been included.

Table 6.7: Table of the differens in Like Sign Muons cuts and the regular WSM cuts.

Table 6.8: Various kinematical quantities are tabulated for WSM with three different cuts : Y $>$ 0 and Evis $>$ 0 GeV(6.8a); Y $>$ 0 and Evis $>$ 100 GeV(6.8b); and Y $>$ .5 and Evis $>$ 100(6.8c). For this tabulation WSM data was made to pass through LSDM cuts.

Table 6.9: Comparision of Opposite Sign Dimuons with WSM. Both the data have been subject to the same cuts. Furthermore the leading

	muon in the dimuons is assumed to be a "neuttrino". The third column depict the "neutral current analog" of OSDM.
Table 6.10:	Comparision of WSM data to LSDM. Same as 6.9.
Table 7.1:	Dependence of angular resolution of the muon upon the momentum and the hadron energy. The angle is presented in milli radians and the muon momentum and hadron energy in GeV.
Table 7.2:	Characteristics of Trimuon events. The first column contains various kinematical attributes. Most of the variables are self explanatory. The momentum asymmetry, η, is defined as follows : $\eta = \frac{P_{\mu 2} - P_{\mu 3}}{P_{\mu 2} + P_{\mu 3}}$ The second and the third column contain data with 2.0 GeV and 4.5 GeV momentum cuts respectively. The trimuon event with $\mu^- \mu^+ \mu^+$ configuration has been removed from the sample before the tabulation of the kinematical properties. The fourth and the fifth columns contain the simulation of hadronic and radiative production of trimuons respectively.
Table 7.3:	Fitted parameters to the inclusive μ^-pair produciton from the decays of various vector mesons. The table has been taken form the paper by Anderson et. al. (see Chapter 7).

Figure Captions

Table 2.1a:

Figure 1.1: The Feynman diagrams of Charge Current (CC:1.1a), Neutral Current (NC:1.1b) and Opposite Sign Dimuon (OSDM:1.1c) interactions of neutrinos. Figure 1.1d and 1.1e Schematic of neutrino induced Wrong Sign Muon (WSM) and Like Sign Dimuons (LSDM). The figure merely illustrates the experimental signatures of the two interactions.

Figure 1.2: The schematic of WSM and LSDM production via a 'Cigar' event. The bound state of the intermidiate vector bosons, Z, and W in the case of WSM and W' and W in the case of LSDM, has been call 'Cigar' by Veltman. A cigar, in general, may decay into four firmion. In order to reproduce the experimental signatures of WSM or LSDM, the other two firmions are chosen to be quarks and consequently they are manifest in the hadron shower.

Figure 1.3: Illustrations of the production mechanism of WSM and LSDM within the context of Composite-model. The model predicts a host of excited intermidiate bosons populating the desert of the minimal standard model. The composite excited bosons may decay into four firmions. This feature is similar to Veltman's model. In the wake of WSM and LSDM events, the other two firmions (see the figure) are taken to be quarks.

Figure 2.1: Overall view of the neutrino beam line as well as the detector with respect to the accelerator.

Figure 2.2: The accelerator magnet current (upper profile) and the 400 Gev primary beam intensity (lower profile) over an extraction cycle. The extraction cycle refers to the operation of the accelerator during the experiment E701.

Figure 2.3a: A conceptual summary of narrow-band focusing of secondaries, produced in the P-Be collison, to achieve the dichromatic neutrino spectrum. The quadrupole Q1 focuses in the horizontal direction and defocuses in the vertical direction, to increase the acceptance, whereas Q2 does just the opposite. The dipoles D1, D2 and D3 provide the required bending to eliminate WBB and secondaries of undesired momenta. The overall effect is one of point-to-parallel focusing. 'PD' refers to the primary dump i.e. to the inserts in the beam line to absorb the primary protons that didnot interact in the target. 'MS' is the momentum defining slit. The aperture of this slit determins $\frac{\Delta P}{P}$, or the momentum byte of the secondary beam. The last dipole D5 is the steering magnet which directs the beam into the decay pipe 'DP'.

Figure 2.3b: The detailed schematic of the narrow-band beam.

Figure 2.3c: A layout of the NBB line illustrating the relative positions of various components and access stations.

Figure 2.4: An overview of the NBB, decay pipe, muon shield (berm) and the Lab-E detector.

Figure 2.5: Logic-diagram of the gating and readout of the primary proton flux, as the proton passes through the Neuhall toroid before impinging the target.

Figure 2.6a: SWIC (Segmented Wire Ionization Chamber) profiles at the expansion port and Target Manhole. These profiles are used to determine whether the beam has been misdirected.

Figure 2.6b: Schematic of an Ionization Chamber. The readout of the right and left halves as well as the top and bottom halves of the chamber provide a quatitative measure of the beam steering.

Figure 2.7: The 'dichromatic band' of neutrino events in Lab-E as seen in E701. The upper band pertains to kaons and the lower to pions.

Figure 2.8: A plot of neutrino flux from various sources. The three body

decay of the koan into an positron, an electron neutrino and a π^0 will be referred to as K_{e3} decay. The corresponding three body decay into μ-leptons will be called $K_{\mu 3}$ decay. The $K_{\mu 3}$ neutrino flux is a little smaller than the K_{e3} flux owing to the larger baranching ratio of the latter.

Figure 3.1: An overview of the neutrino detector. The 6 cart configuration refers to the E616 set up.

Figure 3.2: Schematic of a target cart.

Figure 3.3: Details of a target counter.

Figure 3.4: Illustration of various instruments in the target and the toroid.

Figure 3.5: Figures 3.5a is the logic diagram for muon trigger. Figures 3.5b illustrates the corresponding event. Fig. 3.5b is a WSM.

Figure 3.6: Figures 3.6a is the logic diagram for penetration trigger. Figures 3.6b illustrates a penetration event.

Figure 3.7: Detector configuration during E701.

Figure 4.1a: Histogram of the χ^2 associated with the fitted tracks for WSM sample.

Figure 4.1b: Distubution of polar angles, θ, of WSM events. All the reconstructed events had θ less than 160 milliradians.

Figure 4.2: Distribution of the geometrical acceptance correction for WSM

events. The acceptance has been computed disregarding the production mechanism of such events. It just represents the inverse of the fractional acceptance obtained by integrating over the azimuthal angle and the logitudinal position for a given transverse vertex and a polar angle of a WSM event.

Figure 4.3: Missing energy distribution for CC events. The solid line represent the Monte Carlo, the dotted curve represents the data.

Figures 5.0: The Feynman diagrams for the four backgrounds to WSM. (a) WBB (5.0a), (b) OSDM with μ^- undetected (5.0b), (c) NC induced π^+/K^+ decays producing a μ^+ (5.0c) and (d) Electron neutrino form K_{e3} decay producing an opposite sign dilepton (5.0d).

Figure 5.1: A graph showing the independence of Wrong Sign Wide Band Background from the energy settings of the secondaries. A fixed number of protons were assumed to be delivered at the target for each setting.

Figure 5.2: A comparison of WBB-antineutrino fux at Lab-E from the two sources : target and the dump. The number of protons assumed to have impinged upon the target was 5.58×10^{18} which is the cumulative protons for both the experiments.

Figure 5.3: Acceptance of WBB-antineutrino induced CC interaction in Lab-

E without (5.3a) and with (5.3b) the Y > .5 cut.

Figure 5.4: Distribution of Evis from WBB and Dilepton events (5.4a). The histogram, 5.4b, has events with Y > .5 and Evis > 100 Gev.

Figure 5.5: Integral probability of shower penetration versus the depth of penetration for various shower energies. (See Table 5.7 and its caption).

Figure 5.6: A collation of energy distributions of the three dilepton backgrounds.

Figures 6.1: Evis histogram of the WSM sample is shown in Fig. 6.1a. Fig. 6.1b shows the Evis histogram for events with Evis > 100 GeV and Y > .5.

Figures 6.2: P_{μ}+ histogram of the WSM sample is shown in Fig. 6.2a. Fig. 6.2b shows the $\P_{\mu}$+ histogram for events with Evis > 100 GeV and Y > .5.

Figures 6.3: E_{had} histogram of the WSM sample is shown in Fig. 6.3a. Fig. 6.3b shows the E_{had} histogram for events with Evis > 100 GeV and Y > .5.

Figures 6.4: Missing energy histogram of the WSM sample is shown in Fig. 6.4a. Fig. 6.4b shows the missing energy histogram for events with Evis > 100 GeV and Y > .5.

Figures 6.5: X_{vis} histogram of the WSM sample is shown in Fig. 6.5a. Fig.

6.5b shows the X_{vis} histogram for events with Evis > 100 GeV and Y > .5.

Figures 6.6: Y histogram of the WSM sample is shown in Fig. 6.6a. Fig. 6.6b shows the Y histogram for events with Evis > 100 GeV and Y > .5.

Figures 6.7: Q^2 histogram of the WSM sample is shown in Fig. 6.7a. Fig. 6.7b shows the Q^2 histogram for events with Evis > 100 GeV and Y > .5.

Figure 6.8: A scatter plot of Evis vs Y.

Figure 6.9: The Feyman diagrams depicting a flavour changing NC and subsequent production of a WSM.

Figure 6.9b: The Feyman diagram showing the charm-content of the q-$\overline{q}$ sea of the nucleon and subsequent production of WSM.

Figure 6.10: The Feynman diagram of a flavour changing NC interaction involving the bottom meson. Such an interaction has been found to be less probable than .31%with 90%confidence level.

Figure 6.11: Production of heavy flavour in the nucleon sea. The figure suggests that the production of heavy flavours should scale with the inverse square of their masses.

Figure 7.1a: Histogram of the total visible energy distribution (solid line) of the trimuon events and the corresponding distribution for the backgrounds (dashed line) for these trimuons. The background has been normalized to the data sample.

Figure 7.1b: Evis distribution of the trimuon events. The simulation of trimuons via the production and decay of vector mesons (called Model 1) and the trident production (called Model 2) have also been shown. Unless otherwise mentioned the curves will have the following meaning, (a) the solid line denotes the data, (b) the dashed line represents the corresponding value predicted by Model 1, and (c) the dotted curve shows the distribution for the trident production mechanism. The predictions from the two models have been normalized to the total trimuon sample.

Figure 7.1: Hadron energy distribution.

Figure 7.2: Histograms of the three momenta, $P_{\mu 1}$, $P_{\mu 2}$ and $P_{\mu 3}$, are shown in Figs. 7.2a, 7.2b and 7.2c. The last histogram, 7.2d, shows the vector sum of the second and the third momentum.

Figure 7.3: The scatter plot (7.3a) shows the dependence of the momenta of the 2^{nd} non-leading muon upon the leading muon. Fig. 7.3b and 7.3c are the corresponding plots from the two simulations.

Figure 7.4: The scatter plot (7.4a) shows the dependence of the momenta of the 3^{rd} non-leading muon upon the leading muon. Fig. 7.4b and 7.4c are the corresponding plots from the two simulations.

Figure 7.5: Distribution of the momentum asymmetry, η, between the second and the third muon.

Figure 7.6: Q^2 distribution for the trimuon events.

Figure 7.7: Distribution of the scaling variable X_{vis} is shown in 7.7a. Fig. 7.7b presents the histogram of X (for definition see Chapter 7).

Figure 7.8: Distribution of the scaling variable Y_{vis} is shown in 7.8a. Fig. 7.Yb presents the histogram of Y (for definition see Chapter 7).

Figure 7.9: Histogram of the Feynman scaling variable, X_F, where,

$$X_F = \frac{P_{\mu 2} + P_{\mu 3}}{E_{had} + P_{\mu 2} + P_{\mu 3}}$$

Figure 7.10: The distribution of the invariant dimuon mass, M_{12}

Figure 7.11: The distribution of the invariant dimuon mass, M_{13}

Figure 7.12: The distribution of the invariant dimuon mass, M_{23} is shown in 7.12a. Fig. 7.12b shows the percentage change in the value of M_{23} after smearing.

Figure 7.13: The distribution of the invariant trimuon mass, M_{123}

Figures 7.14: 7.14a shows the dependence of the dimuon mass M_{12} on the trimuon mass M_{123}. Scatterplots 7.14b and 7.14c illustrate the simulation of this dependence for the hadronic and the trident production of trimuons.

Figures 7.15: 7.15a shows the dependence of the dimuon mass M_{13} on the trimuon mass M_{123}. Scatterplots 7.15b and 7.15c illustrate the simulation of this dependence for the hadronic and the trident production of trimuons.

Figures 7.16: 7.16a shows the dependence of the dimuon mass M_{23} on the trimuon mass M_{123}. Scatterplots 7.16b and 7.16c illustrate the simulation of this dependence for the hadronic and the trident production of trimuons.

Figures 7.17: Distribution of $P_{\mu 2}$ vs the azimuthal angle, ϕ_{12}.

Figures 7.18: Distribution of the azimuthal angle, ϕ_{12}, associated with the muons 1 and 2.

Figures 7.19: Distribution of the azimuthal angle, ϕ_{13}, associated with the muons 1 and 3.

Figures 7.20: Distribution of the azimuthal angle, ϕ_{123}, associated with the muons 1 and (2 + 3).

Figure 7.21: Scatter plots showing the correlation between the momenta of the non leading muons and the azimuthal angles ($P_{\mu 2}$ vs ϕ_{12}).

Figure 7.22: Scatter plots showing the correlation between the momenta of the non leading muons and the azimuthal angles ($P_{\mu 3}$ vs ϕ_{13}).

Figure 7.23: P_T distribution of the non-leading muon 2.

Figure 7.24: P_T distribution of the non-leading muon 3.

Figure 7.25: P_T distribution of the vector sum of the two non-leading muons 2 and 3.

Figure 7.26: Schematic of hadronic component of trimuon production.

Figure 7.27: The Feyman diagram showing the radiative component of trimuon production.

Figure 7.28: Heavy muon procution

Figure 7.29: The Feyman diagram showing a trimuon event via heavy quark cascade.

Figure C.1: Spin considerations for $\nu, \overline{\nu}$ scattering off $q, \overline{q}$.

Figure D.1: Momentum distribution of the secondary paricles (π^+, π^-, K^+, K^-) produced in P-BeO collision.

Figure G: Computer generated schematic of the 23 trimuon events.

Figure I.1: Set up for the E744/E652 Test Run

TABLE 2.1a

Characteristcs Parameters of NO Dichromatic Train

Incident energy of the primary proton beam	400 Gev
Intensity of the incident beam	.5 X 10^{13} to 2 X 10^{13}
Fractional momentum spread of the incident beam	$<$ .5%
Spot-size on the production target	.5mm X 2mm
Targetting angles : Horizontal	11.96 mrad
Vertical	1.125 mrad
Target : Berilium Oxide	304.8 mm
Solid Angle Acceptance	11.5 msr
Momentum selection byte	10%
Distance between target to exit	53 meters
Transmission efficiency	.1%
beam : Horizontal	.15 mrad
Vertical	.20 mrad
Momenta of the transmitted secondaries	50-350 Gev
Momentum spread of the secondary beam	10%
Size of the exiting secondary beam	13cmX4cm

TABLE 2.1b

Mean-Momenta and Divergences of Secondary Beam

Setting	<P>:Pi	<P> :K	RMS x	RMS y	/P
120	119.5	122.4	.16 mr	.23 mr	10.1%
140	139.2	142.2	.15 mr	.21 mr	9.9%
165	166.3	169.8	.13 mr	.20 mr	10.0%
200	197.0	200.6	.15 mr	.20 mr	9.6%
250	243.8	247.0	.16 mr	.20 mr	9.4%

TABLE 3.1

The Lab-E Neutrino Detector specifications

Attributes	Estimates
Total tonnage of the detector	~ 1020 Tons
Target tonnage	~ 640 "
Toroid tonnage	~ 380 "
Fiducial tonnage : E616	~ 432 "
E701	~ 288 "
Trnasverse cross-section	~ 120" X 120"
Fiducial Transverse size	108" X 108"
Scintillator : spacing in target	per 11 cm of Fe
" " toroid	per 22 cm of Fe
Spark Chamber : spacing in target	per 23 cm of Fe
" " toroid	per 80 cm of Fe
Pperp kick delivered by the magnet	2.45 Gev/c total
" " " " each toroid	.8 Gev/c

TABLE 3.2

Apparatus Resolution

Quantities	Resolution
Position resolution of spark-chambers	.5 mm
Momentum resolution	11%
Hadron energy resolution	$.89/\sqrt{E}$

TABLE 3.3

E616 versus E701

E616	E701
6 target carts were used	4 target carts were used equivalently the tonnage was 2/3 of E616.
There were spark chambers in the half-toroid gaps, in addition to the chambers in the toroid gaps.	There were no chambers in the half gap. However each toroid gap contained each toroid gap contained five chambers.

TABLE 4.1a

Reduction of Initial Data

Beam Setting : 250 Gev

E616		Cuts	E701	
85,500			60,917	
		Trigger1 or Trigger3		
64,800			32,684	
		Place cut		
48,000			24,246	
		Number of Tracks > 0		
46,000			23,250	
		Vertex Cut		
43,500			21,704	
		Hole Cut		
42,300			21,027	
		ZT2 Cut		
30,850			17,500	
		Rtore Cut		
30,078			16,751	
MU+	MU-		MU+	MU-
328	29,750		261	16,490

TABLE 4.1b

Reduction of Initial Data

Beam Setting : 200 Gev

E616		Cuts	E701	
73,527			40,000	
		Trigger1 or Trigger3		
57,225			29,800	
		Place cut		
41,650			23,368	
		Number of Tracks > 0		
40,000			22,606	
		Vertex Cut		
37,074			20,406	
		Hole Cut		
36,135			19,800	
		ZT2 Cut		
25,561			15,340	
		Rtore Cut		
26,602			15,730	
MU+	MU-		MU+	MU-
178	25,383		245	15,485

TABLE 4.1c

Reduction of Initial Data

Beam Setting : 165 Gev

E616		Cuts	E701	
54,661			33,291	
		Trigger1 or Trigger3		
43,490			23,900	
		Place cut		
33,236			17,620	
		Number of Tracks > 0		
31,923			17,314	
		Vertex Cut		
30,623			16,256	
		Hole Cut		
30,002			15,808	
		ZT2 Cut		
20,857			12,172	
		Rtore Cut		
20,515			12,112	
MU+	MU-		MU+	MU-
136	20,379		121	11,996

TABLE 4.1d

Reduction of Initial Data

Beam Setting : 140 Gev

E616		Cuts	E701	
34,450			45,342	
		Trigger1 or Trigger3		
27,533			33,402	
		Place cut		
21,206			25,332	
		Number of Tracks > 0		
20,482			17,324	
		Vertex Cut		
19,613			23,031	
		Hole Cut		
19,290			22,500	
		ZT2 Cut		
12,577			16,812	
		Rtore Cut		
12,616			16,597	
MU+	MU-		MU+	MU-
60	12,556		153	16,444

TABLE 4.1e

Reduction of Initial Data

Beam Setting : 120 Gev for e616 and 100 Gev for E701

E616		Cuts	E701	
24,058			28,163	
		Trigger1 or Trigger3		
19,363			21,461	
		Place cut		
14,706			16,375	
		Number of Tracks > 0		
14,189			15,955	
		Vertex Cut		
13,646			14,762	
		Hole Cut		
13,348			14,443	
		ZT2 Cut		
8,595			10,111	
		Rtore Cut		
8,674			9,874	
MU+	MU-		MU+	MU-
51	8,623		63	9,801

TABLE 4.2a

Ambiguous events

Events from E616

Run	Event	P	Rtore
1371	6064	default	68.6 inches
1793	5814	default	68.0 "
1615	2243	default	65.3 "
1765	2594	default	65.9 "
1451	4623	default	68.4 "
1729	4238	default	66.6 "
1451	4623	default	68.4 "
1426	6573	-493 ± 49	68.1 "
1623	5954	-369 ± 297	68.2 "
1861	2439	-111 ± 73	67.1 "
1471	2986	-300 ± 253	67.5 "

TABLE 4.2b

Ambiguous events

Events from E701

Run	Event	P	Rtore
366	1381	default	66.6 "
381	2313	default	68.8 "
395	2468	default	67.7 "
453	6126	default	66.7 "
549	2118	default	68.7 "
552	230	default	68.7 "
685	598	default	65.9 "
701	934	default	68.0 "
720	793	default	68.4 "
704	90	default	68.7 "
756	4686	default	66.4 "
767	1367	default	67.0 "
802	2710	default	67.8 "
767	1376	-212 ± 616	67.7 "
586	5194	-109 ± 40	68.7 "

TABLE 5.1a

Flux and Live-Time for Close Slit Data

For E616 :

Setting	No. of Incident Protons		Live-Time	
	Fast Spill	Slow Spill	Fast Spill	Slow Spill
250 Gev	$.57 \times 10^{17}$	$.42 \times 10^{17}$	11547	64427
200 Gev	$.48 \times 10^{17}$	$.50 \times 10^{17}$	6516	66557
165 Gev	$.15 \times 10^{17}$	$.15 \times 10^{17}$	2505	24729
140 Gev	$.12 \times 10^{17}$	$.13 \times 10^{17}$	1710	20590
120 Gev	$.17 \times 10^{17}$	$.17 \times 10^{17}$	3548	20917

TABLE 5.1b

Flux and Live-Time for Close Slit Data

For E701 :

Setting	No. of Incident Protons		Live-Time	
	Fast Spill	Ping	Fast Spill	Ping
250 Gev	$.50 \times 10^{17}$	0	4345	0
200 Gev	$.20 \times 10^{17}$	0	2857	0
165 Gev	$.26 \times 10^{17}$	0	2366	0
140 Gev	$.22 \times 10^{17}$	0	2446	0
100 Gev	$.14 \times 10^{17}$	0	1272	0

TABLE 5.1c

Cosmic Ray Live-Time for Close-Slit Data

Setting	Live-Time : E616		Live-Time : E701	
	Fast Spill	Slow Spill	Fast spill	Ping
250 Gev	70606	17723	66505	0
200 Gev	71253	17963	38360	0
165 Gev	25685	6433	17548	0
140 Gev	22648	5709	30117	0
120 Gev	22143	5602	0	0
100 Gev	0	0	17963	0

TABLE 5.2a

Close-Slit WSM Events

Events from E616

Setting	Run	Event	Evis	Y
250 Gev	1363	76	49.6 Gev	.455
250 "	1833	2099	22.3 "	.102
250 "	2010	27	89.9 "	.192
250 "	2010	1724	24.7 "	.246
250 "	2011	548	82.2 "	.418
250 "	2011	1492	38.9 "	.261
200 "	1784	6530	82.5 "	.080
200 "	2059	813	25.4 "	.226
200 "	2060	3245	48.0 "	.449
200 "	2126	2278	24.5 "	.086
200 "	2126	2893	19.1 "	.235
165 "	1730	871	24.6 "	.261
140 "	<---------- No WSM Event ---------->			
120 "	2021	3046	46.1 "	.270
120 "	2022	1550	34.6 "	.304

TABLE 5.2b

Close-Slit Data with WSM

Events from E701

Setting	Run	Event	Evis	Y
250 "	824	2038	23.3 "	.084
250 "	824	2540	55.2 "	.575
250 "	825	2686	27.8 "	.186
200 "	819	432	33.0 "	.167
165 "	<---------- No WSM Event ---------->			
140 "	821	1429	41.6 "	.078
100 "	<---------- No WSM Event ---------->			

TABLE 5.3a

Flux and Live-Time of the Primary Beam

For E616 :

Setting	No. of Incident Protons		Live-Time	
	Fast Spill	Slow spill	Fast spill	Slow spill
250 Gev	5.63×10^{17}	5.43×10^{17}	72107	858126
200 Gev	3.01×10^{17}	3.53×10^{17}	42833	598446
165 Gev	2.07×10^{17}	2.95×10^{17}	29449	426267
140 Gev	1.38×10^{17}	1.87×10^{17}	19149	283132
120 Gev	1.10×10^{17}	1.51×10^{17}	14741	205078

TABLE 5.3b

Flux and Live-Time of the Primary Beam

For E701:

Setting	No. of Incident Protons		Live-Time	
	Fast Spill	Ping	Fast spill	Ping
250 Gev	6.38×10^{17}	3.36×10^{17}	70452	118836
200 Gev	3.36×10^{17}	1.65×10^{17}	40673	274293
165 Gev	3.77×10^{17}	0	28982	0
140 Gev	2.05×10^{17}	2.84×10^{17}	41497	305394
100 Gev	1.75×10^{17}	1.84×10^{17}	28470	126421

TABLE 5.4a

Secondary Flux and Cosmic Ray Live-Time

For E616:

Setting	No. of Secondaries		CR Live-Time	
	Fast Spill	Slow Spill	Fast spill	Slow Spill
250 Gev	5.32×10^{15}	4.90×10^{15}	1095023	26695
200 Gev	2.07×10^{15}	2.44×10^{15}	698495	176049
165 Gev	1.12×10^{15}	1.64×10^{15}	489472	338332
140 Gev	0.67×10^{15}	0.84×10^{15}	338322	85083
120 Gev	0.48×10^{15}	0.64×10^{15}	254569	85083

TABLE 5.4b

Secondary Flux and Cosmic Ray Live-Time

For E701:

Setting	No. of Secondaries		CR Live-Time	
	Fast Spill	Ping	Fast spill	Ping
250 Gev	5.24×10^{15}	$.22 \times 10^{15}$	1047627	0
200 Gev	2.40×10^{15}	1.14×10^{15}	1185681	0
165 Gev	1.62×10^{15}	0	484979	0
140 Gev	1.20×10^{15}	0.83×10^{15}	1121702	0
100 Gev	0.71×10^{15}	0.29×10^{15}	610377	0

TABLE 5.4c

Particle Fractions in the Secondary Beam

For E616:

Setting	Pions	Kaons	Protons
250 Gev	.0775	.0127	.910
200 Gev	.192	.0271	.779
165 Gev	.311	.0399	.645
140 Gev	.420	.0450	.522
120 Gev	.518	.0559	.411

TABLE 5.5

Number of Surviving Secondaries vs Distance from the target

Number of protons delivered on the target : 10

Distance travelled by the secondary pions and kaons	No. of surviving secondaries
3.0 Feet	131,856
5.0 "	44,437
7.0 "	1,027
8.0 "	8

TABLE 5.6

Primary-Dump Positions For various Settings

Setting	x	y	X	Y	Z (m)
250 Gev	4.8 mr	-2.2 mr	.3413	.0582	13.8
200 "	6.3 mr	-1.8 mr	.3525	.0615	13.8
165 "	8.8 mr	-0.1 mr	.3182	.0709	8.2

Table 5.7

Integral Probability Distribution,
Hadron shower penetration for 15, 25, and 50 GeV/c
('2 Cart' Configuration)

Counter	15 GeV/c (%)	25 GeV/c (%)	50 GeV/c (%)
1	100.0	100.0	100.0
2	100.0	100.0	100.0
3	100.0	100.0	100.0
4	100.0	100.0	100.0
5	94.9	98.6	99.9
6	79.4	91.3	98.1
7	64.7	80.0	94.7
8	49.1	67.3	87.9
9	35.1	52.1	76.7
10	23.0	37.9	62.5
11	14.3	26.9	49.6
12	8.8	17.7	38.0
13	5.4	11.7	28.3
14	3.6	8.4	19.9
15	2.5	6.0	14.6
16	1.3	3.6	9.7
17	.7	2.2	6.6
18	.5	1.3	4.2
19	.3	.7	2.8
20	.2	.5	2.0
21	.1	.3	1.2
22	.04	.2	1.0
23	.04	.2	.8
24	.04	.2	.6
25	.0	.1	.5
26	.0	.05	.3
27	.0	.0	.3
28	.0	.0	.3

Table 5.7...cont.

Integral Probability Distribution,
Hadron shower penetration for 100, 200, and 300 GeV/c

Counter	100 GeV (%)		200 GeV (%)		300 GeV (%)
	2 cart	3 cart	2 cart	3 cart	3 cart
1	100.0	100.0	100.0	100.0	100.0
2	100.0	100.0	100.0	100.0	100.0
3	100.0	100.0	100.0	100.0	100.0
4	100.0	100.0	100.0	100.0	100.0
5	100.0	100.0	100.0	100.0	100.0
6	99.5	99.6	99.9	99.9	100.0
7	98.9	98.8	99.7	99.6	99.9
8	96.7	96.4	99.2	99.2	99.8
9	92.8	91.4	98.1	98.4	99.4
10	85.7	82.1	96.0	95.0	98.4
11	75.9	70.9	92.3	90.8	96.4
12	63.9	58.2	85.9	81.7	92.1
13	48.5	46.6	75.5	72.1	85.2
14	38.5	35.8	63.9	61.6	75.7
15	30.2	27.5	53.6	48.9	65.2
16	21.6	19.9	41.7	37.5	52.1
17	14.7	14.3	32.0	28.4	39.7
18	10.1	10.5	24.4	21.2	32.1
19	7.1	6.9	18.3	15.2	23.8
20	4.5	5.0	13.9	10.4	17.7
21	3.0	3.5	9.4	8.0	13.2
22	2.1	2.6	7.1	6.1	10.2
23	1.5	1.8	5.0	4.7	7.9
24	1.1	1.3	3.6	3.5	6.1
25	.7	1.0	2.9	2.4	4.7
26	.5	.7	2.3	2.0	3.6
27	.4	.6	2.1	1.8	3.0
28	.2	.5	1.7	1.6	2.5
29	-	.4	-	1.0	2.1
30	-	.4	-	1.0	1.9
31	-	.4	-	.8	1.8
32	-	.3	-	.8	1.5
33	-	.3	-	.7	1.3
34	-	.3	-	.5	1.2
35	-	.3	-	.5	1.2
36	-	.2	-	.5	1.1
37	-	.2	-	.4	1.0
38	-	.2	-	.4	.9
39	-	.2	-	.4	.8
40	-	.1	-	.4	.8
41	-	.1	-	.4	.8
42	-	.1	-	.4	.6

TABLE 6.1a

Data and Backgrounds for Wrong Sign Muons

CUTS : Y > 0

Type of interaction	Evis < 100	s Evis > 100
Data		
Charge Current Events	102,353	61,636
Wrong Sign Muons	400 ± 20	43 ± 6.6
Closed Slit Data	375 ± 85.9	0 ± 19.7
Monte Carlo Simulation of Backgrounds		
Wide Band Background		
WBB originating from PI-/K- decays in the dichro train	312.9	12.42
WBB originating from Pi-/K- decays in the primary dump	75.9	1.53
TOTAL WBB (TRAIN + DUMP)	388.8	13.95
Dilepton Backgrounds		
Missing MU- in OSDM	3.40	3.41
NC induced Pi-/K- decays	3.50	3.22
KE3 induced dilepton prodn.	1.50	1.81
TOTAL DILEPTON BACKGROUND	8.40	8.48
Total background for WSM		
	397.2	22.4

TABLE 6.1b

Data and Backgrounds for Wrong Sign Muons

CUTS : Y > .5

Type of interaction	Evis < 100	s Evis > 100
Data		
Charge Current Events	22,159	24,624
Wrong Sign Muons	58 ± 7.6	24 ± 4.9
Closed Slit Data	19.7±19.7	0 ± 19.7
Monte Carlo Simulation of Backgrounds		
Wide Band Background		
WBB originating from PI-/K- decays in the dichro train	33.39	2.63
WBB originating from Pi-/K- decays in the primary dump	6.79	.34
TOTAL WBB (TRAIN + DUMP)	40.18	2.97
Dilepton Backgrounds		
Missing MU- in OSDM	2.95	3.17
NC induced Pi-/K- decays	3.08	3.22
KE3 induced dilepton prodn.	1.5	1.81
TOTAL DILEPTON BACKGROUND	7.53	8.20
Total background for WSM		
	47.7	11.2

TABLE 6.2a

Characteristcs of WSM and Backgrounds

CUTS : Y > 0. and Evis > 0 Gev

Kinematical Quantities	Data	Backgrounds		
		WBB	Dilepton	Total
<n> with Evis<100 Gev	400±20	388.8	8.3	397
<n> with Evis>100 Gev	43±6.6	22.4	8.4	14.0
<Evis>	53.3±1.7	39.4	104.3	42.0
<P,>	35.7±1.2	25.5	19.9	25.2
<Ehad>	17.6±1.3	14.8	76.0	17.7
<Emis>	2.0±1.40	7.3	19.9	7.8
<X>	.233±.01	.24	.108	.235
<Y>	.270±.01	.353	.664	.368
<Q'>	4.0±.30	5.2	6.9	5.10

TABLE 6.2b

Characteristcs of WSM and Backgrounds

CUTS : Y > .5 and Evis > 0 Gev

Kinematical Quantities	Data	Backgrounds		
		WBB	Dilepton	Total
<n> with Evis<100 Gev	58±7.6	40.2	7.53	47.7
<n> with Evis>100 Gev	24±4.9	3.0	8.20	11.2
<Evis>	80.8±5.2	52.0	106.7	66.4
<P,>	22.3±1.6	15.2	19.2	15.8
<Ehad>	58.5±4.3	36.5	85.1	49.9
<Emis>	5.8±3.8	2.9	22.0	7.6
<X>	.087±.01	.152	.105	.140
<Y>	.688±.014	.708	.785	.737
<Q'>	7.8±1.3	10.6	4.8	8.9

TABLE 6.2c

Characteristcs of WSM and Backgrounds

CUTS : Y > 0. and Evis > 100 Gev

Kinematical Quantities	Data	Backgrounds		
		WBB	Dilepton	Total
<n> with Evis<100 Gev	0	0	0	0
<n> with Evis>100 Gev	43±6.6	14.0	8.40	22.4
<Evis>	140.±4.8	125.0	145.3	132.7
<P,>	70.4±7.6	80.3	23.2	54.8
<Ehad>	70.0±7.5	45.2	98.6	68.9
<Emis>	16.6±6.1	17.0	20.6	18.6
<X>	.174±.03	0.205	0.091	0.162
<Y>	.499±.05	0.356	0.632	0.479
<Q'>	10.5±2.0	14.6	9.3	11.8

TABLE 6.2d

Characteristcs of WSM and Backgrounds

CUTS : Y > .5 and Evis > 100 Gev

Kinematical Quantities	Data	Backgrounds		
		WBB	Dilepton	Total
<n> with Evis<100 Gev	0	0	0	0
<n> with Evis>100 Gev	24±4.9	3.0	8.2	11.2
<Evis>	143.2±6.8	125.4	145.4	140.1
<P,>	32.8±4.4	35.5	23.7	26.9
<Ehad>	110.4±5.4	90.0	119.0	111.4
<Emis>	23.9±8.	15.6	24.4	22.2
<X>	.063±.016	0.144	0.091	0.105
<Y>	.777±.025	0.717	0.827	0.798
<Q'>	12.5±3.4	23.6	5.90	10.2

TABLE 6.3

Characteristcs of CC Events

CUTS : Identical to the cuts applied to WSM
(no Y or Evis cut)

Kinematical Quantities	CC Events
<n> with Evis<100 Gev	102,353
<n> with Evis>100 Gev	61,636
<Evis>	120.5
<P,>	67.0
<Ehad>	53.0
<Emis>	00.0
<X>	0.208
<Y>	0.440
<Q'>	19.10

TABLE 6.4

Acceptance-Corrected CC and WSM Events

CUTS ON WSM EVENTS : Evis > 100 Gev

	No Y Cut	Y > .5
CC events :"Raw"	163,989	46,783
CC events : "Weighted"	218,290	76,688
Number of excess WSM : "Raw"	20.7 ± 7.9	12.8 ± 5.4
Models	Accetance-corrected WSM	
	No Y Cut	Y > .5
WBB	21.27	53.7
OSDM with MU- mis	33.10	19.74
NC induced Pi-/K-	106.0	73.15
Ke3 induced	124.9	69.12
ALL Dileptons	61.9	37.13
WBB and Dilepton	41.88	40.11

TABLE 6.5

Acceptance-Corrected Rates of WSM Events

CUTS ON WSM EVENTS : Evis > 100 Gev

Models	Accetance-corrected rates of WSM	
	No Y Cut	Y > .5
WBB	$.97 \times 10^{-4}$	2.5×10^{-4}
OSDM with MU-missing	1.5×10^{-4}	$.9 \times 10^{-4}$
NC induced Pi-/K-decays	4.9×10^{-4}	3.4×10^{-4}
Ke3 induced	5.7×10^{-4}	3.2×10^{-4}
ALL Dileptons	2.8×10^{-4}	1.7×10^{-4}
WBB and Dilepton	1.9×10^{-4}	1.8×10^{-4}

TABLE 6.6

Limits on the Rates of WSM

CUTS ON WSM EVENTS : Evis > 100 Gev

Rates	No Y Cut		Y > .5	
	Raw	Weighted	Raw	Weighted
Rate < 99.7 % Confidence	$2.1X10^{-4}$	$3.1X10^{-4}$	$1.3X10^{-4}$	$3.1X10^{-4}$

TABLE 6.7

Differences in LSDM and WSM Cuts

Cuts	WSM	LSDM
(1) Cut on Hadron energy : Eh	Eh > 0 Gev	Eh > 2 Gev
(2) Cut on Muon momentum : P	P > 7 Gev	P > 9 Gev
(3) Vertex Cut	+ 54" square	+ 50" square
(4) Radius at the front face of toroid	< 65"	< 64"
(5) Hole Cut	< .2	< .3
(6) Angle Cut	< 200 mrad	< 350 mrad
(7) Place Cut for E616 only	Place > 20	Place > 17

TABLE 6.8a

Characteristcs of WSM with LSDM Cuts

CUTS : Y > 0. and Evis > 0 Gev

Kinematical Quantities	Data	Backgrounds		
		WBB	Dilepton	Total
<n> with Evis<100 Gev	272±17	234.9	6.8	241.7
<n> with Evis>100 Gev	33±5.7	10.3	7.5	17.8
<Evis>	59.0±2.0	42.9	106.7	46.4
<P,>	37.5±1.4	26.2	21.5	25.9
<Ehad>	21.6±1.6	17.0	76.7	20.8
<Emis>	0.0±1.60	6.5	23.3	7.5
<X>	.199±.01	.217	.118	.210
<Y>	.316±.02	.404	.653	.420
<Q'>	4.9±.40	5.8	7.0	5.90

TABLE 6.8b

Characteristcs of WSM with LSDM Cuts

CUTS : Y > 0. and Evis > 100 Gev

Kinematical Quantities	Data	Backgrounds		
		WBB	Dilepton	Total
<n> with Evis<100 Gev	0	0	0	0
<n> with Evis>100 Gev	33±5.7	10.3	7.5	17.8
<Evis>	145.2±5.7	125.2	145.7	133.9
<P,>	68.7±8.5	77.9	24.7	51.8
<Ehad>	76.5±8.8	46.8	98.3	71.9
<Emis>	13.6±7.4	18.5	22.0	20.2
<X>	.163±.034	.197	.093	.153
<Y>	.523±.06	.375	.628	.499
<Q'>	11.9±2.5	14.6	9.3	12.00

TABLE 6.8c

Characteristcs of WSM with LSDM Cuts

CUTS : Y > .5 and Evis > 100 Gev

Kinematical Quantities	Data	Backgrounds		
		WBB	Dilepton	Total
<n> with Evis<100 Gev	0	0	0	0
<n> with Evis>100 Gev	20±4.5	00.47	7.3	7.74
<Evis>	148.8±7.5	127.0	145.8	144.6
<P,>	35.3±4.9	35.2	24.9	25.5
<Ehad>	113.5±6.2	91.9	118.0	116.4
<Emis>	20.1±9.5	16.8	25.9	25.3
<X>	.064±.019	.140	.094	.096
<Y>	.767±.028	.724	.817	.812
<Q'>	13.2±4.1	23.5	5.7	6.74

TABLE 6.9

"Neutral Current Analog" of OSDM and WSM

Kinematical Quantities	OSDM data	"NC analog" of OSDM data Y>.5,Evis>100	WSM data Y>.5,Evis>100
<n> with Evis<100 Gev	40 ± 6.3	0.0	0.0
<n> with Evis>100 Gev	163 ± 12.8	67 ± 8.2	20 ± 4.5
<Data-Back>	152 ± 12.9	56 ± 8.3	12 ± 4.7
<Evis>	150.7±3.7	136.0±3.2	148.8±7.5
<P,> :			
Lead Mu-	61.9±2.8	--	35.3+4.9
Non Lead Mu+	23.8±1.1	25.8±1.7	--
<Ehad>	64.6±2.7	109.2±3.5	113.5±6.2
<Emis>	8.8±1.9	23.5±3.1	20.1±9.5
<X>	.195±.012	---	---
<Y>	.422±.013	.802±.012	.767±.028
<Q'>	20.9±1.4	---	---

TABLE 6.10

"Neutral Current Analog" of LSDM and WSM

Kinematical Quantities	LSDM data	"NC analog" of LSDM data Y>.5,Evis>100	WSM data Y>.5,Evis>100
<n> with Evis<100 Gev	2 ± 1.4	0	0
<n> with Evis>100 Gev	15 ± 3.9	6 ± 2.5	20 ± 4.5
<Data-Back>			12.3+4.70
<Evis>	151.3±10.1	137.3±10.8	148.8±7.50
<P,> :			
Lead MU-	58.2±8.7	--	35.3±4.9
Non Lead MU+	17.2±1.3	18.2±1.7	--
<Ehad>	76.1±9.2	118.7±10.7	113.5±6.2
<Emis>	12.5±4.1	26.5±7.7	20.1±9.5
<X>	.270±.039	---	---
<Y>	.498±.045	.858±.018	.767±.028
<Q'>	30.9±7.6	---	---

TABLE 7.1

Dependence of Angle Resolution upon P_μ and Ehad

Hadron Energy in Gev	$\delta\theta$ mrad
Ehad < 10	.16 + 84.4/P
10 < Ehad < 25	.28 + 79.2/P
25 < Ehad < 50	.16 + 105.5/P
50 < Ehad < 100	.15 + 107.7/P
100 < Ehad < 200	.10 + 129.7/P
Ehad > 200	.00 + 154.8/P

TABLE 7.2

Characteristics of Trimuon Events

Kinematical Quantities	Data P,,>2.0	Data P,,>4.5	Hadronic Prodn P,,>4.5	Radiative Prodn P,,>4.5
<n>	23 ± 4.8	11 ± 3.3		
<n-backgrnd>	19.2±4.9	9.7 ± 3.4	4.0 ± .8	1.7±.85
<Evis>	135±10.4	149.+17.0	160.7	139.5
<Ehad>	65.8±11.1	58.6+16.3	70.4	46.8
<Q'>	13.1±2.7	13.2+4.3	27.5	13.5
<PMU1>	52.1±9.1	69.3+13.7	61.4	58.2
<PMU2>	9.7±2.5	10.5+2.5	13.7	16.1
<PMU3>	8.0±1.2	10.2+1.7	13.6	16.1
<PMU2+PMU3>	17.6±2.8	20.7+3.4	26.8	28.6
<,,>	.022±.079	-.015+.100	00.0	00.0
<Pt2>	.75±.152	.54+.078	.69	.60
<Pt3>	.47±.07	.45+.05	.68	.60
<Pt2+Pt3>	1.07±.157	.80+.058	1.14	1.03
<Xvis>	.116±.030	.163+.059	.247	.182
<X>	.115±.035	.175+.071	.175	.108
<Yvis>	.461±.060	.375+.049	.436	.325
<Y>	.611±.058	.530+.079	.619	.581
<XF>	.325±.062	.365+.053	.305	.423
<M12>	1.55±.27	1.72+.34	2.68	1.19
<M13>	1.79±.35	1.91+.38	2.66	1.18
<M23>	.817±.119	.747+.184	.792	.228
<M123>	2.70±.40	2.78+48	3.96	1.63
<,,12>	85.3±12.1	102.7+18.2	127.6	66.1
<,,13>	91.7±11.3	99.9+17.2	127.2	65.7
<,,123>	87.4±12.4	106.1+18.1	140.2	64.5

TABLE 7.3

Parametrization of Inclusive μ-Pair Production Cross Section

SOURCE	A (nb)	b (Gev/c $)^{-1}$	c
ρ	(4.28±.85)X10^{4}	3.79 ± .09	4.32 ± .13
ω	(7.60±1.5)X10^{4}	3.79 ± .09	4.32 ± .13
ϕ	(2.20±0.4)X10^{4}	3.93 ± .27	5.57 ± .38
J	140 ± 42	2.08 ± .26	3.76 ± .48
	CONTINUUM MASS RANGE		
0.00-0.45	(4.28±.85)X10	3.79 ± .09	4.32 ± .13
0.45-0.65	(7.60±1.5)X10	3.79 ± .09	4.32 ± .13
0.65-0.93	(2.20±0.4)X10	3.93 ± .27	5.57 ± .38
0.93-1.13	140 ± 42	2.08 ± .26	3.76 ± .48
1.13-2.00	140 ± 42	2.08 ± .26	3.76 ± .48

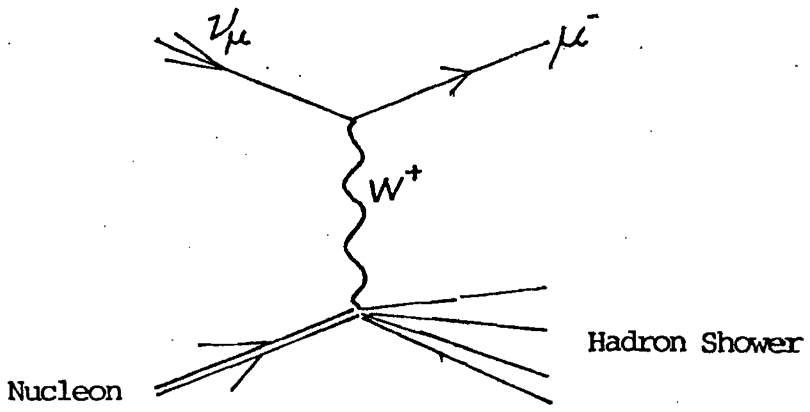

Fig. 1.1a : Neutrino Charge Current (CC) Event

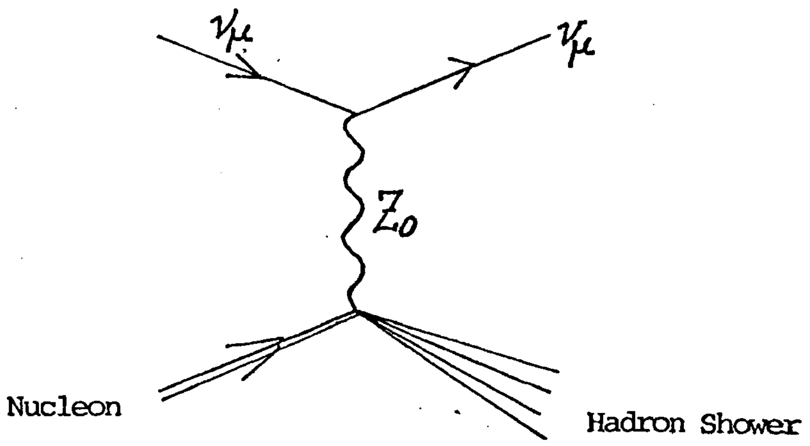

Fig. 1.1b : Neutrino Neutral Current (NC) Event

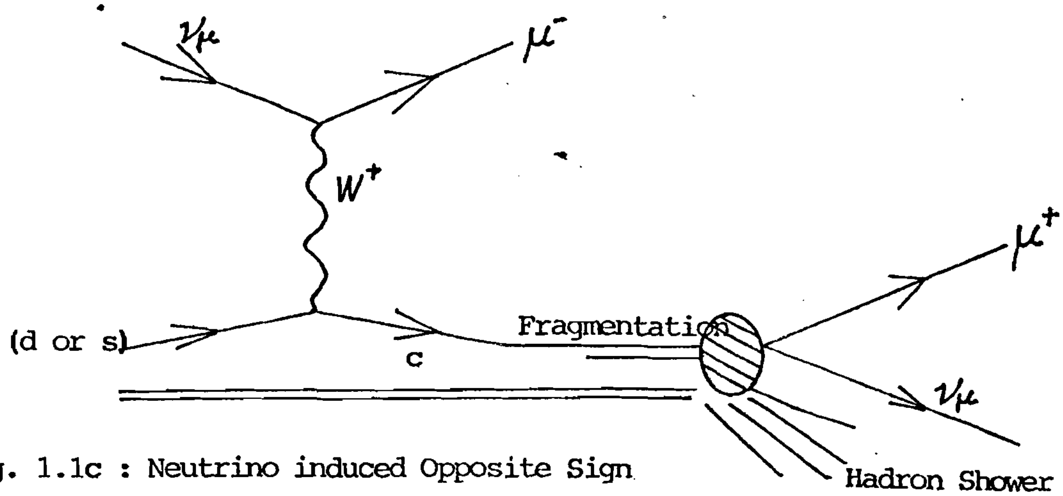

Fig. 1.1c : Neutrino induced Opposite Sign Dimuon (OSDM) Event

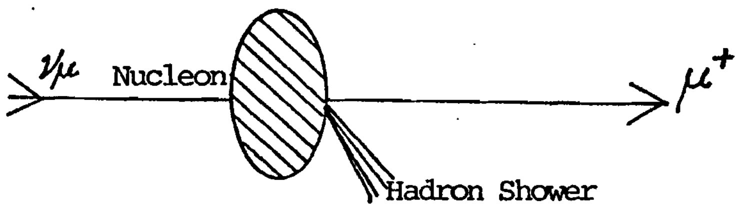

Fig. 1.1d : Schematic of Neutrino induced
Wrong Sign Muon (WSM)

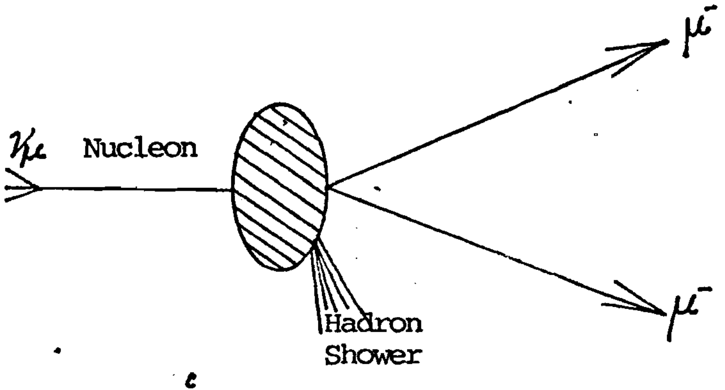

Fig. 1.1e : Schematic of Neutrino induced
Like Sign Dimuon (LSDM)

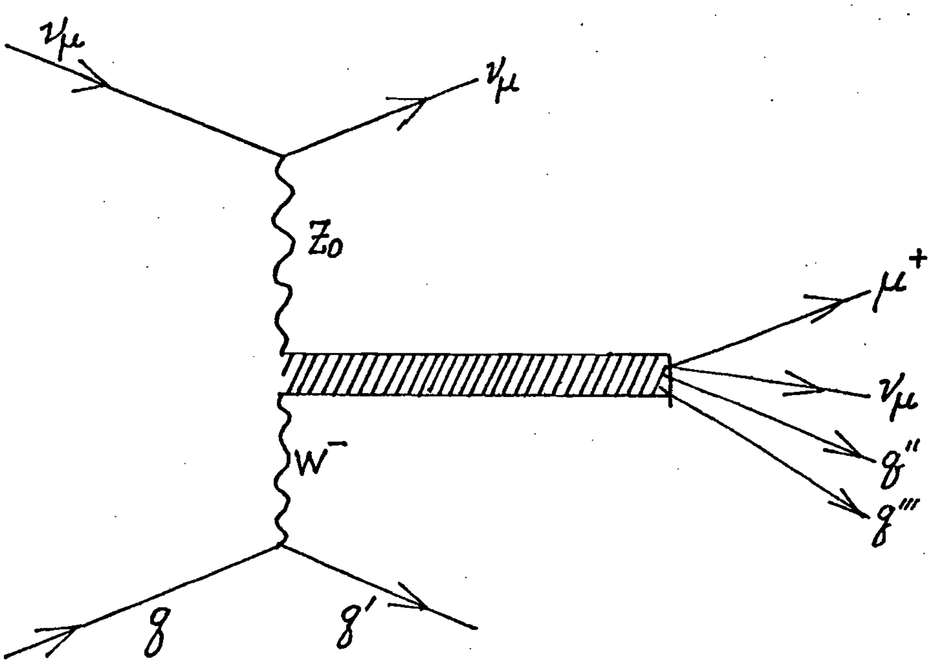

Fig. 1.2a : A WSM signature via production of a bound state of $Z_0 - W^-$

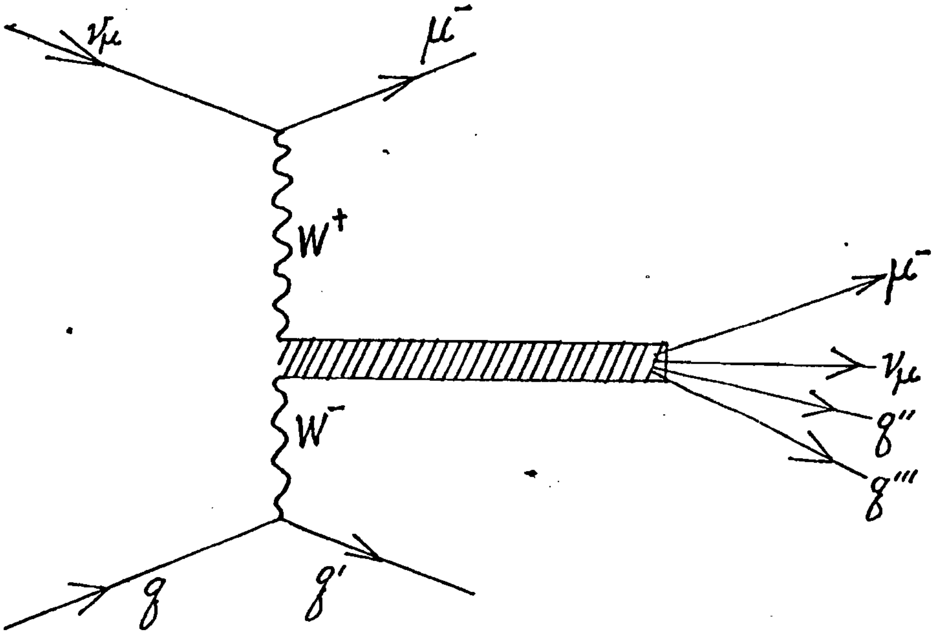

Fig. 1.2b : A LSDM signature via production of a bound state of $W^+ - W^-$.

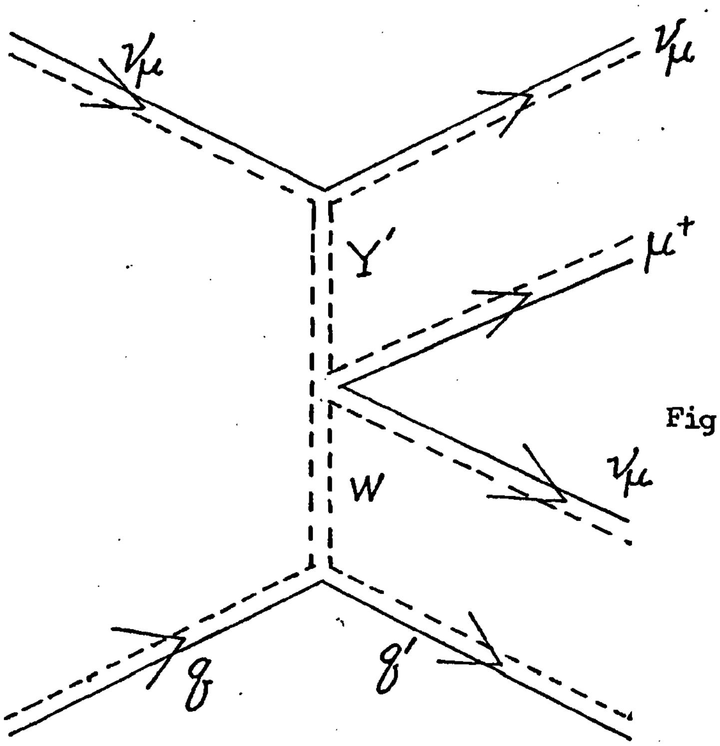

Fig. 1.3a : A Composite-model explanation of WSM. Y' & W' are excited states of bosons mediating weak interaction.

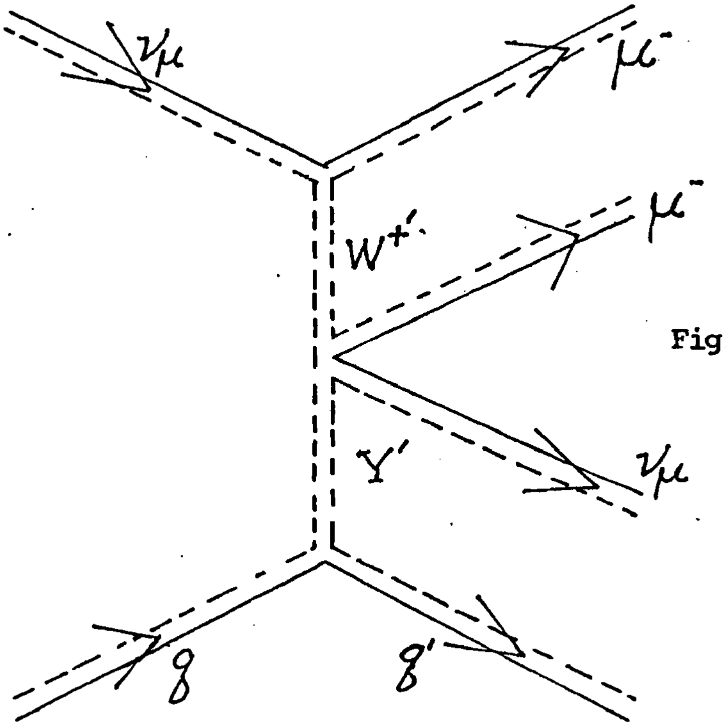

Fig. 1.3b : A Composite-model explanation of LSDM.

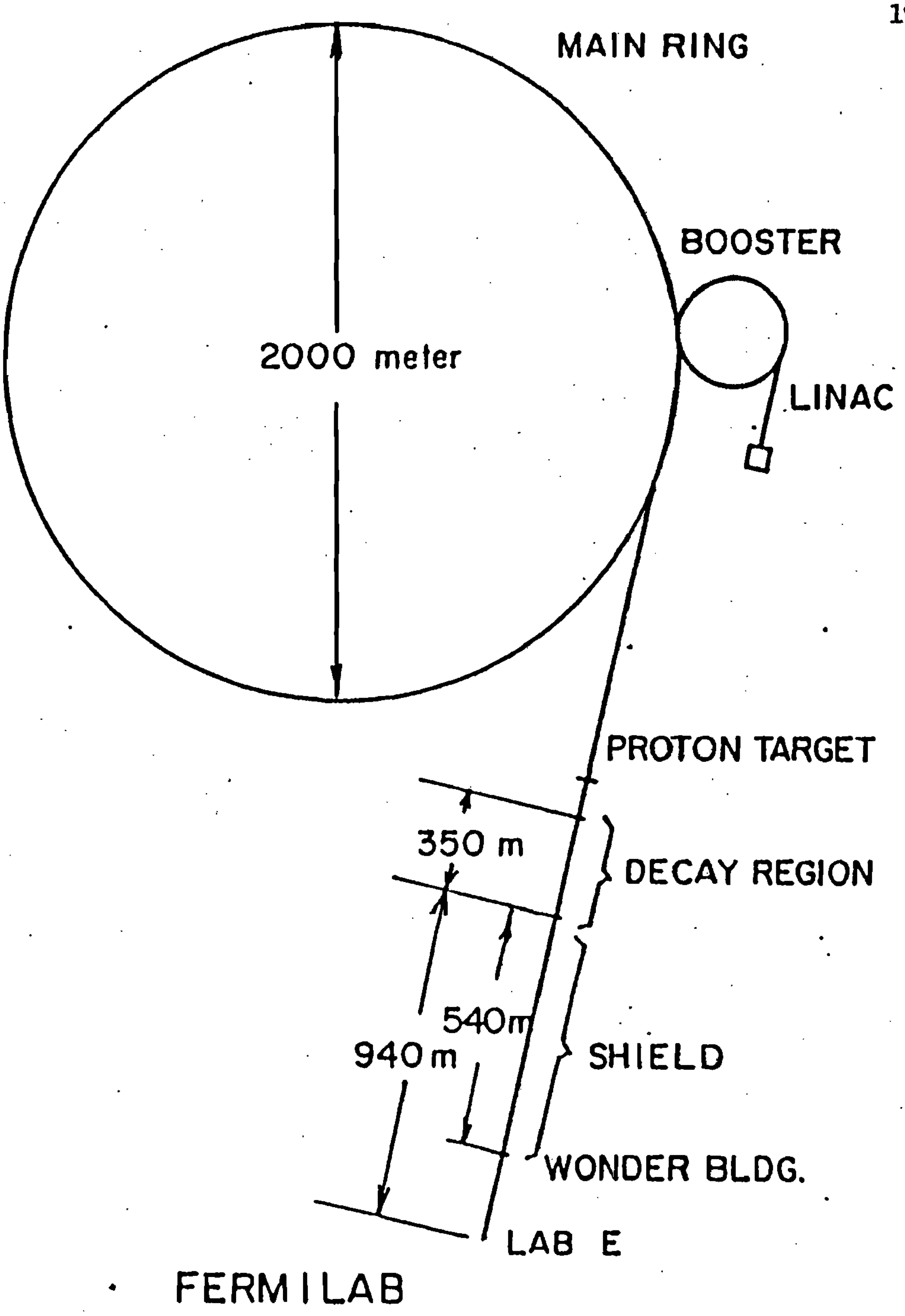
MAIN RING
2000 meter
BOOSTER
LINAC
PROTON TARGET
350 m
DECAY REGION
540m
940 m
SHIELD
WONDER BLDG.
LAB E
FERMILAB

Fig. 2.1

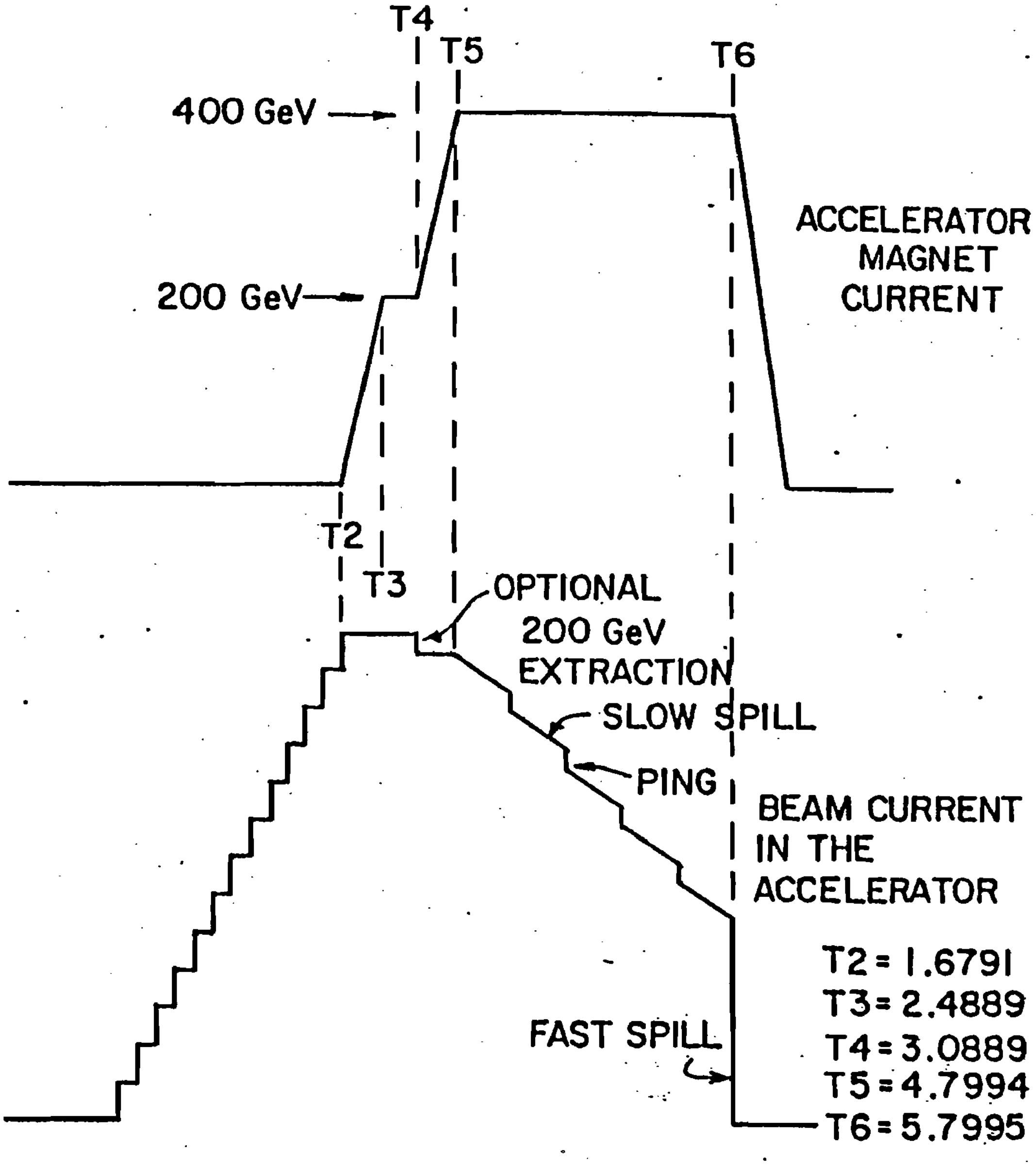
T4
T5
T6
400 GeV
200 GeV
ACCELERATOR MAGNET CURRENT
T2
T3
OPTIONAL 200 GeV EXTRACTION
SLOW SPILL
PING
BEAM CURRENT IN THE ACCELERATOR
T2 = 1.6791
T3 = 2.4889
T4 = 3.0889
T5 = 4.7994
T6 = 5.7995
FAST SPILL

Fig. 2.2

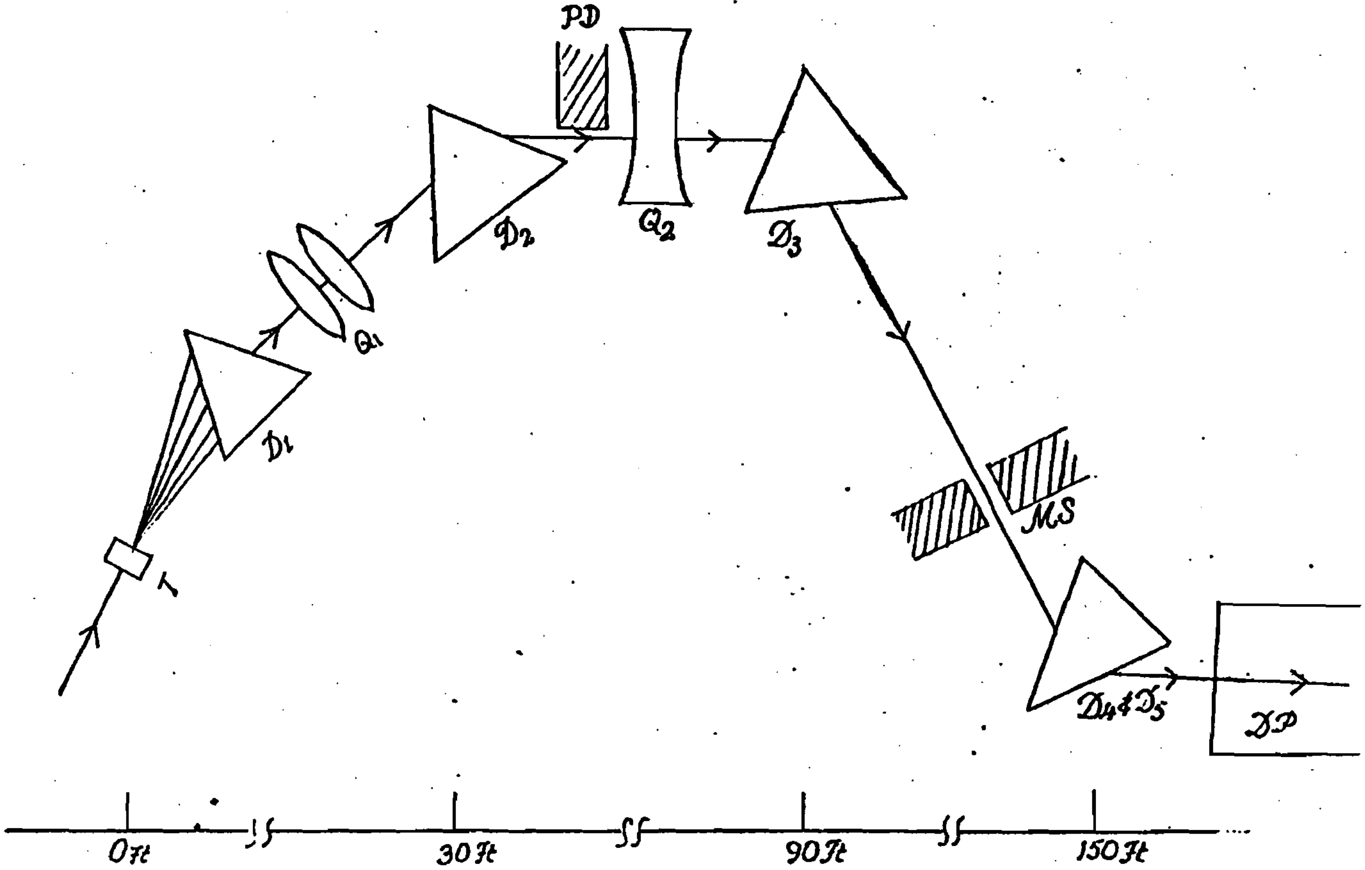

Fig. 2.3a

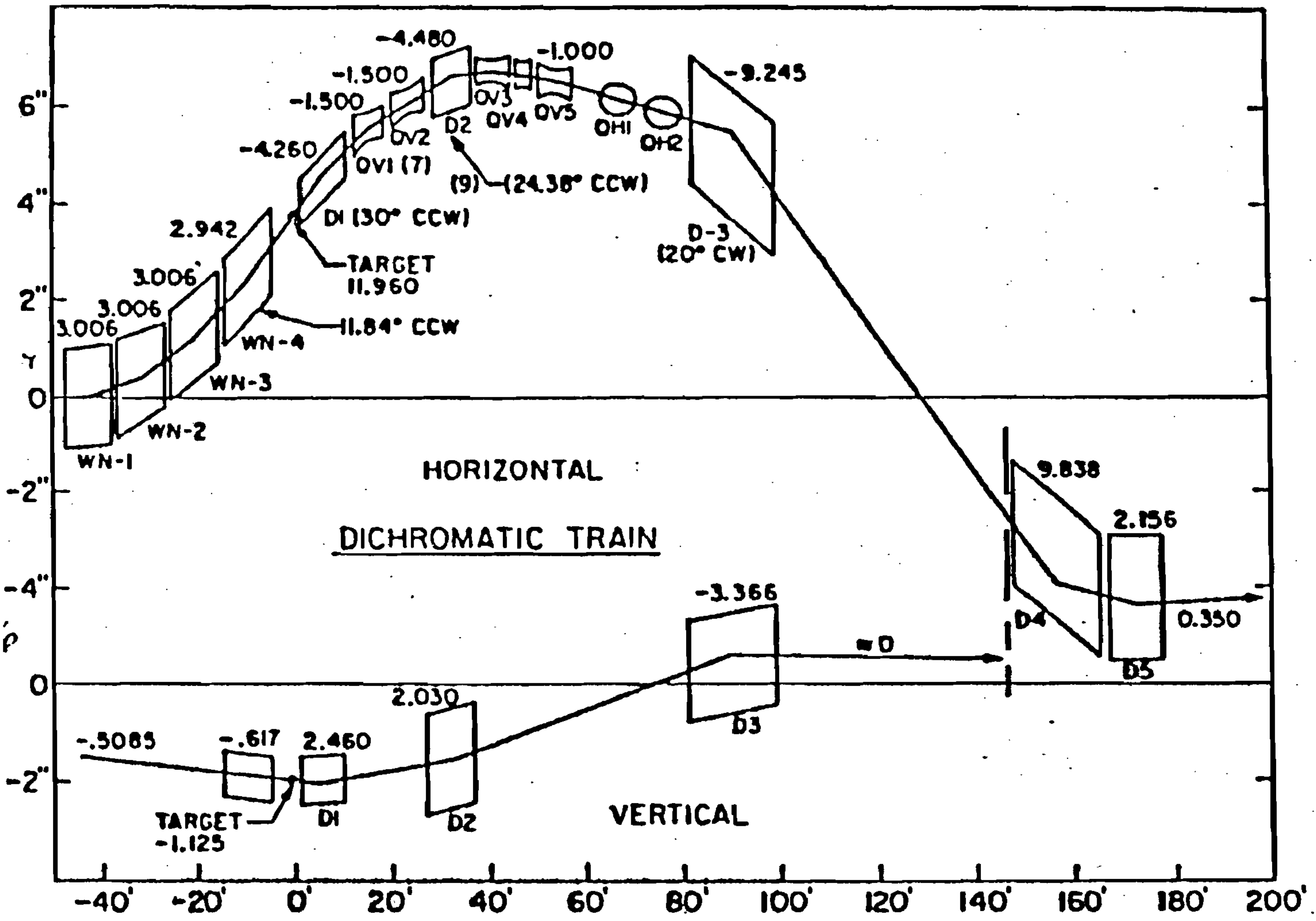
HORIZONTAL
DICHROMATIC TRAIN
VERTICAL
6"
4"
2"
Y
0
-2"
-4"
ρ'
0
-2"
3.006
3.006
3.006
2.942
-4.260
-1.500
-1.500
-4.480
-1.000
-9.245
WN-1
WN-2
WN-3
WN-4
11.84° CCW
TARGET
11.960
DI (30° CCW)
QV1 (7)
QV2
D2
QV3
QV4
QV5
(9)—(24.38° CCW)
QH1
QH2
D-3
(20° CW)
9.838
2.156
D4
D5
0.350
-3.366
∞D
D3
-.5085
-.617
2.460
2.030
TARGET
-1.125
DI
D2
-40'
-20'
0'
20'
40'
60'
80'
100'
120'
140'
160'
180'
200'

Fig. 2.3b

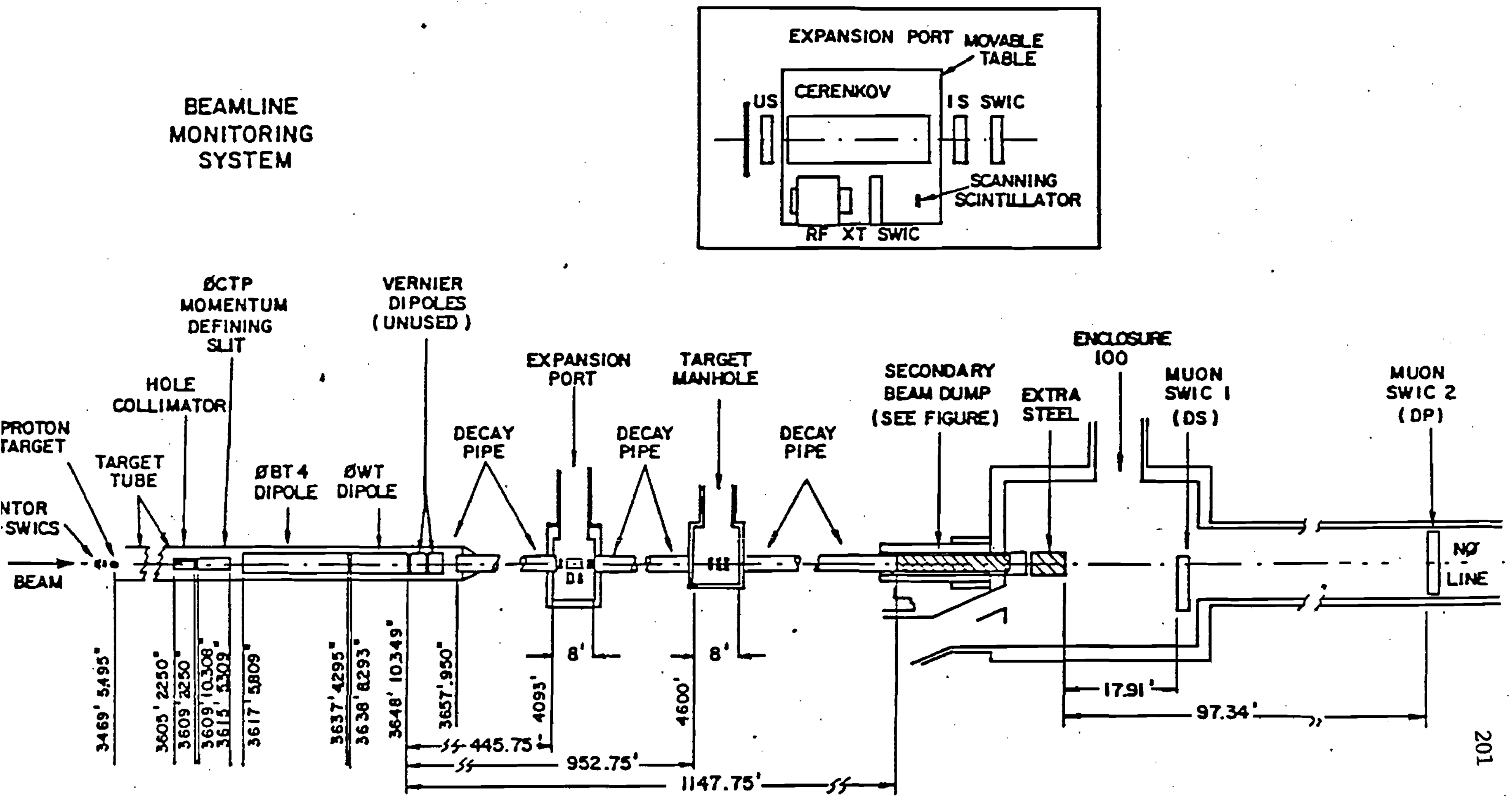
BEAMLINE MONITORING SYSTEM
EXPANSION PORT
MOVABLE TABLE
US
CERENKOV
IS
SWIC
SCANNING SCINTILLATOR
RF
XT
SWIC
ØCTP MOMENTUM DEFINING SLIT
VERNIER DIPOLES (UNUSED)
HOLE COLLIMATOR
PROTON TARGET
TARGET TUBE
NTOR SWICS
BEAM
ØBT4 DIPOLE
ØWT DIPOLE
DECAY PIPE
EXPANSION PORT
D8
DECAY PIPE
TARGET MANHOLE
DECAY PIPE
SECONDARY BEAM DUMP (SEE FIGURE)
EXTRA STEEL
ENCLOSURE 100
MUON SWIC 1 (DS)
MUON SWIC 2 (DP)
NØ LINE
3469' 5.495"
3605' 2250"
3609' 2250"
3609' 10.308"
3615' 3309"
3617' 5809"
3637' 4295"
3638' 8293"
3648' 10349"
3657' 950"
4093'
8'
4600'
8'
445.75'
952.75'
1147.75'
17.91'
97.34'

Fig. 2.3c

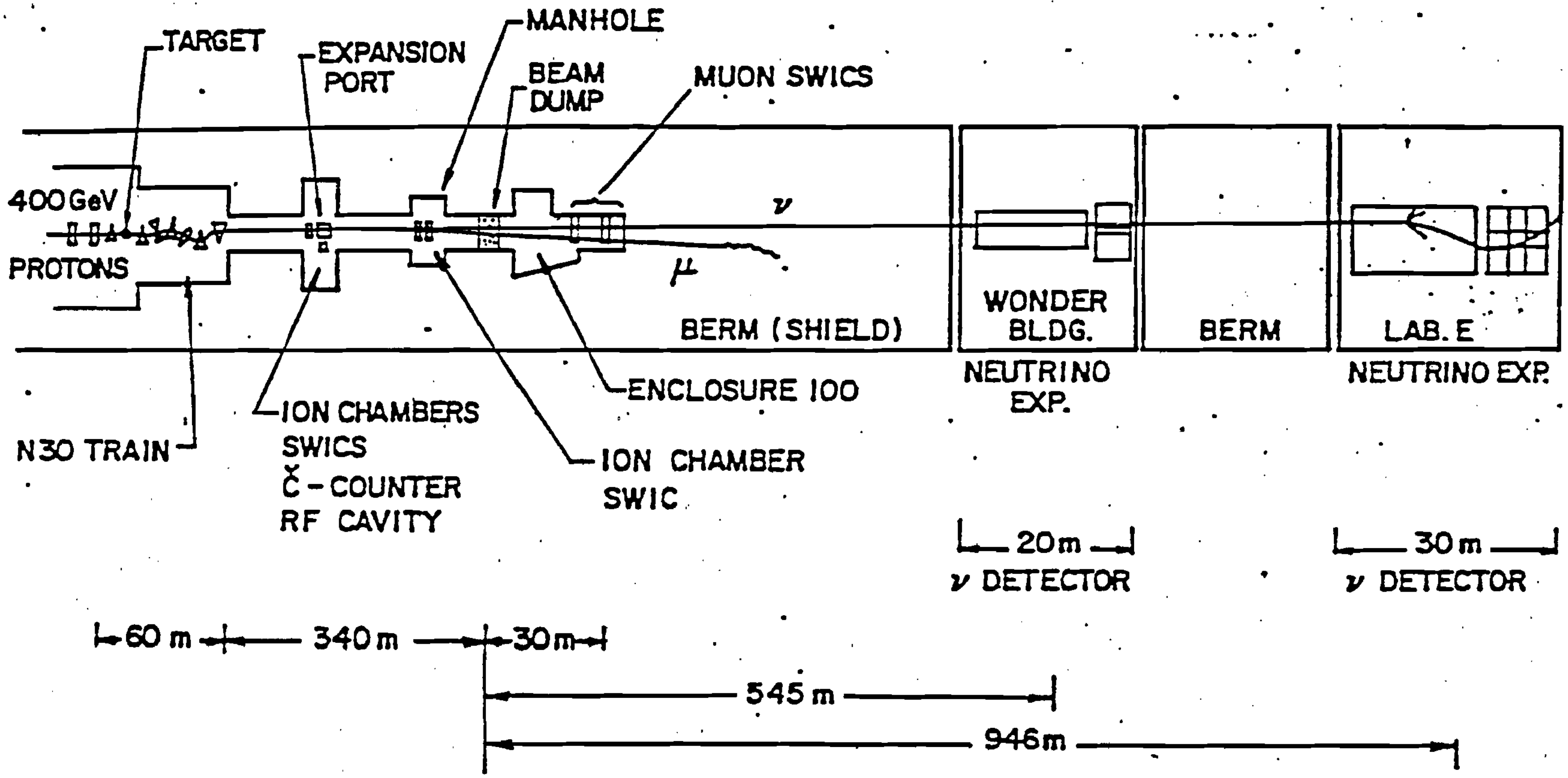
TARGET
EXPANSION PORT
MANHOLE
BEAM DUMP
MUON SWICS
400 GeV PROTONS
ν
μ
BERM (SHIELD)
WONDER BLDG.
NEUTRINO EXP.
BERM
LAB. E
NEUTRINO EXP.
N30 TRAIN
ION CHAMBERS
SWICS
Č - COUNTER
RF CAVITY
ENCLOSURE 100
ION CHAMBER
SWIC
20 m
ν DETECTOR
30 m
ν DETECTOR
60 m
340 m
30 m
545 m
946 m

Fig, 2.4

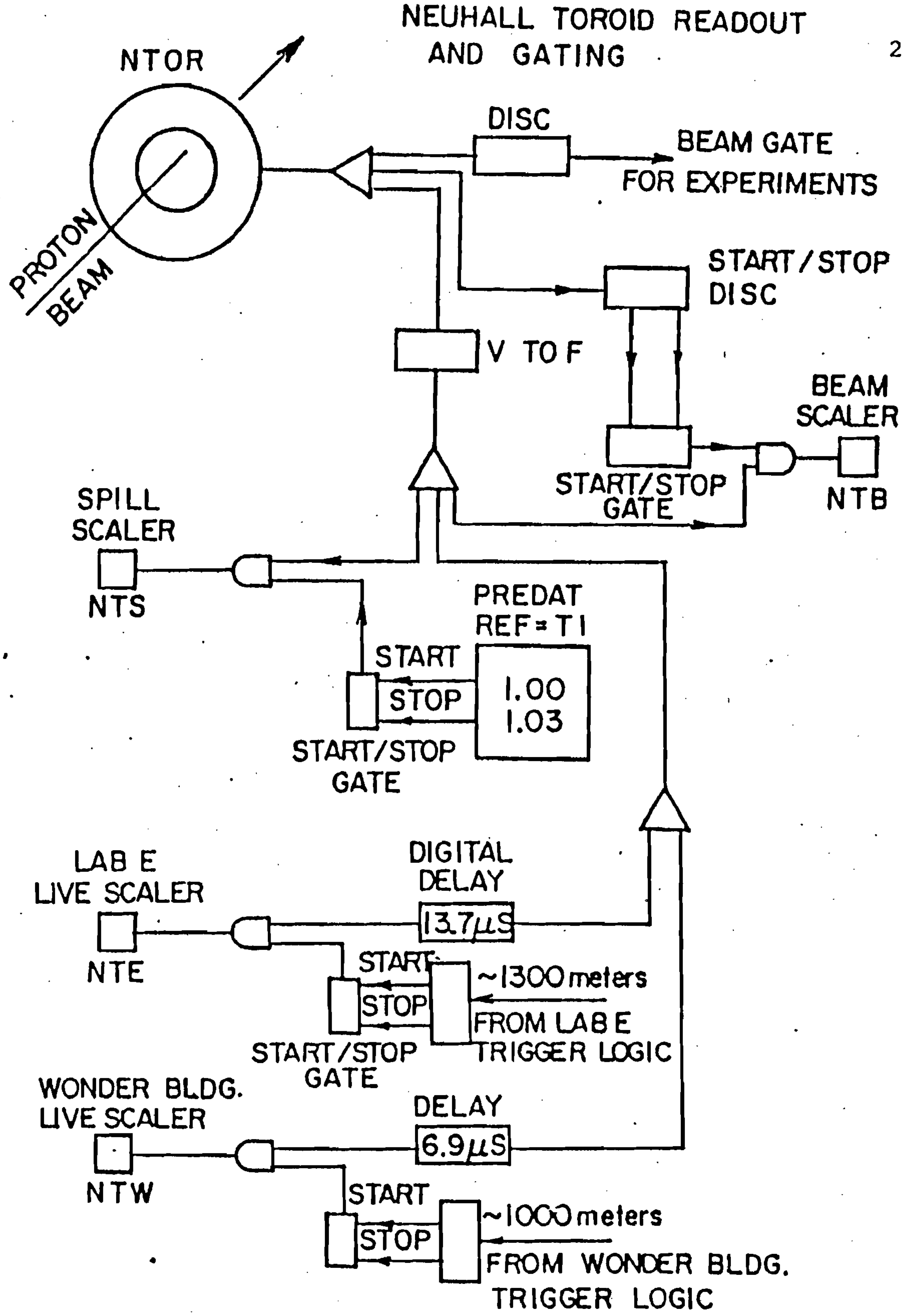
NEUHALL TOROID READOUT AND GATING
NTOR
PROTON BEAM
DISC
BEAM GATE FOR EXPERIMENTS
START / STOP DISC
V TOF
BEAM SCALER
START/STOP GATE
NTB
SPILL SCALER
NTS
PREDAT REF = T1
START
STOP
1.00
1.03
START/STOP GATE
LAB E LIVE SCALER
NTE
DIGITAL DELAY
13.7μS
START
STOP
~1300 meters
FROM LAB E TRIGGER LOGIC
START/STOP GATE
WONDER BLDG. LIVE SCALER
NTW
DELAY
6.9μS
START
STOP
~1000 meters
FROM WONDER BLDG. TRIGGER LOGIC

Fig. 2.5

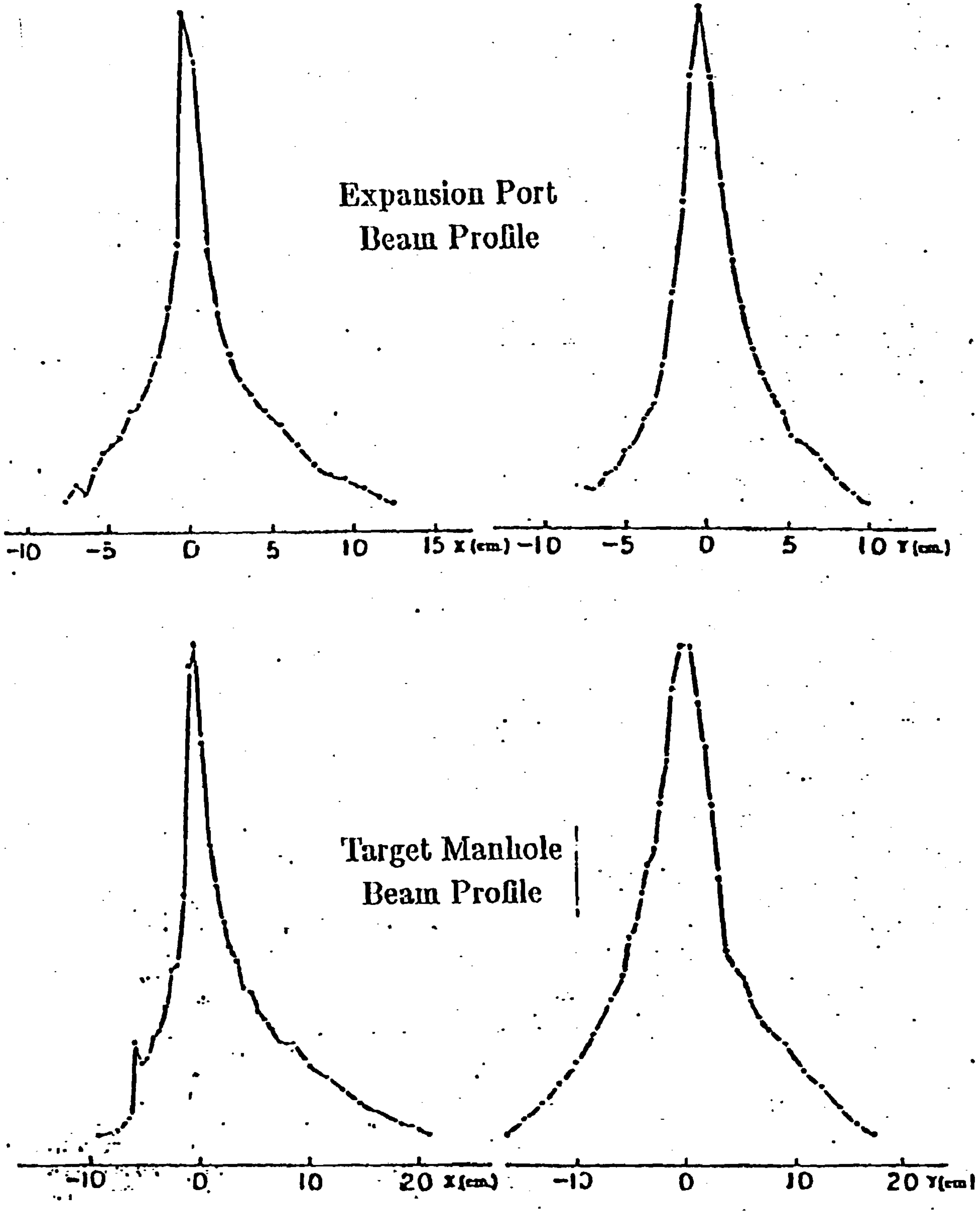

Expansion Port
Beam Profile

Target Manhole
Beam Profile

Fig. 2.6a

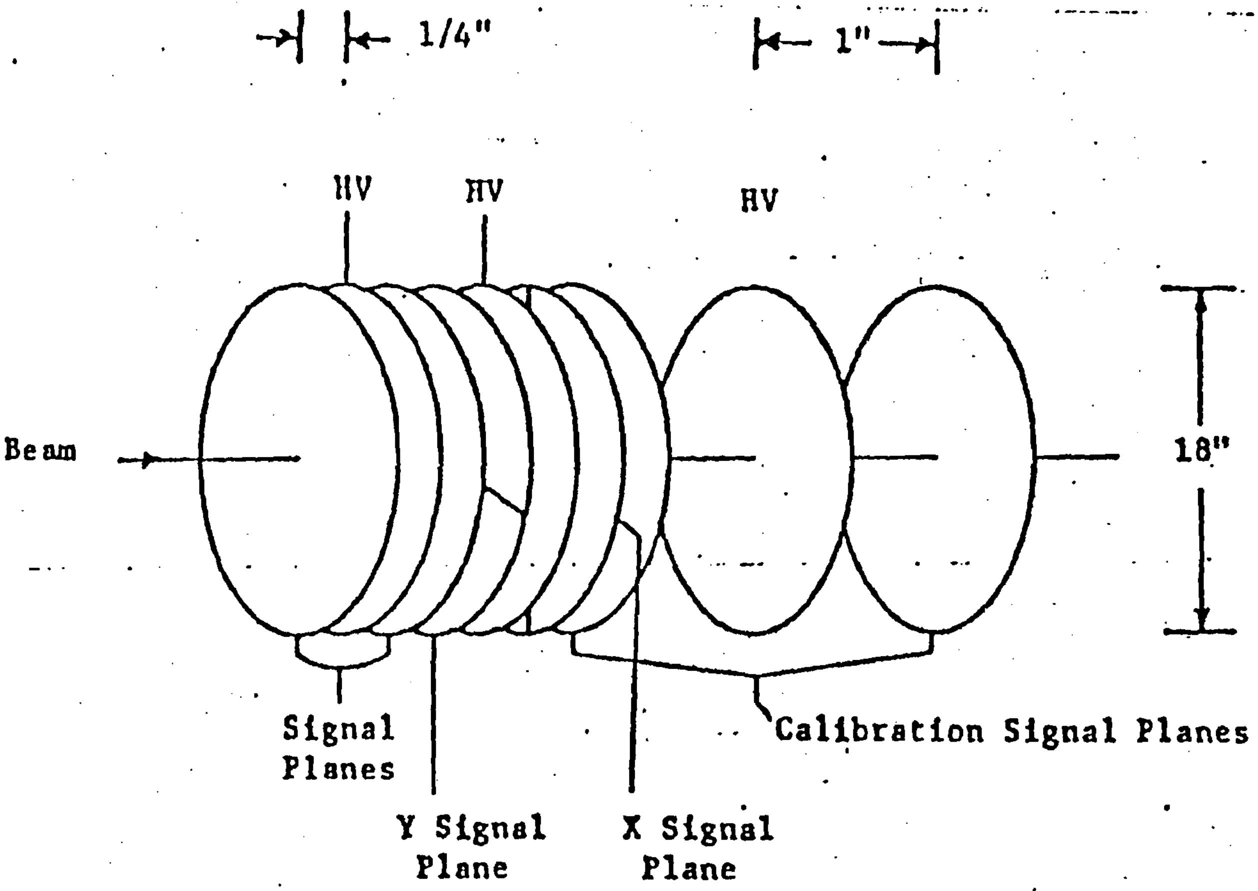
1/4"
1"
HV
HV
HV
Beam
18"
Signal Planes
Y Signal Plane
X Signal Plane
Calibration Signal Planes

Fig. 2.6b

Lab E

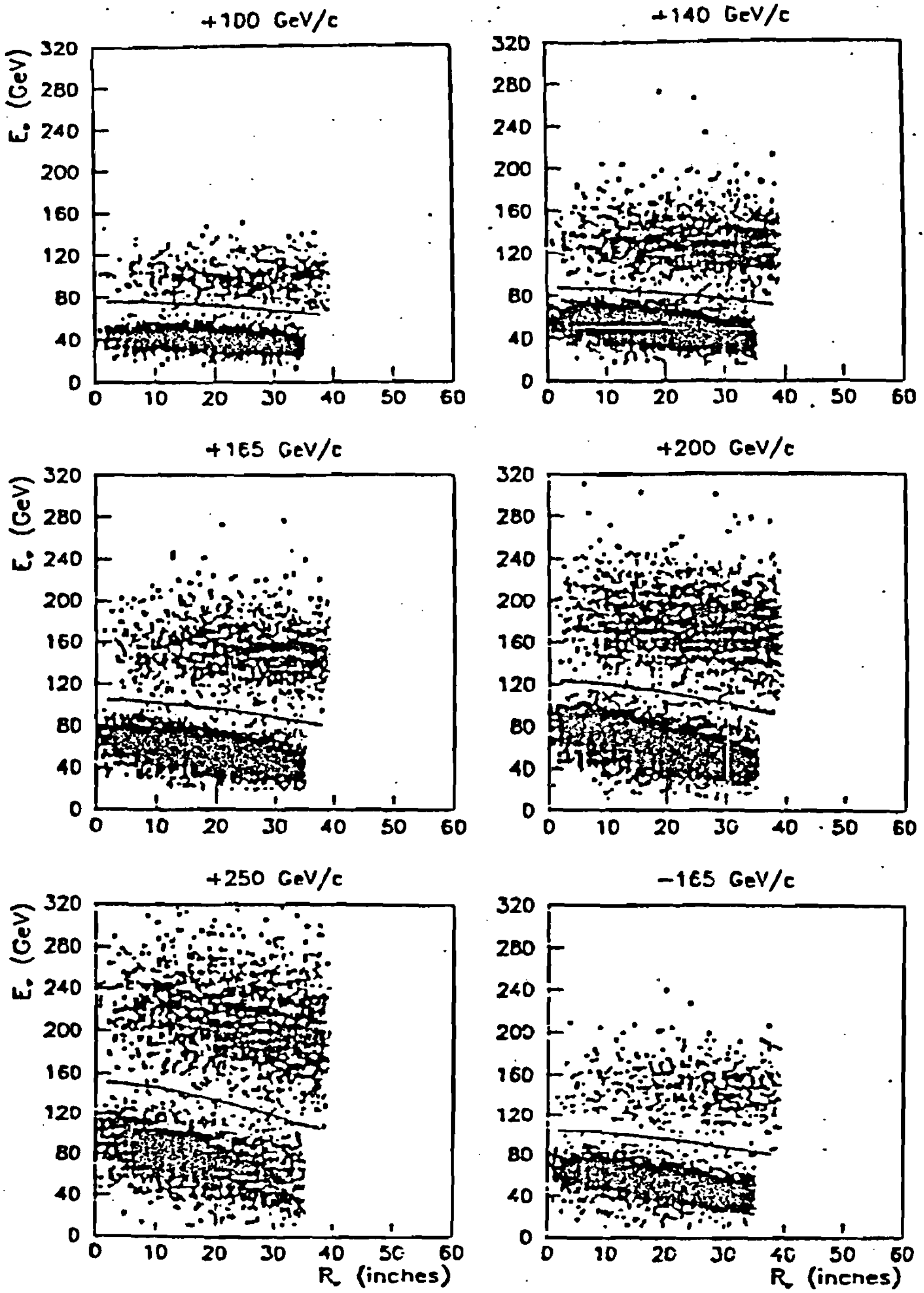
+100 GeV/c
+140 GeV/c
+165 GeV/c
+200 GeV/c
+250 GeV/c
−165 GeV/c
E (GeV)
R (inches)
0
40
80
120
160
200
240
280
320
0
10
20
30
40
50
60

Fig. 2.7

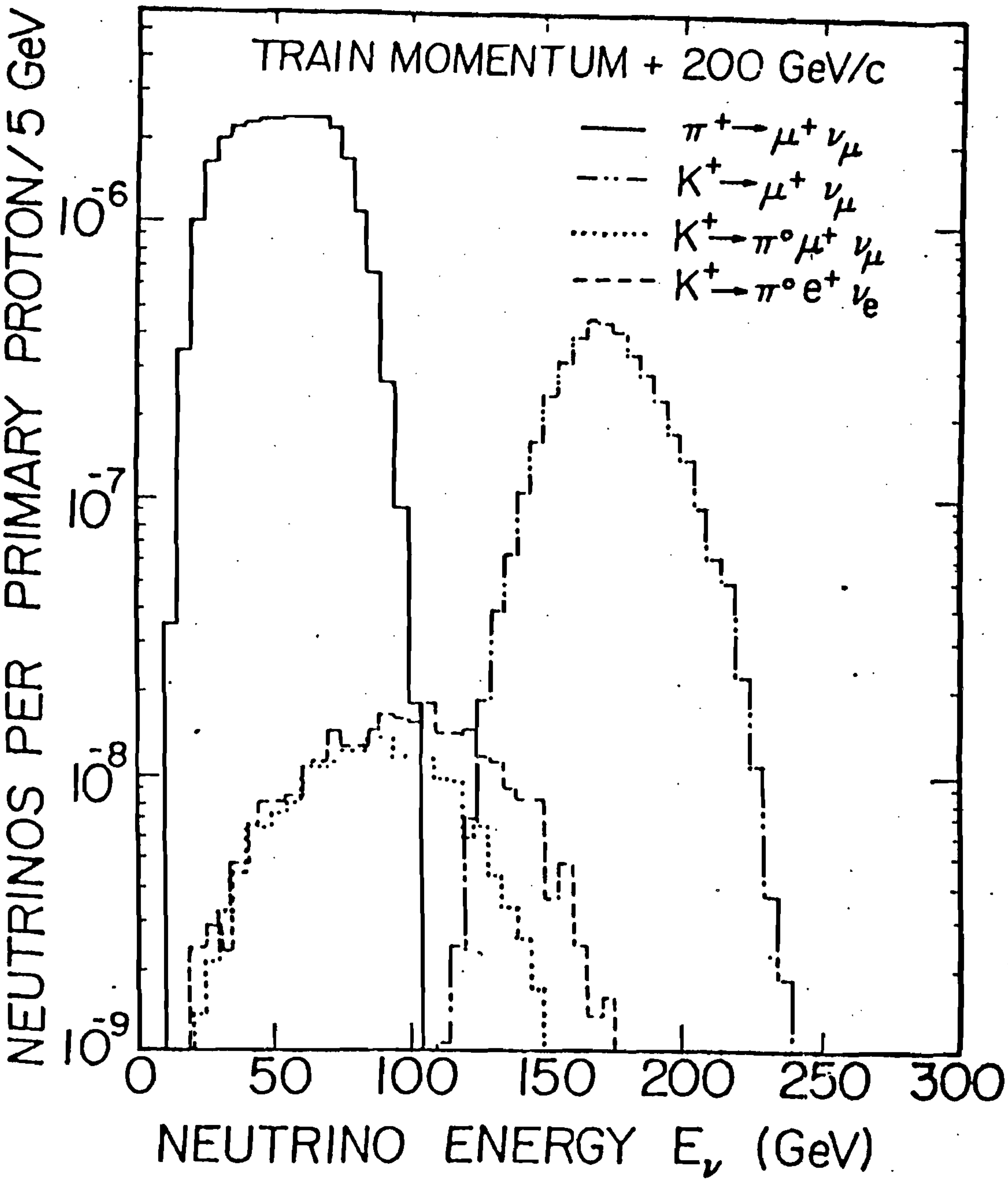
TRAIN MOMENTUM + 200 GeV/c
$\pi^+ \to \mu^+ \nu_\mu$
$K^+ \to \mu^+ \nu_\mu$
$K^+ \to \pi^\circ \mu^+ \nu_\mu$
$K^+ \to \pi^\circ e^+ \nu_e$
NEUTRINOS PER PRIMARY PROTON / 5 GeV
10^{-6}
10^{-7}
10^{-8}
10^{-9}
0
50
100
150
200
250
300
NEUTRINO ENERGY E_ν (GeV)

Fig. 2.8

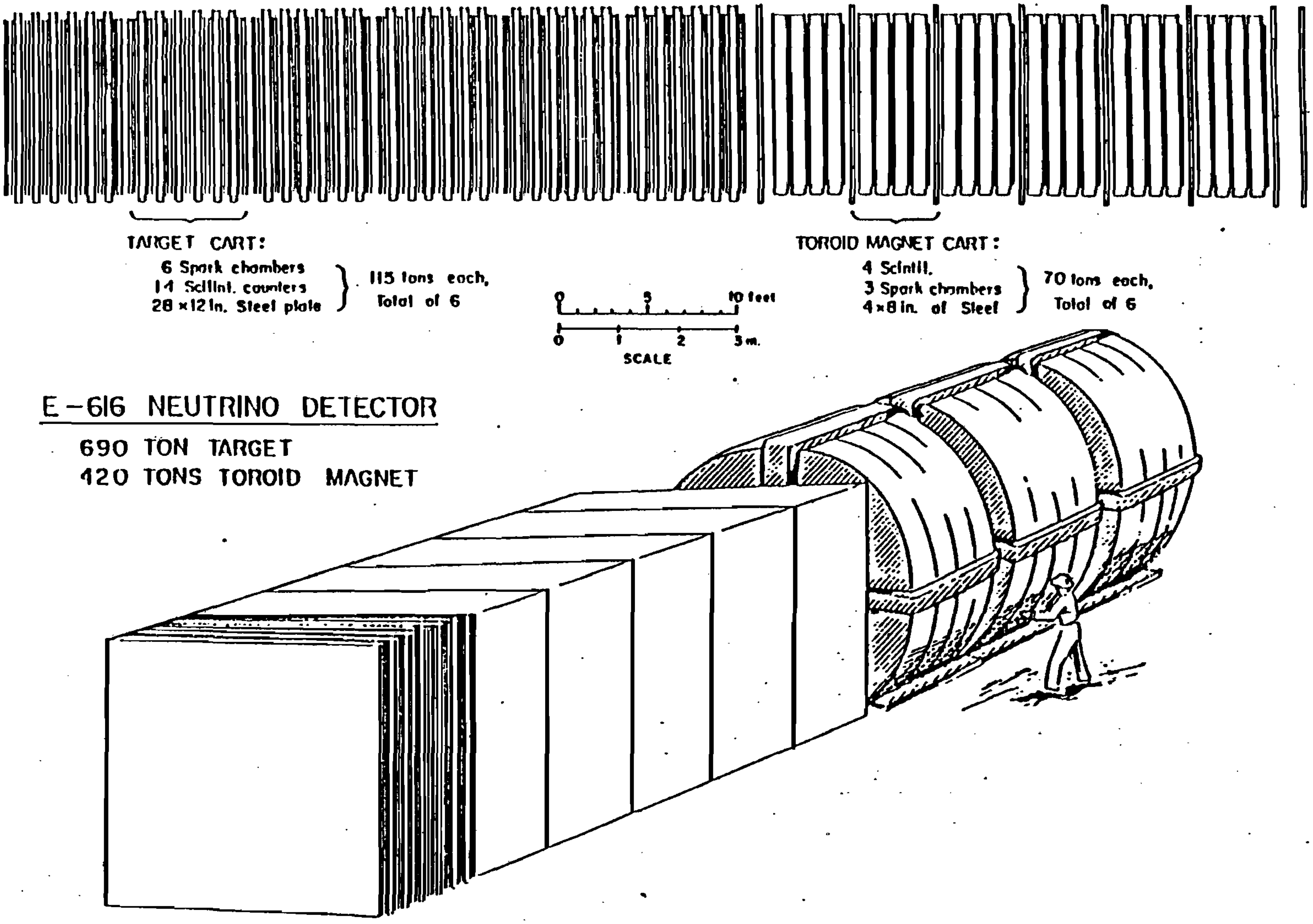
TARGET CART:
6 Spark chambers
14 Scintil. counters
28 × 12 in. Steel plate
115 tons each,
Total of 6
0
5
10 feet
0
1
2
3 m.
SCALE
TOROID MAGNET CART:
4 Scintil.
3 Spark chambers
4 × 8 in. of Steel
70 tons each,
Total of 6
E-616 NEUTRINO DETECTOR
690 TON TARGET
420 TONS TOROID MAGNET

Fig. 3.1

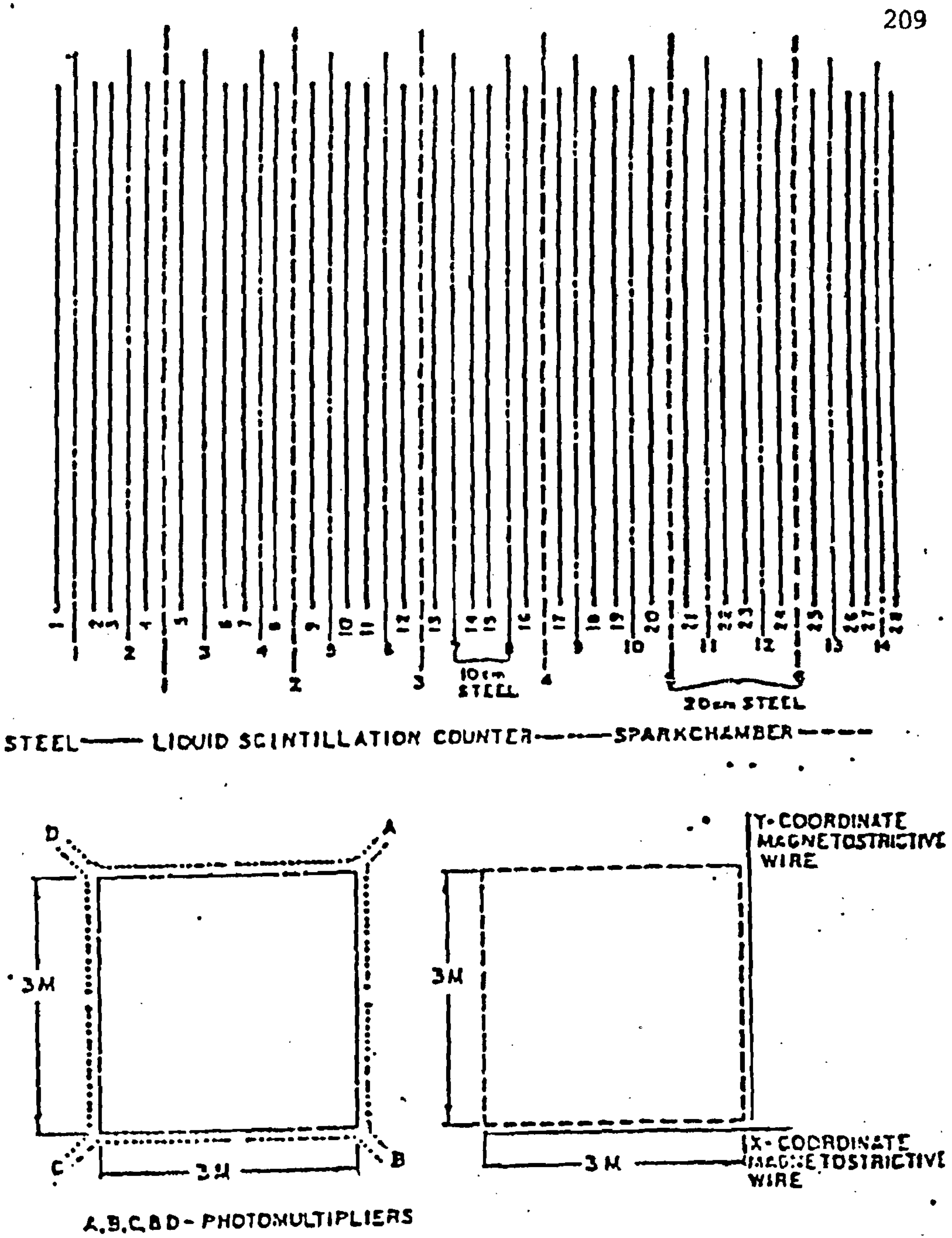

TARGET CART

Fig. 3.2

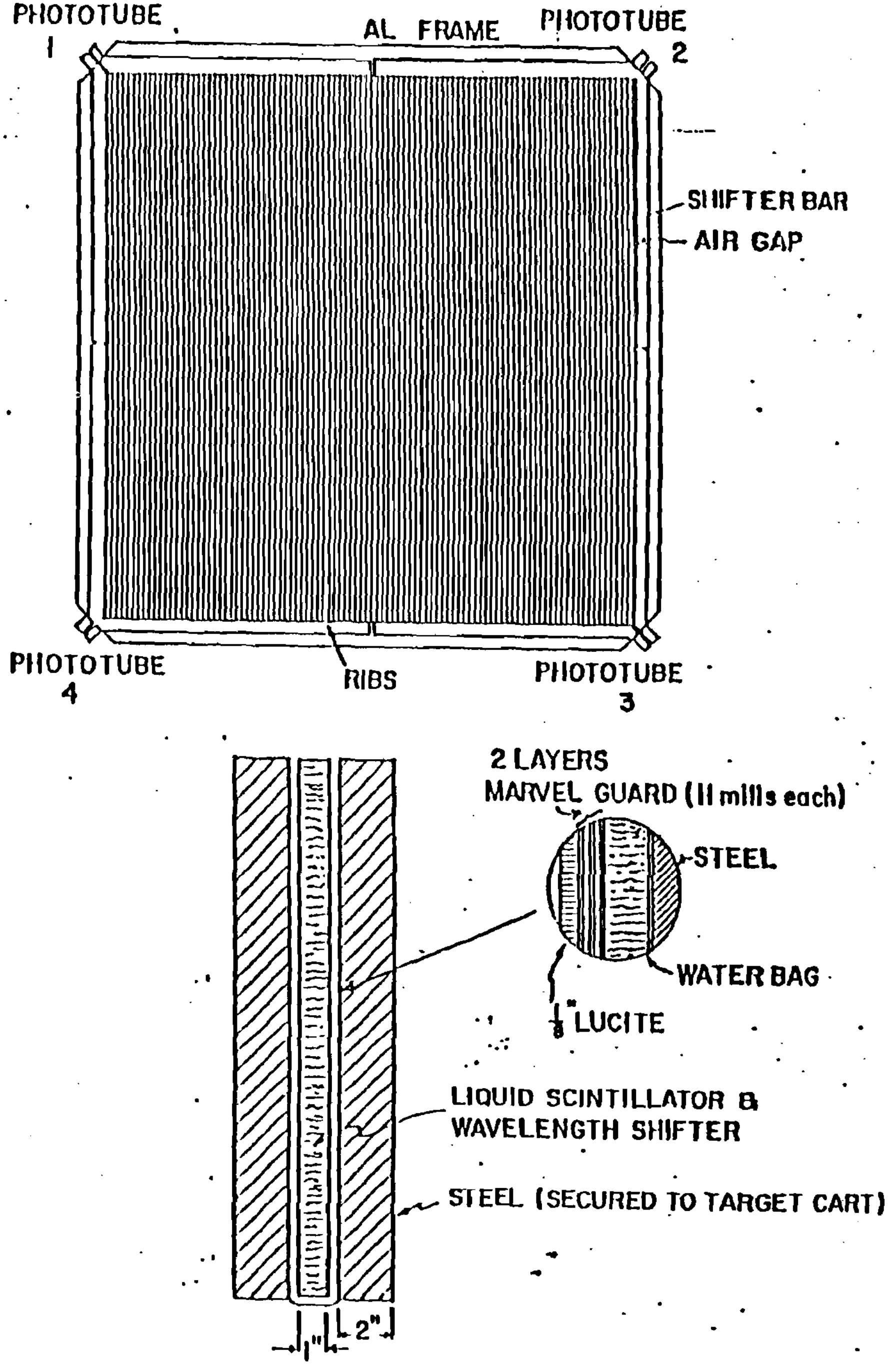
PHOTOTUBE 1
AL FRAME
PHOTOTUBE 2
SHIFTER BAR
AIR GAP
PHOTOTUBE 4
RIBS
PHOTOTUBE 3
2 LAYERS MARVEL GUARD (11 mills each)
STEEL
WATER BAG
1/8" LUCITE
LIQUID SCINTILLATOR & WAVELENGTH SHIFTER
STEEL (SECURED TO TARGET CART)
1"
2"

Fig. 3.3

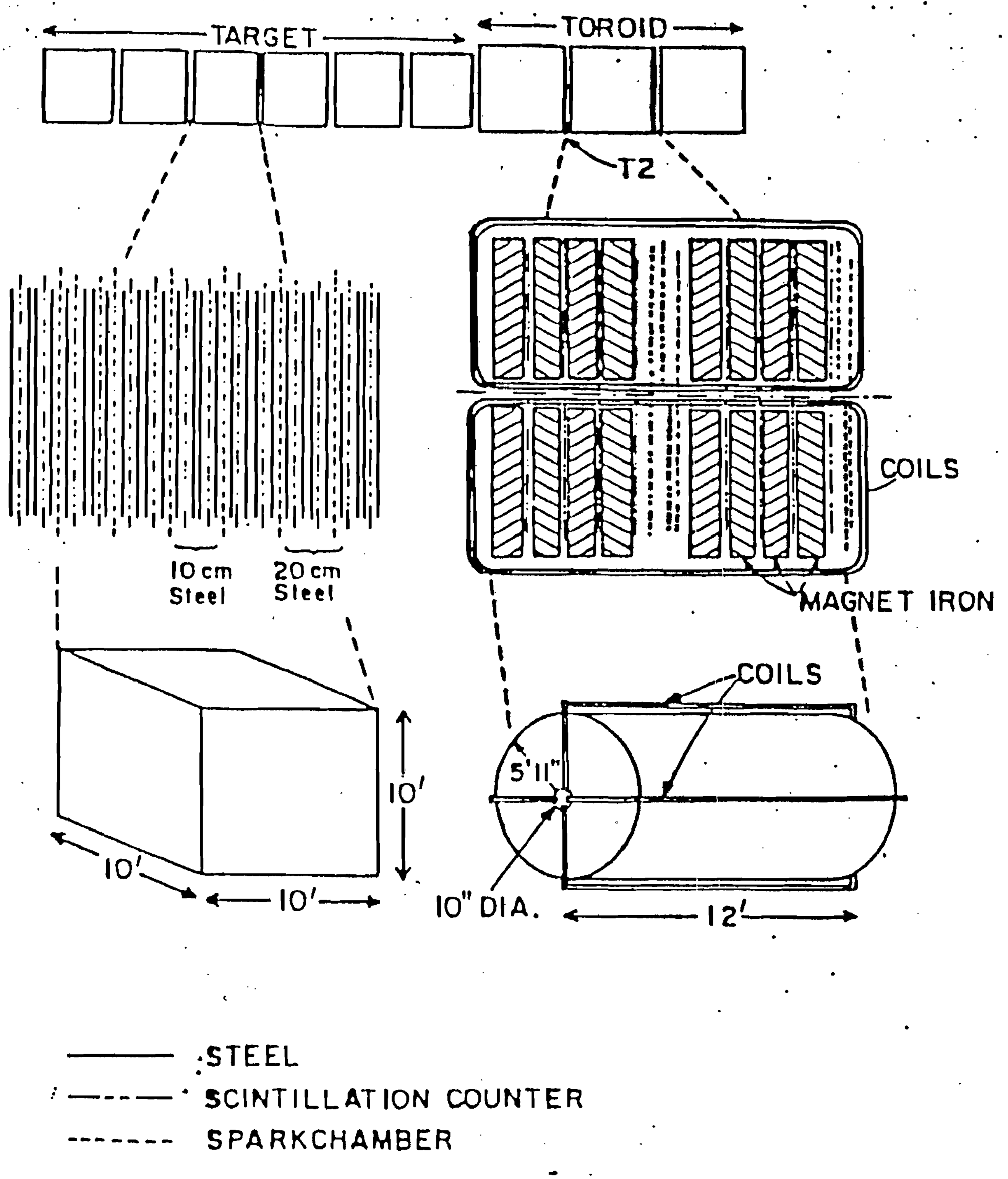
TARGET
TOROID
T2
10 cm Steel
20 cm Steel
COILS
MAGNET IRON
COILS
5'11"
10"DIA.
10'
10'
10'
12'
STEEL
SCINTILLATION COUNTER
SPARKCHAMBER

Fig. 3.4

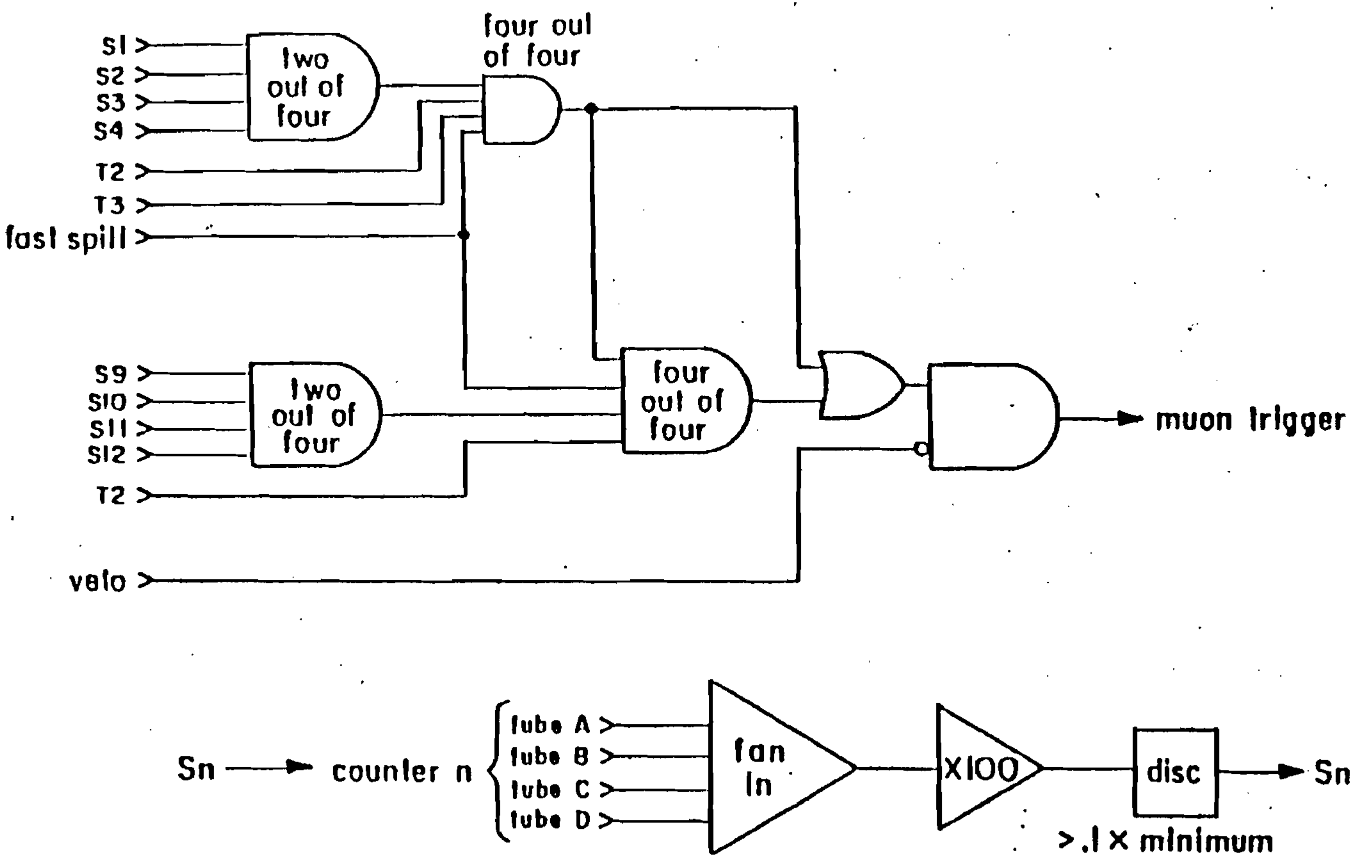

Muon Trigger

Muon trigger logic. In the above: veto refers to the or'ed output of a wall of veto counters in front of the detector, T2 and T3 refers to the output of trigger counters in the toroids, and fast spill is the output of a discriminator on a proton intensity monitor.

Fig. 3.5a

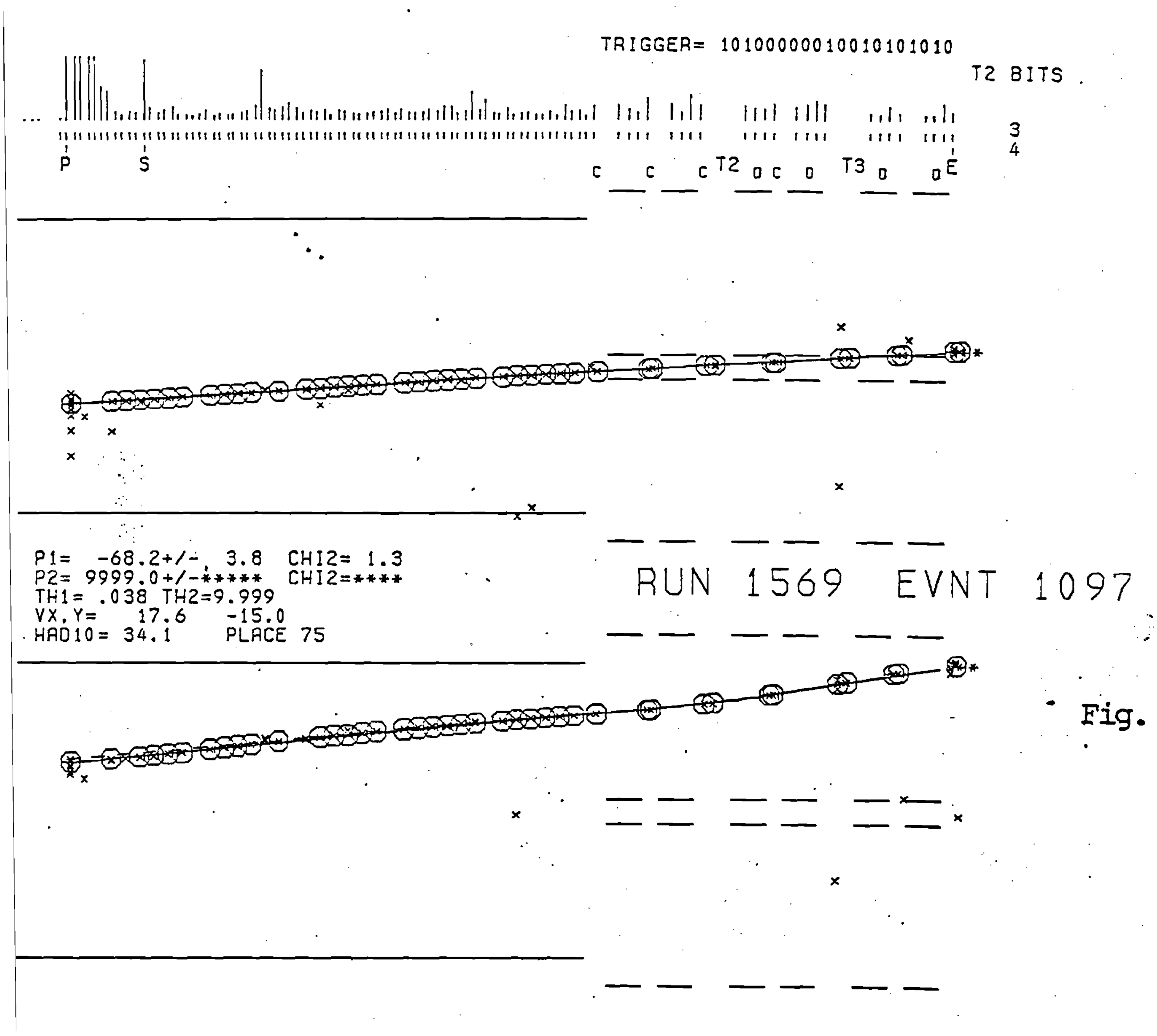

```
TRIGGER= 10100000010010101010

P1=  -68.2+/-  3.8  CHI2= 1.3
P2= 9999.0+/-*****  CHI2=****
TH1= .038 TH2=9.999
VX,Y=   17.6   -15.0
HAD10= 34.1     PLACE 75

RUN 1569  EVNT 1097
```

Fig. 3.5b

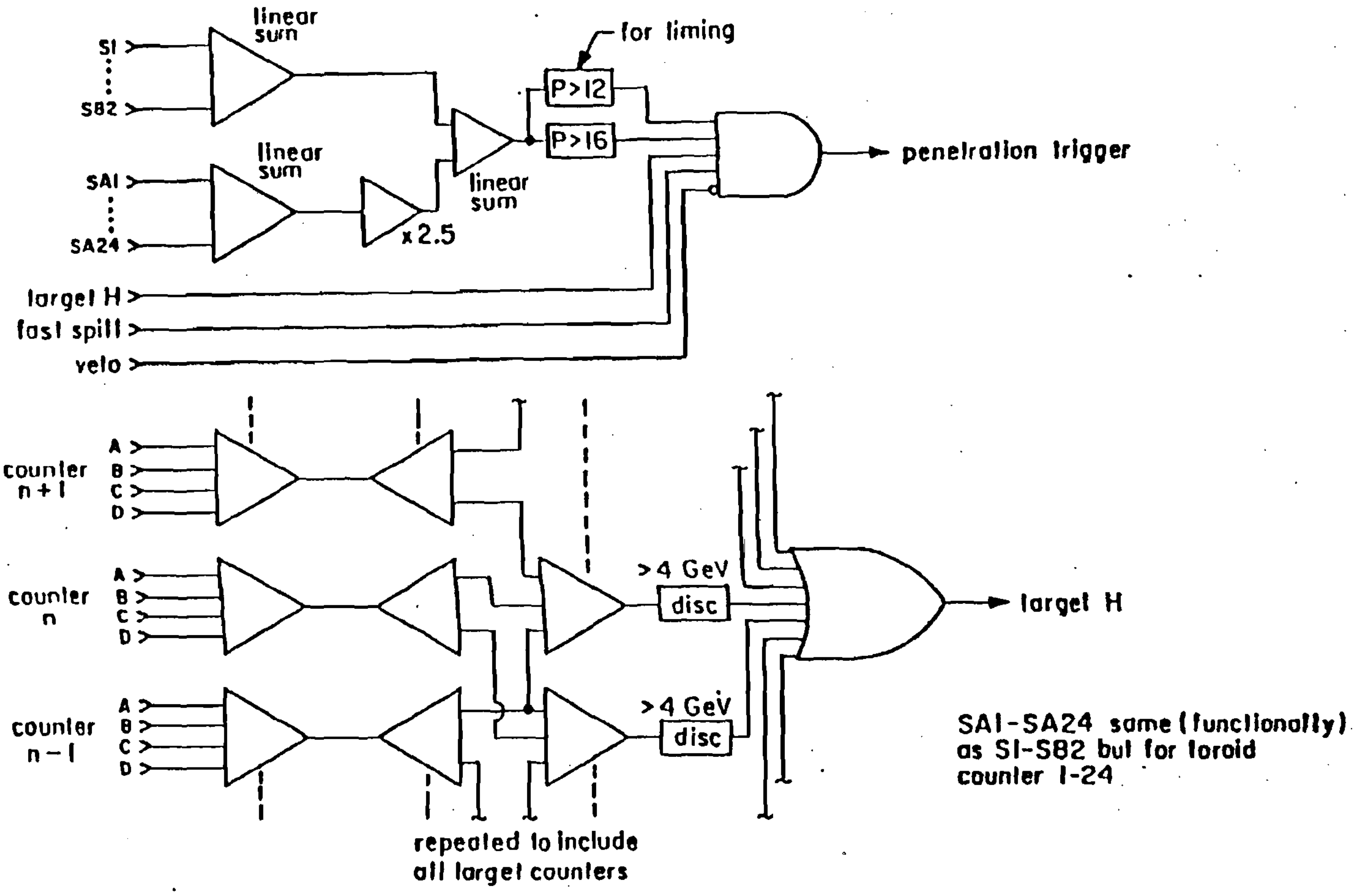

Penetration Trigger

Figure 3-10: Penetration trigger logic. In the above, P>12 and P>16 are discriminators with thresholds set to fire if more than 12 or 16 target s's are on respectively. For the definition of veto and fast spill see figure 3-8.

Fig. 3.6a

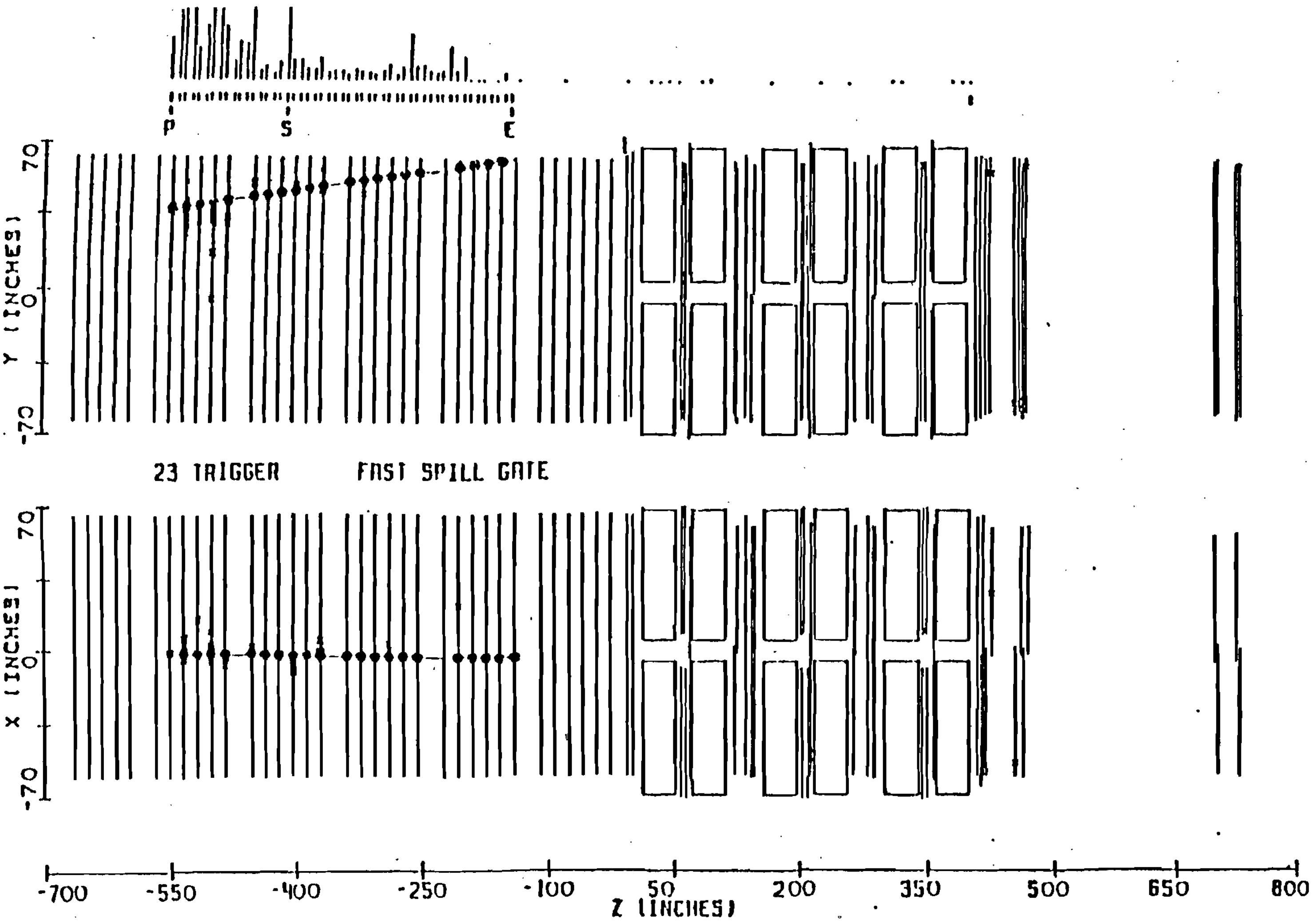
P
S
E
70
Y (INCHES)
0
-70
23 TRIGGER
FAST SPILL GATE
70
X (INCHES)
0
-70
-700
-550
-400
-250
-100
50
200
350
500
650
800
Z (INCHES)

Fig. 3.6b

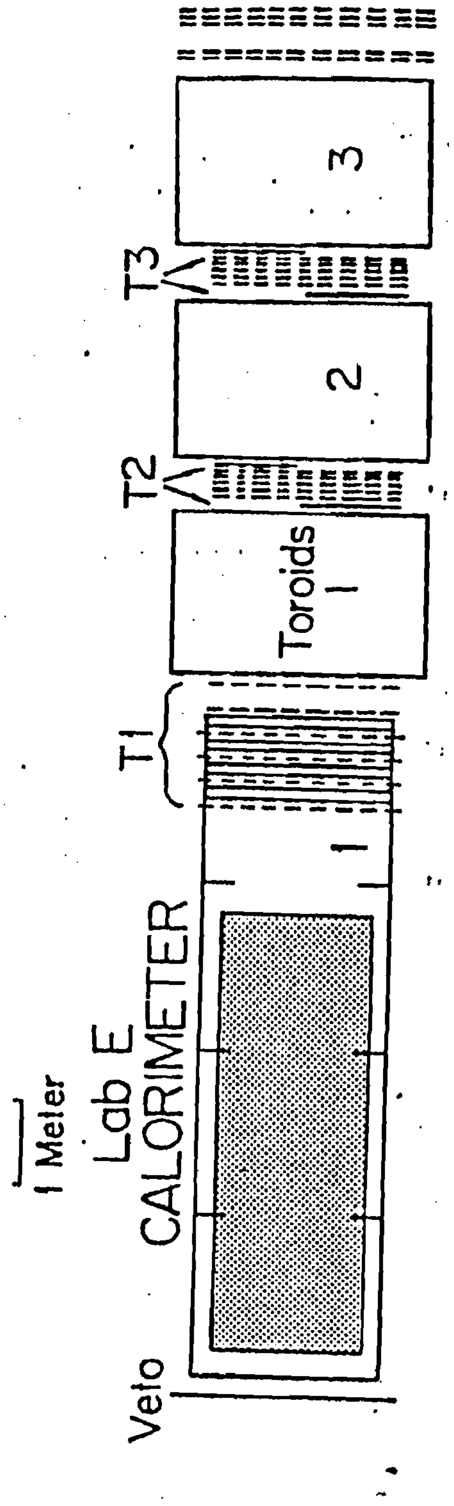

Fig. 3.7

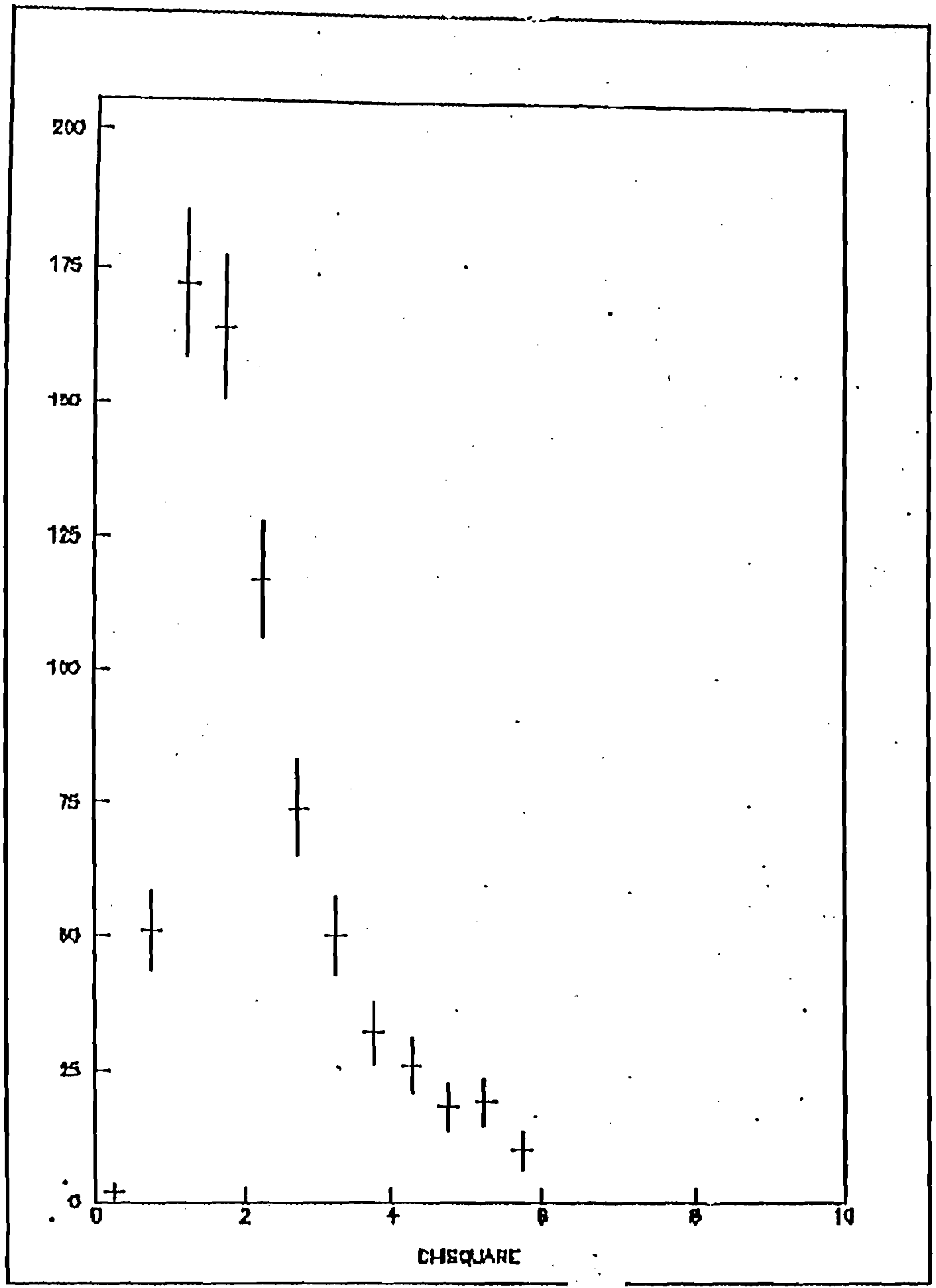

Fig. 4.1a

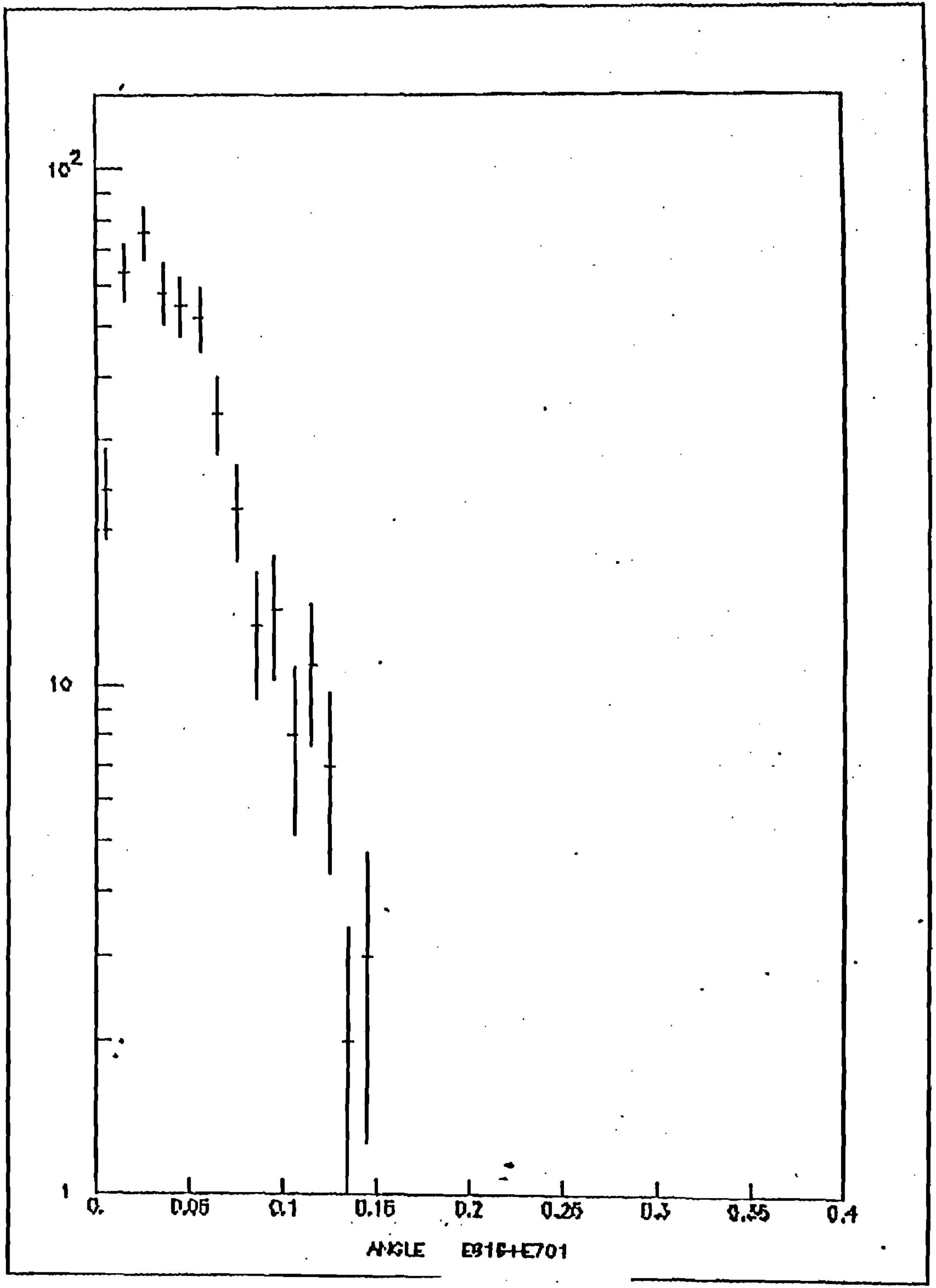

Fig. 4.1b

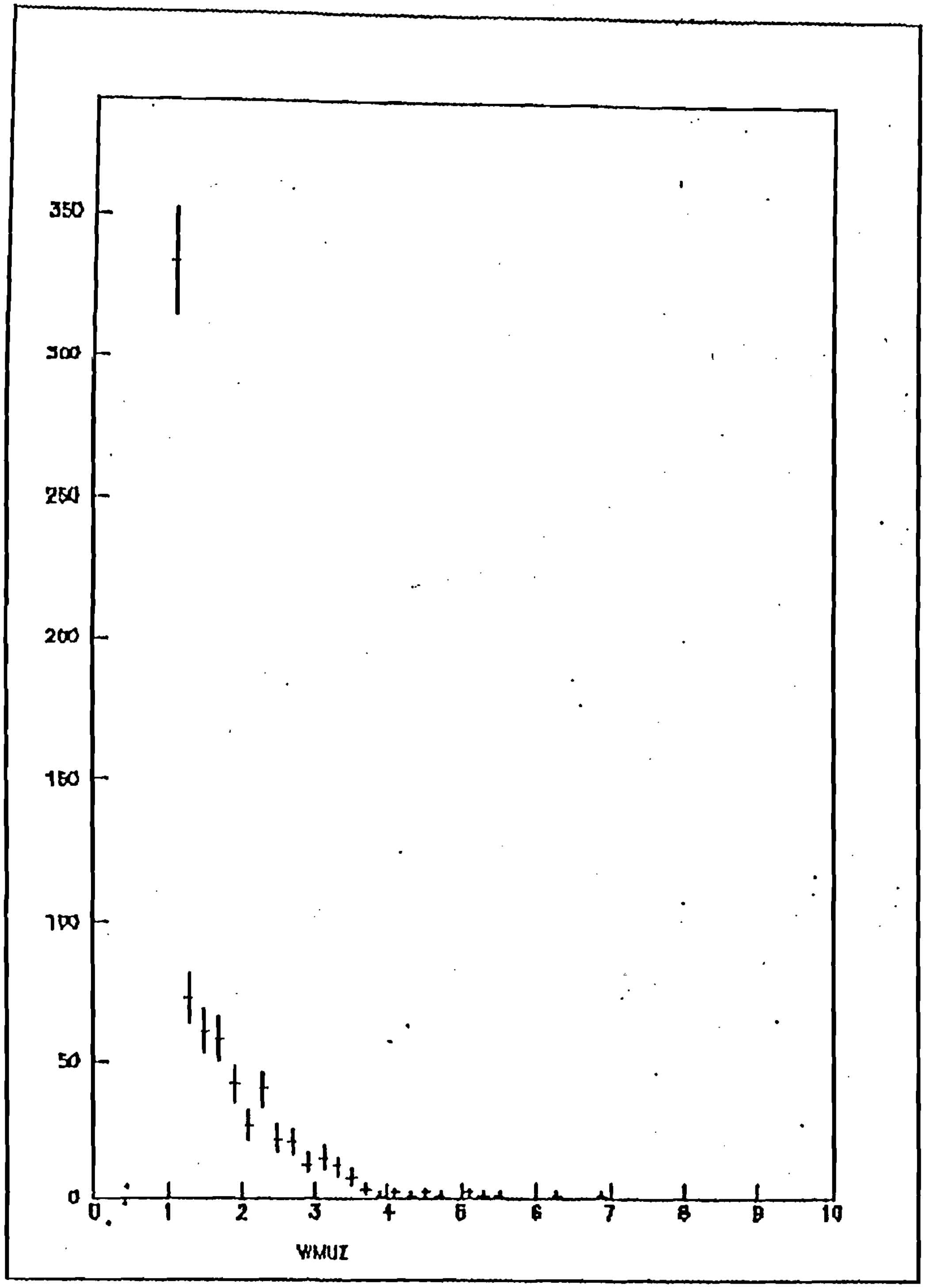

Fig. 4.2

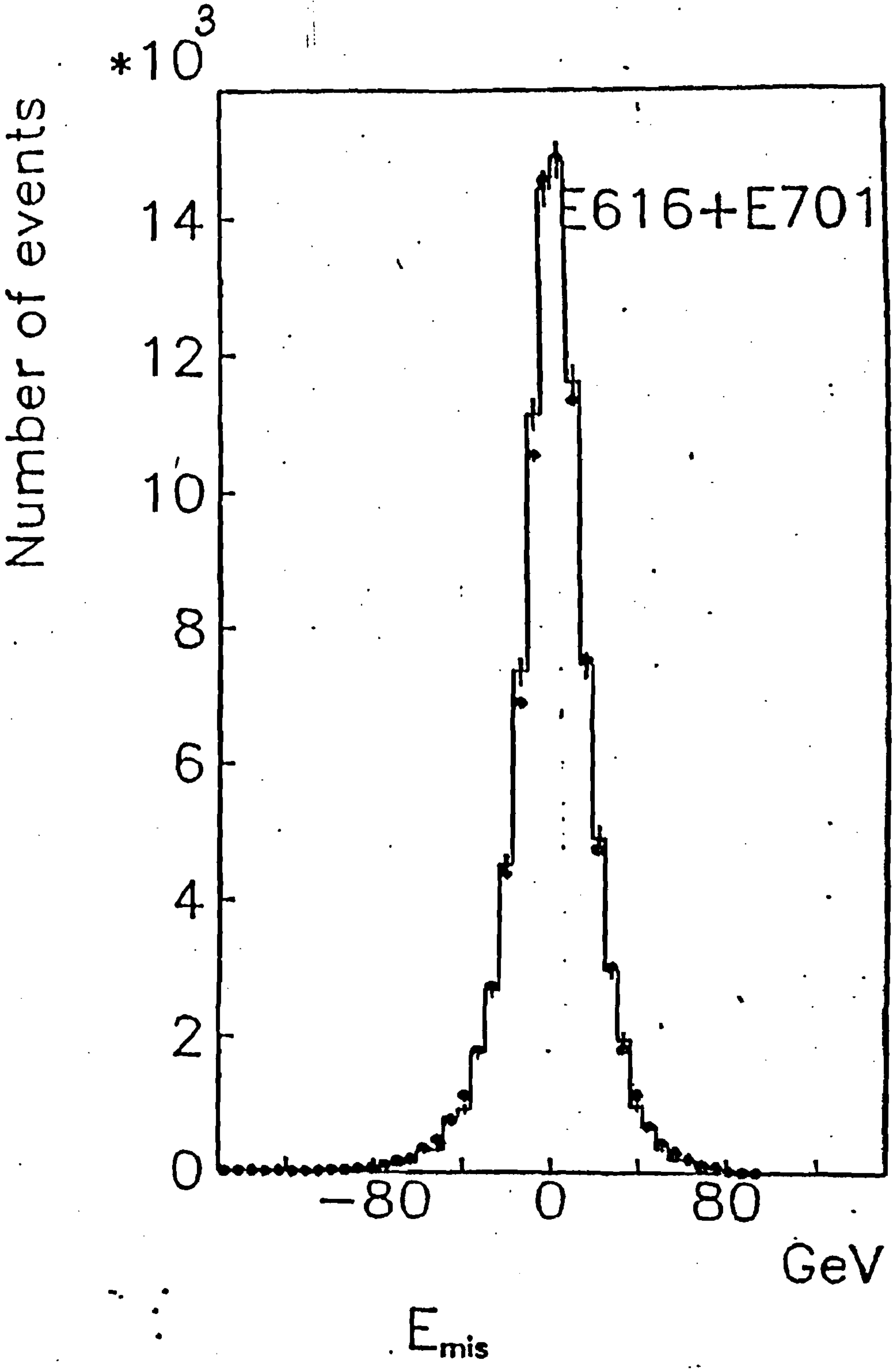

Fig. 4.3

Fig. 5.0 : Feynman diagrams of the four backgrounds producing WSM

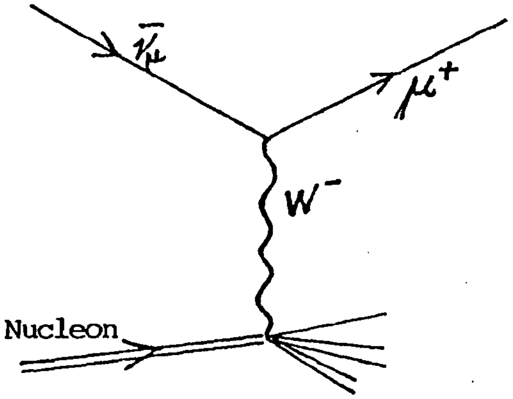

Fig. 5.0a : Wide Band Background (WBB)

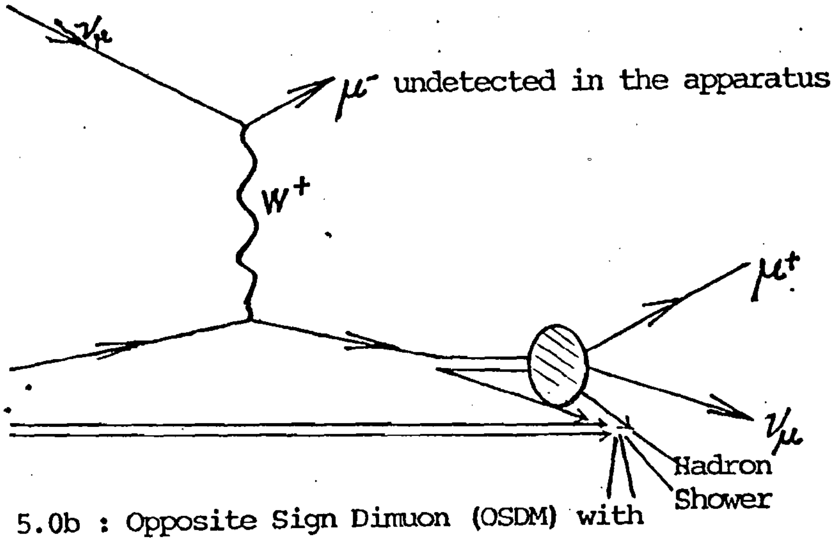

Fig. 5.0b : Opposite Sign Dimuon (OSDM) with its leading muon $(\mu)^-$ missing.

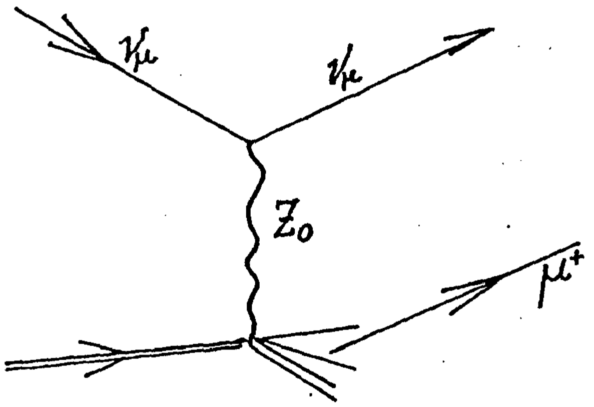

Fig. 5.0c : Neutral Current induced hadron shower may produce π^+/K^+, which, subsequently, may decay into a μ^+ and ν_μ.

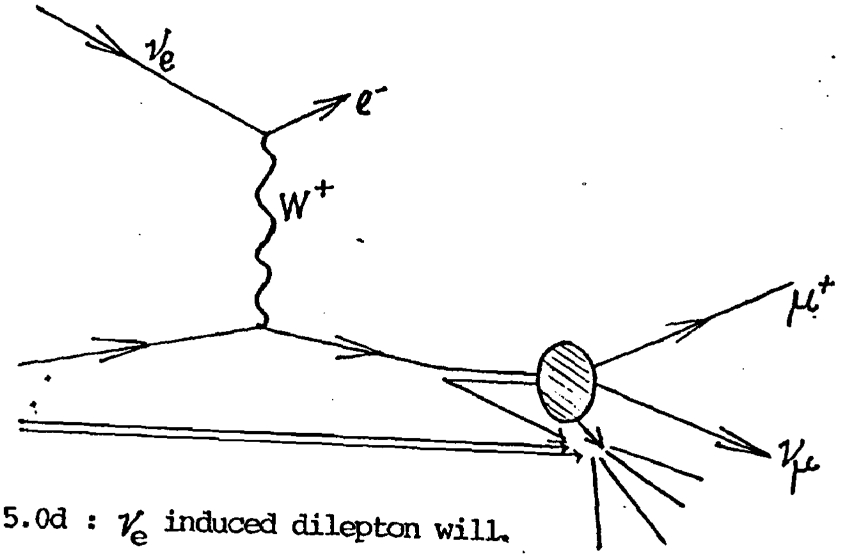

Fig. 5.0d : ν_e induced dilepton will appear to be a WSM. ν_e is produced in the three body decay of kaons.

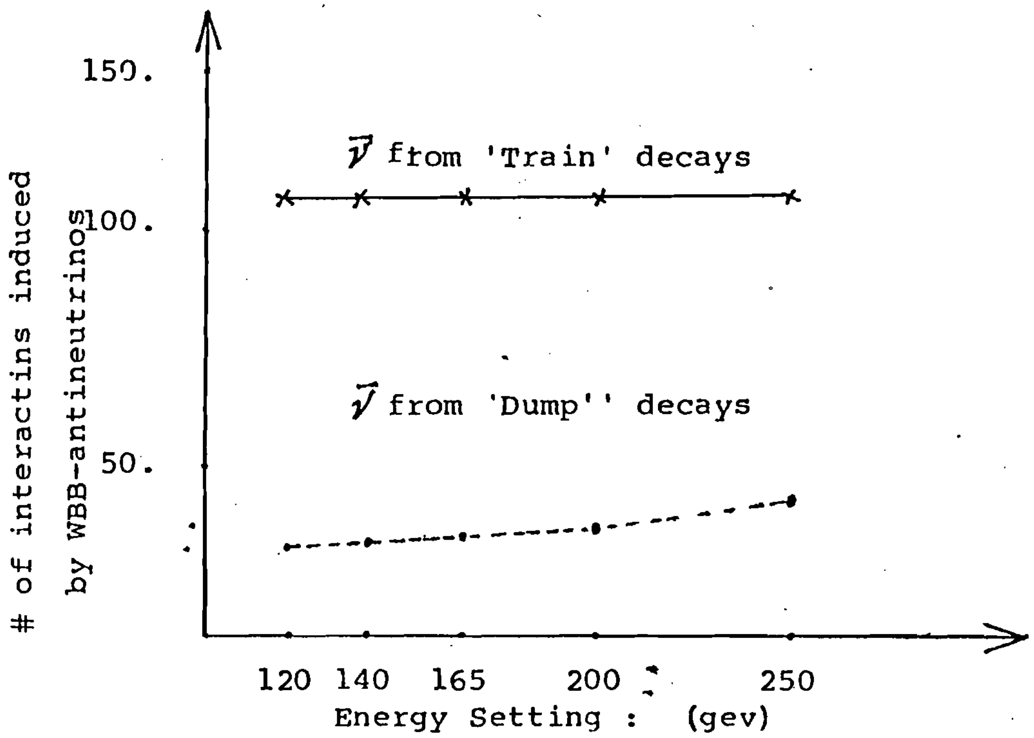
$\bar{\nu}$ from 'Train' decays
$\bar{\nu}$ from 'Dump'' decays
150.
100.
50.
# of interactins induced
by WBB-antineutrinos
120
140
165
200
250
Energy Setting : (gev)

Fig. 5.1

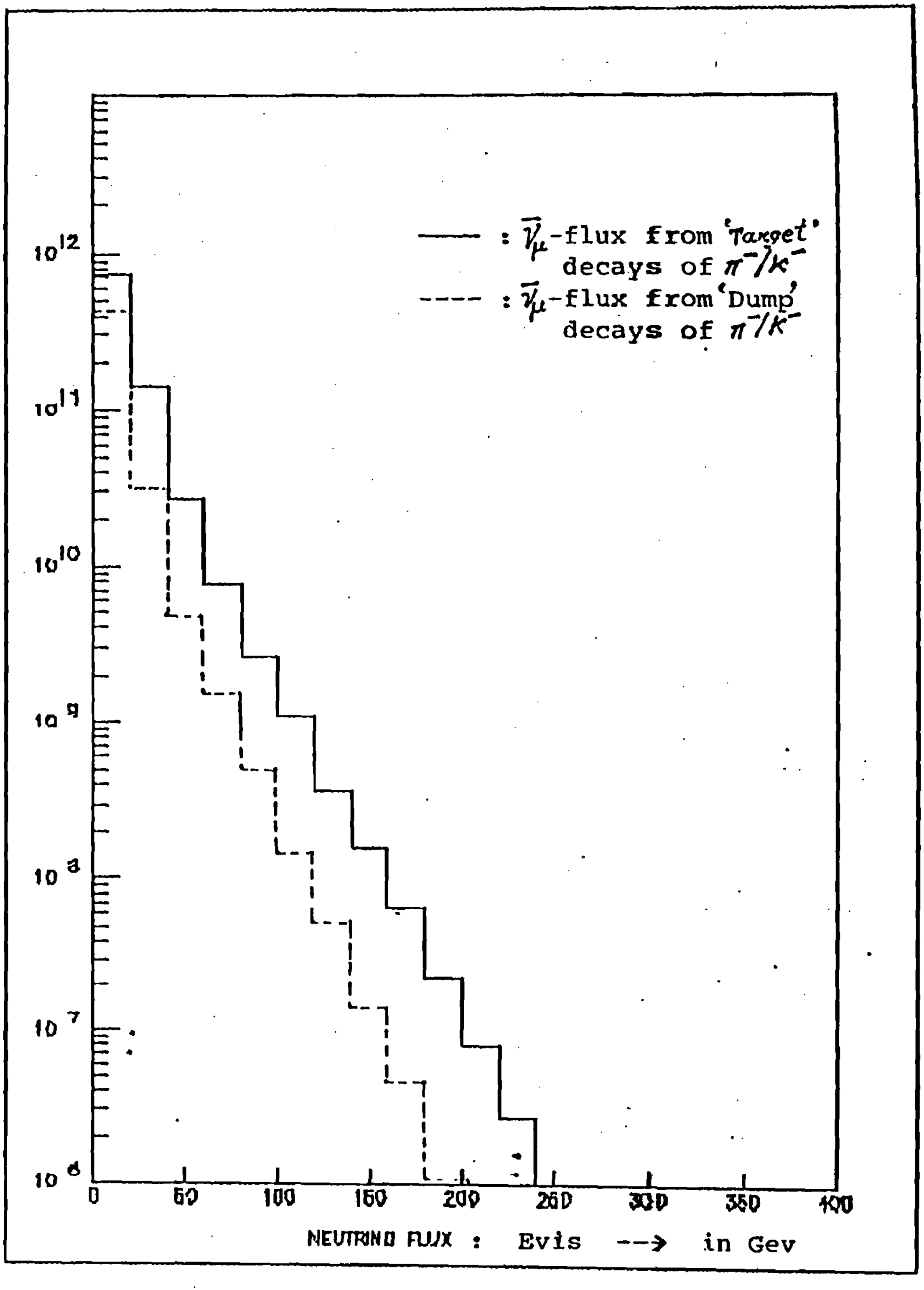

: $\bar{\nu}_\mu$-flux from 'Target' decays of π^-/K^-
: $\bar{\nu}_\mu$-flux from 'Dump' decays of π^-/K^-
10^{12}
10^{11}
10^{10}
10^{9}
10^{8}
10^{7}
10^{6}
0
50
100
150
200
250
300
350
400
NEUTRINO FLUX : Evis ---> in Gev

Fig. 5.2

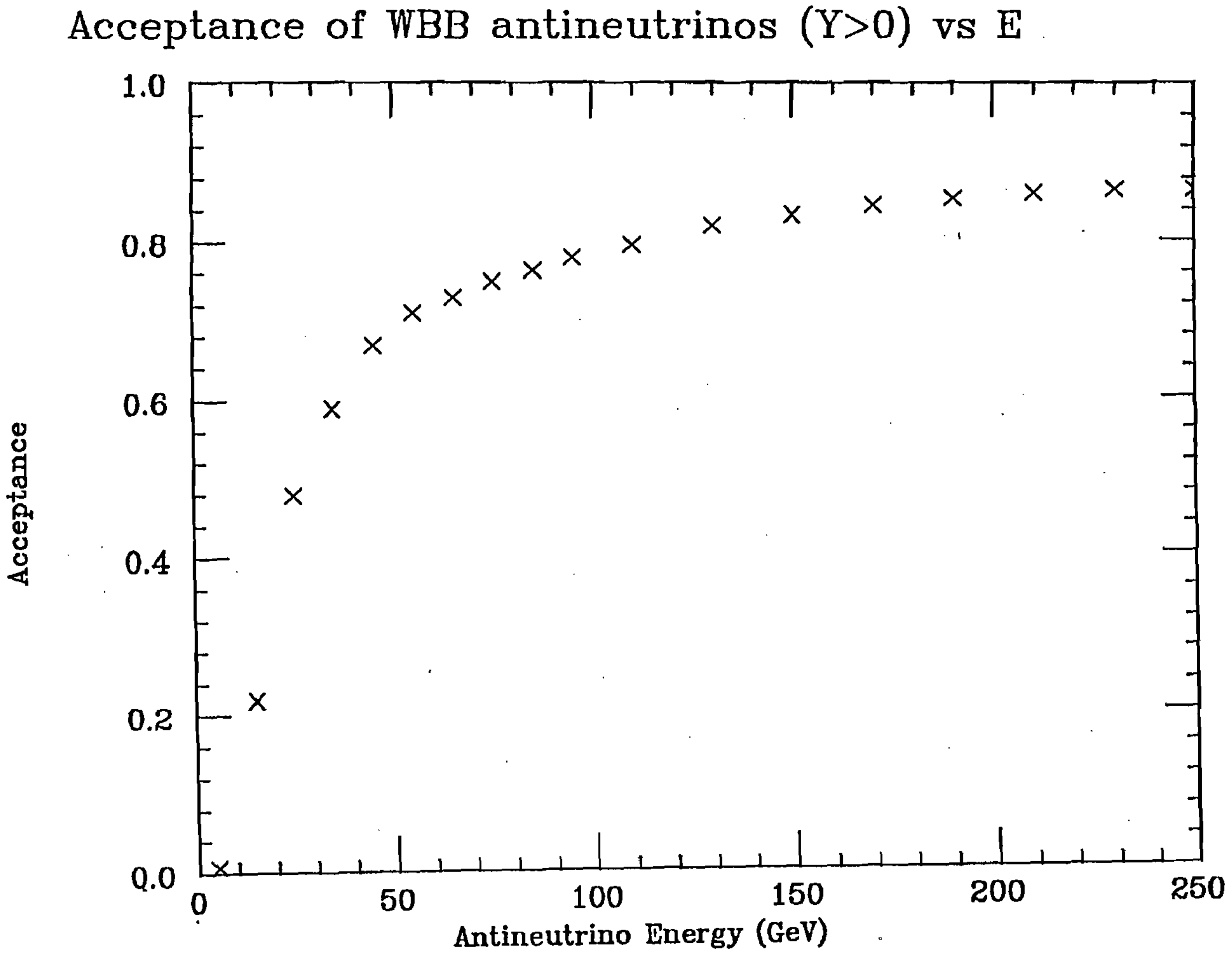
Acceptance of WBB antineutrinos (Y>0) vs E
1.0
0.8
0.6
0.4
0.2
0.0
Acceptance
0
50
100
150
200
250
Antineutrino Energy (GeV)

Fig. 5.3a

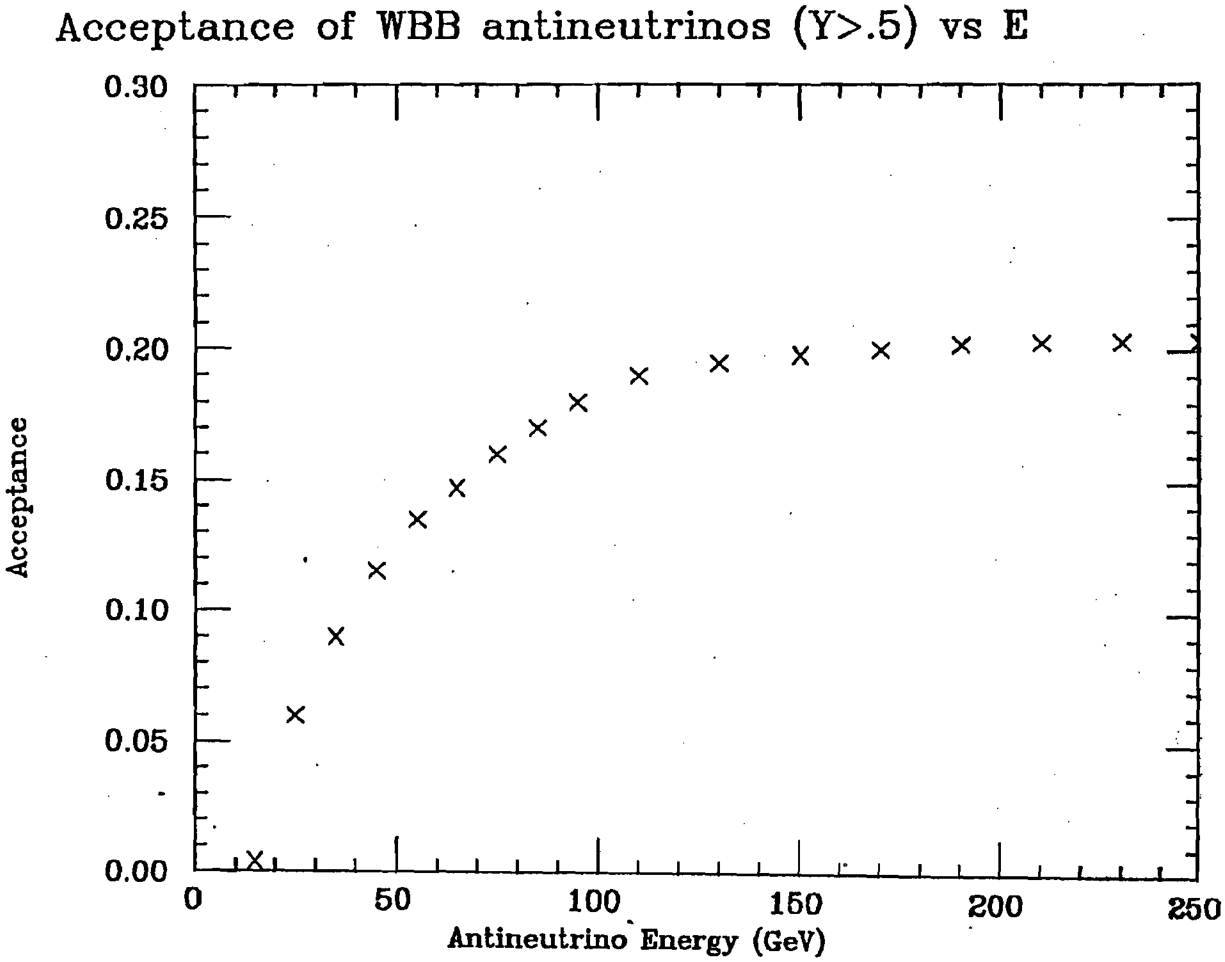
Acceptance of WBB antineutrinos (Y>.5) vs E
0.30
0.25
0.20
0.15
0.10
0.05
0.00
Acceptance
0
50
100
150
200
250
Antineutrino Energy (GeV)

Fig. 5.3b

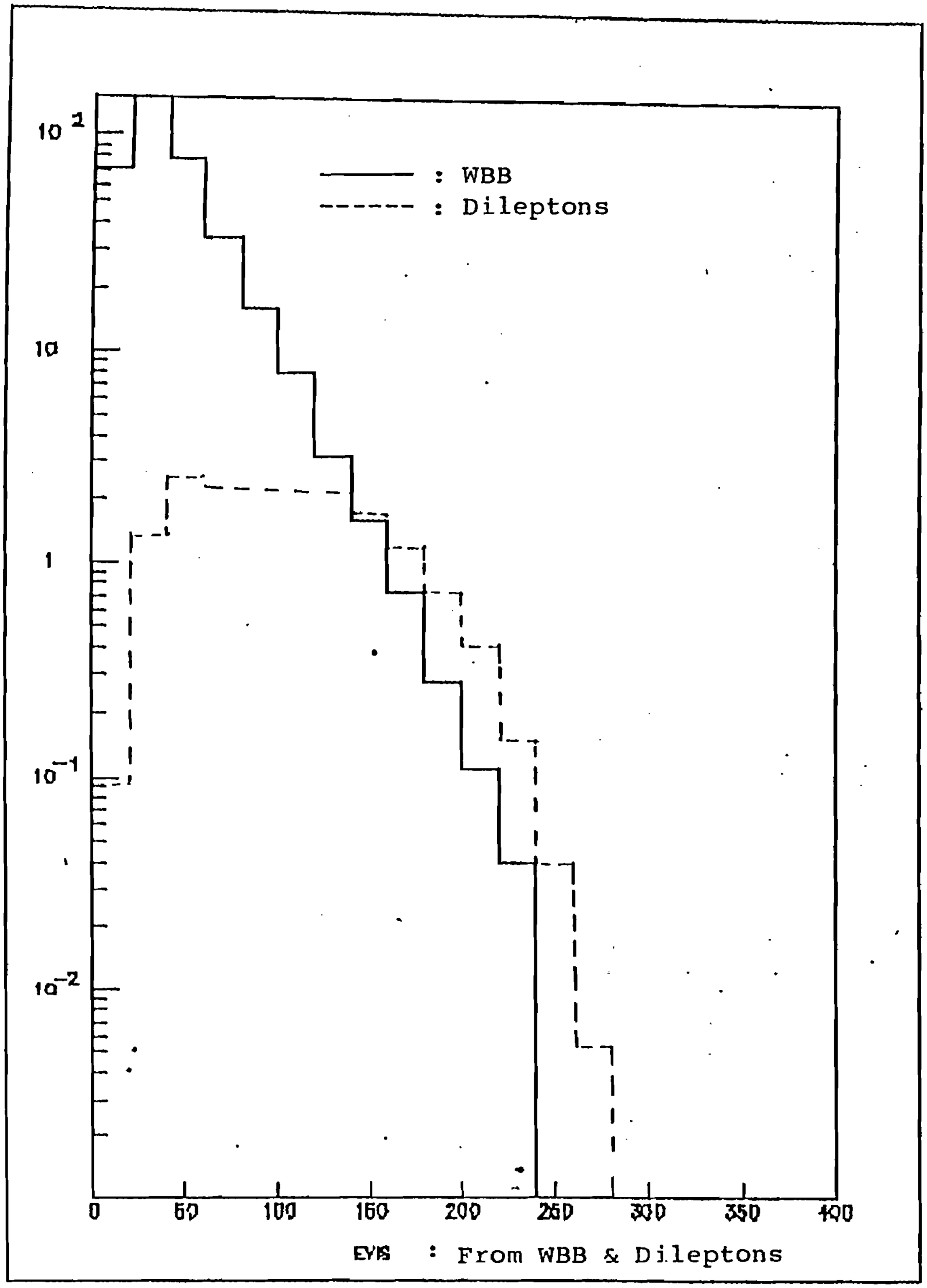
10 1
10
1
10⁻¹
10⁻²
: WBB
: Dileptons
0
50
100
150
200
250
300
350
400
EVIS : From WBB & Dileptons

Fig. 5.4a

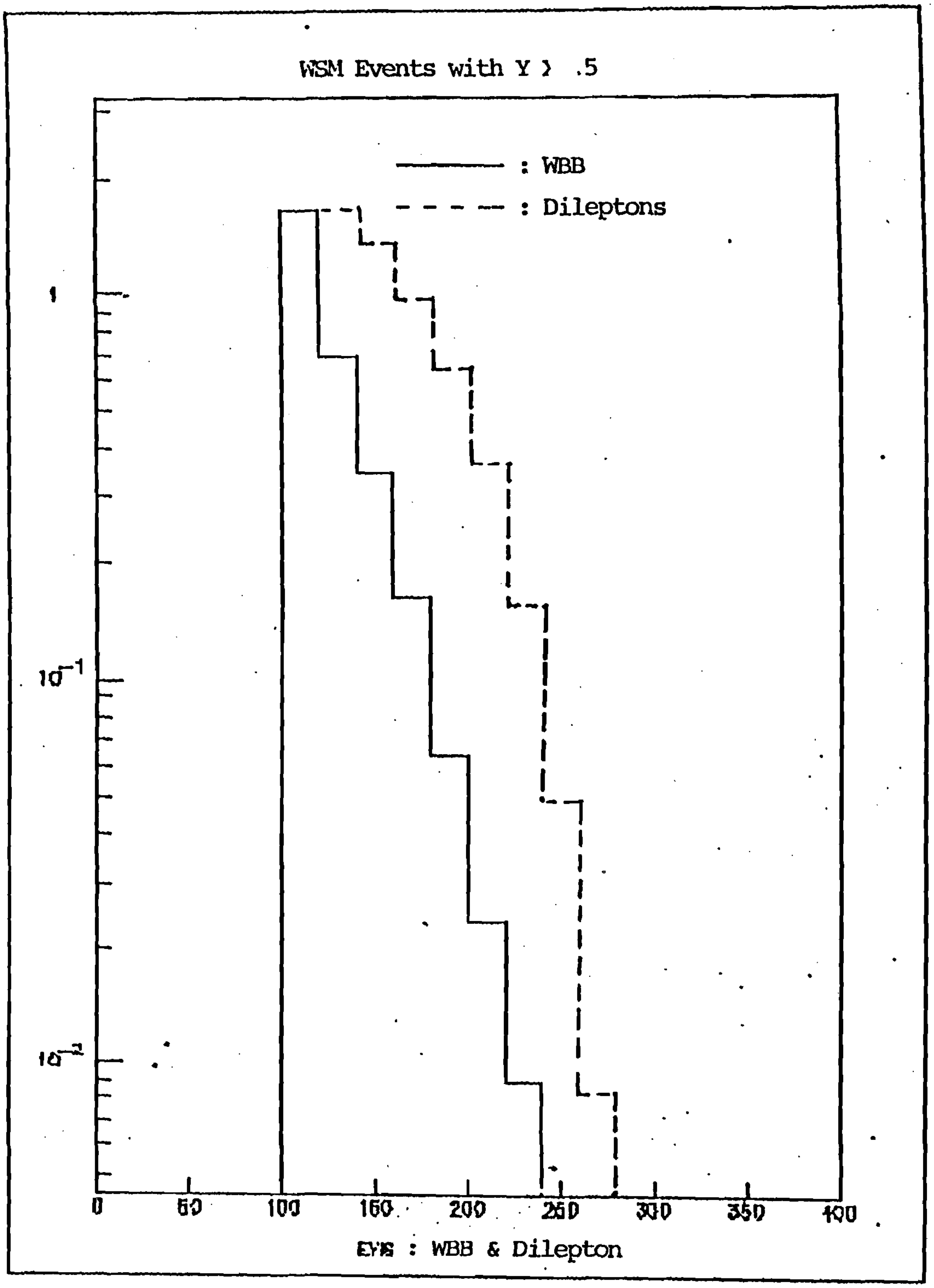
WSM Events with Y > .5
: WBB
: Dileptons
1
10^{-1}
10^{-2}
0
50
100
150
200
250
300
350
400
EVIS : WBB & Dilepton

Fig. 5.4b

Fig. 5.5

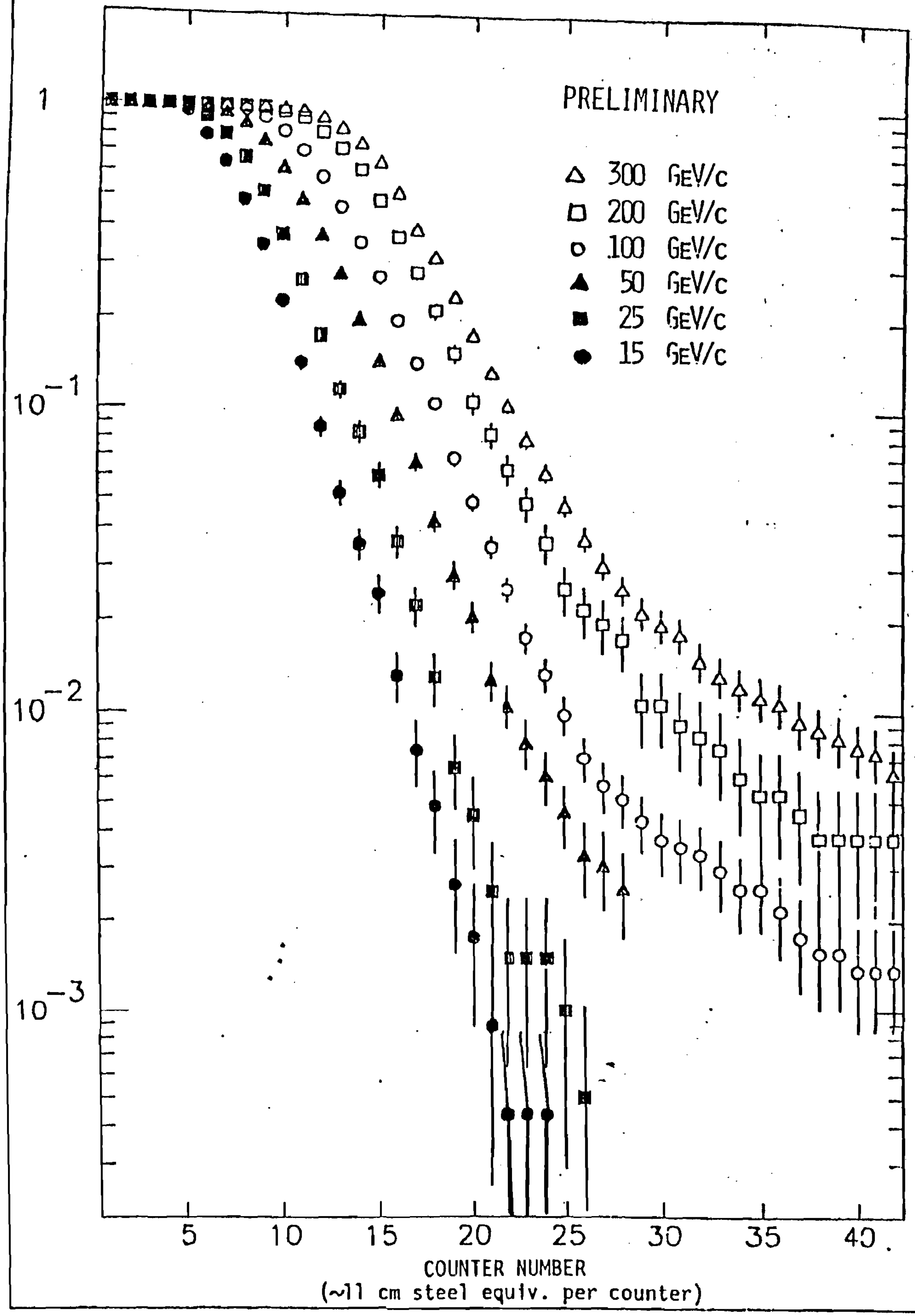
PRELIMINARY
△ 300 GeV/c
□ 200 GeV/c
○ 100 GeV/c
▲ 50 GeV/c
■ 25 GeV/c
● 15 GeV/c
1
10⁻¹
10⁻²
10⁻³
5
10
15
20
25
30
35
40
COUNTER NUMBER
(~11 cm steel equiv. per counter)

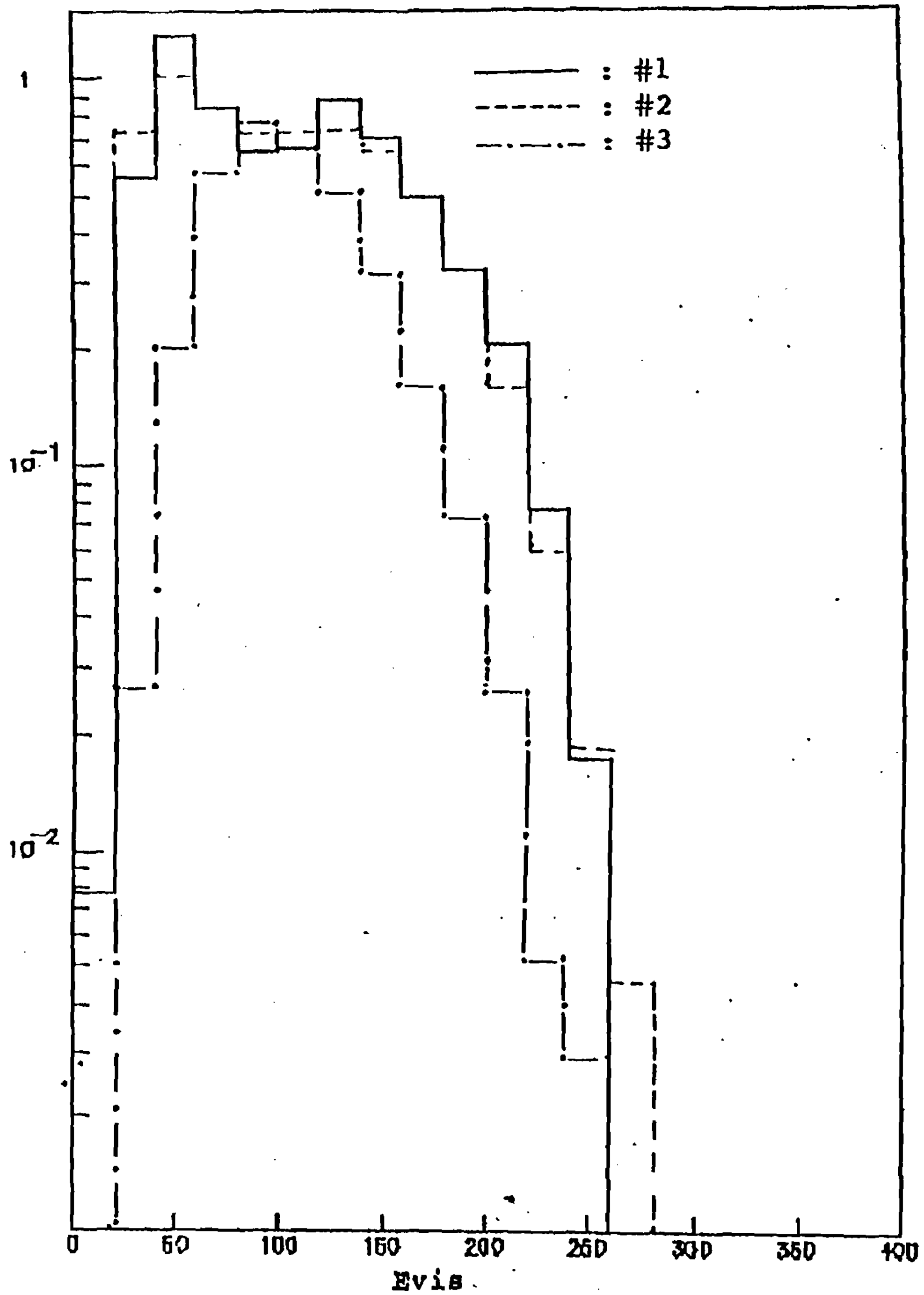

For #1, OSDM with μ^- missing, #2 NC induced π^+/K^+ decay & #3 KE3 induced $e^-\mu^+$

Fig. 5.6

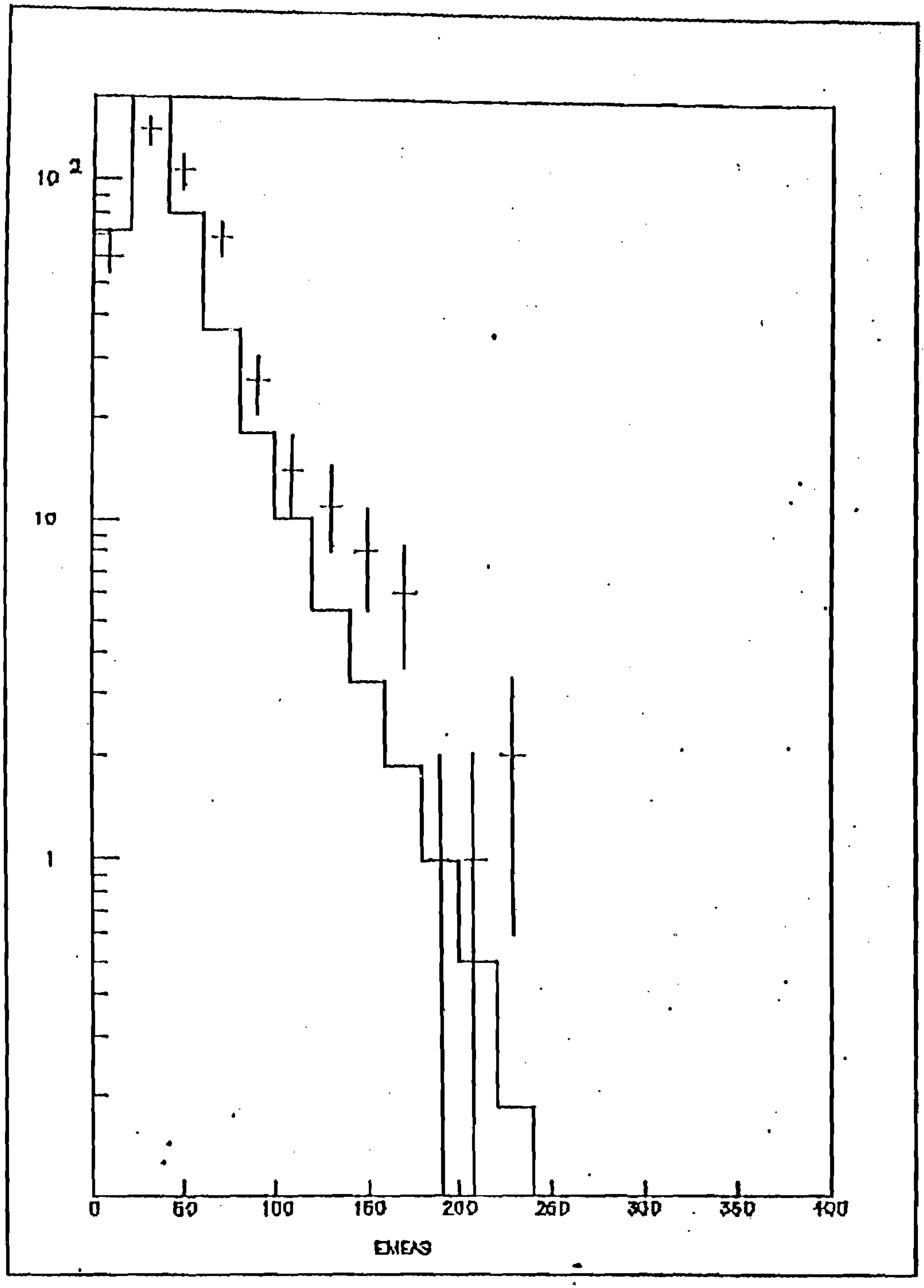

Fig.6.1a

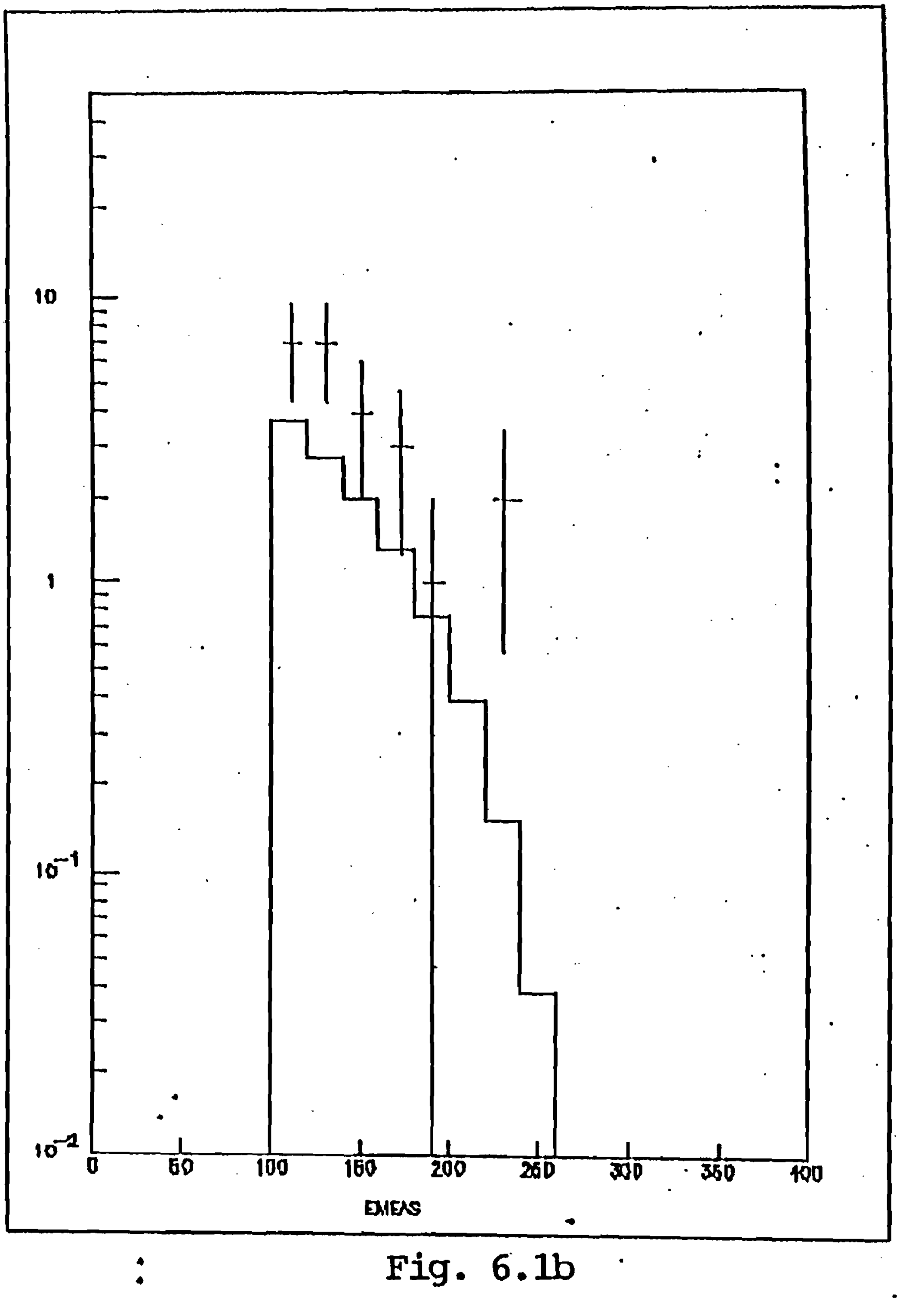

Fig. 6.1b

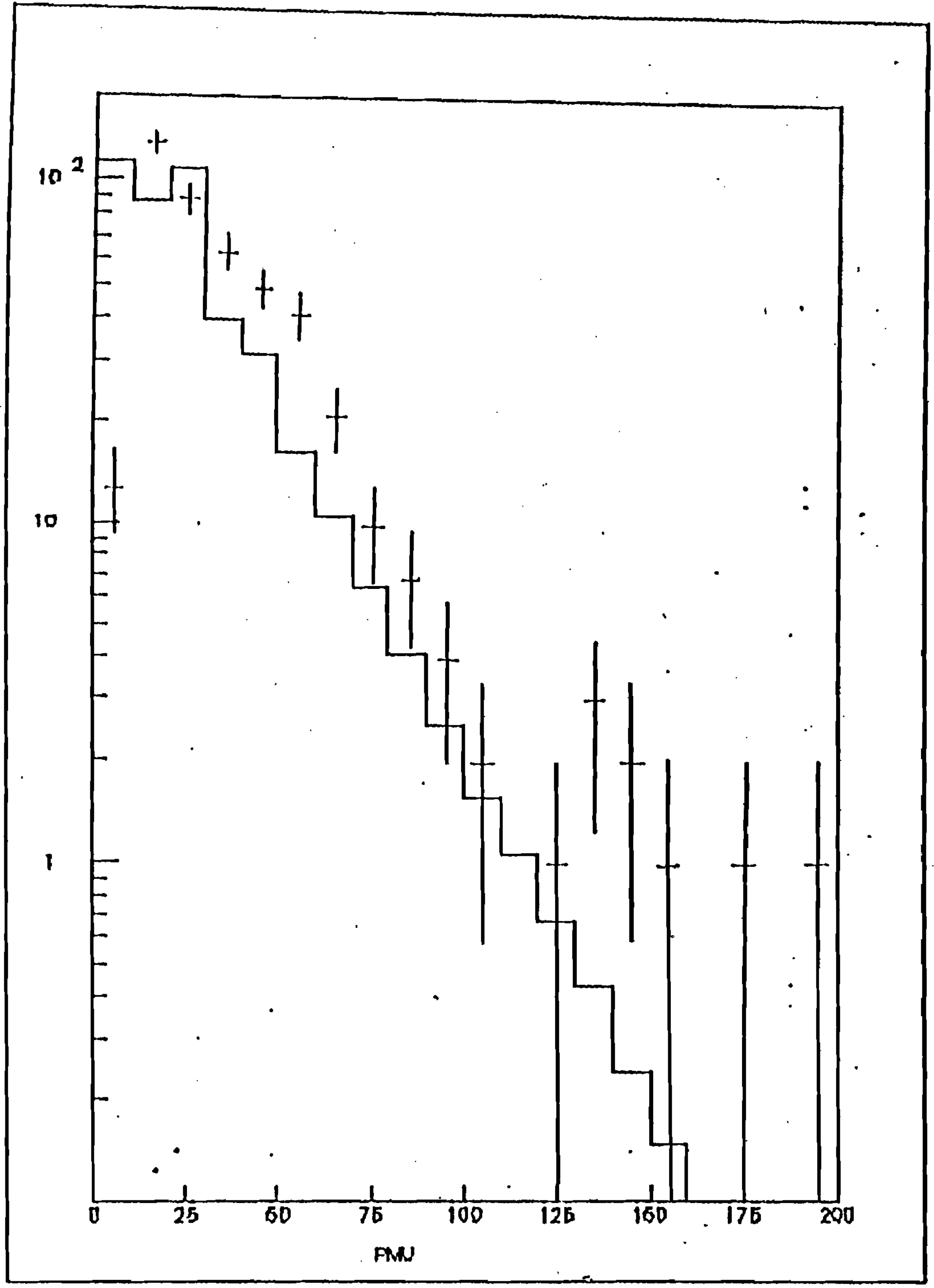

Fig. 6.2a

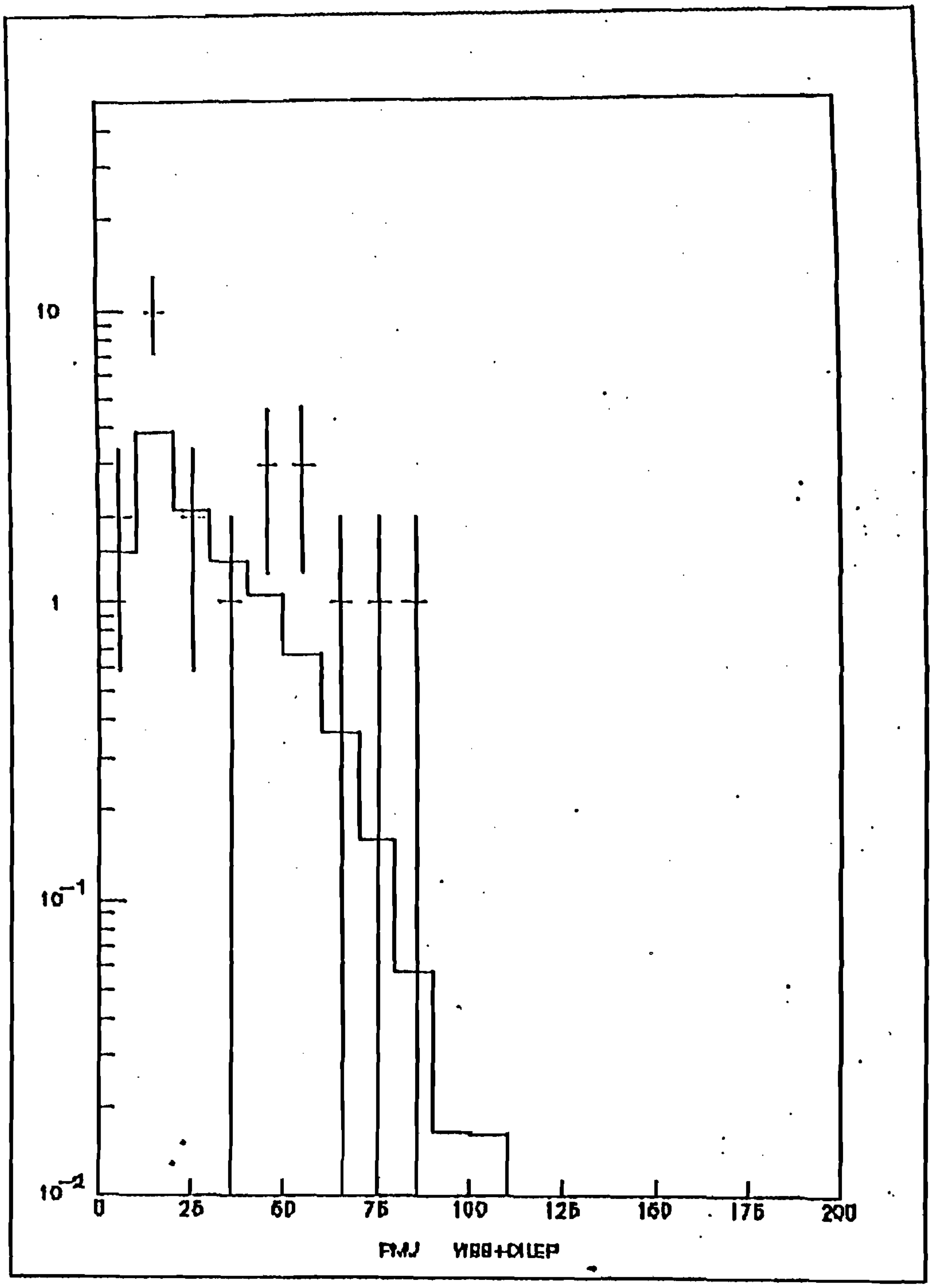

Fig. 6.2b

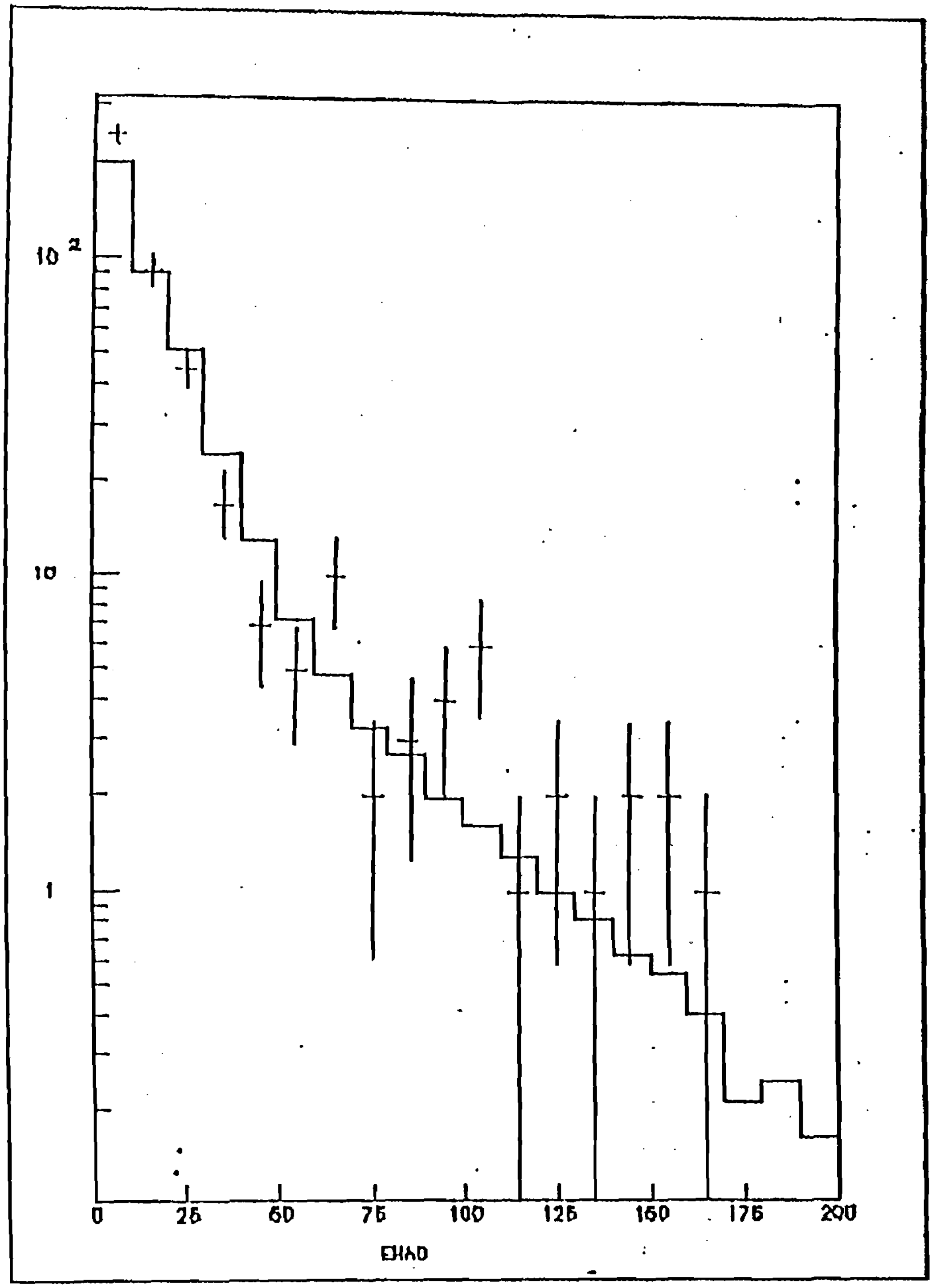

Fig. 6.3a

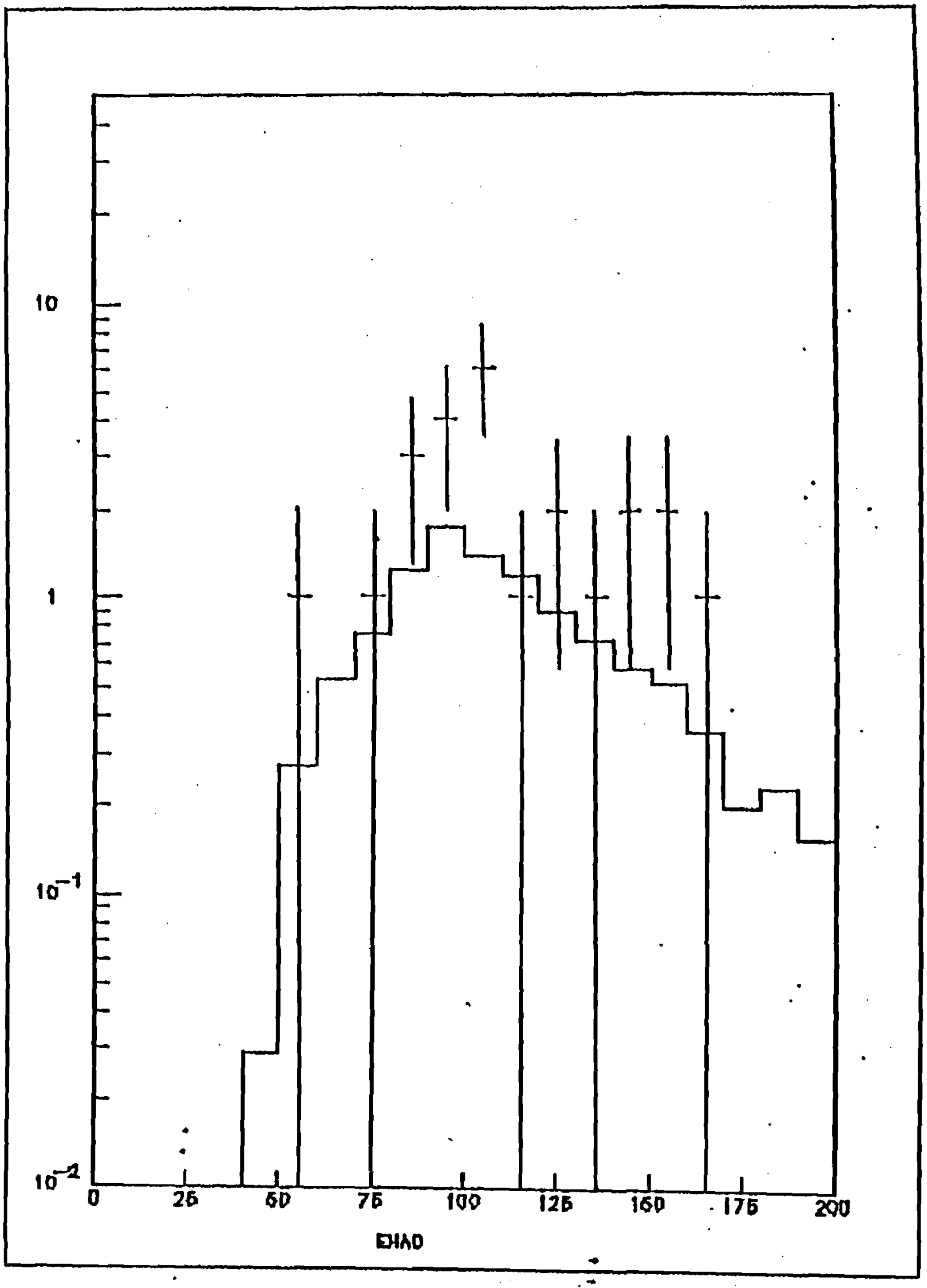

Fig. 6.3b

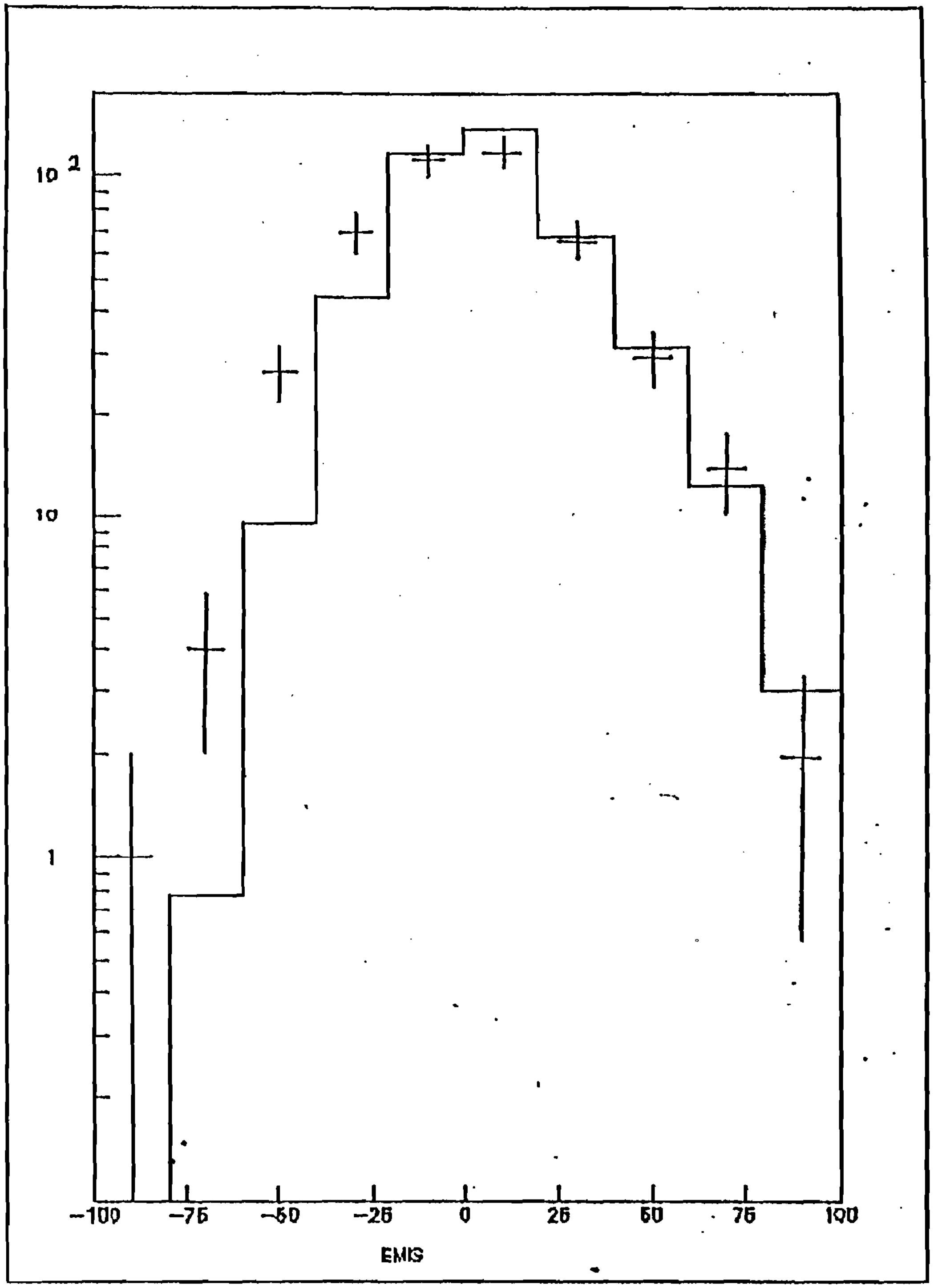

Fig. 6.4a

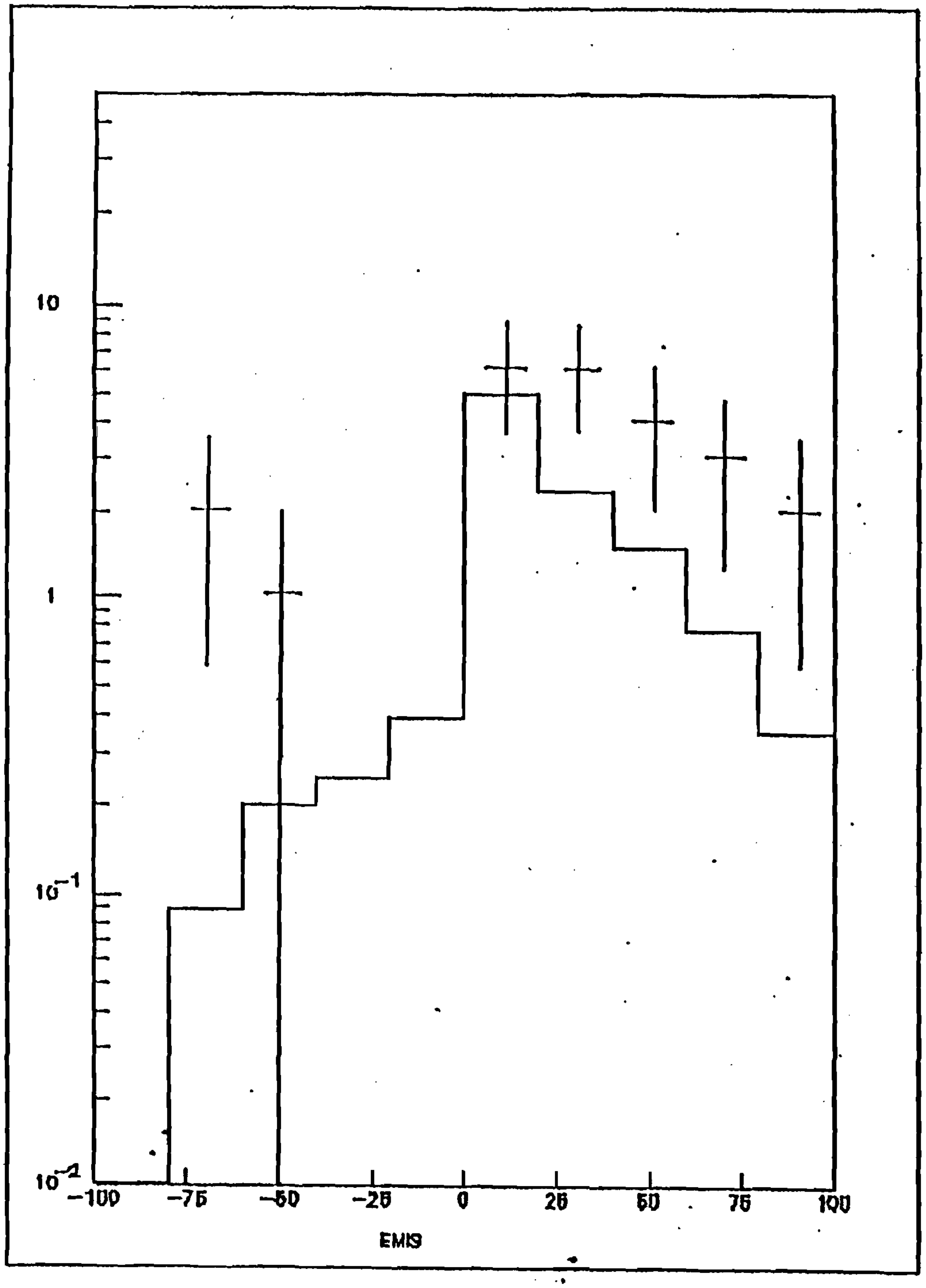

Fig. 6.4b

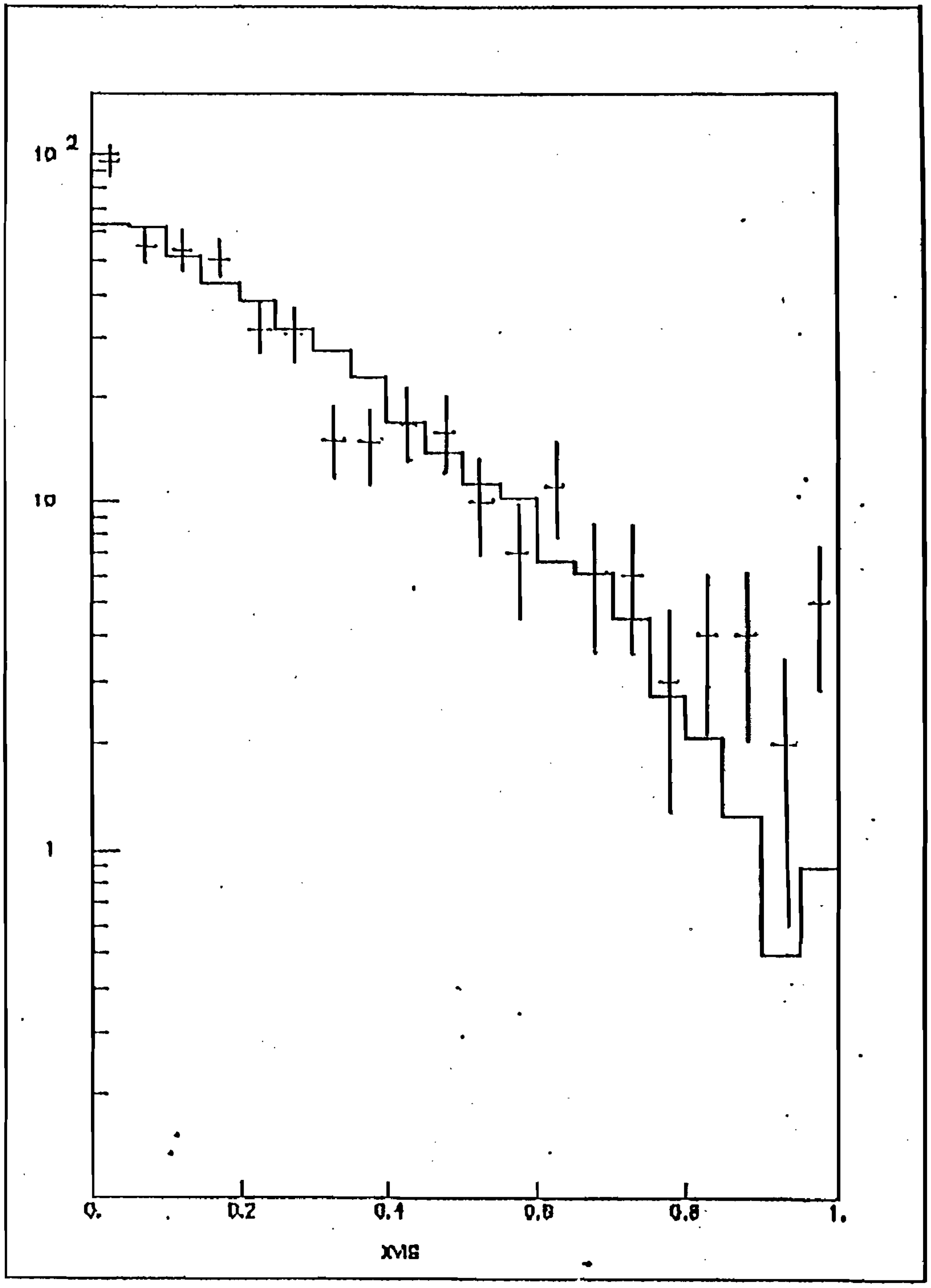

Fig. 6.5a

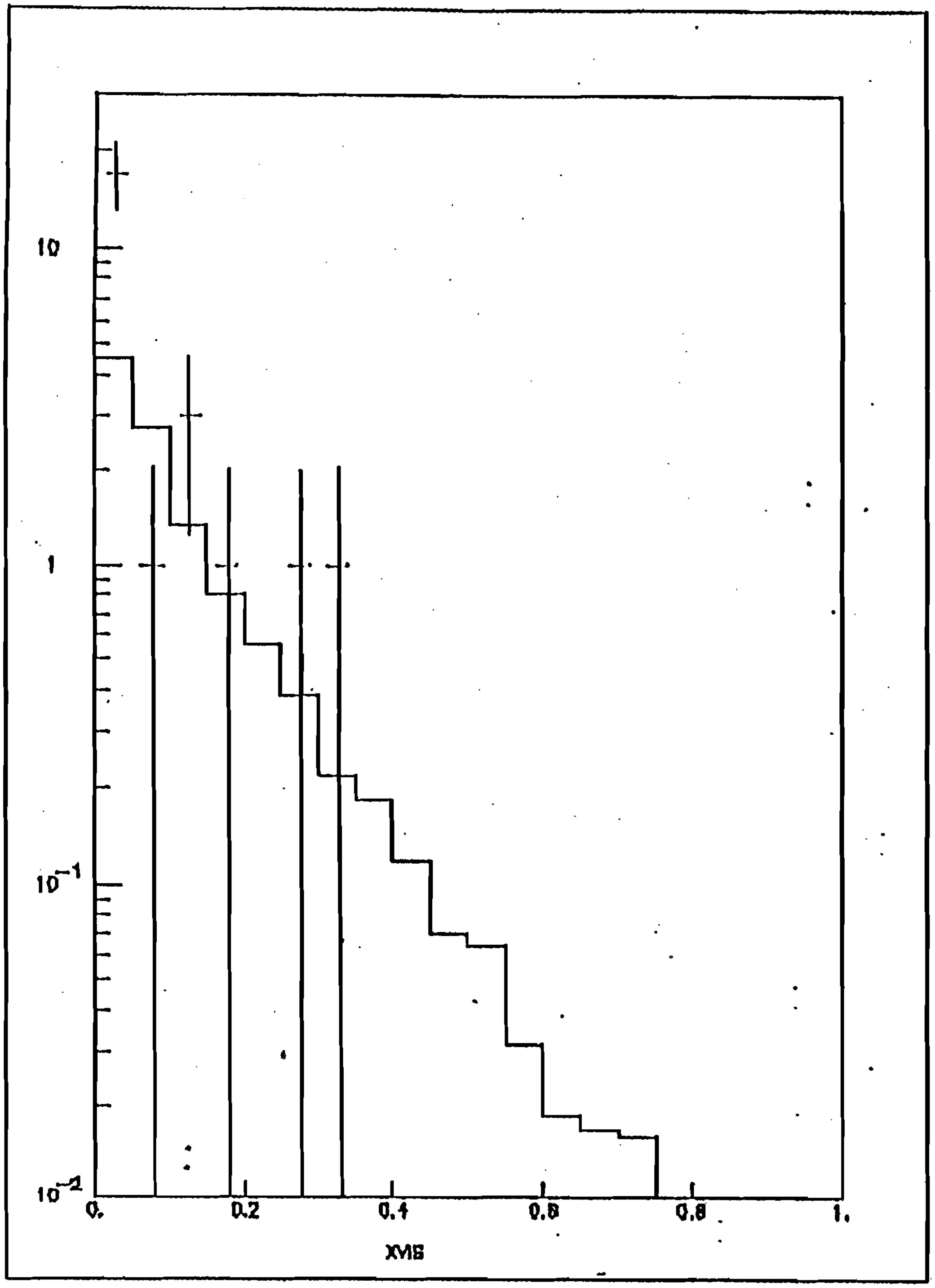

Fig. 6.5b

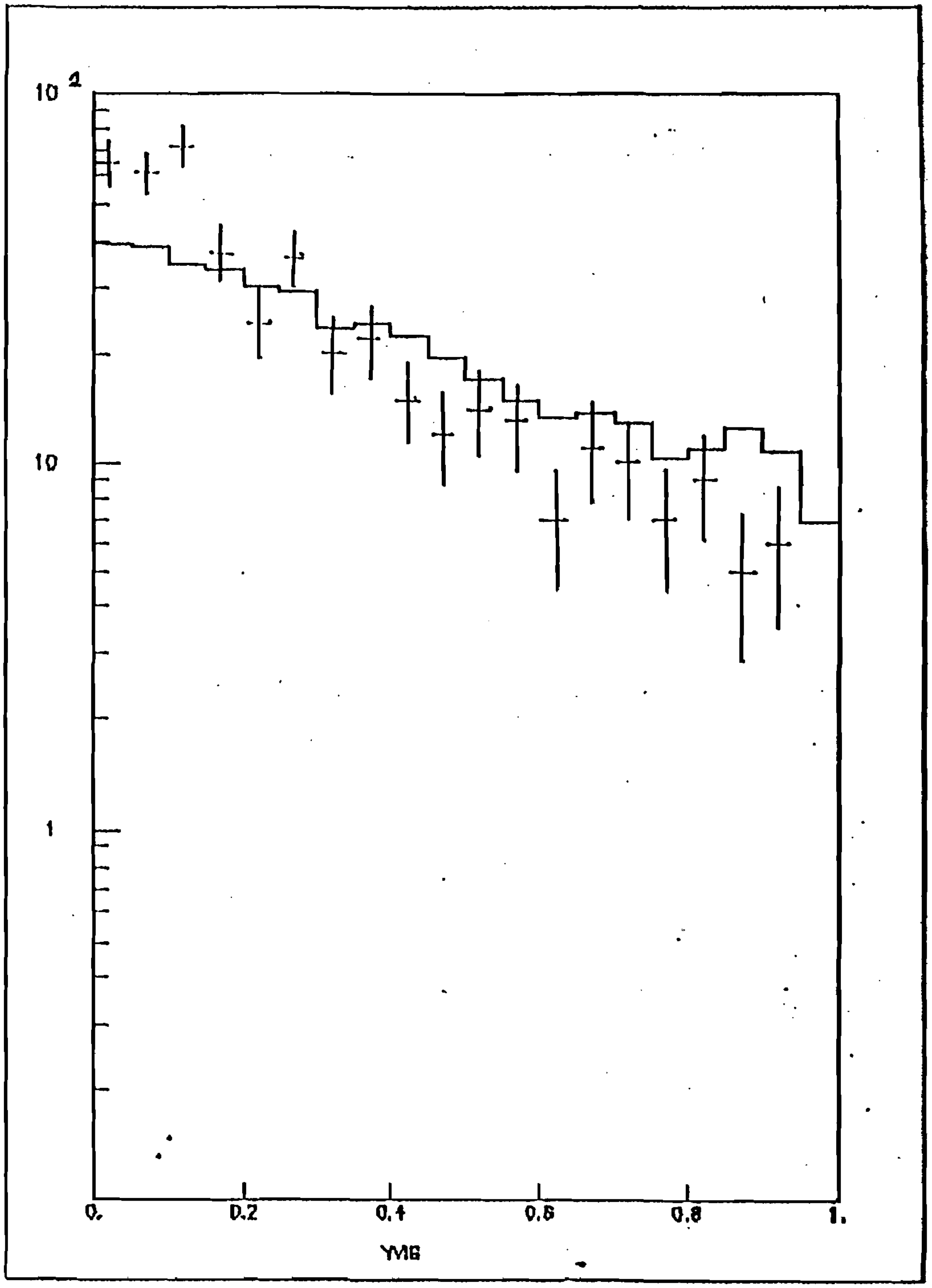

Fig. 6.6a

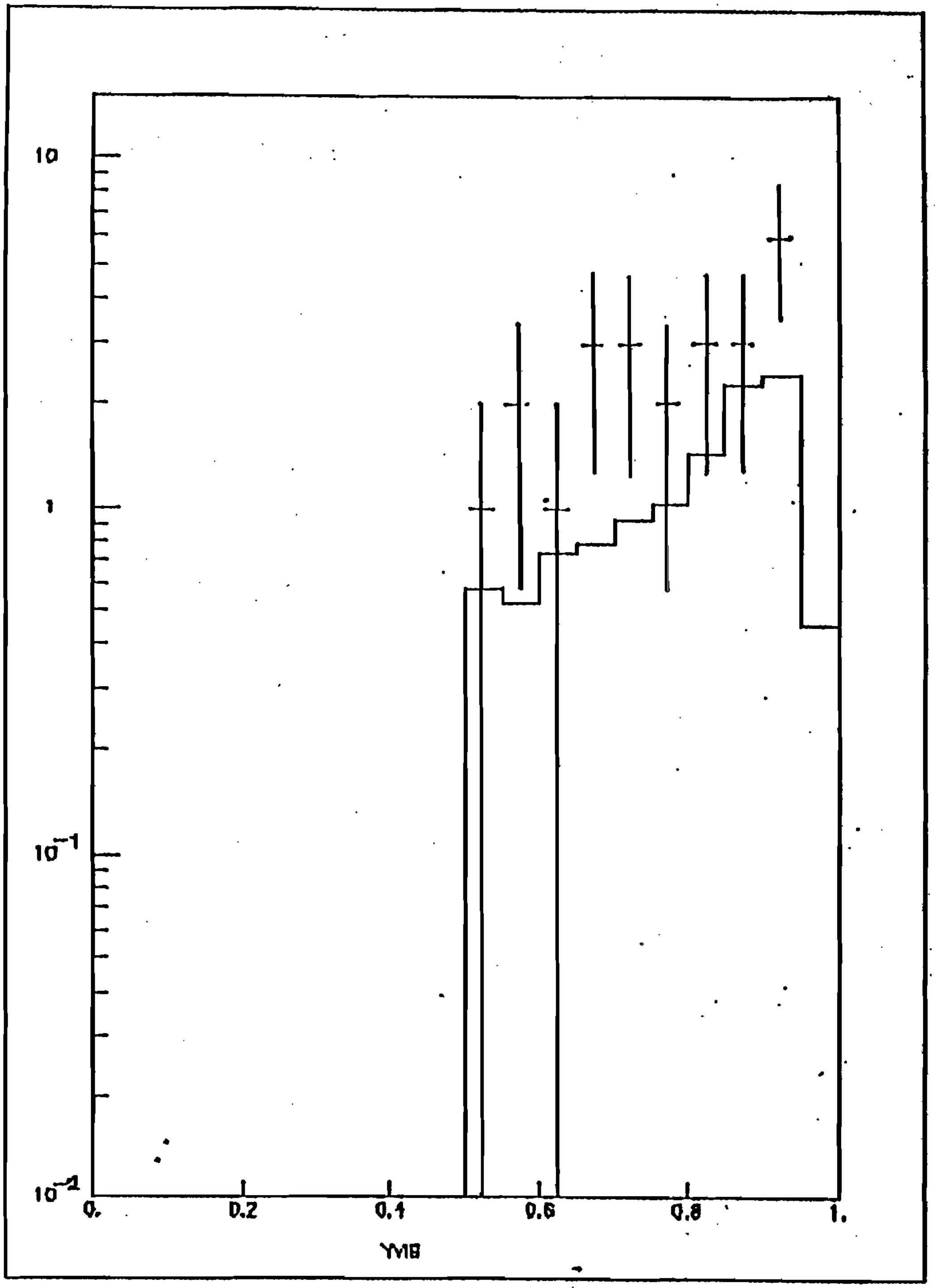

Fig. 6.6b

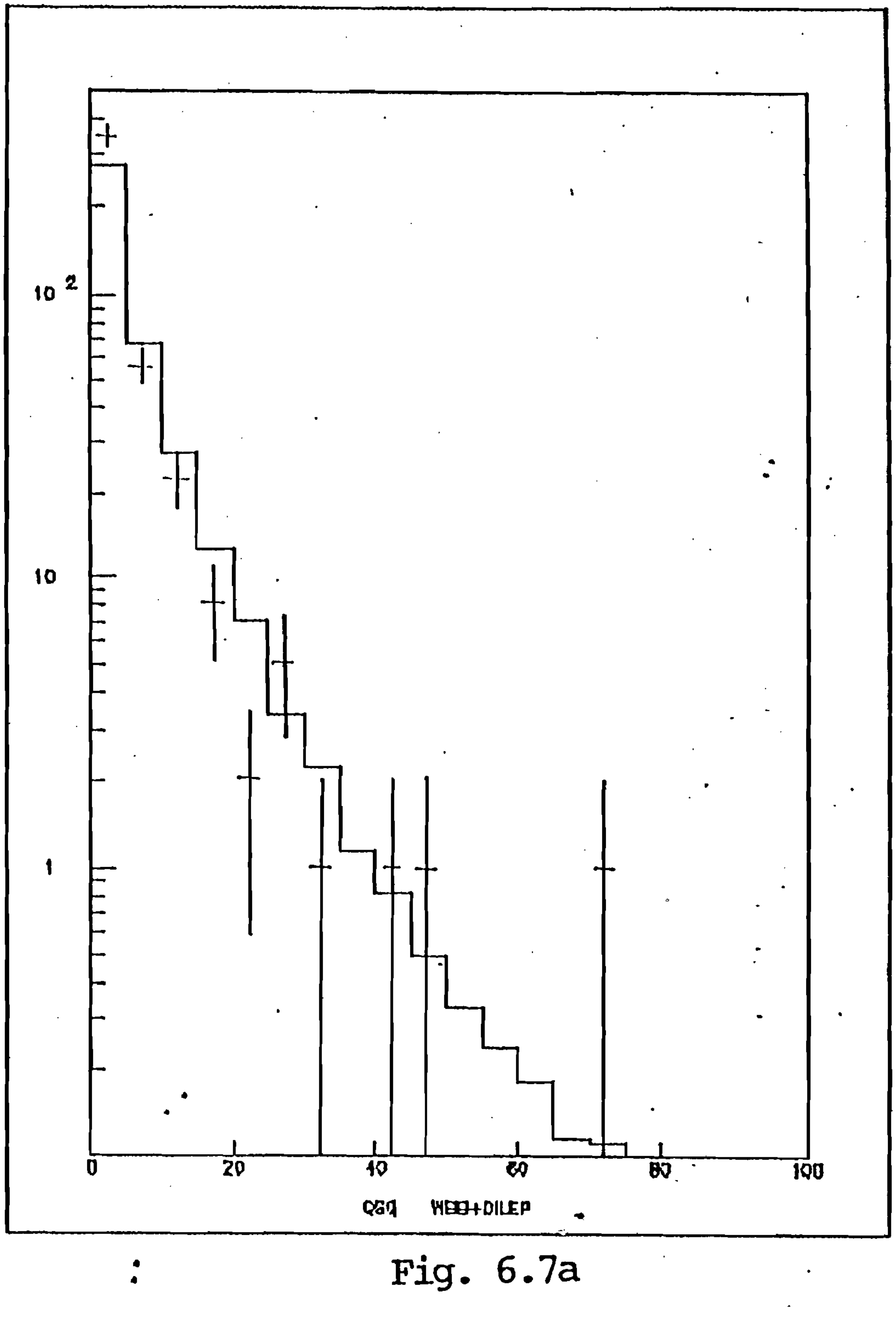

Fig. 6.7a

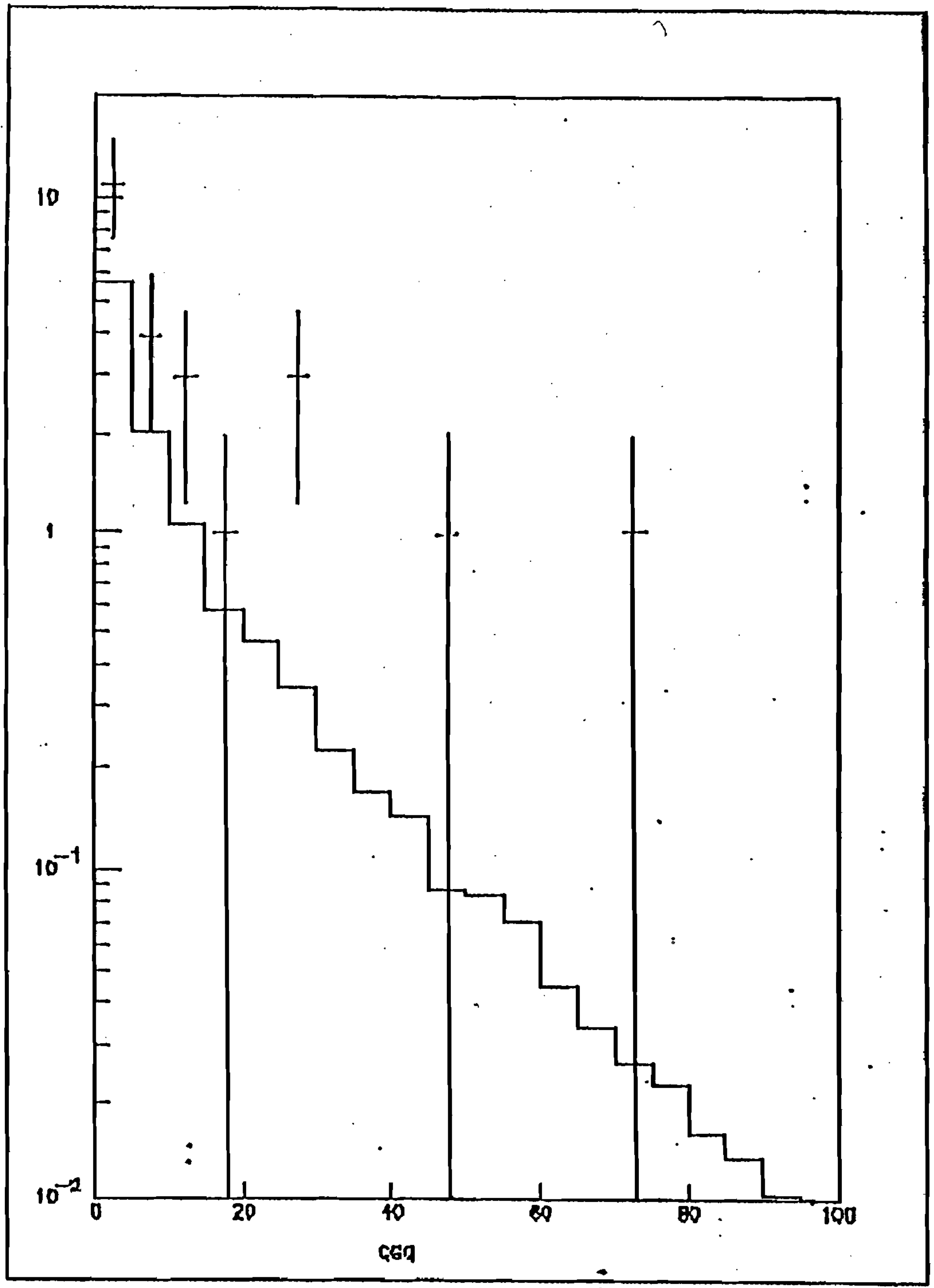

Fig. 6.7b

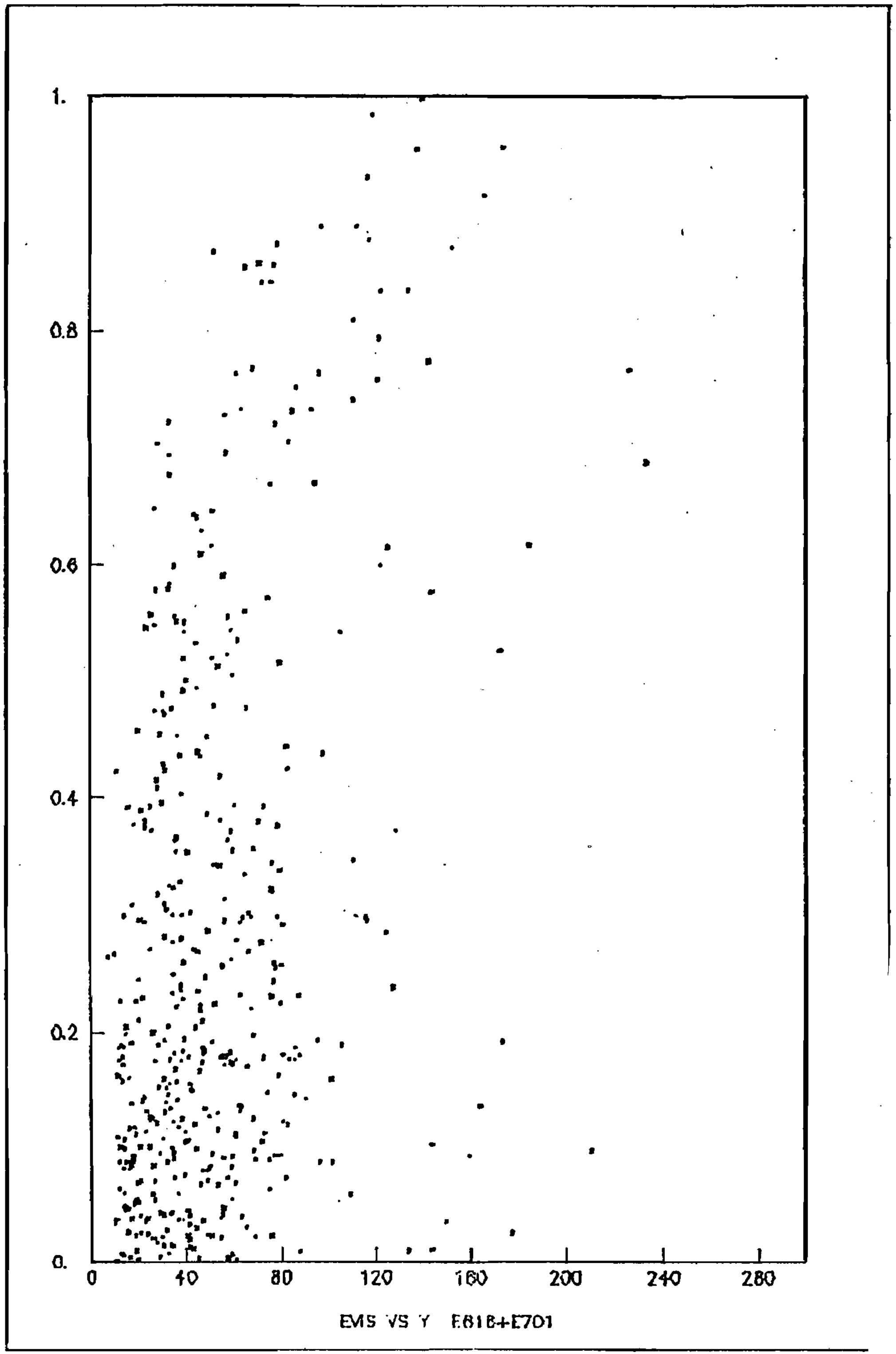

Fig. 6.8

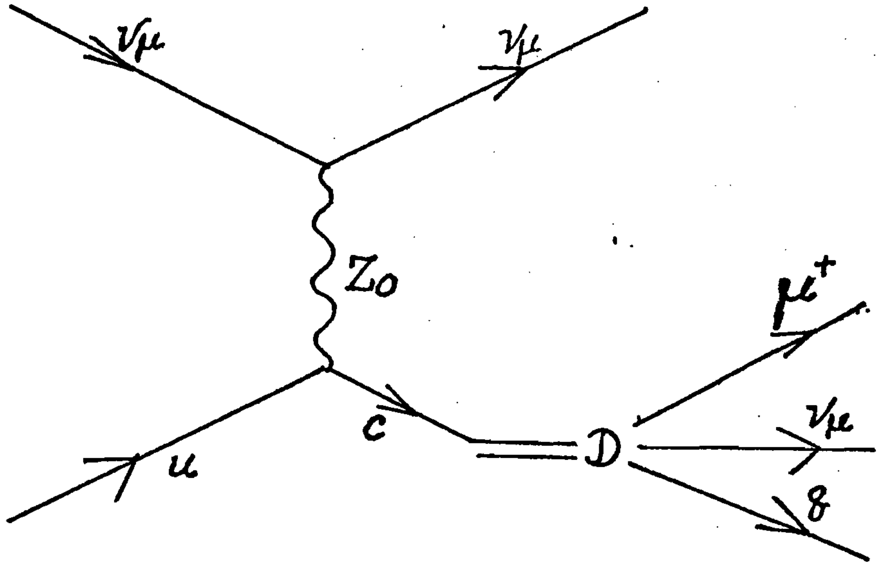

Fig. 6.9a: Flavour changing Neutral Current giving rise to a WSM.

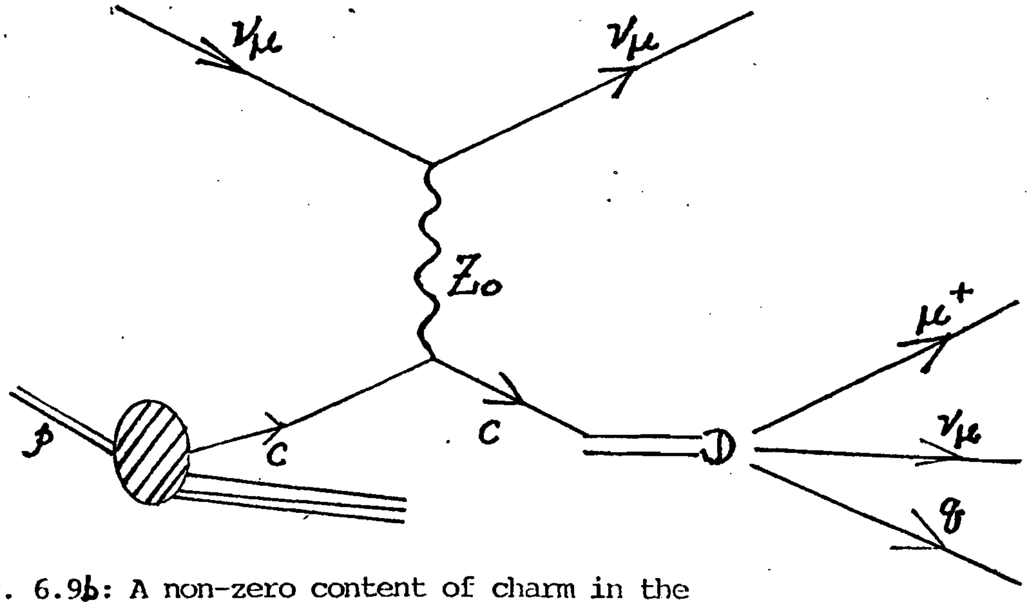

Fig. 6.9b: A non-zero content of charm in the nucleon quark-antiquark sea may produce a WSM in a neutral current interaction.

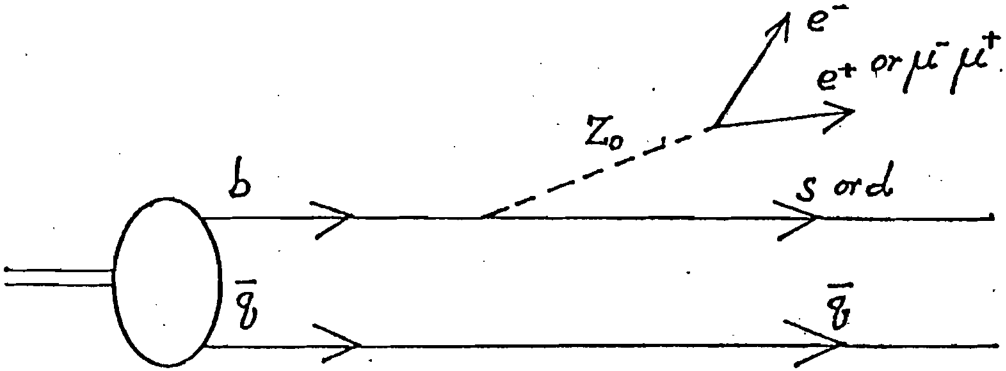

Fig. 6.10 : Flavour Changing Neutral Current Decay of Bottom Meson

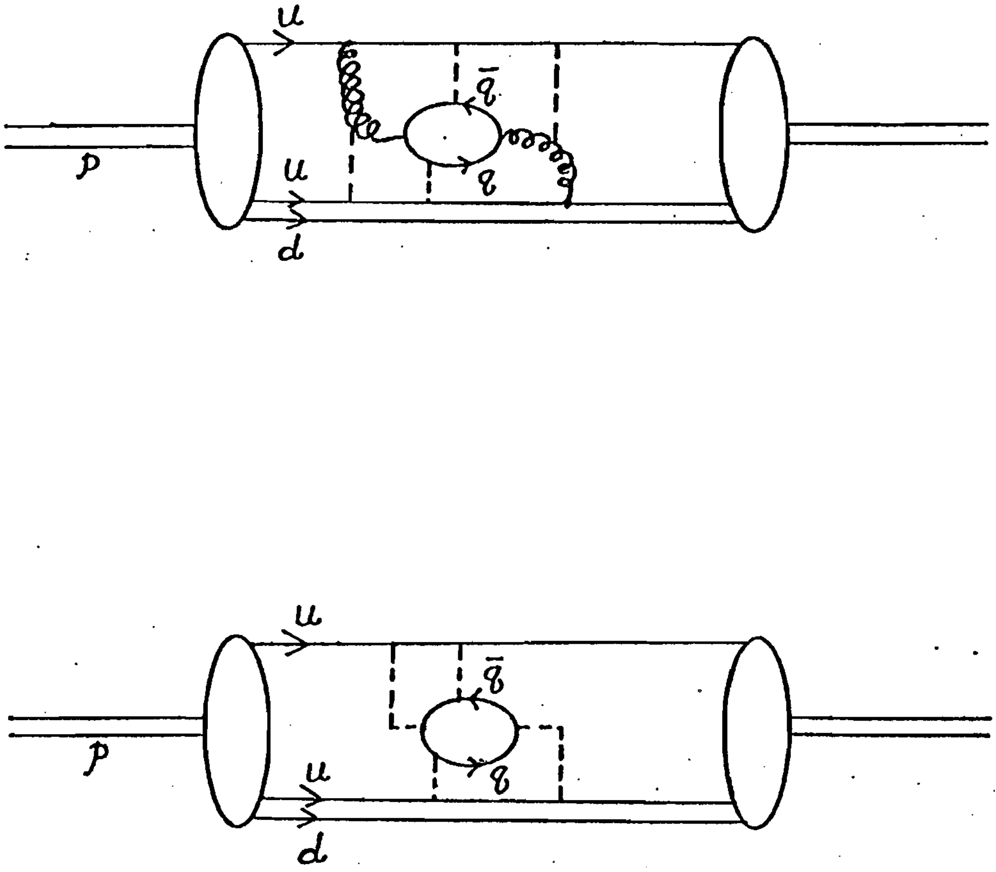

Fig. 6.11: Heavy Flavour Production in the nucleon Sea. The curly and the dashed lines represent the transeverse and the logitudinal gluons respectively.

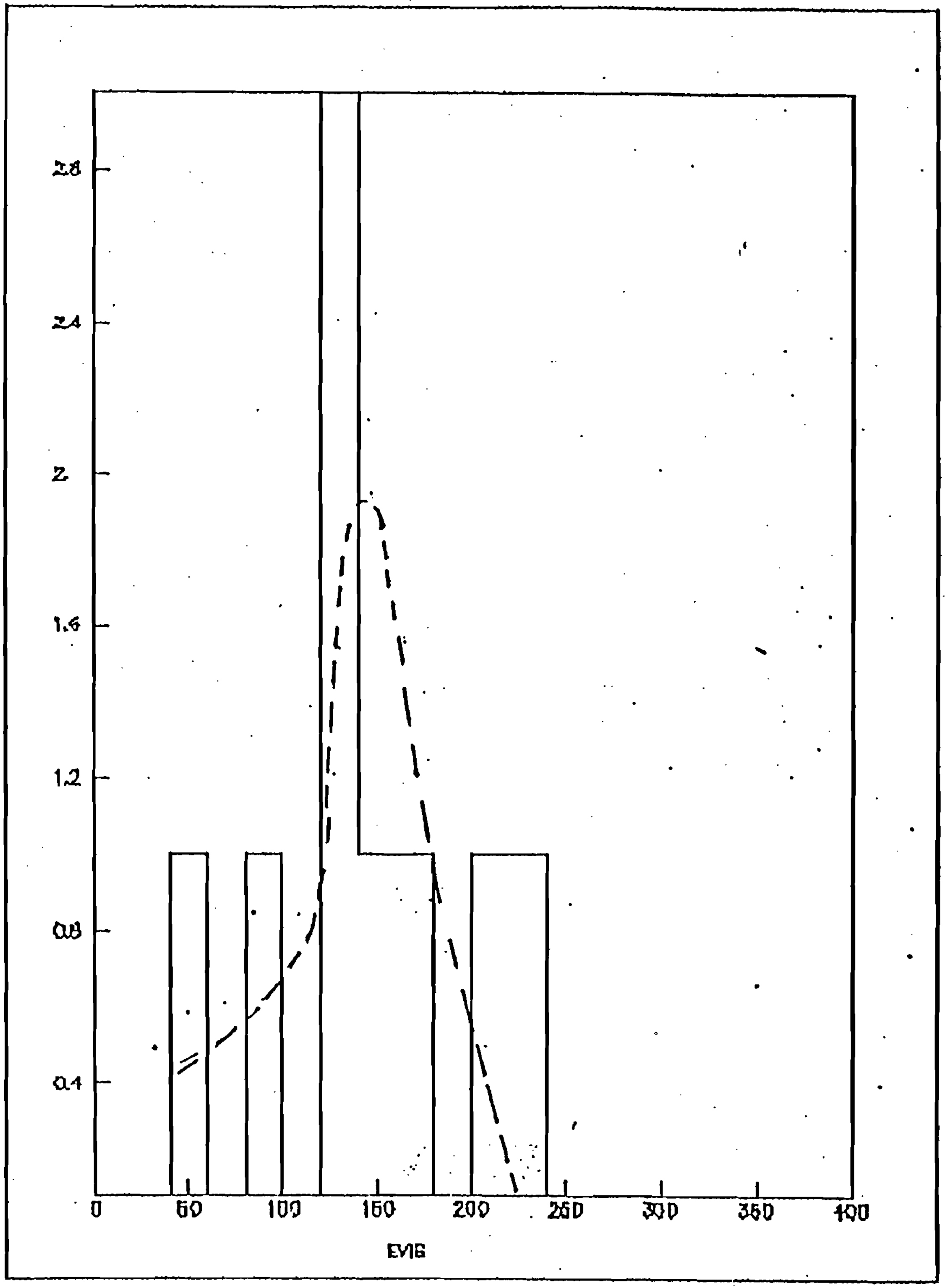

Fig. 7.1a : Evis Distribution of Trimuon events (solid line) and the background (broken line).

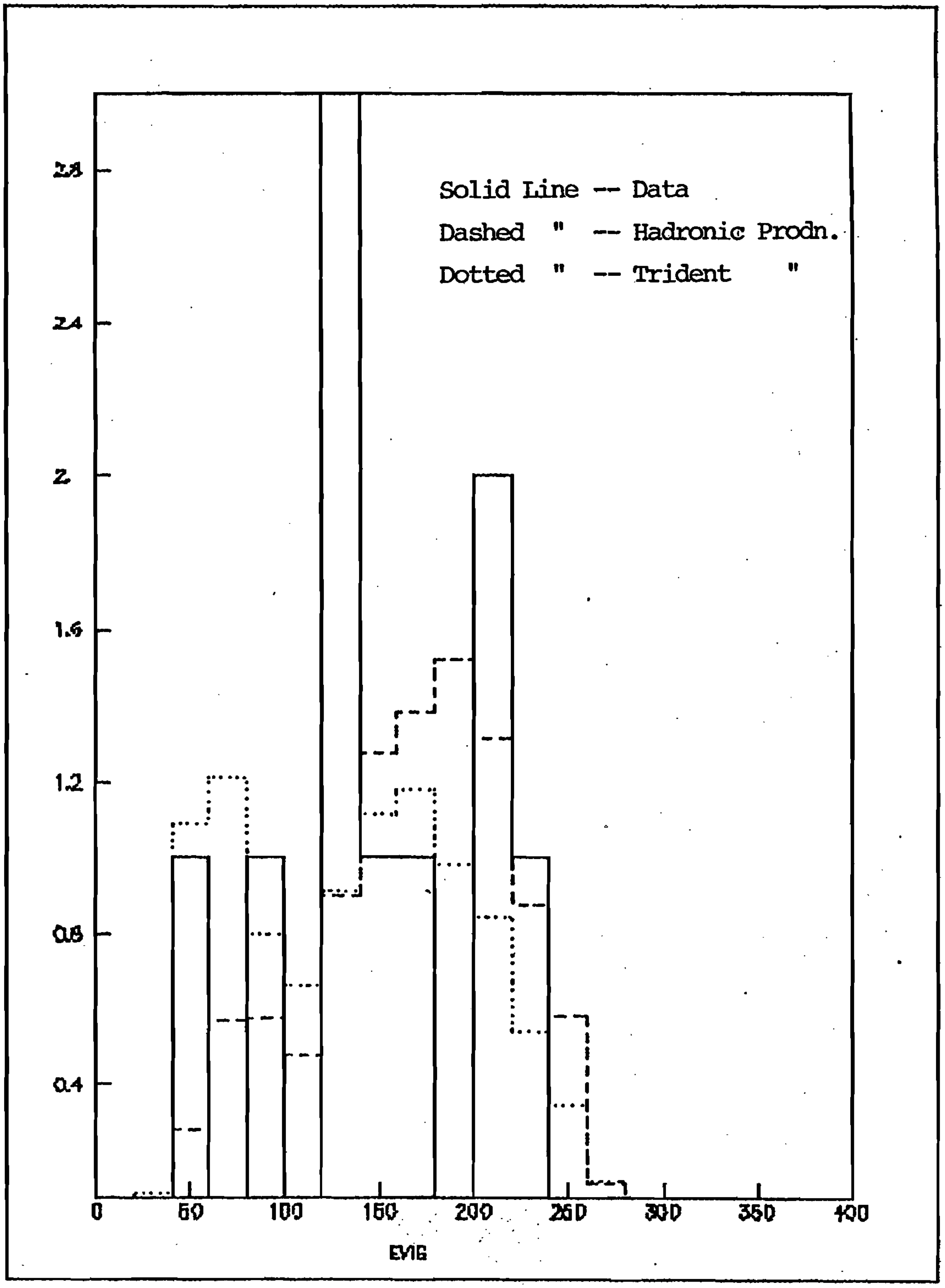

Fig. 7.1b : Total Visible Energy of the data vs the two Models

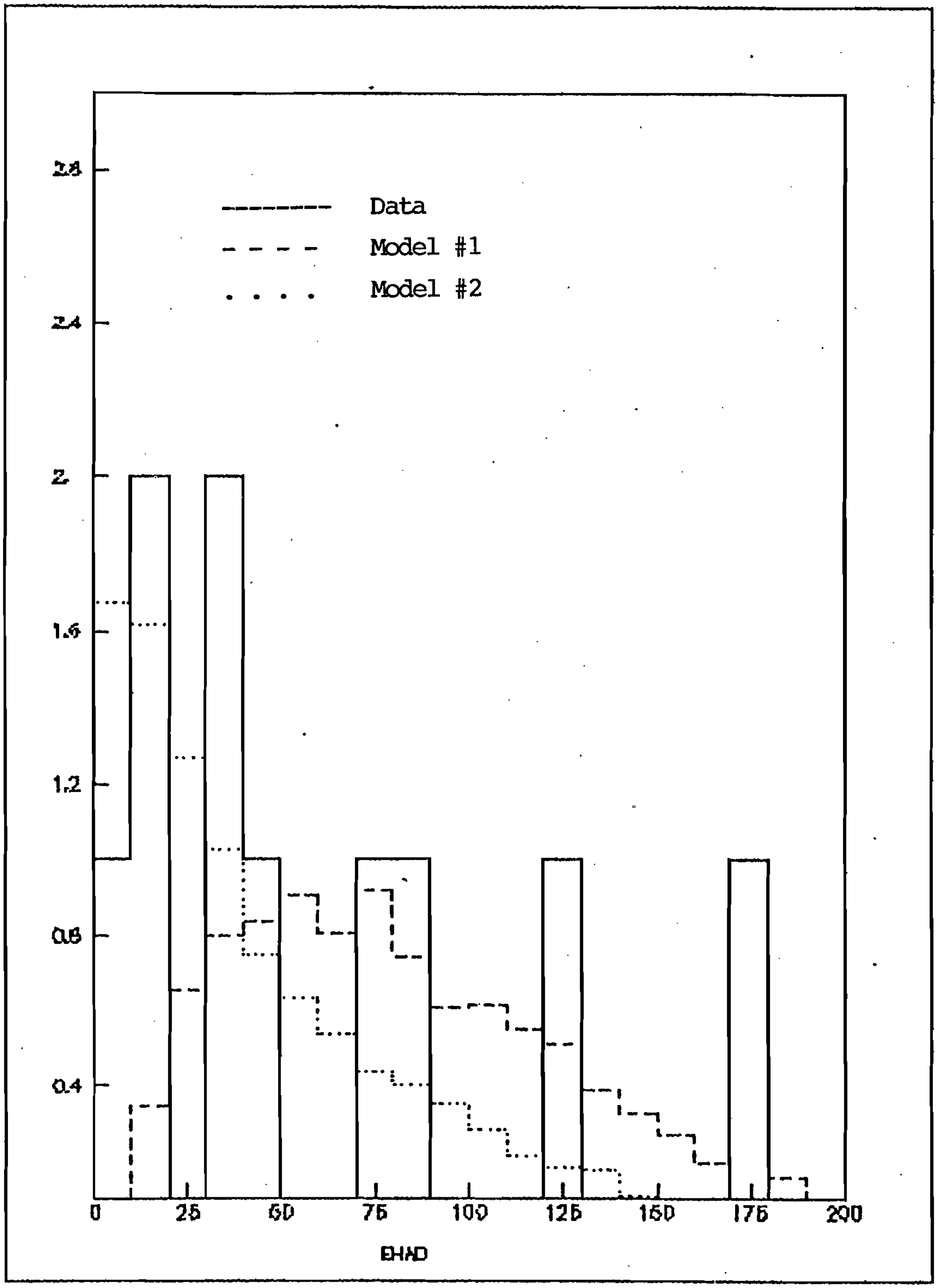

Fig. 7.1c : Hadron Energy Distribution

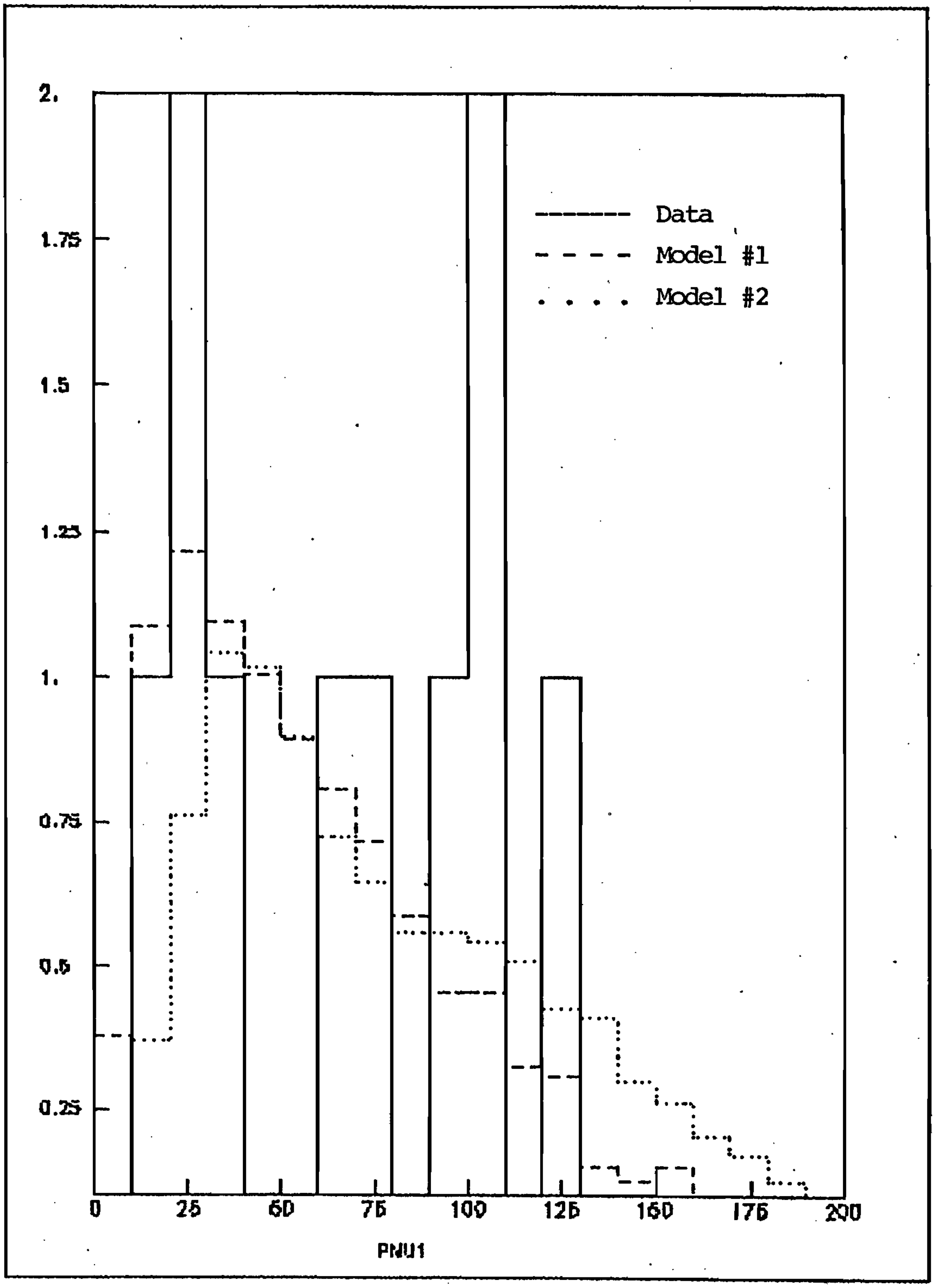

Fig. 7.2a : Momentum of the Leading Muon or 'PMU1'

PMU2 and PMU3

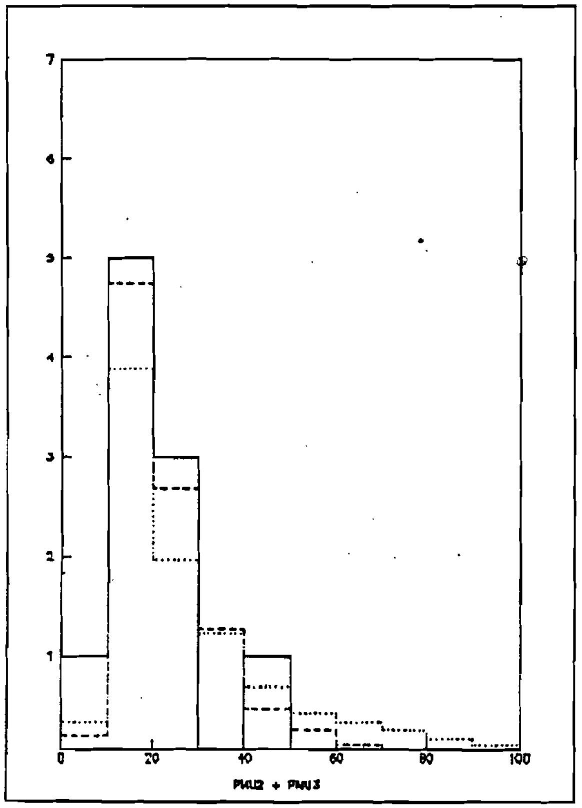

Fig. 7.2d : PMU2 + PMU3

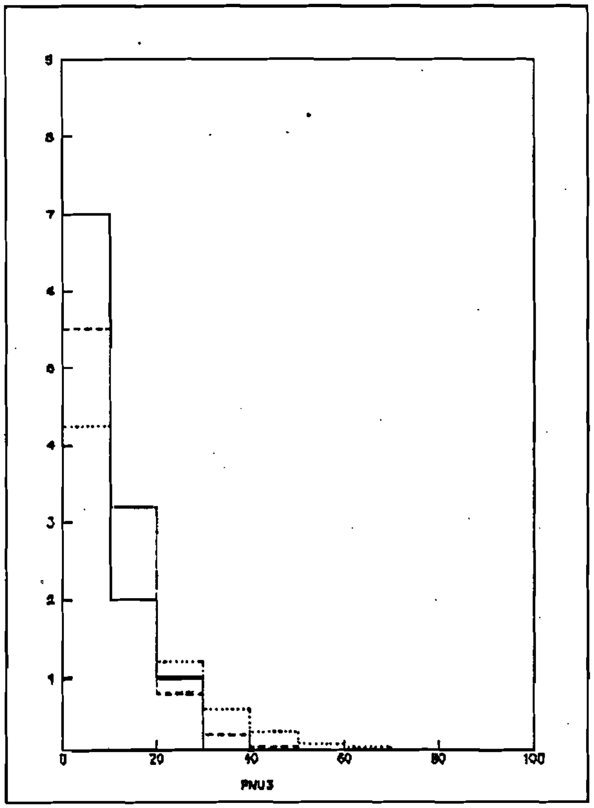

Fig. 7.2c : PMU3

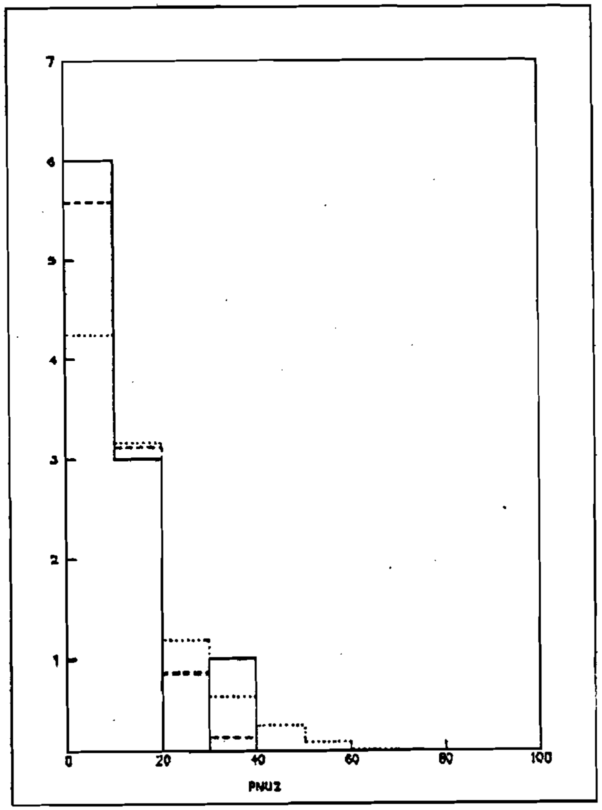

Fig. 7.2b : PMU2

Distributions of the "second" and the "third" momenta

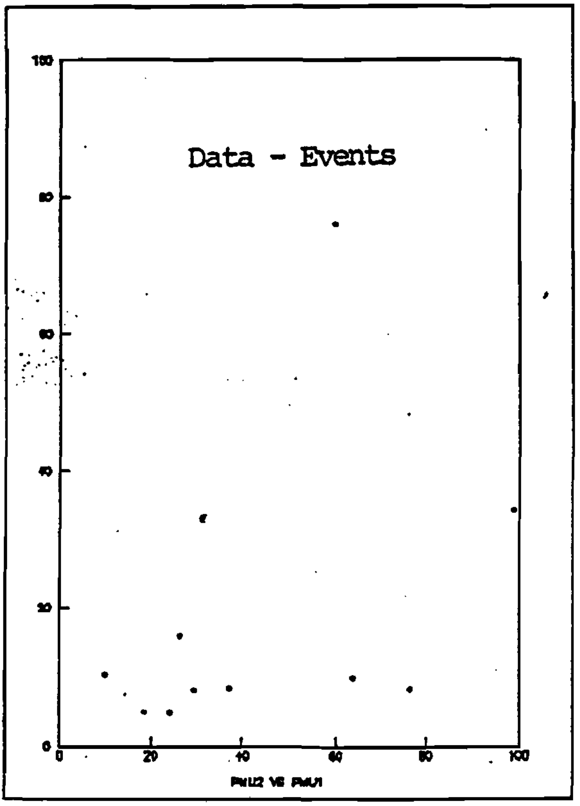

Fig. 7.3a : PMU2 vs PMU1
Data

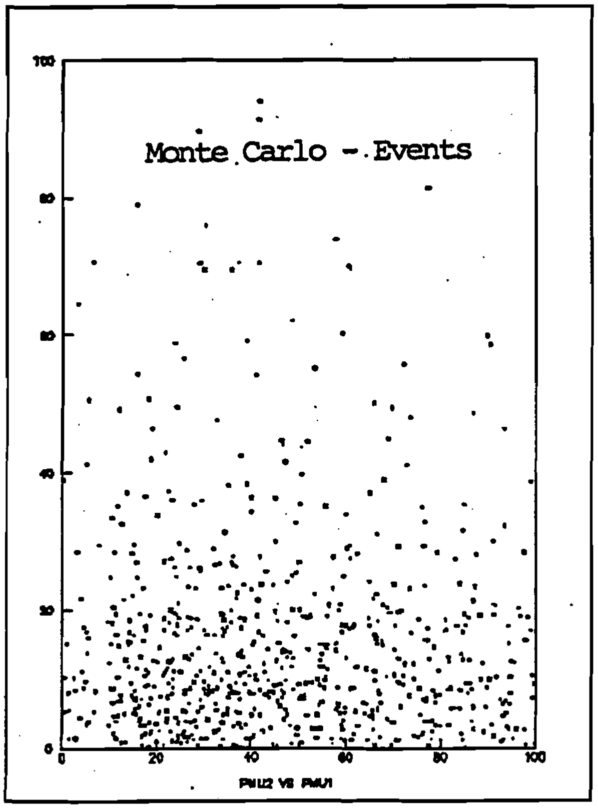

Fig. 7.3b : PMU2 vs PMU1
Hadronic Prodn. Model

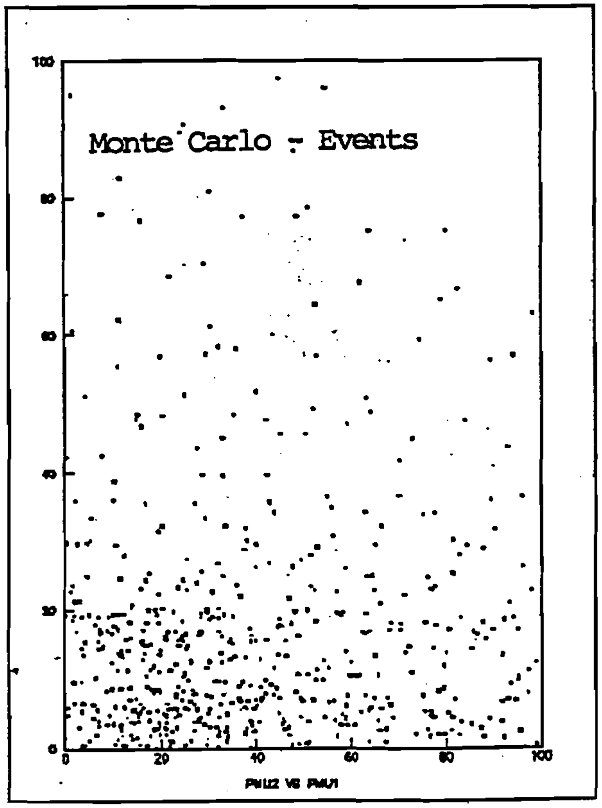

Fig. 7.3c : PMU2 vs PMU1
Radiative Prodn. M

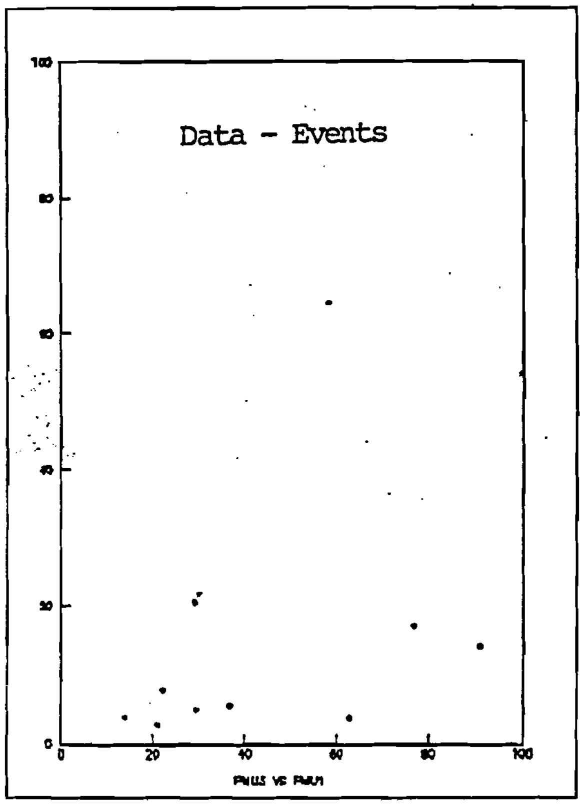

Fig. 7.4a : PMU3 vs PMU1

Data

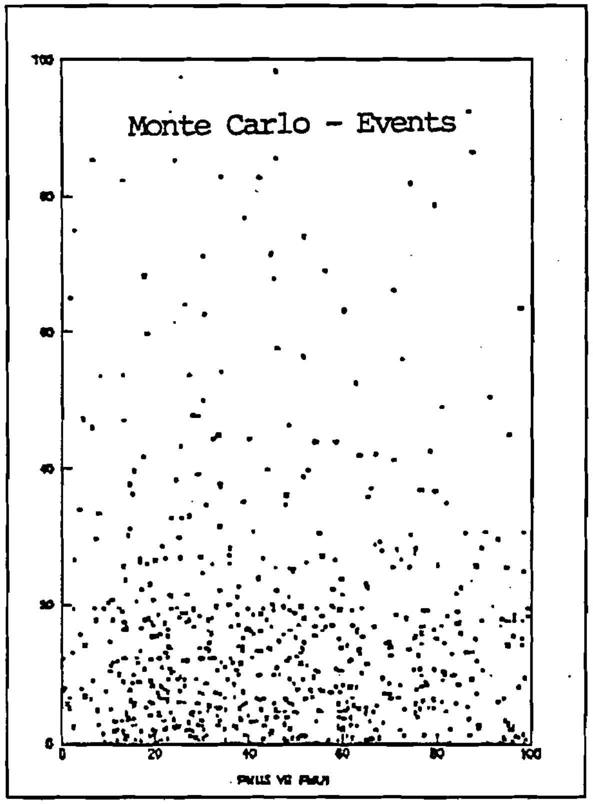

Fig. 7.4b : PMU3 vs PMU1

Hadronic Prodn. MOdel

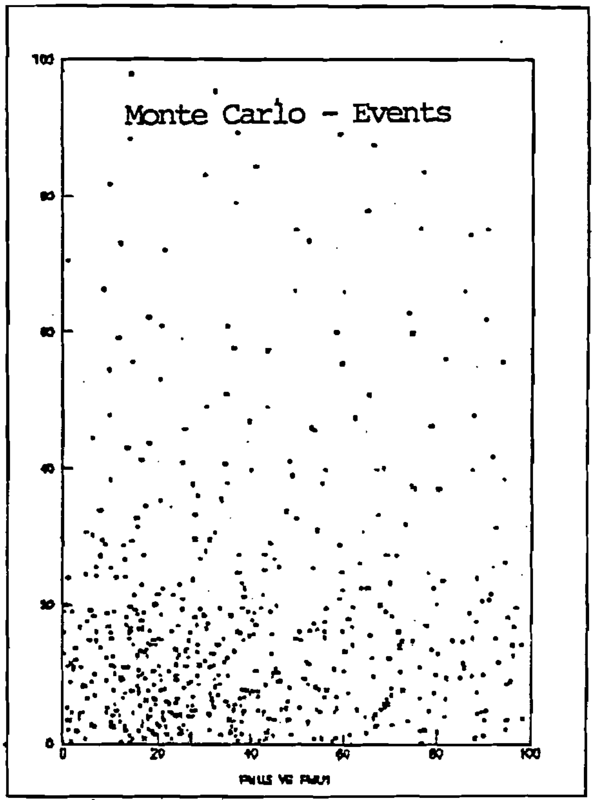

Fig. 7.4c : PMU3 vs PMU1

Radiative Prodn. Model

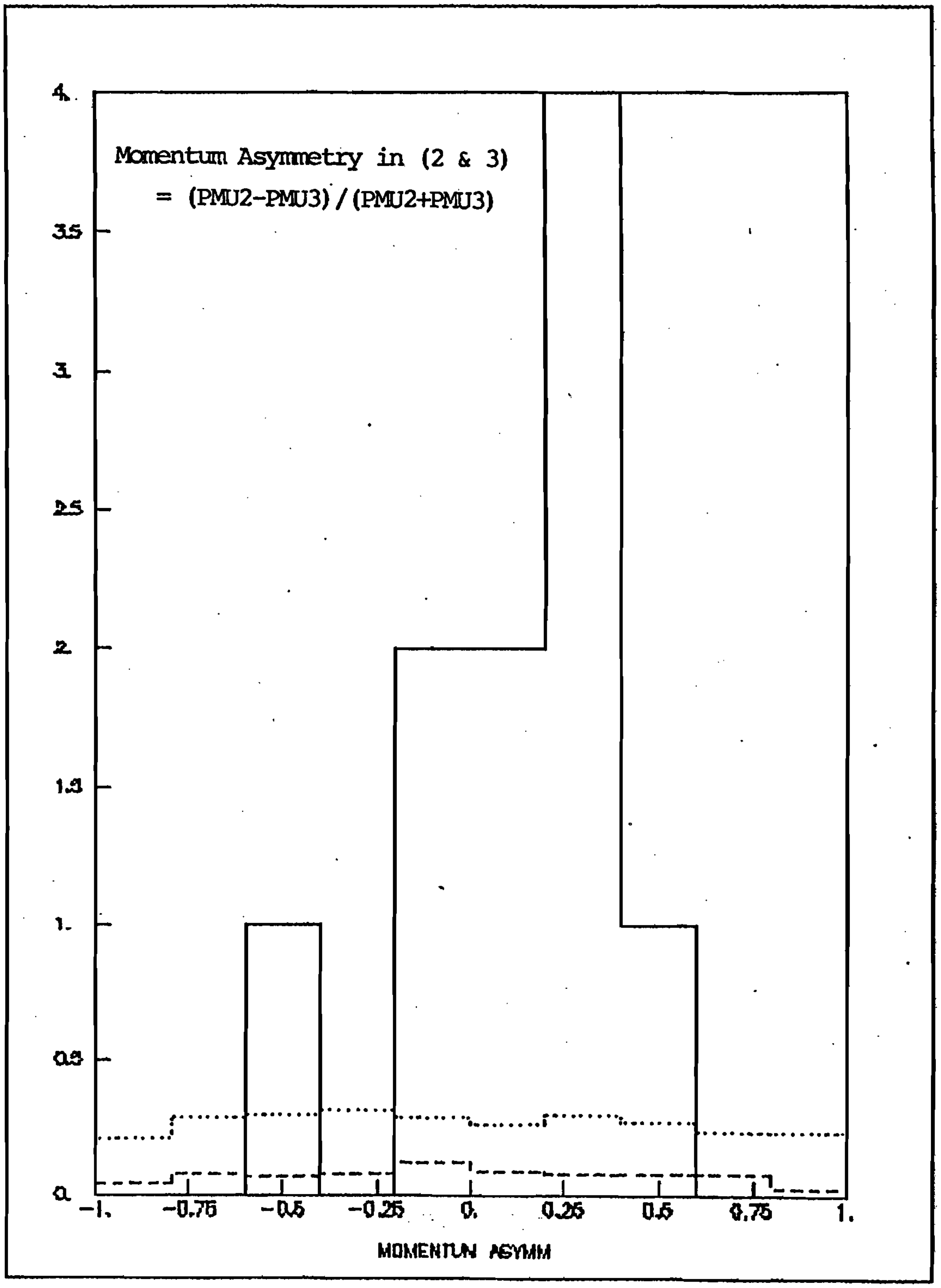

Fig. 7.5 : Momentum Asymmetry of the second and the third muons

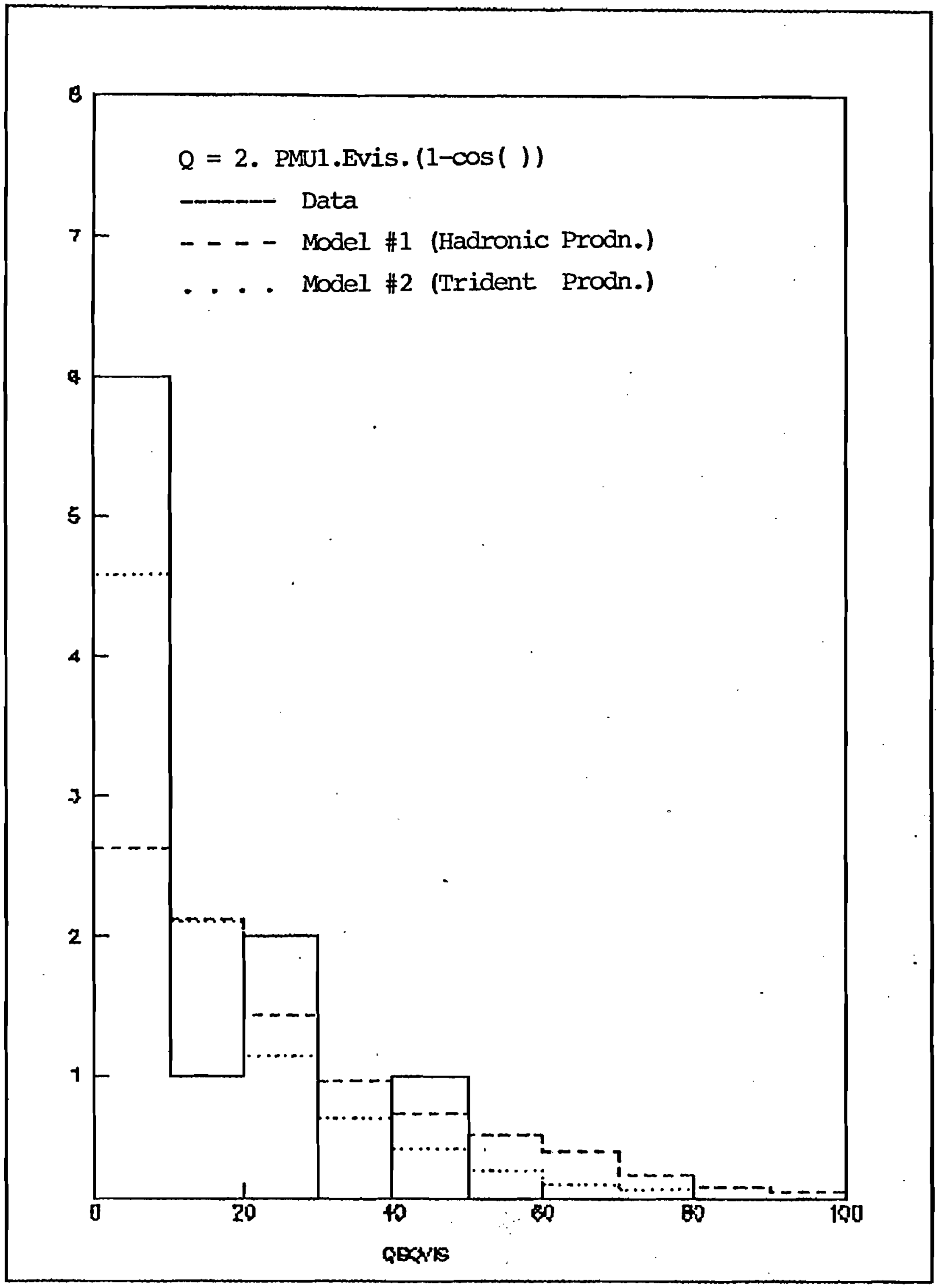

Fig. 7.6 : Q distribution for the data and the two models

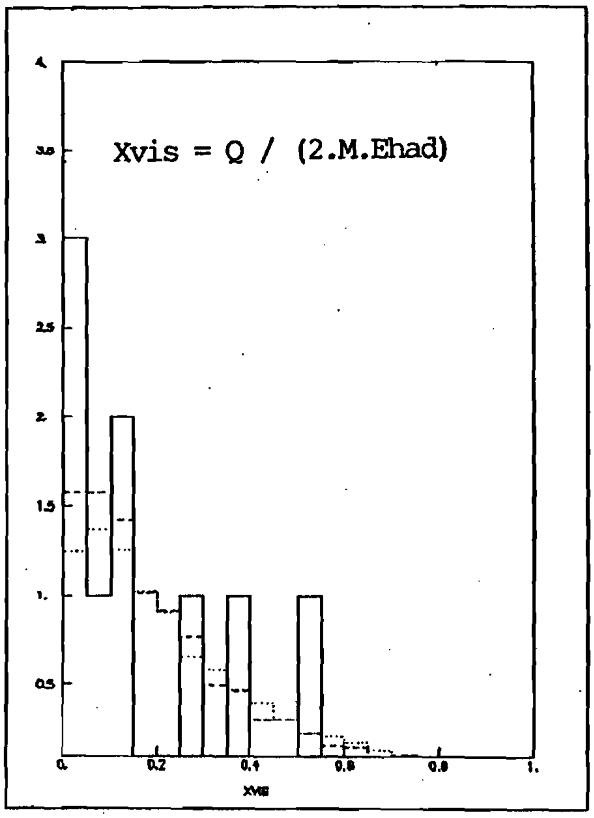

Fig. 7.7a : Xvis Distribution

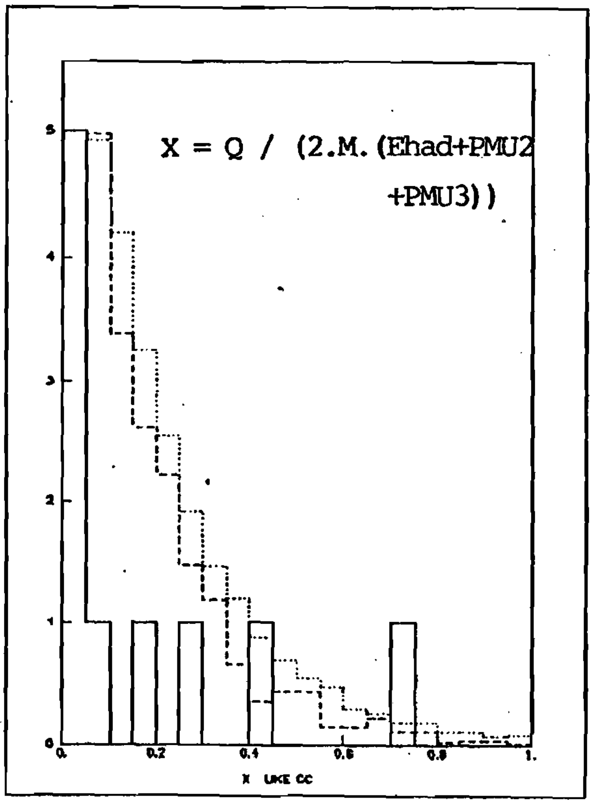

Fig. 7.7b : X (like CC) Distribution

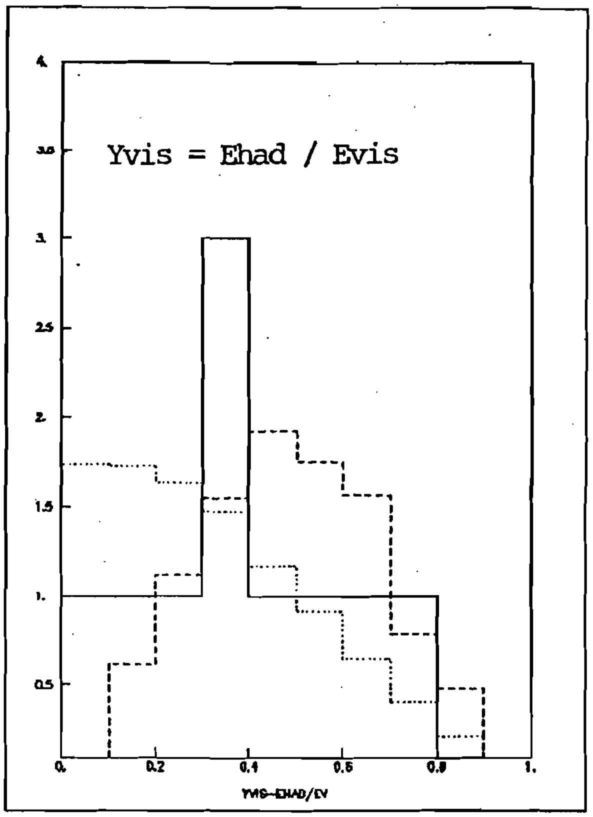

Fig. 7.8a : Yvis Distribution

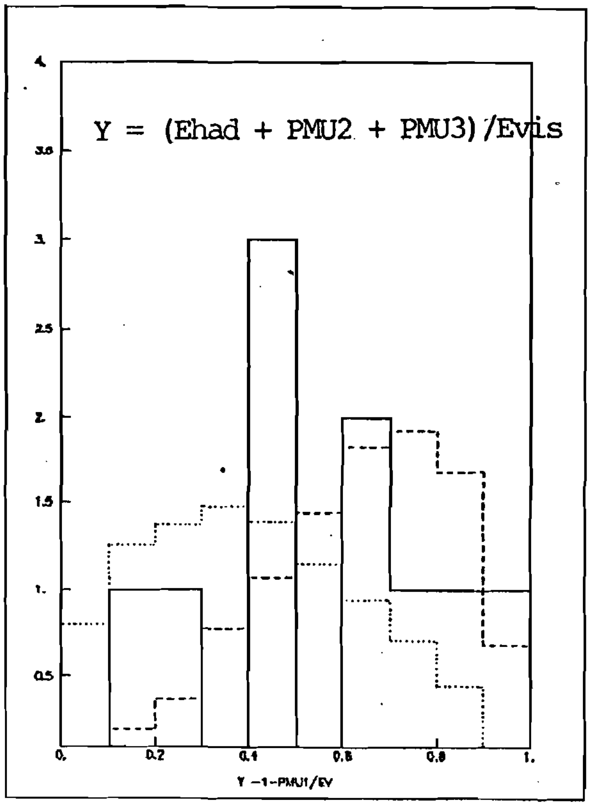

Fig. 7.8b : Y (Like CC) Distribution

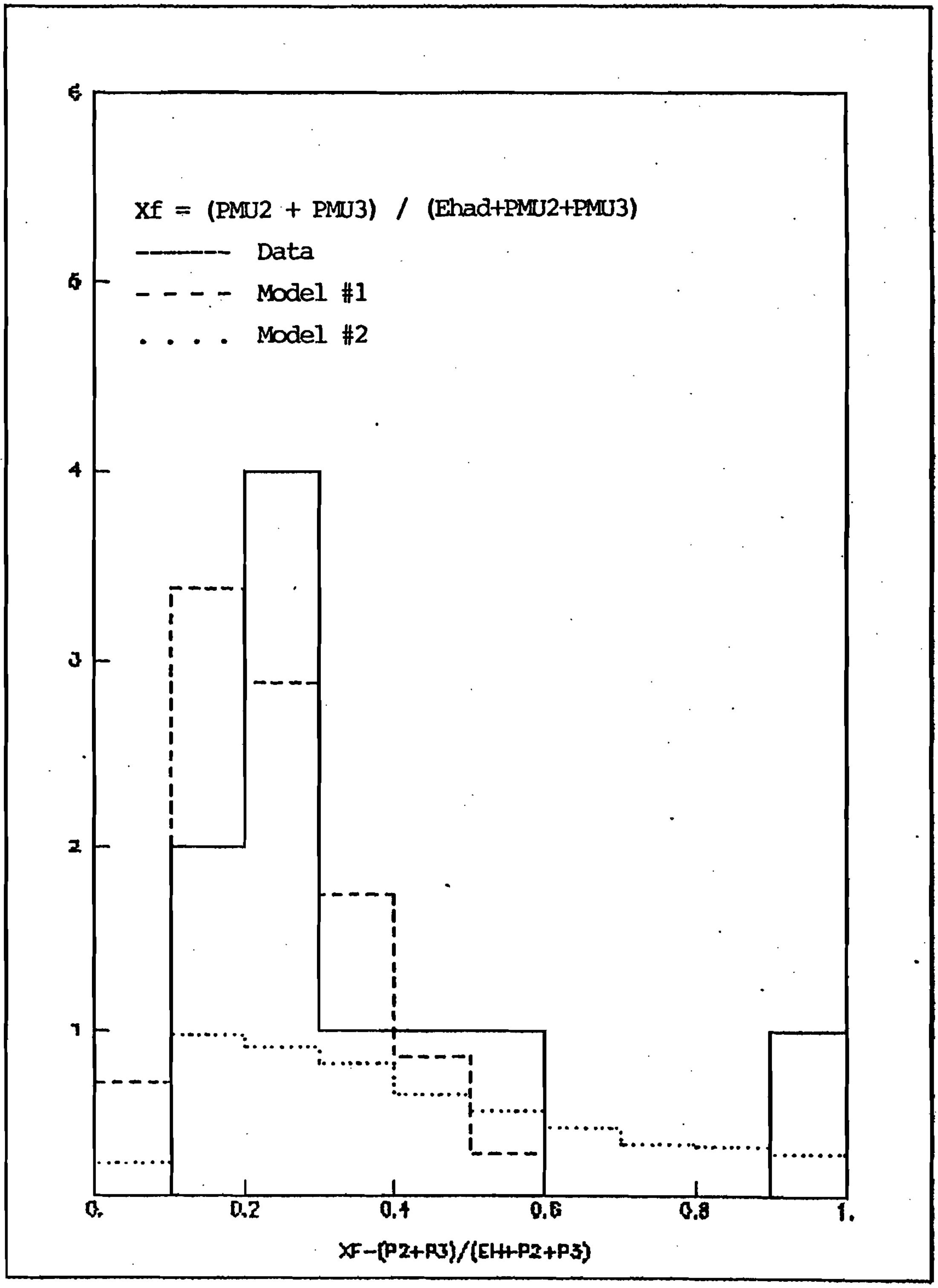

Fig. 7.9 : Xf Distribution for the data and the two models
Xf is the Feyman scaling variable for Model #1

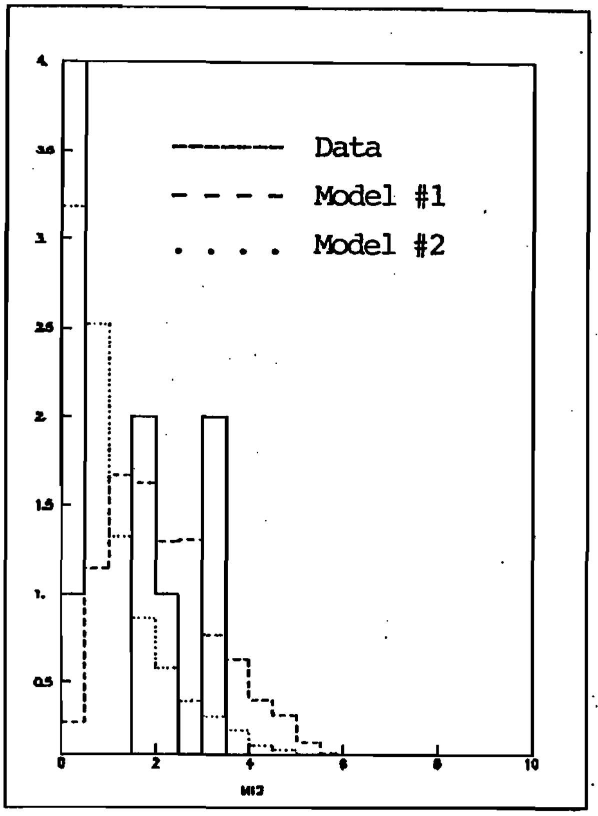

Fig. 7.10 : M12 Distribution

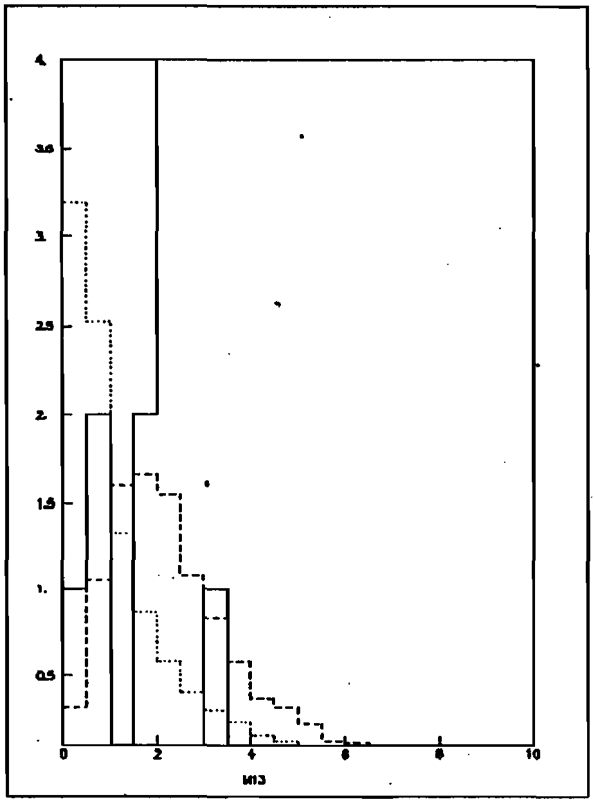

Fig. 7.11 : M13 Distribution

M23 Distribution

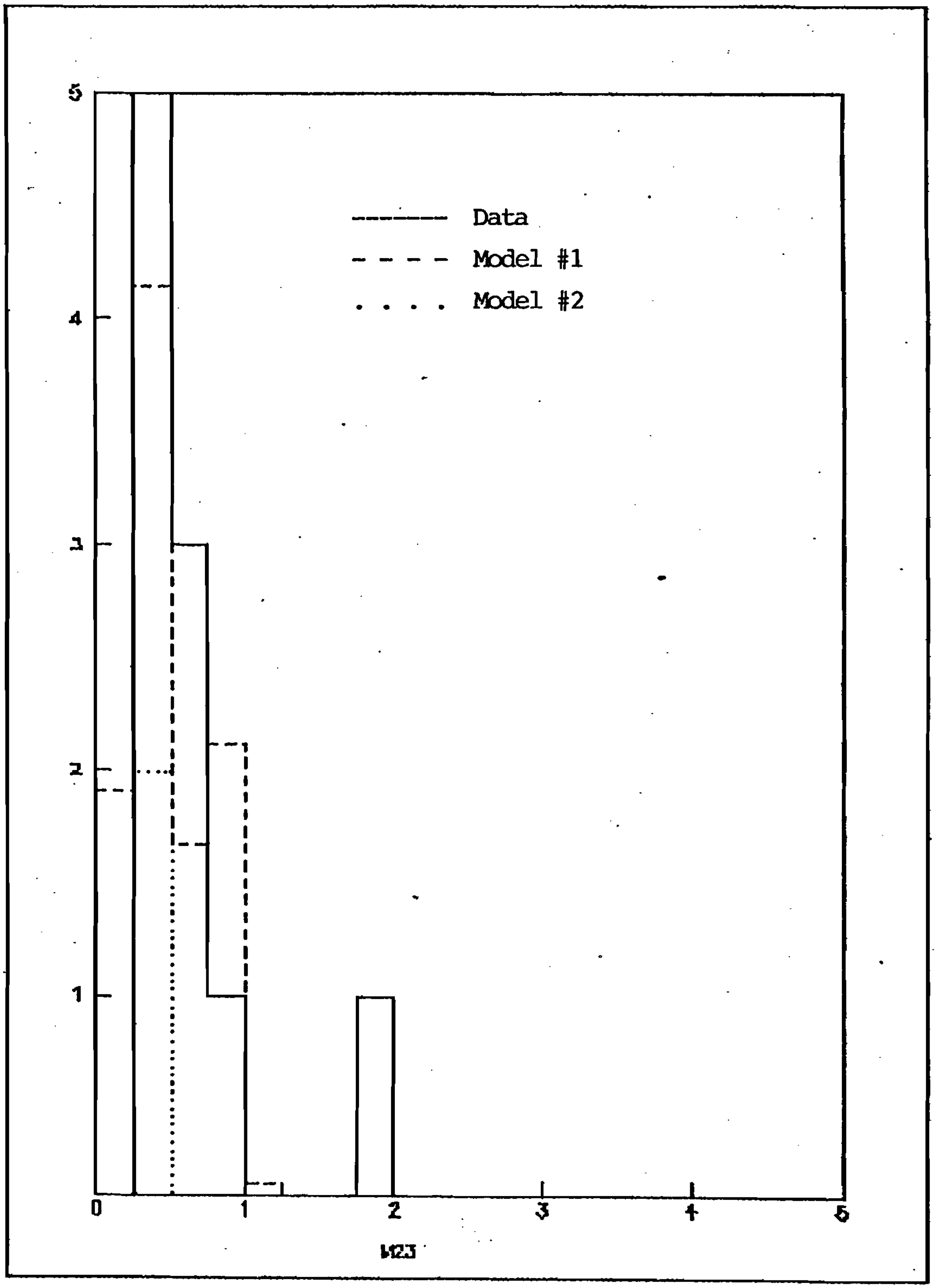

Fig. 7.12b : M23 from the data and the smeared prediction from the simulation of Model #1 & #2

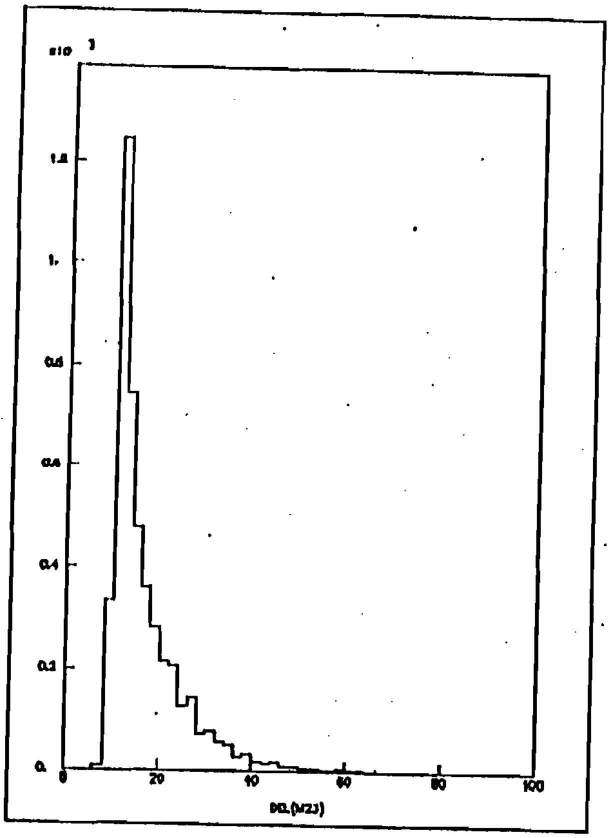

Fig. 7.12c : Percentage change in M23 after smearing

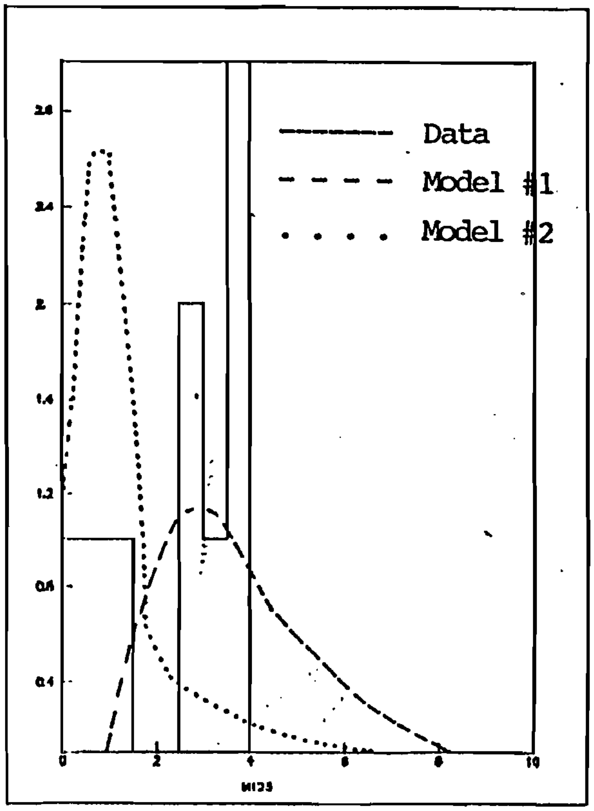

Fig. 7.13 : M123, the trimuon mass Distribution

M12 vs M123

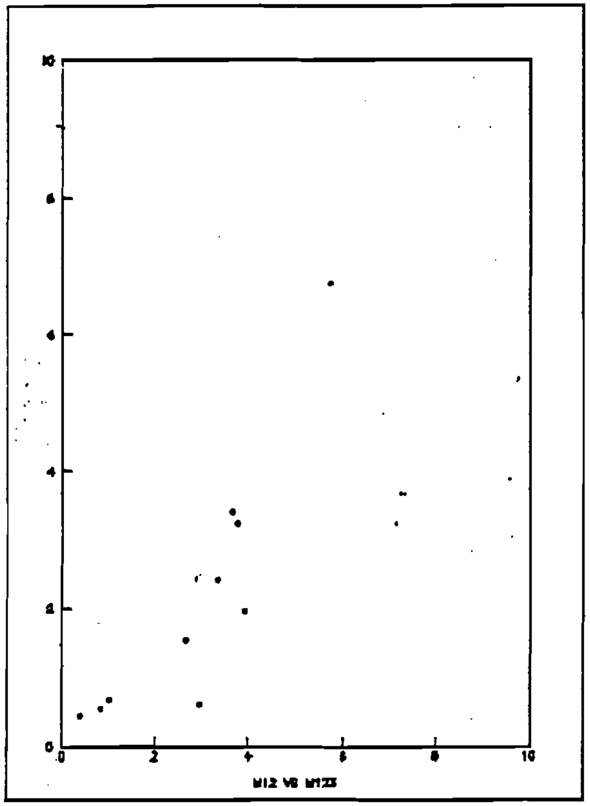

Fig. 7.14a : M12 vs M123

Data

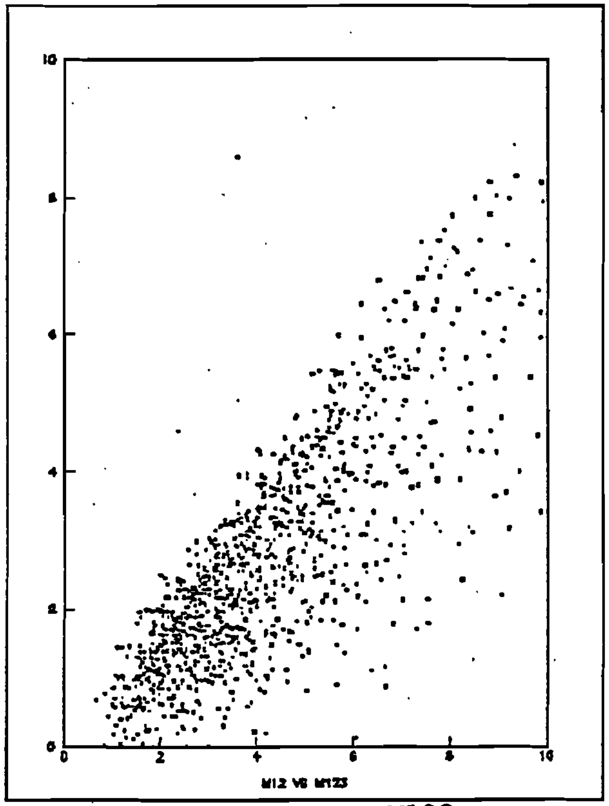

Fig. 7.14b : M12 vs M123

Monte Carlo Events from Hadronic Production of 3

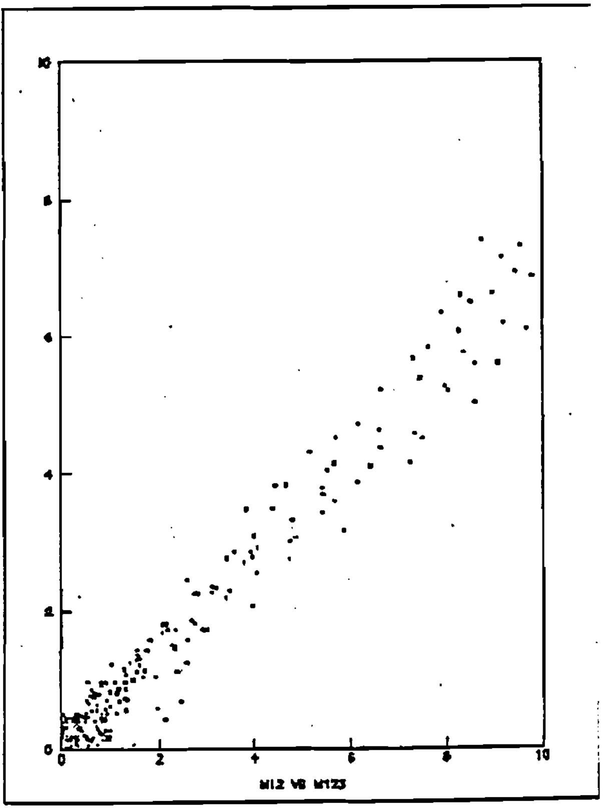

Fig. 7.14c : M12 vs M123

Monte Carlo Events from Ra -diative Prodn. of 3

M13 vs M123

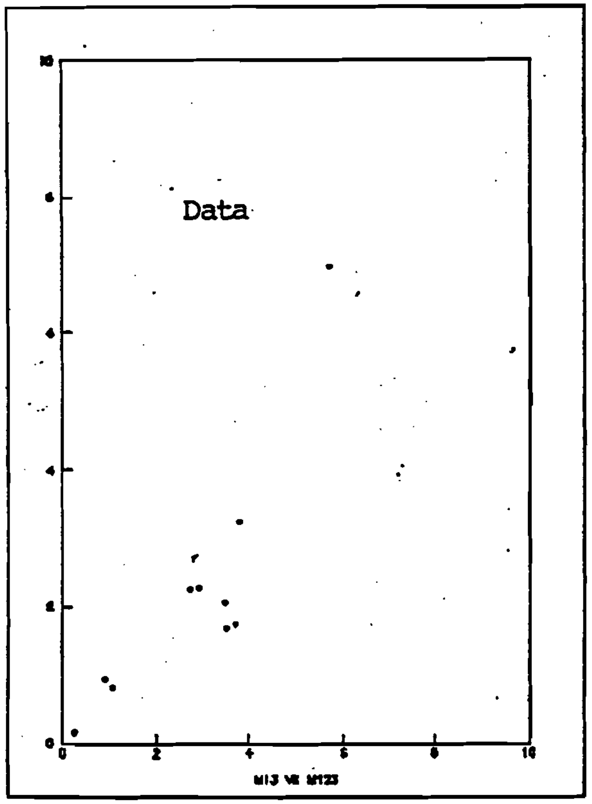

Fig. 7.15a : m13 vs M123

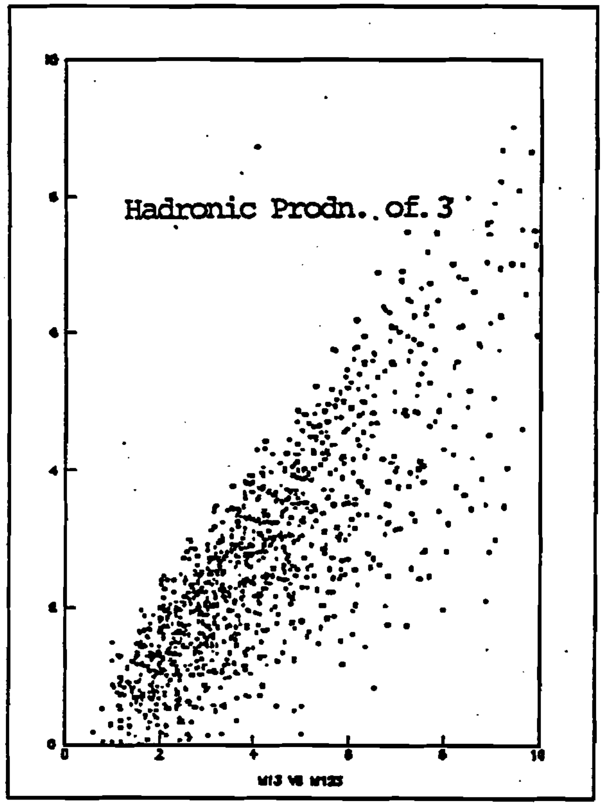

Fig. 7.15b : M13 vs M123

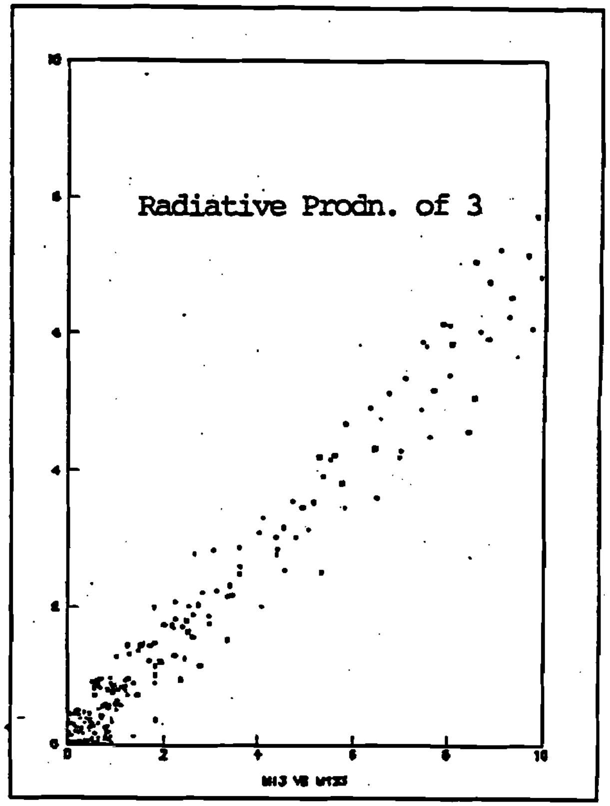

Fig. 7.15c : M13 vs M123

M23 vs M123

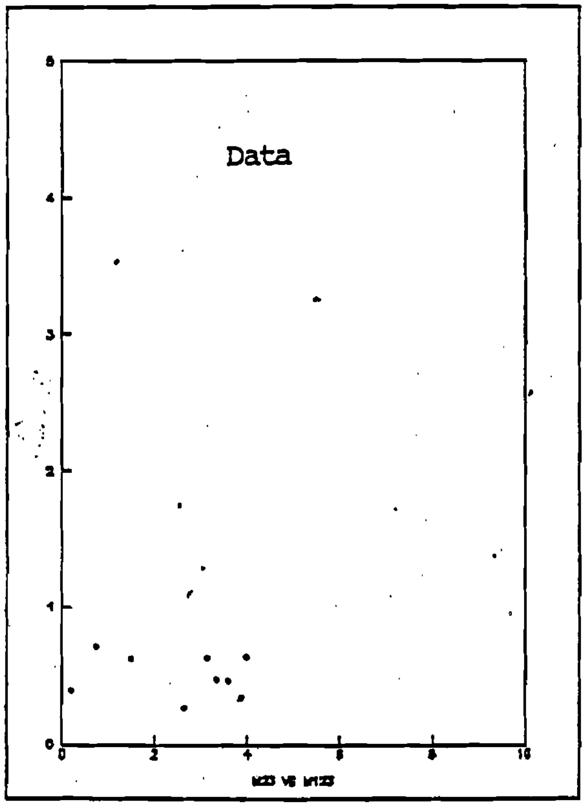

Fig. 7.16a : M23 vs M123

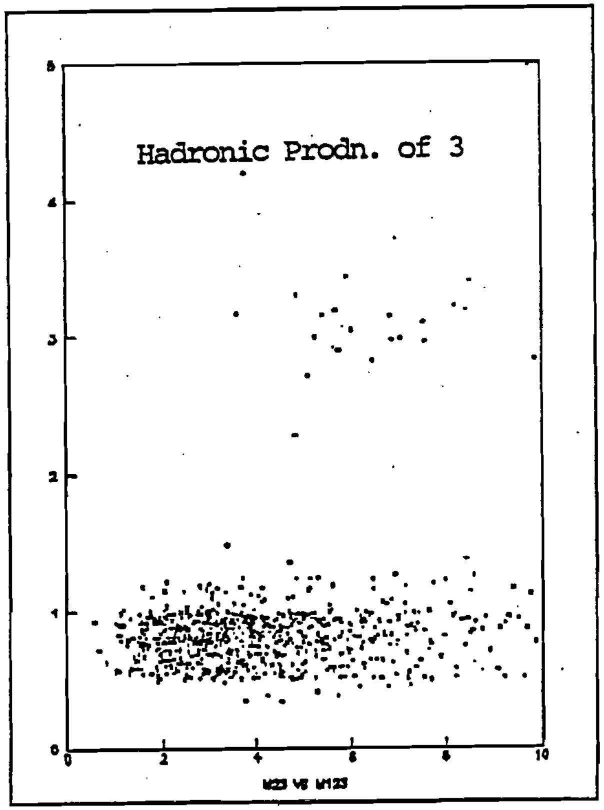

Fig. 7.16b : M23 vs M123

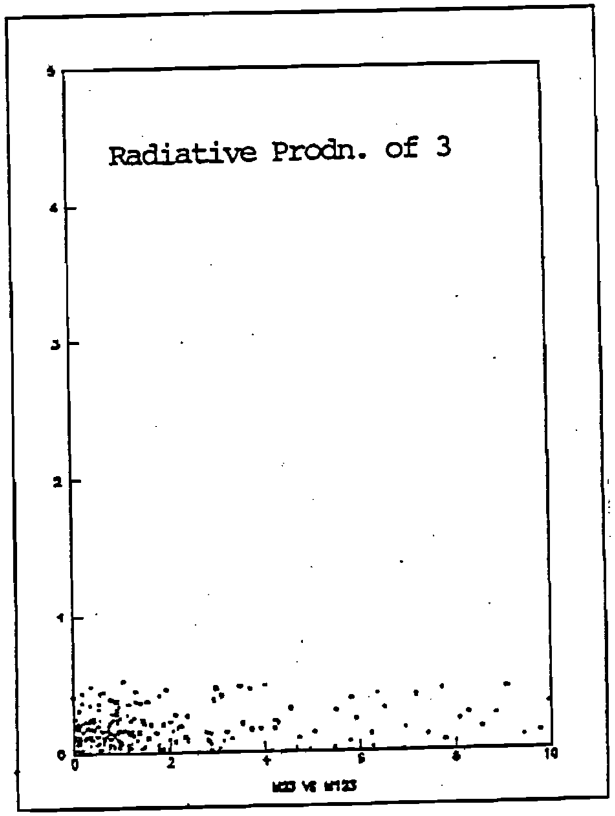

Fig. 7.16c : m23 vs M123

The "Phi" Distributions

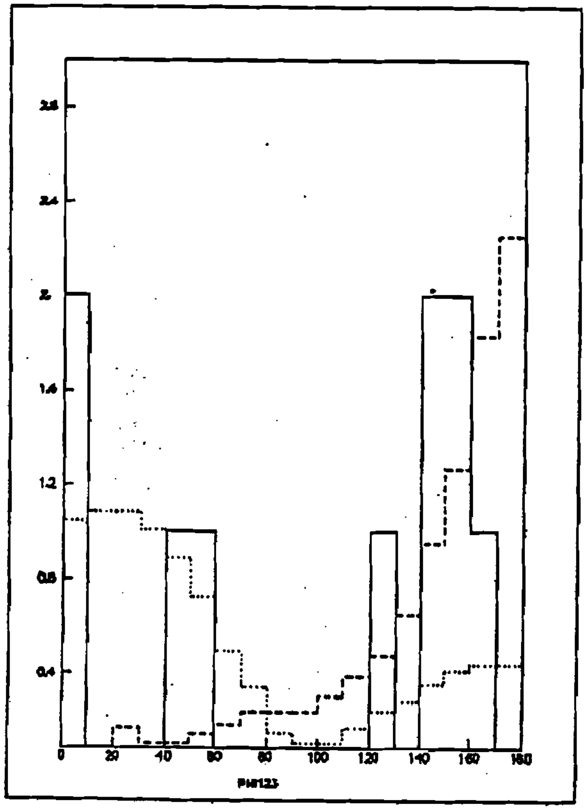

Fig. 7.20 : φ_{23} Distribution

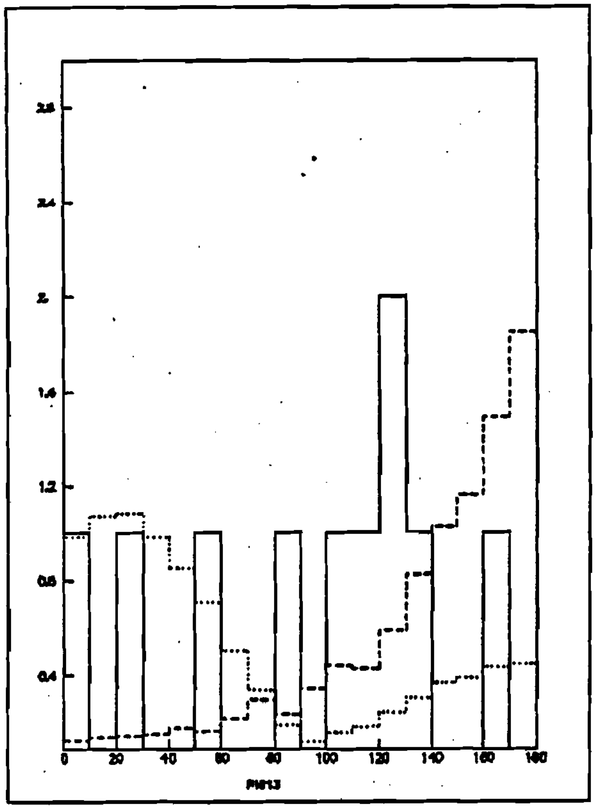

Fig. 7.19 : φ_{13} Distribution

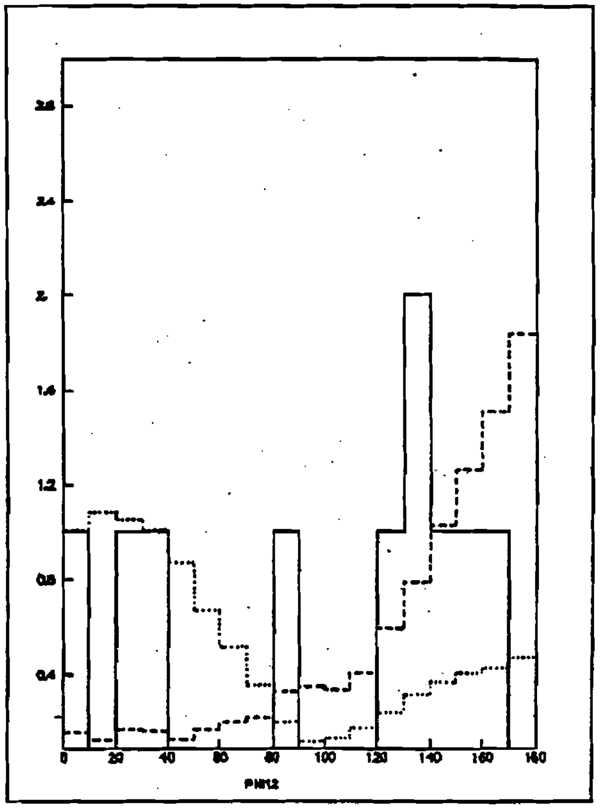

Fig. 7.18 : φ_{12} Distribution

PMU2 vs "Phi12" Scatterplots

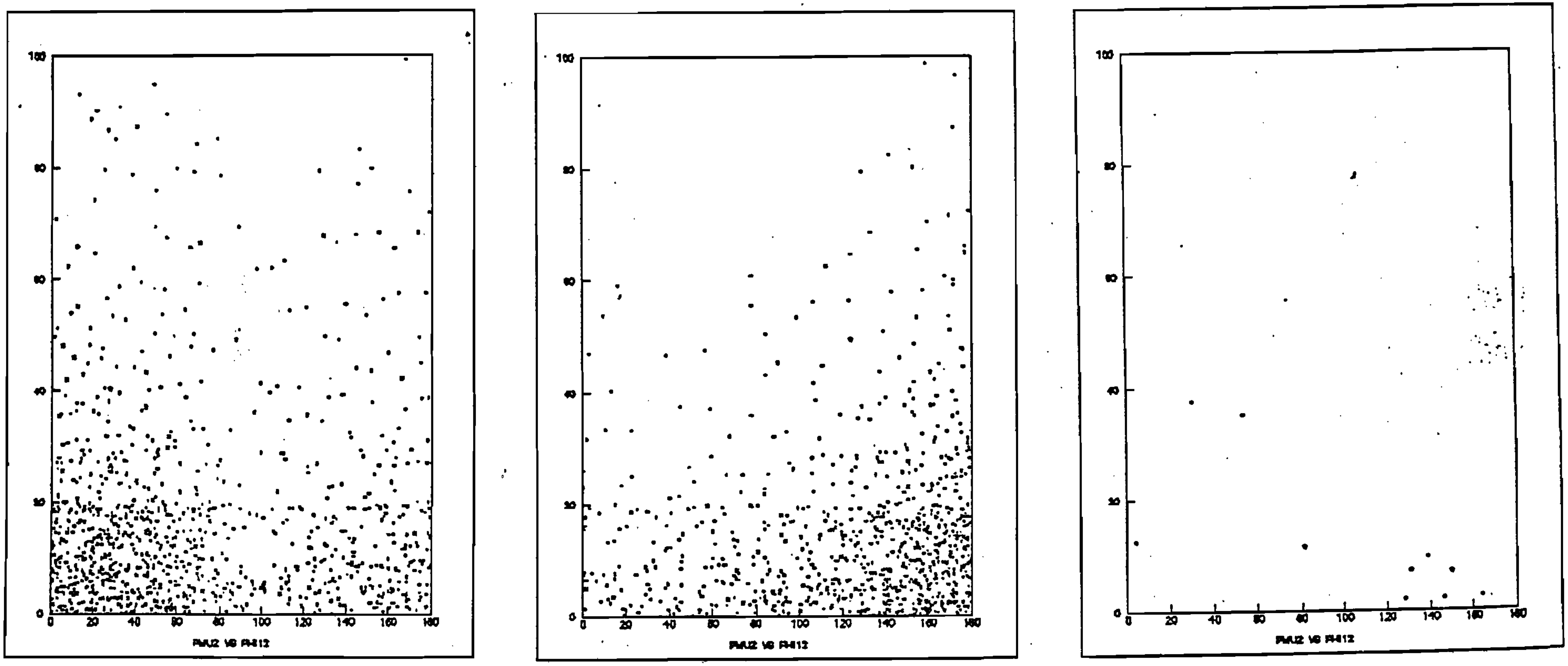

(c) Hadronic Production

(b) Radiative Production

(a) Data

Fig. 7.21 PmU2 vs φ_{12}

PMU3 vs "Phi13" Scatterplots

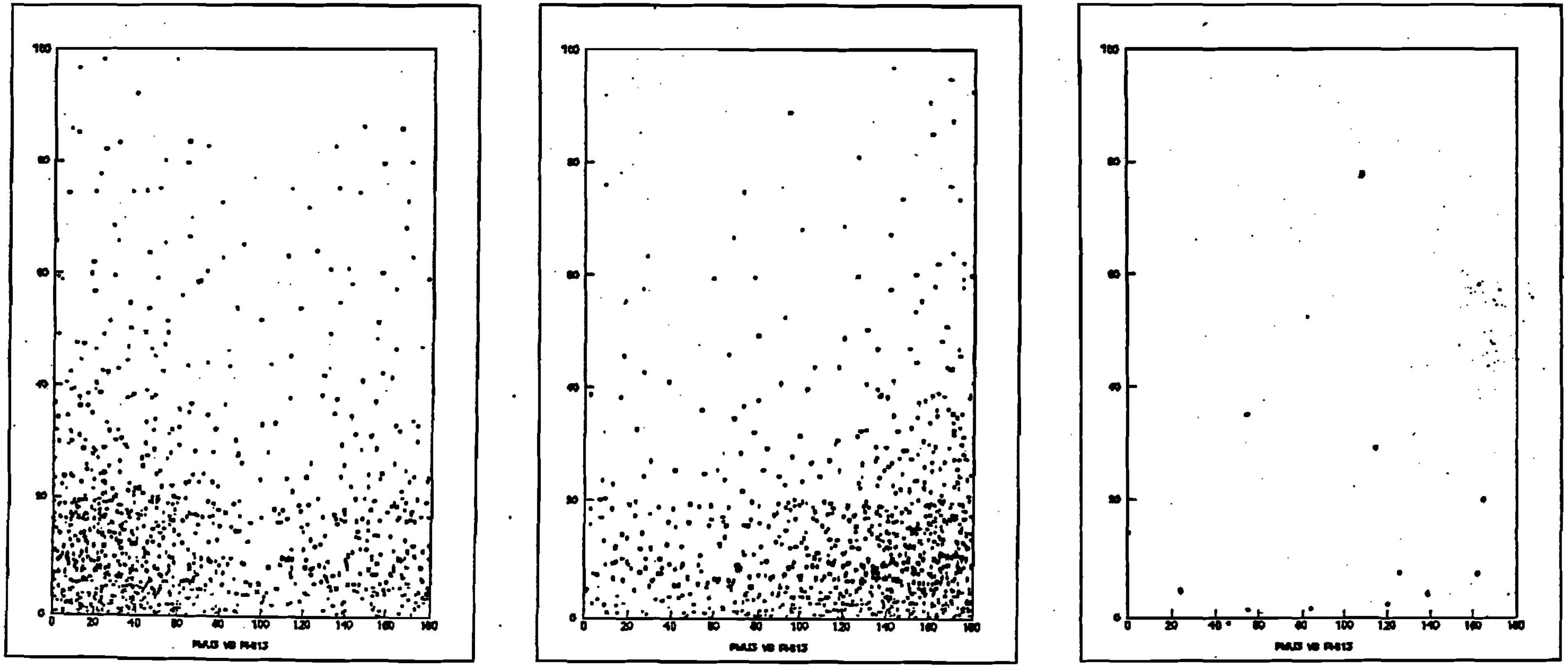

(c) Hadronic Production

(b) Radiative Production

(a) Data

Fig. 7.22 : PMU3 vs φ_{13}

The P_T Distributions

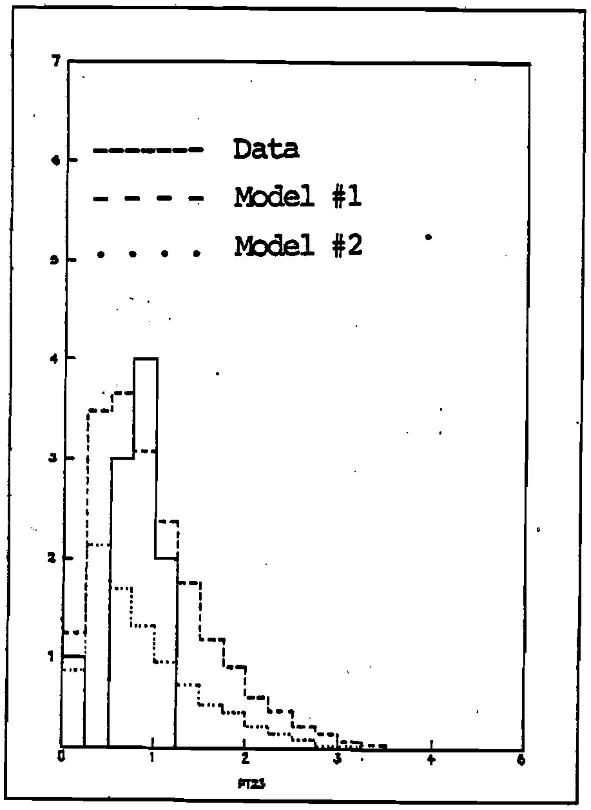

Fig. 7.25 : $\mathcal{P}^T_{23}$ Distribution

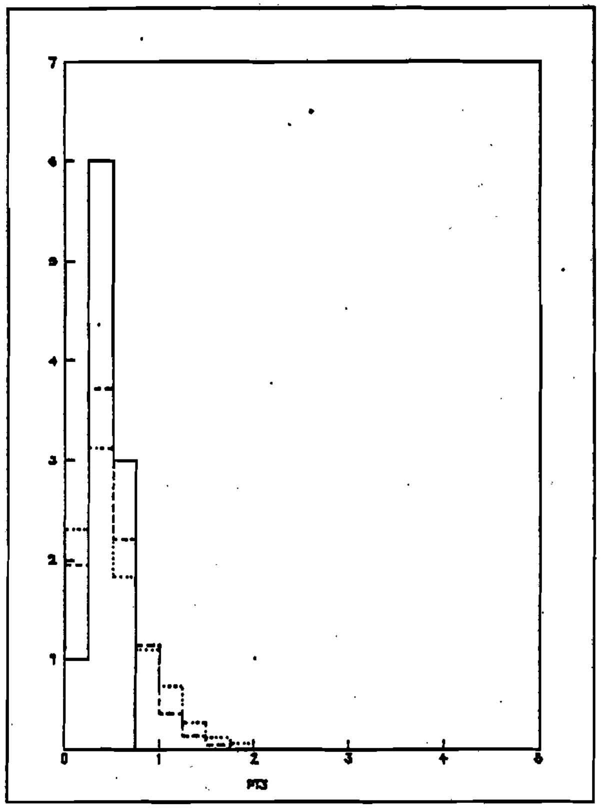

Fig. 7.24 : $\mathcal{P}^T_3$ Distribution

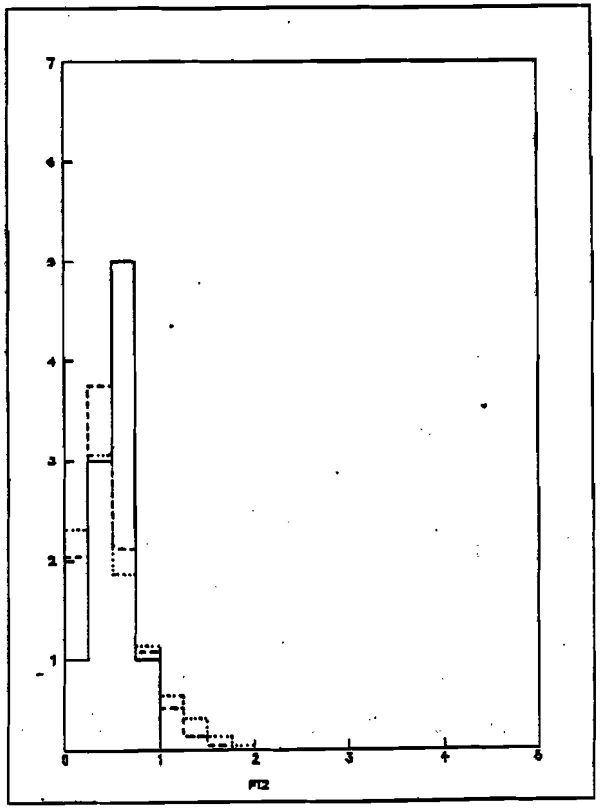

Fig. 7.23 : $\mathcal{P}^T_2$ Distribution

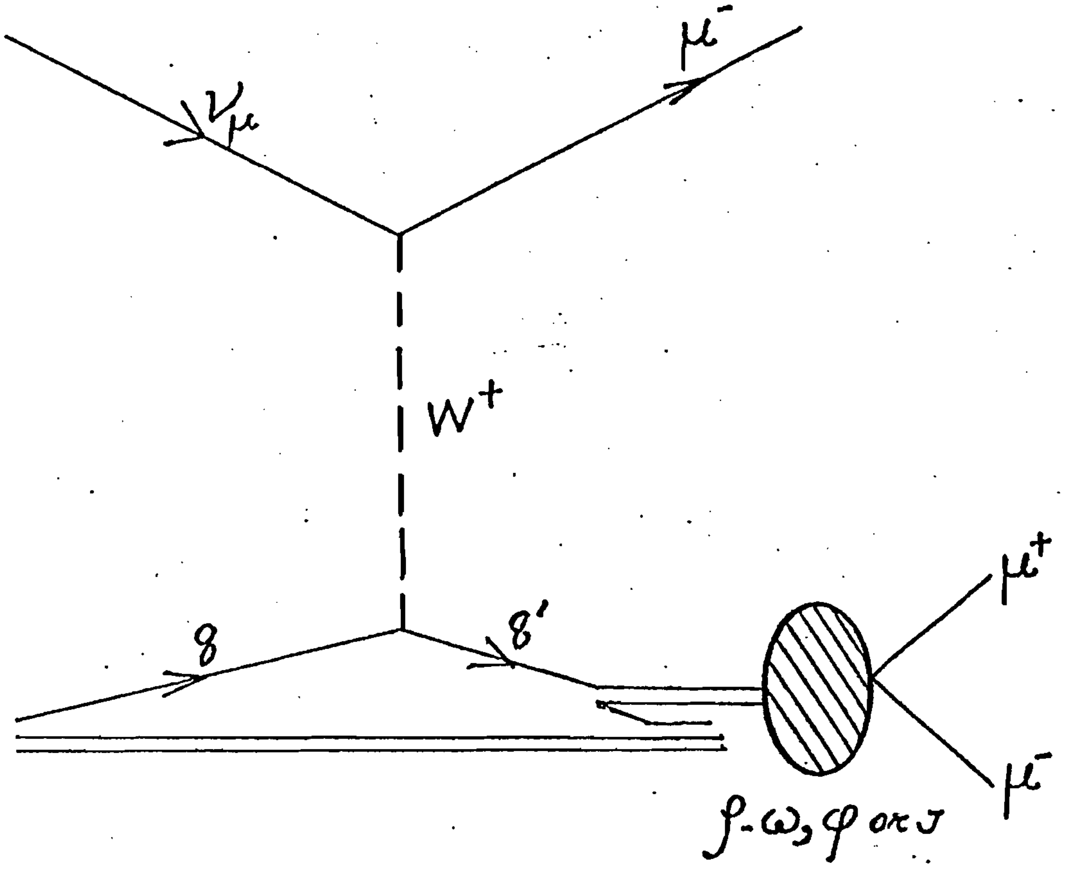

Fig. 7.26 : Schematic of Hadronic production of 3μ

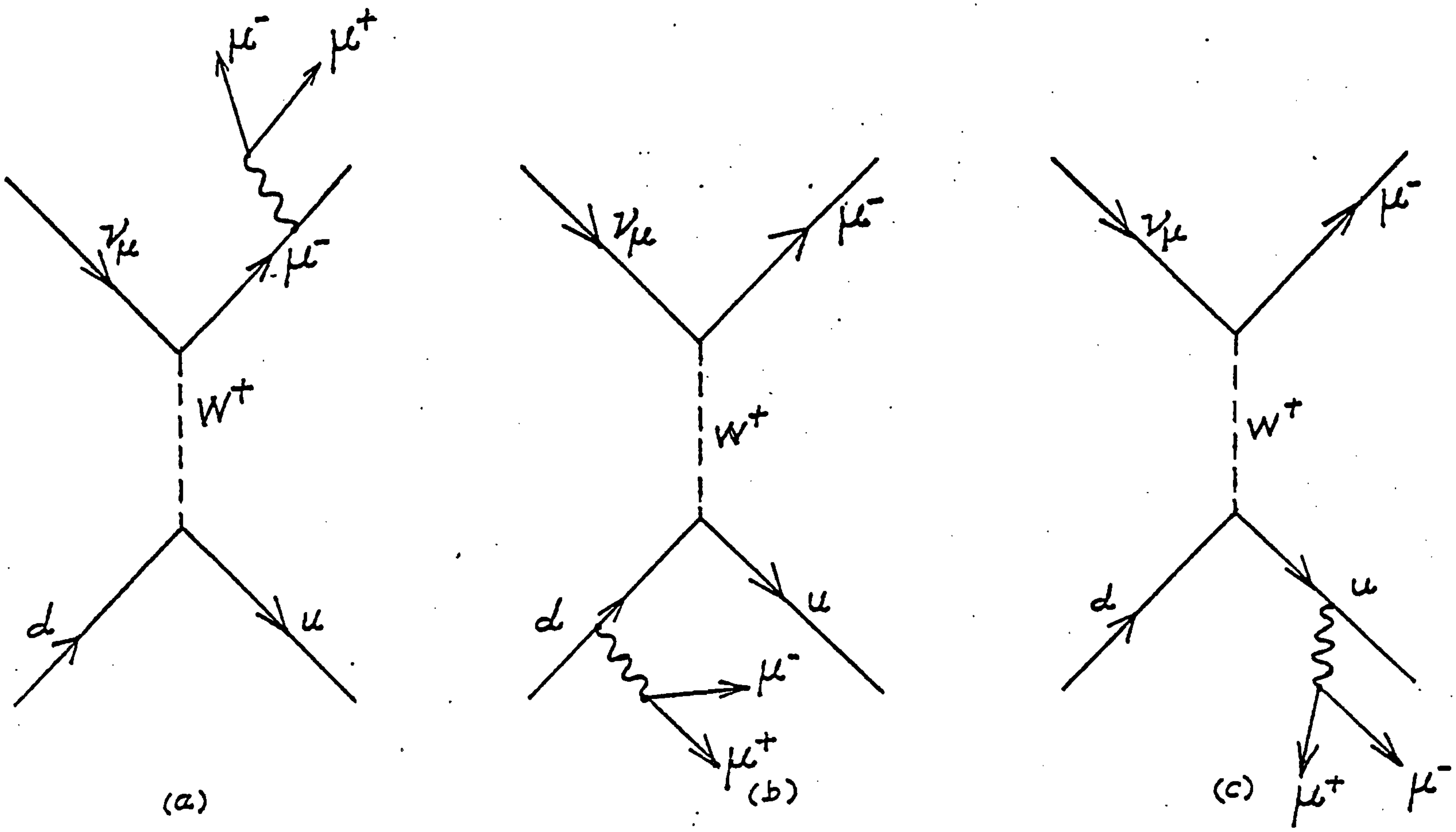

Fig. 7.27a : Trident Production off the muon. Figs. b & c show the same off the interacting quarks

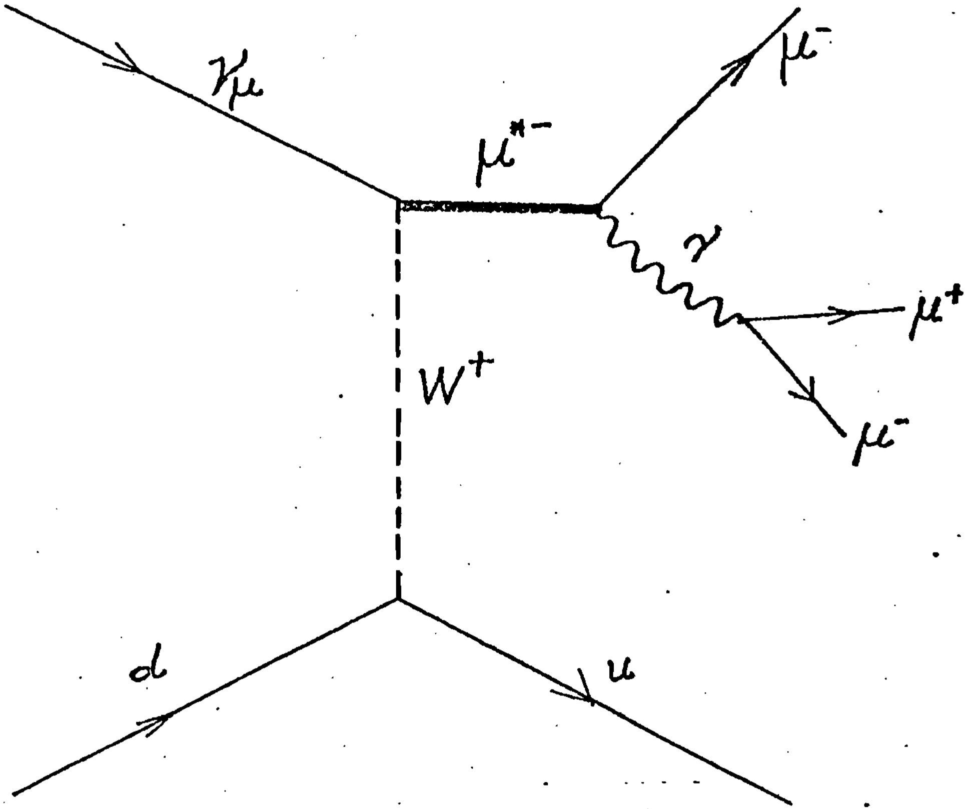

Fig. 7.28 : Heavy Muon Production

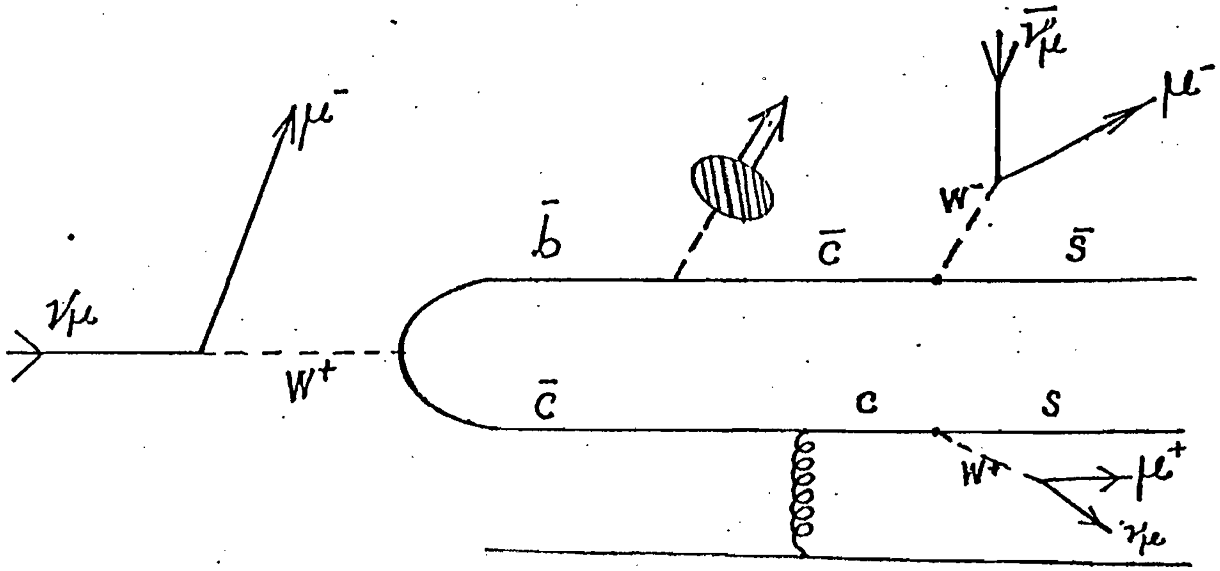

Fig. 7.29 : Quark Cascade producing 3μ events

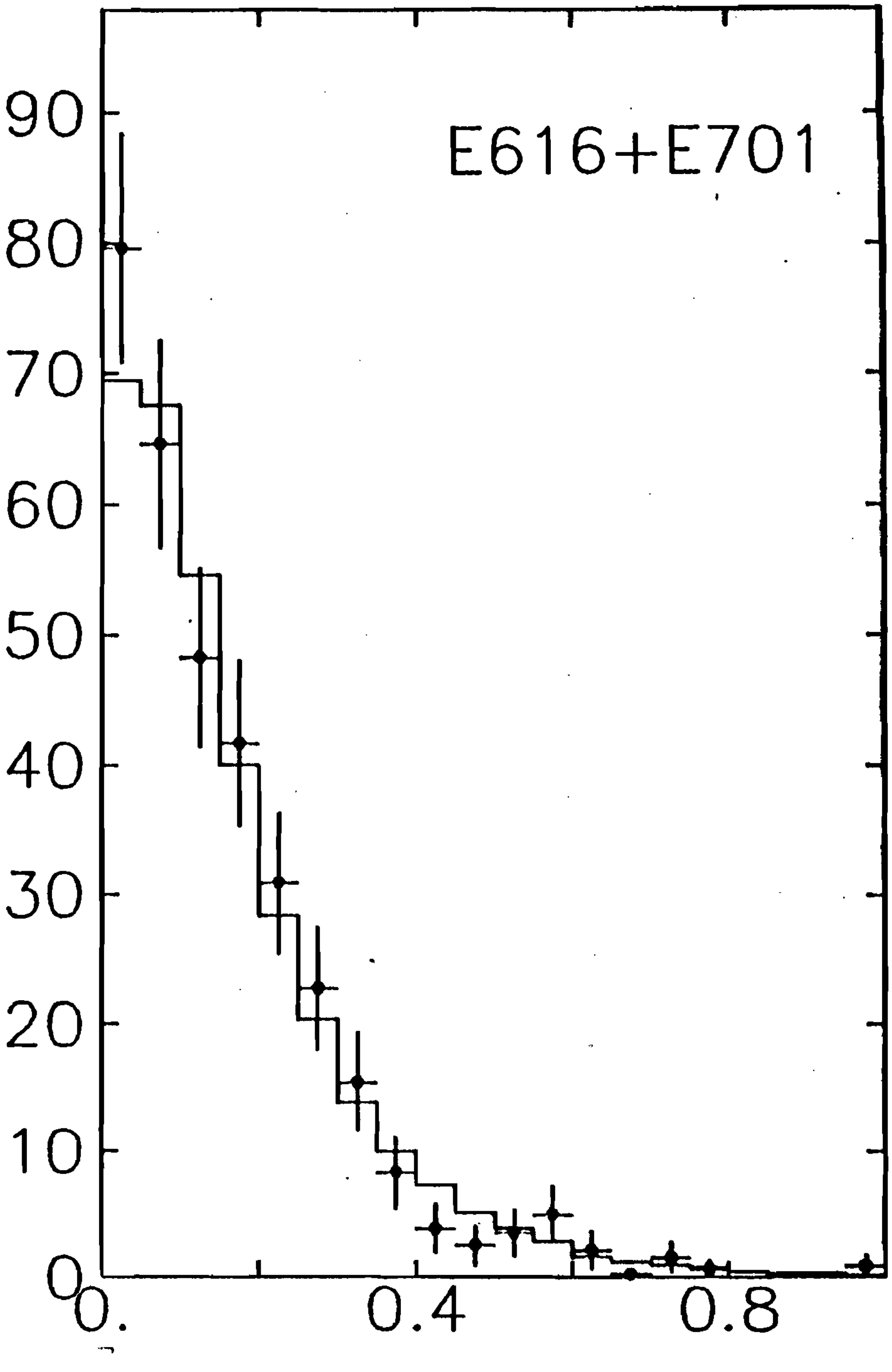

Fig. 5.7: Comparision of OSDM data (Error bars) with Monte Carlo (Solid line)

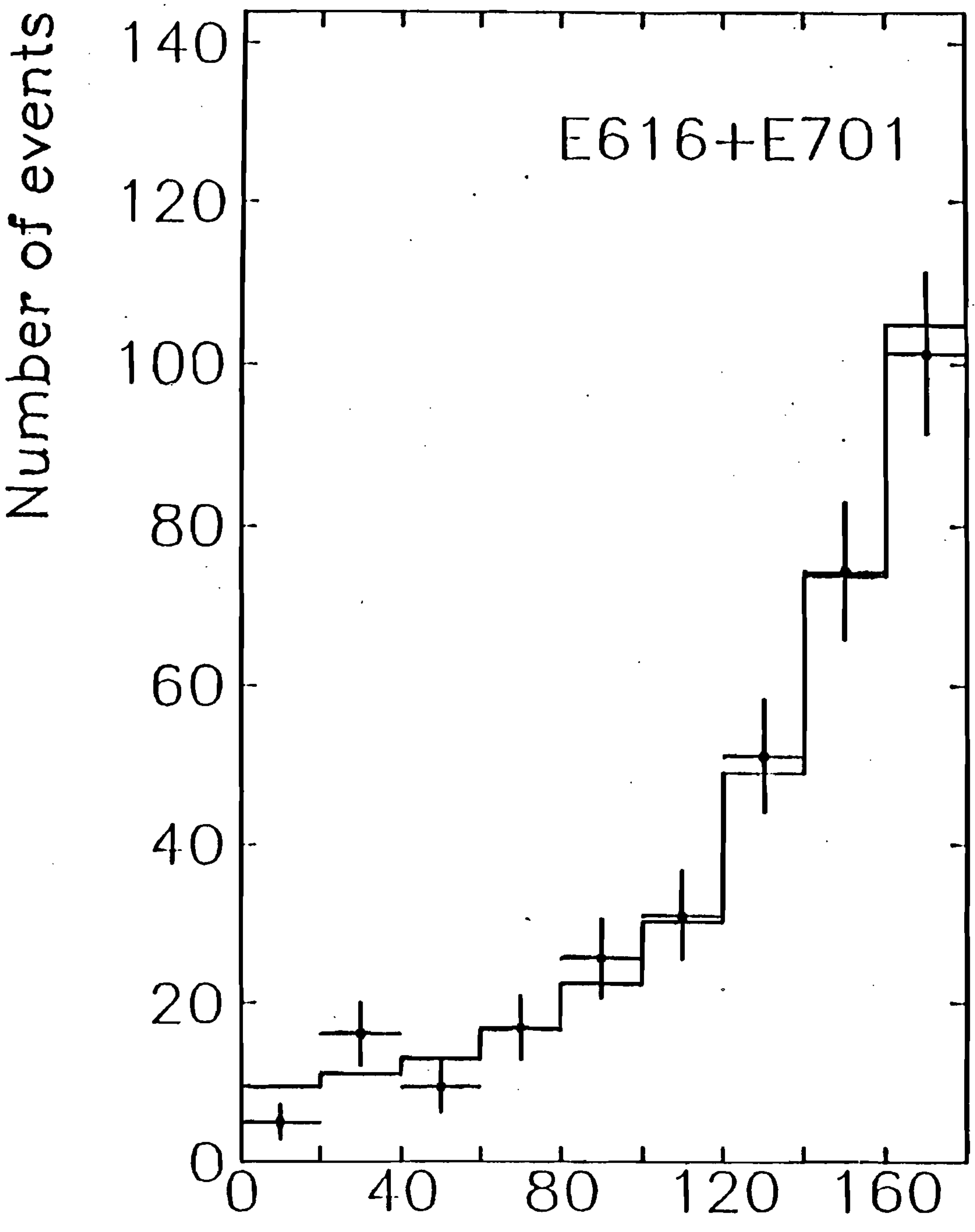

Fig. 5.7: Comparision of OSDM data with MC

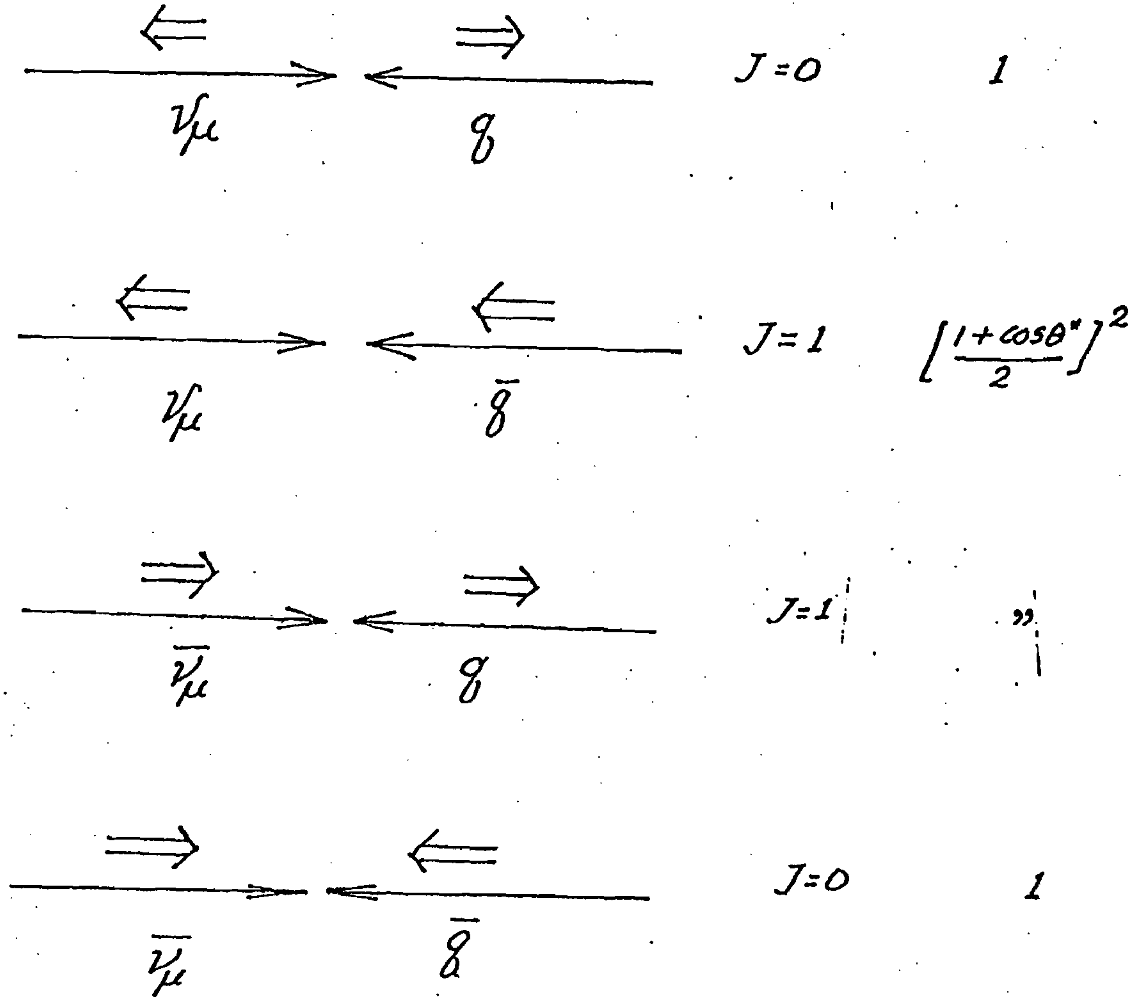

Fig. C.1 Spin consideration for $\nu_\mu \bar{\nu}_\mu$ scattering

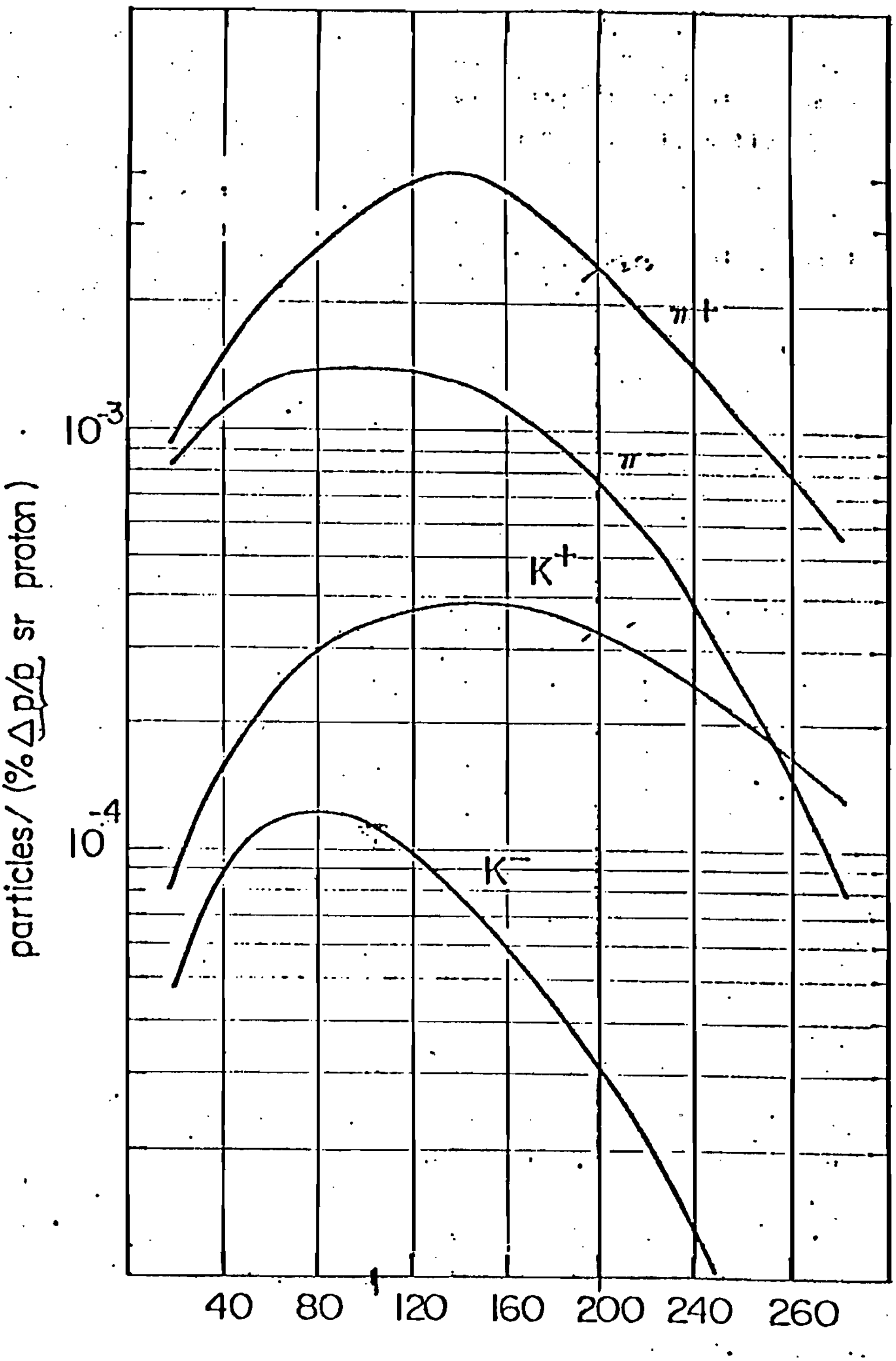

Fig. D.1 Momentum distribution of seco -ndary particles

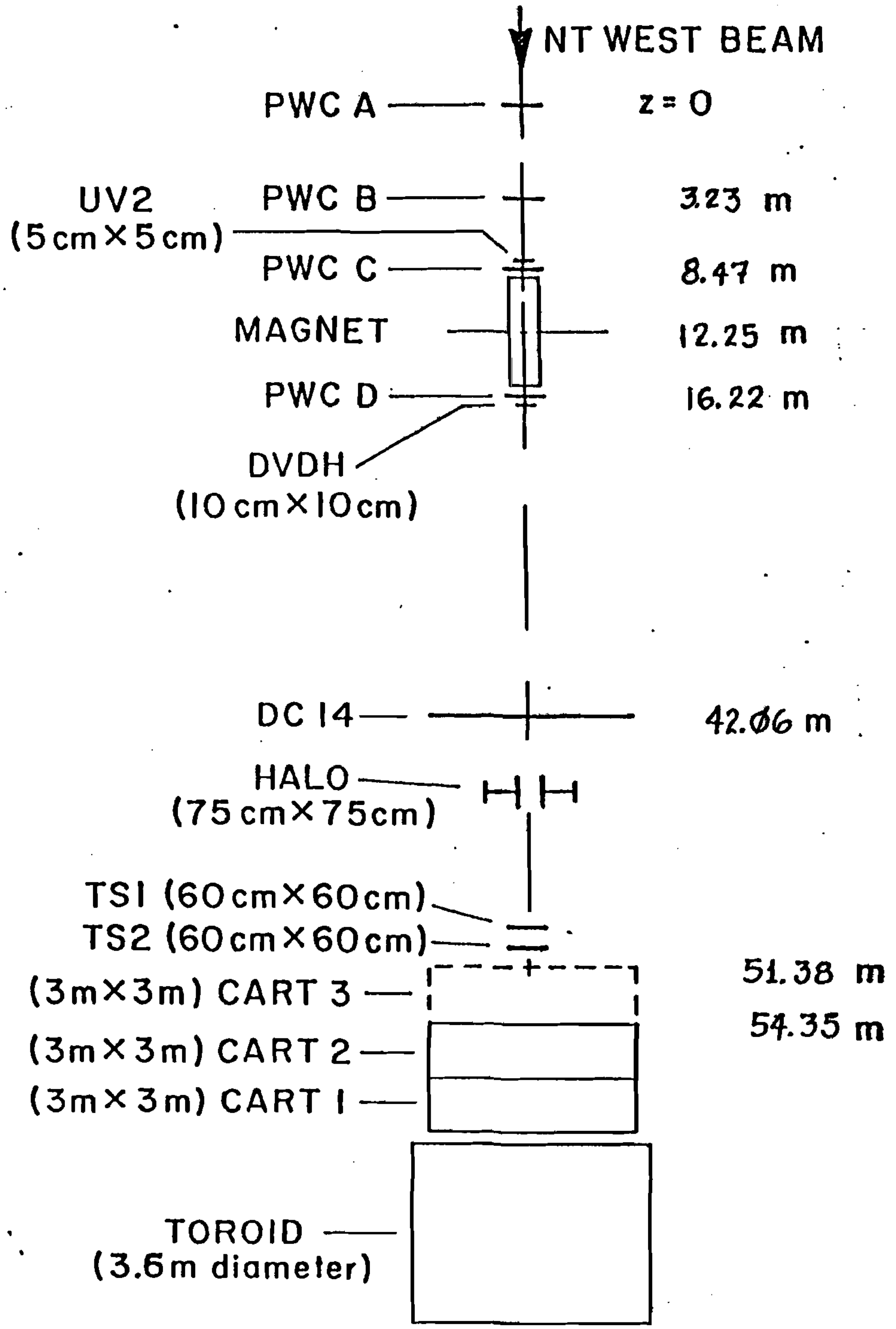
NT WEST BEAM
PWC A
z = 0
UV2
(5 cm × 5 cm)
PWC B
3.23 m
PWC C
8.47 m
MAGNET
12.25 m
PWC D
16.22 m
DVDH
(10 cm × 10 cm)
DC 14
42.06 m
HALO
(75 cm × 75 cm)
TS1 (60 cm × 60 cm)
TS2 (60 cm × 60 cm)
(3m × 3m) CART 3
51.38 m
54.35 m
(3m × 3m) CART 2
(3m × 3m) CART 1
TOROID
(3.6m diameter)

Fig. I.1

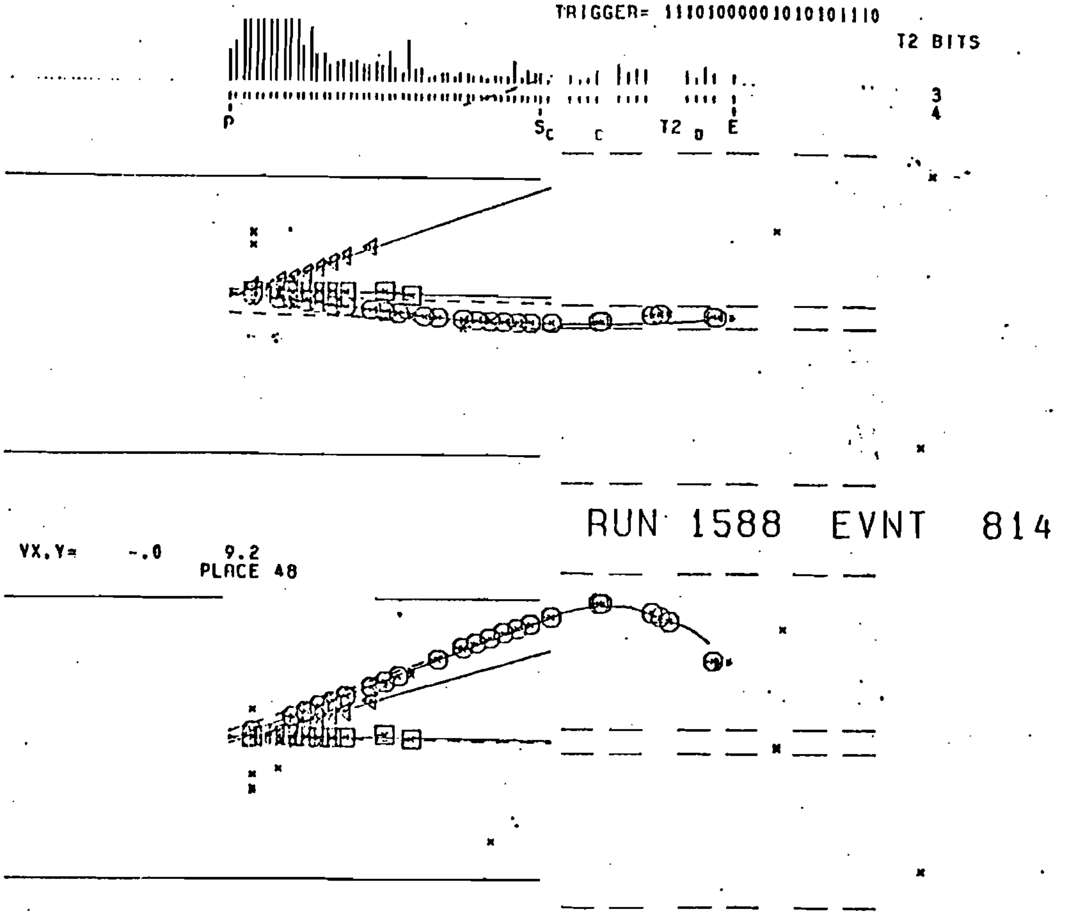
TRIGGER= 11101000001010101110
T2 BITS
3
4
P
S C
C
T2
D
E
RUN 1588 EVNT 814
VX,Y= -.0 9.2
PLACE 48

Fig. G.1

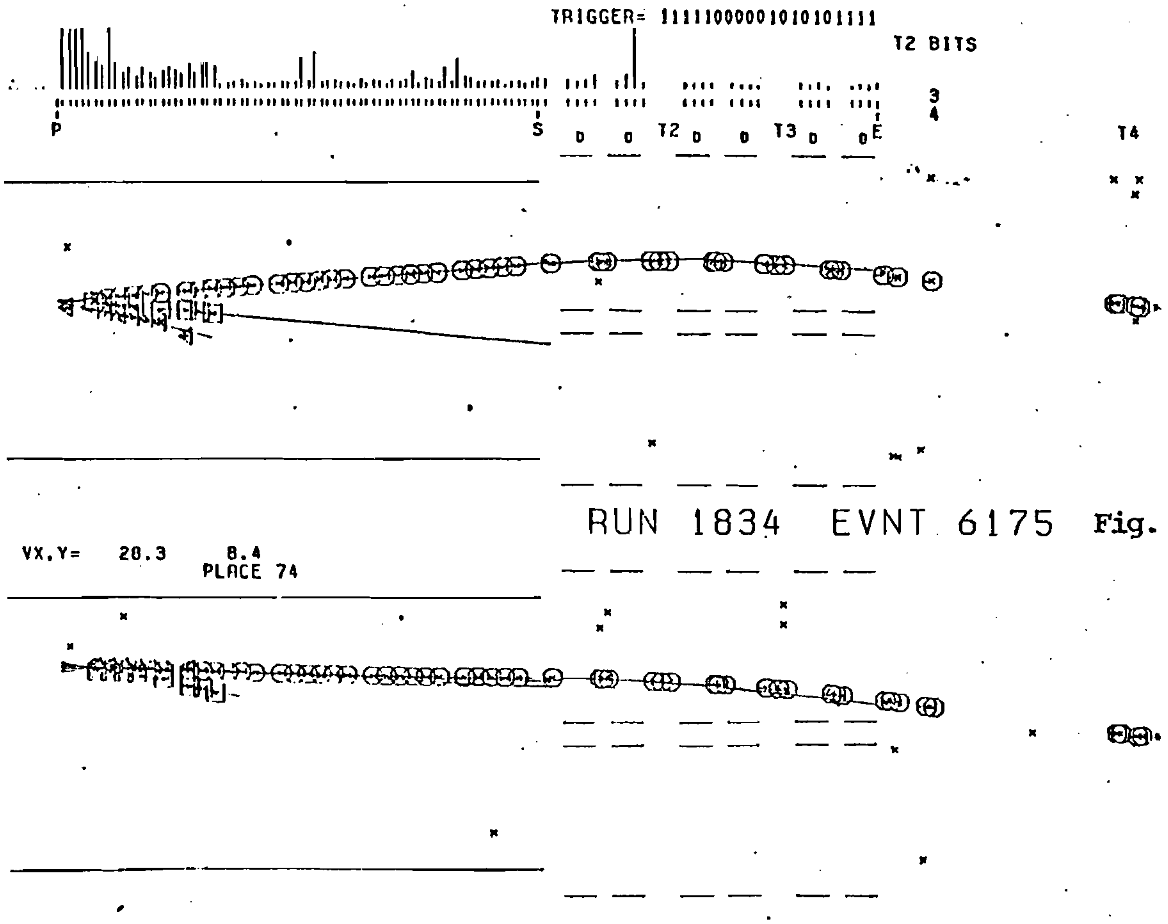
TRIGGER= 11111000001010101111
T2 BITS
3
4
T4
P
S
D
D
T2
D
D
T3
D
D
E
RUN 1834 EVNT 6175
VX,Y= 28.3 8.4
PLACE 74

Fig. G.2

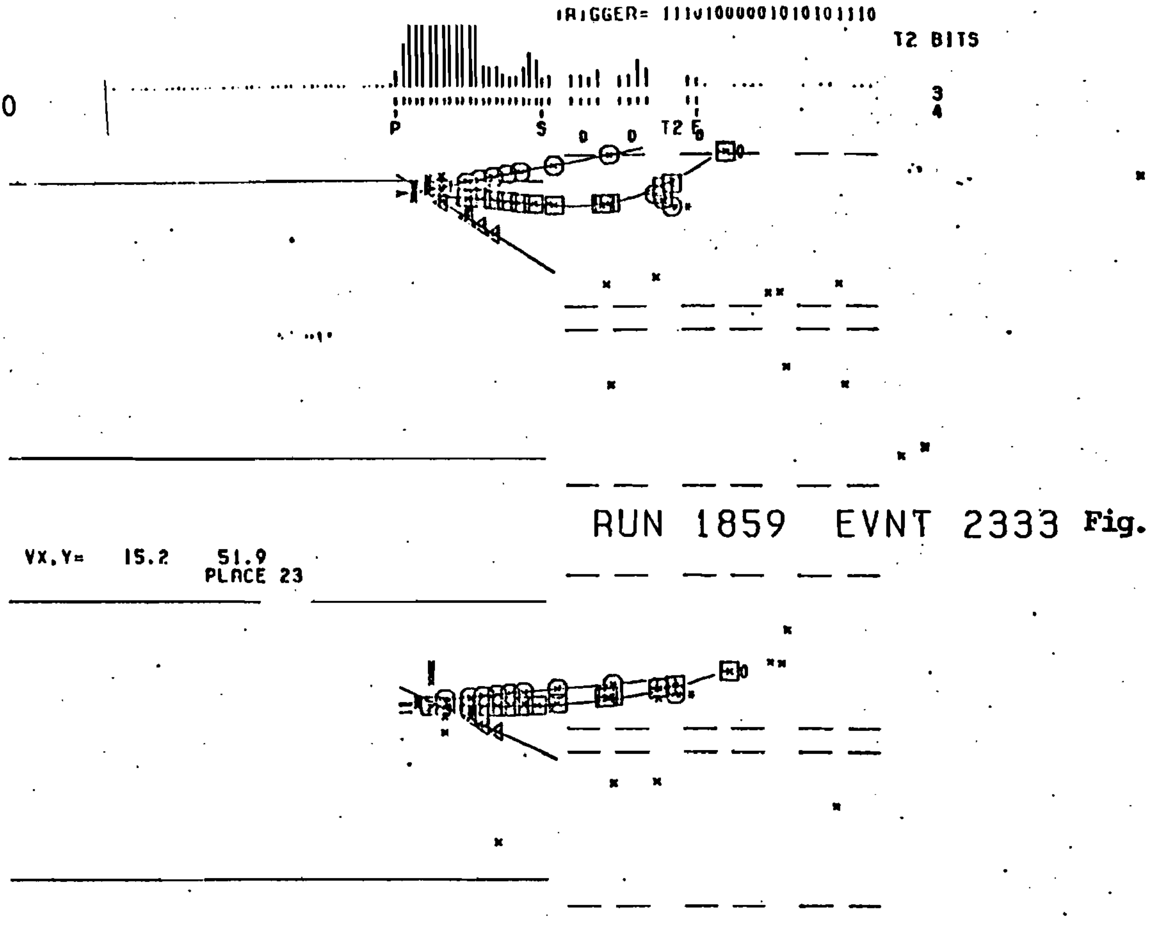
TRIGGER= 11101000001010101110
T2 BITS
3
4
P
S
0
0
T2
E
RUN 1859 EVNT 2333
VX,Y= 15.2 51.9
PLACE 23

Fig. G.3

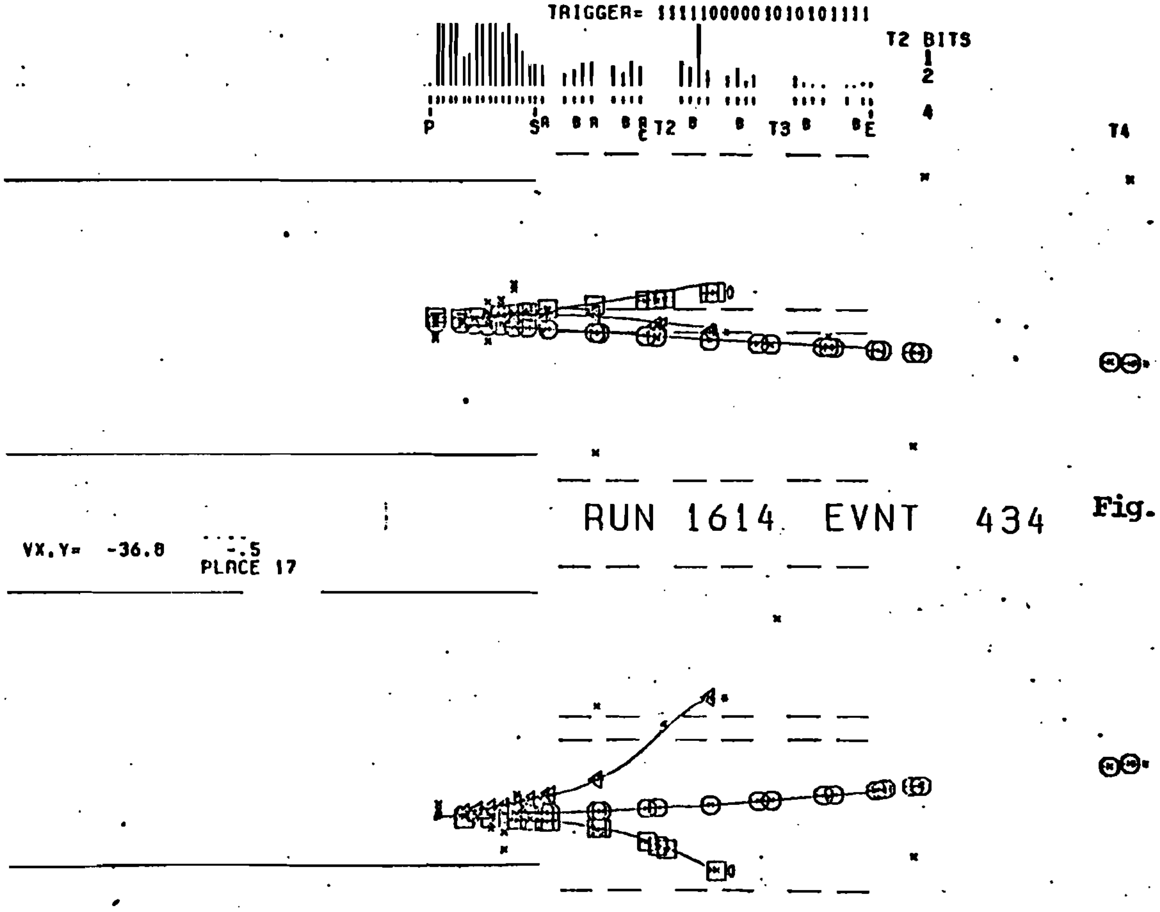
TRIGGER= 1111100000101010101111
T2 BITS
1
2
4
P
S
A
A
E
T2
T3
E
T4
RUN 1614 EVNT 434
VX,Y= -36.8 -.5
PLACE 17

Fig. G.4

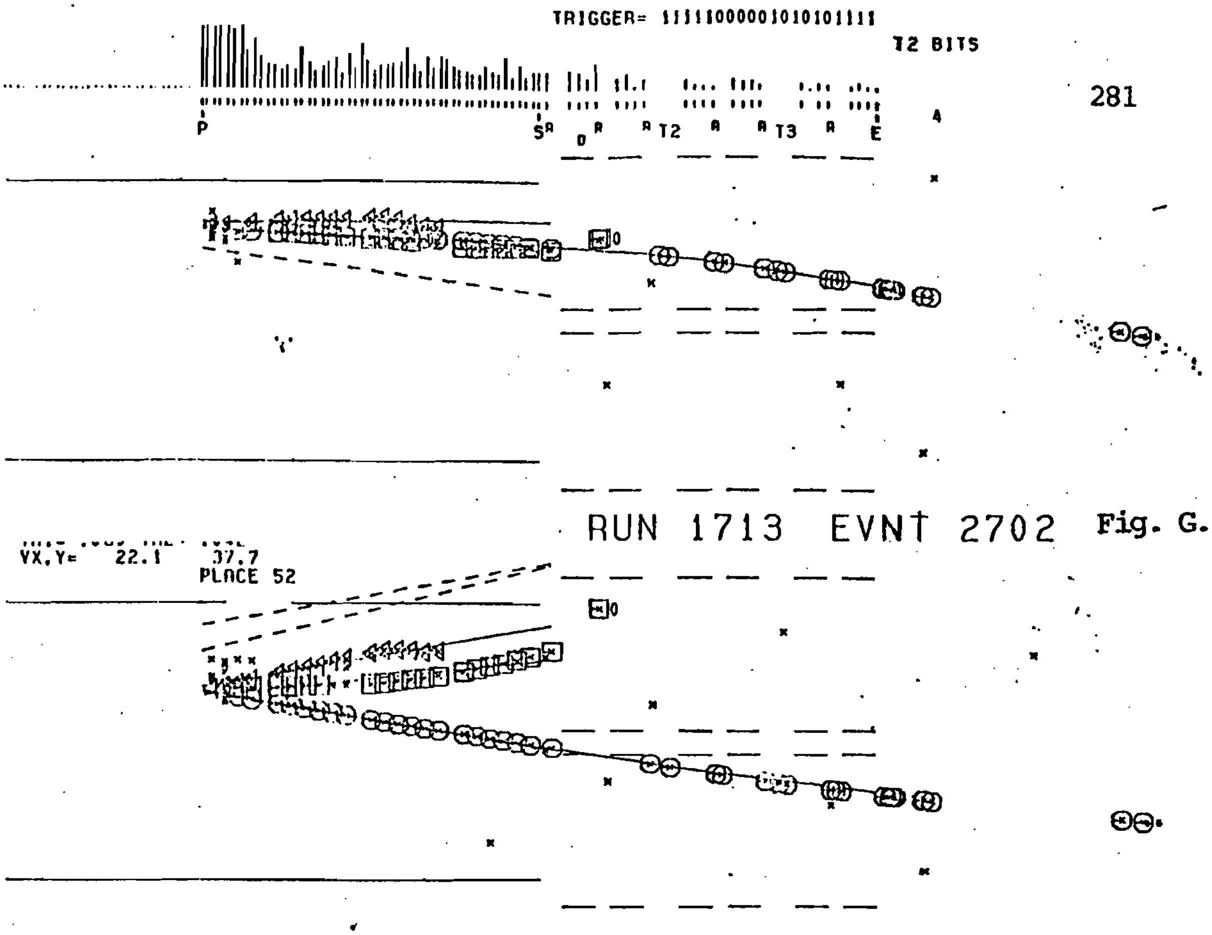
TRIGGER= 11111000001010101111
T2 BITS
P
S
A
D
A
A
T2
A
A
T3
A
E
4
0
RUN 1713 EVNT 2702
VX,Y= 22.1 37.7
PLACE 52
0

Fig. G.5

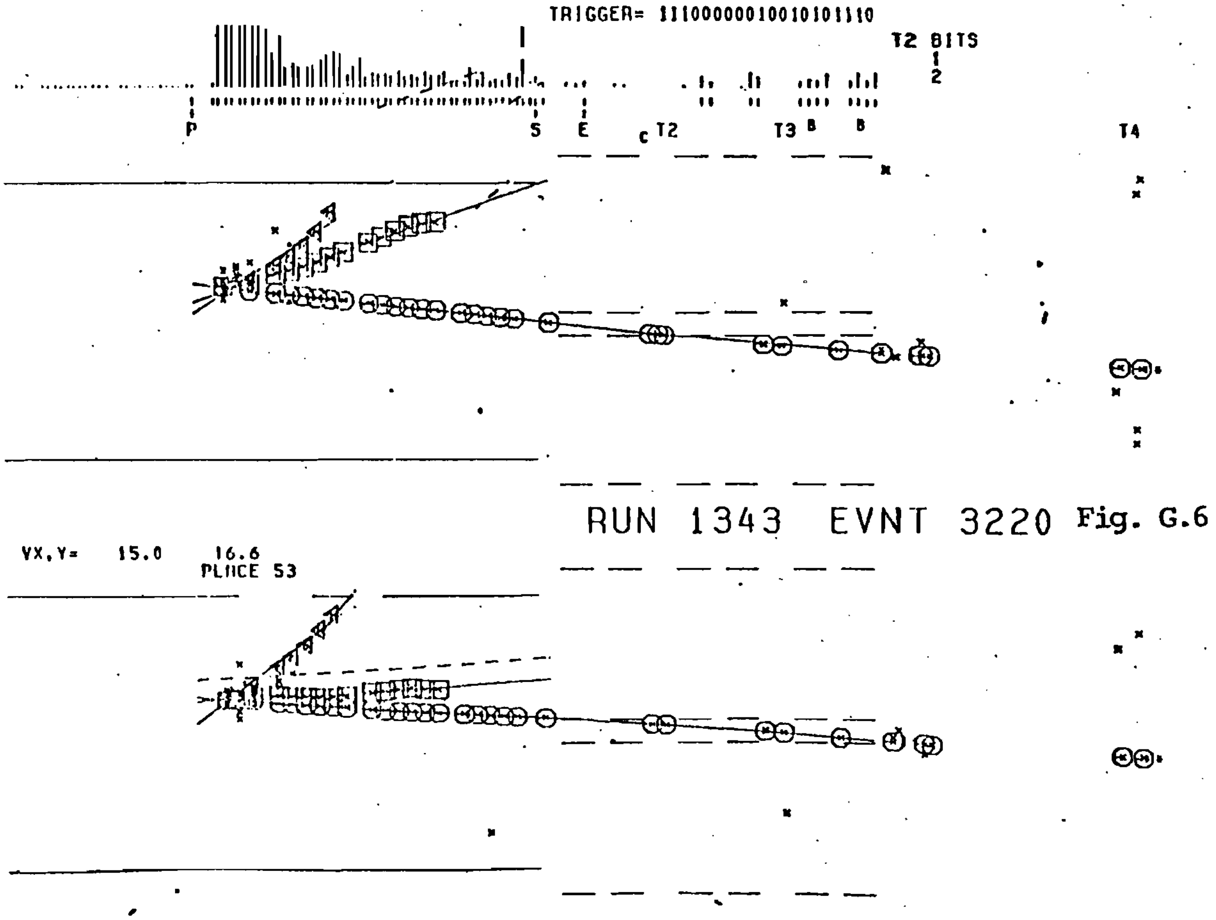
TRIGGER= 111000000010010101110
T2 BITS
1
2
P
S
E
C
T2
T3
B
B
T4
RUN 1343 EVNT 3220
VX,Y= 15.0 16.6
PLACE 53

Fig. G.6

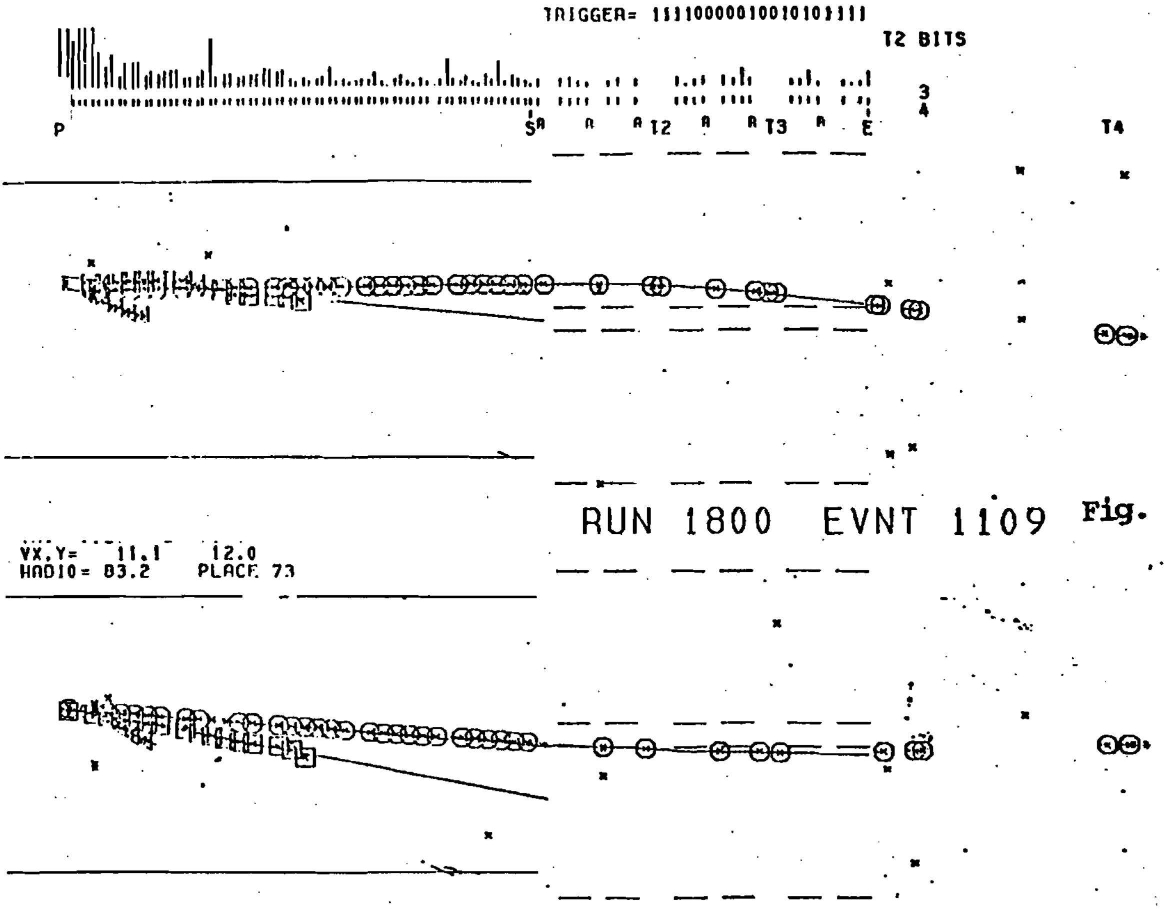
TRIGGER= 11110000010010101111
T2 BITS
P
S
A
A
A
T2
A
A
T3
A
E
3
4
T4
RUN 1800 EVNT 1109
VX,Y= 11.1 12.0
HADIO= 83.2 PLACE 73

Fig. G.7

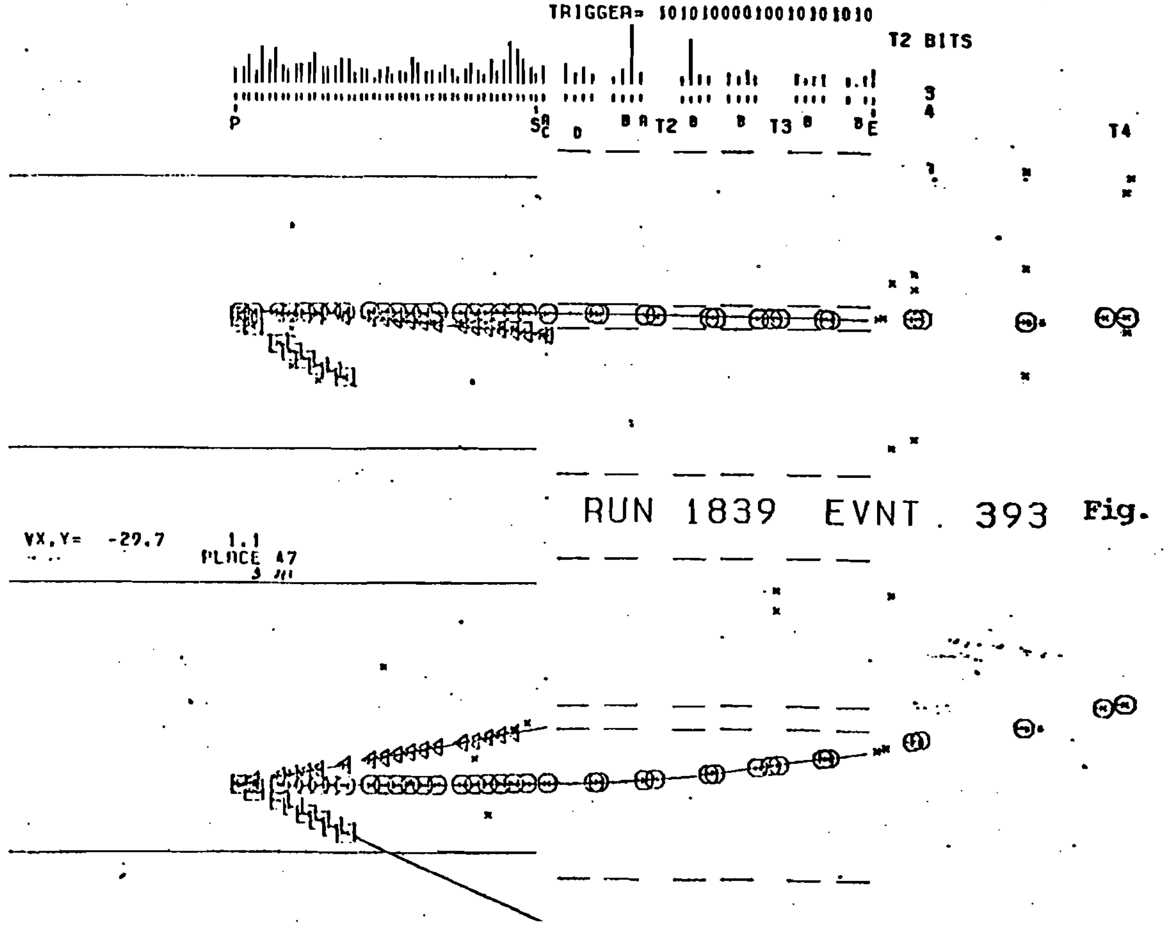
TRIGGER= 10101000010010101010
T2 BITS
P
S
A
C
D
B
A
T2
B
B
T3
B
B
E
3
4
T4
RUN 1839 EVNT 393
VX,Y= -29.7 1.1
PLACE 47

Fig. G.8

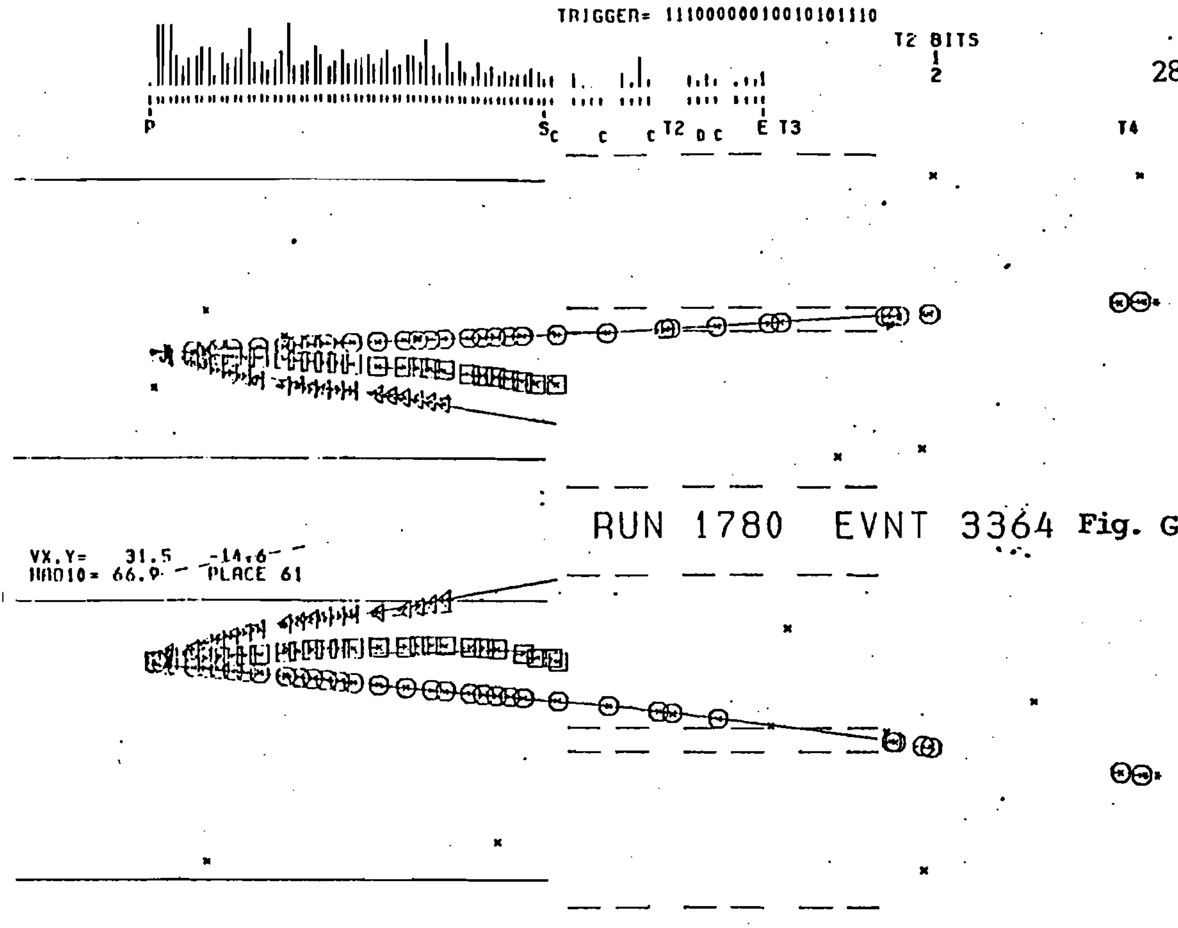

Fig. G.9

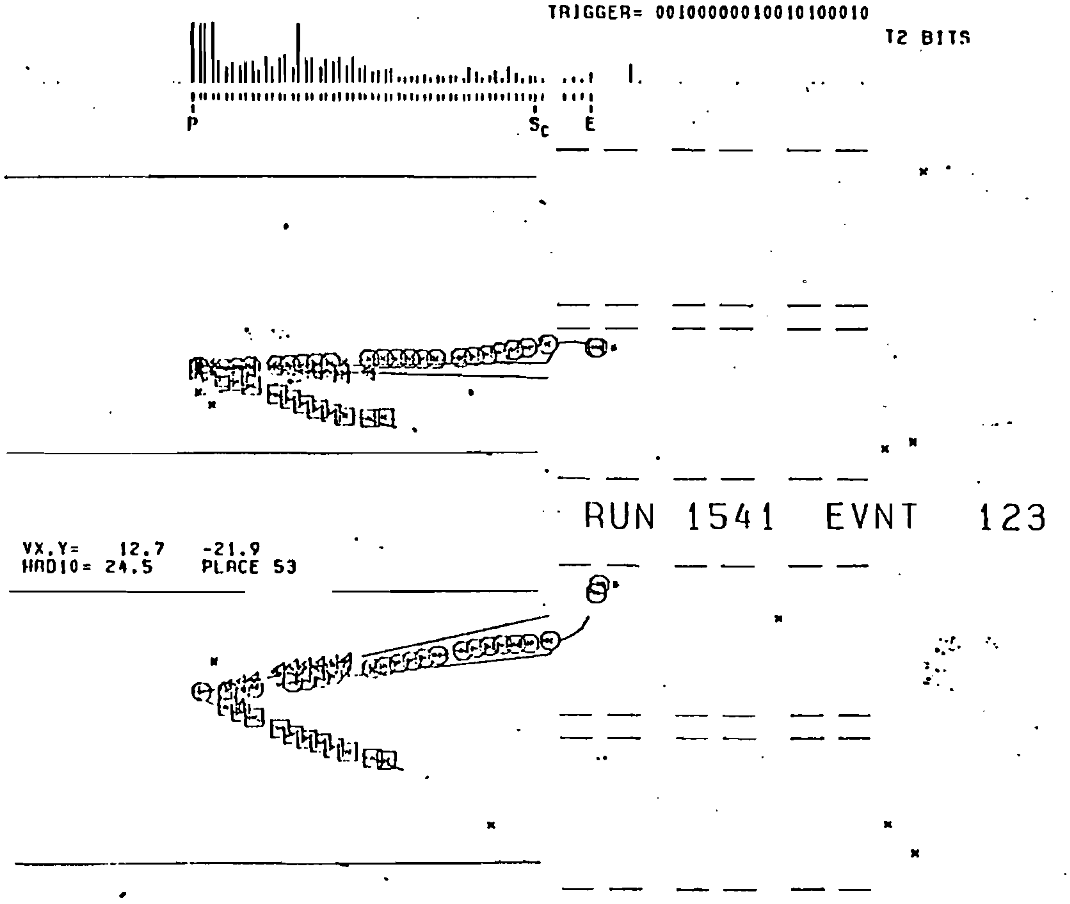

Fig. G.10

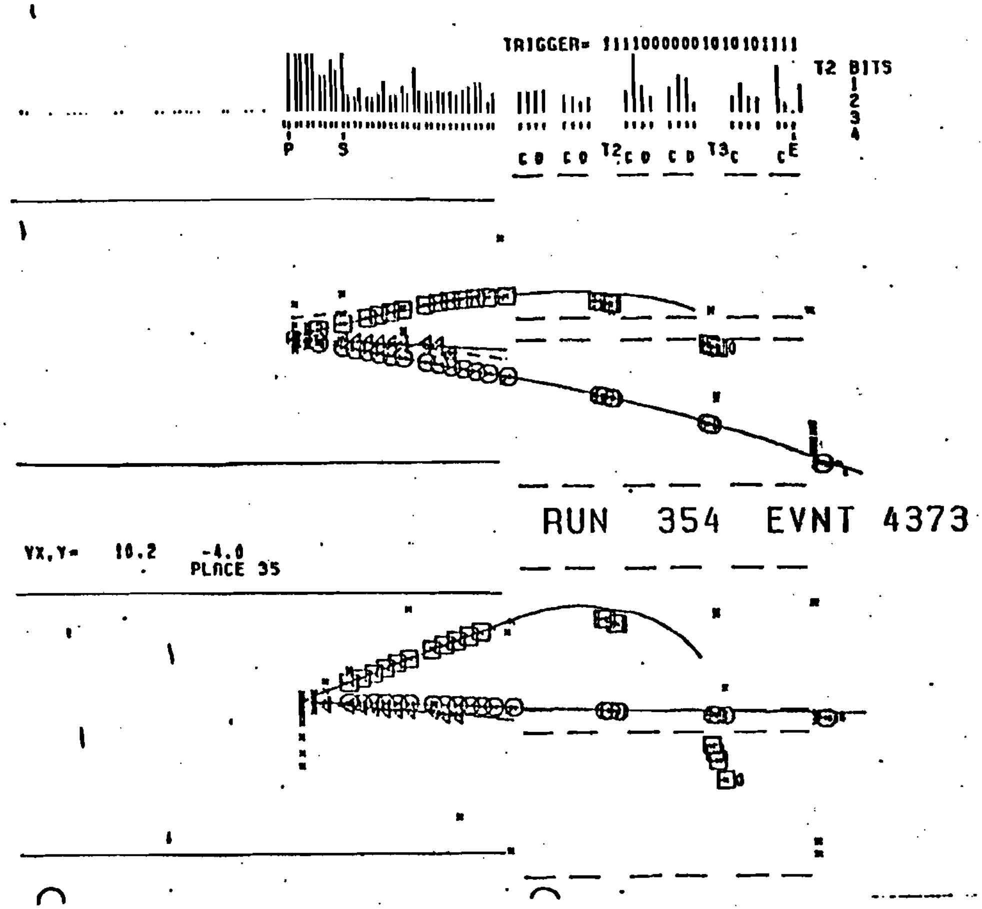

Fig. G.11

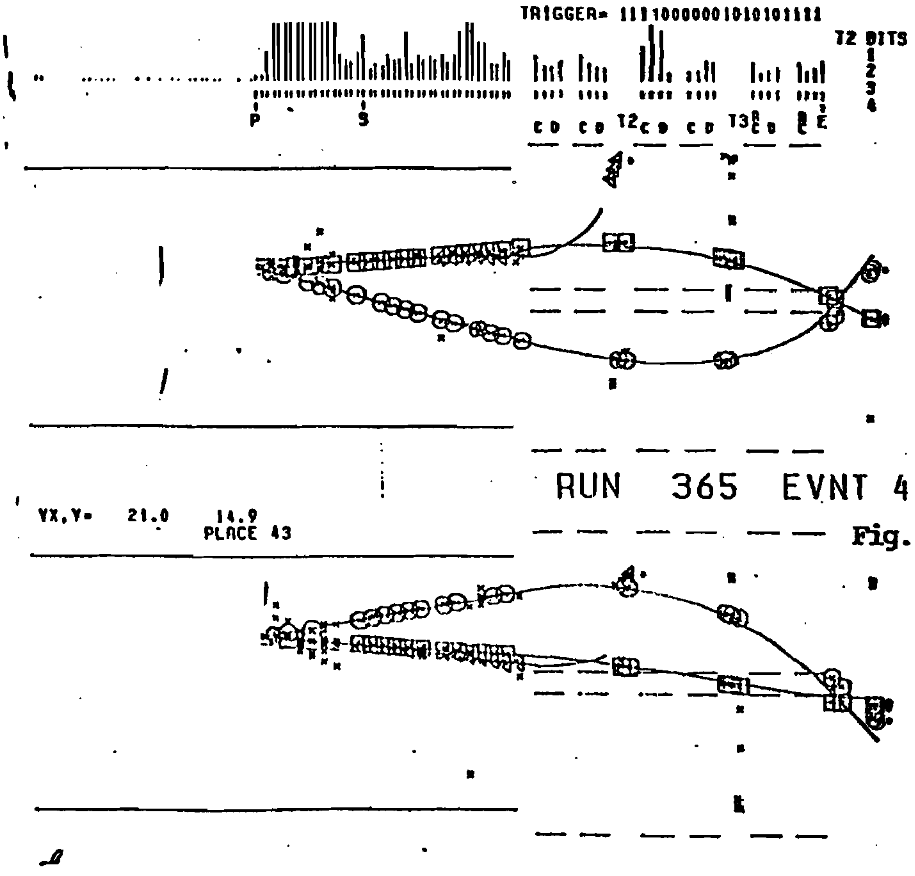

Fig. G.12

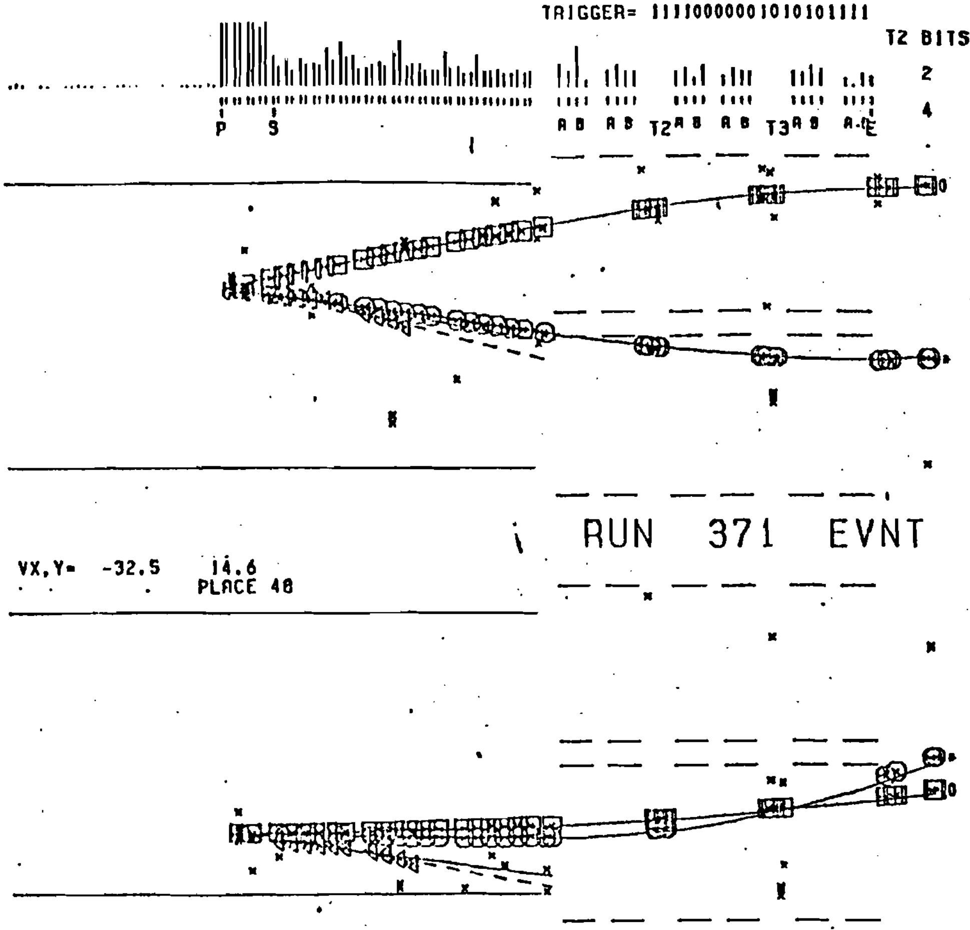

Fig. G.13

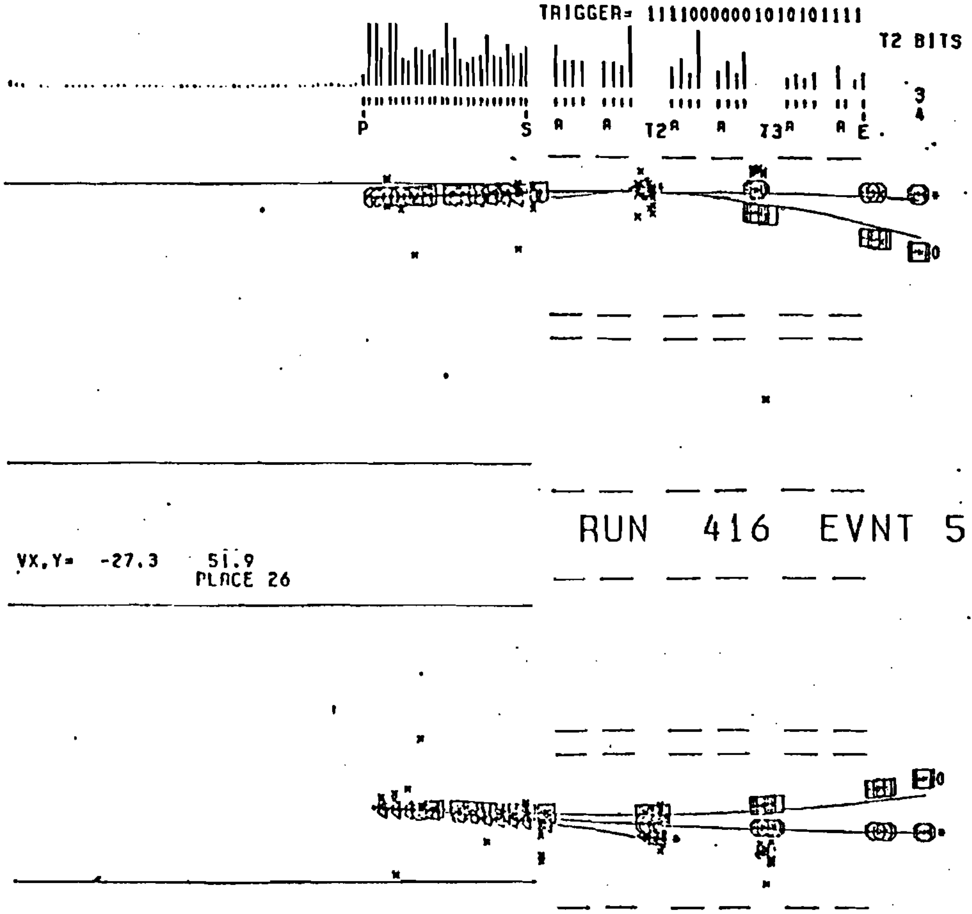

Fig. G.14

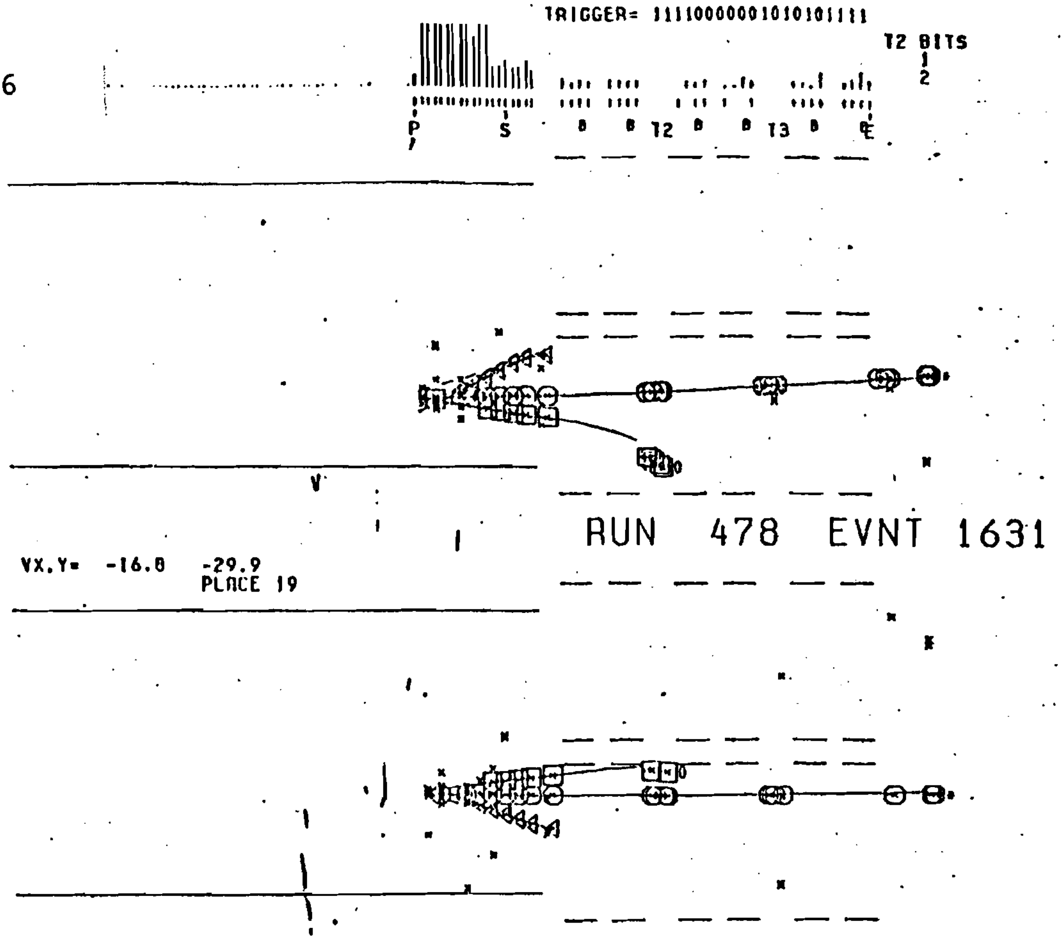

Fig. G.15

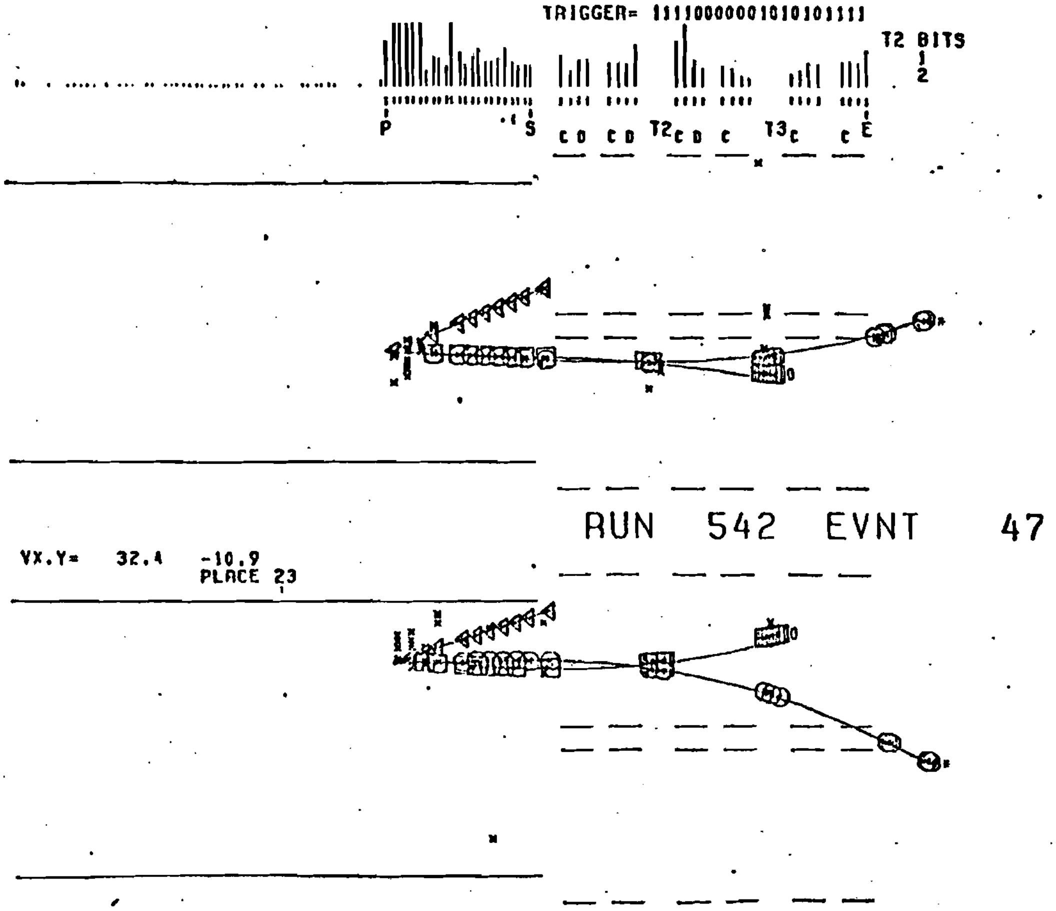

Fig. g.16

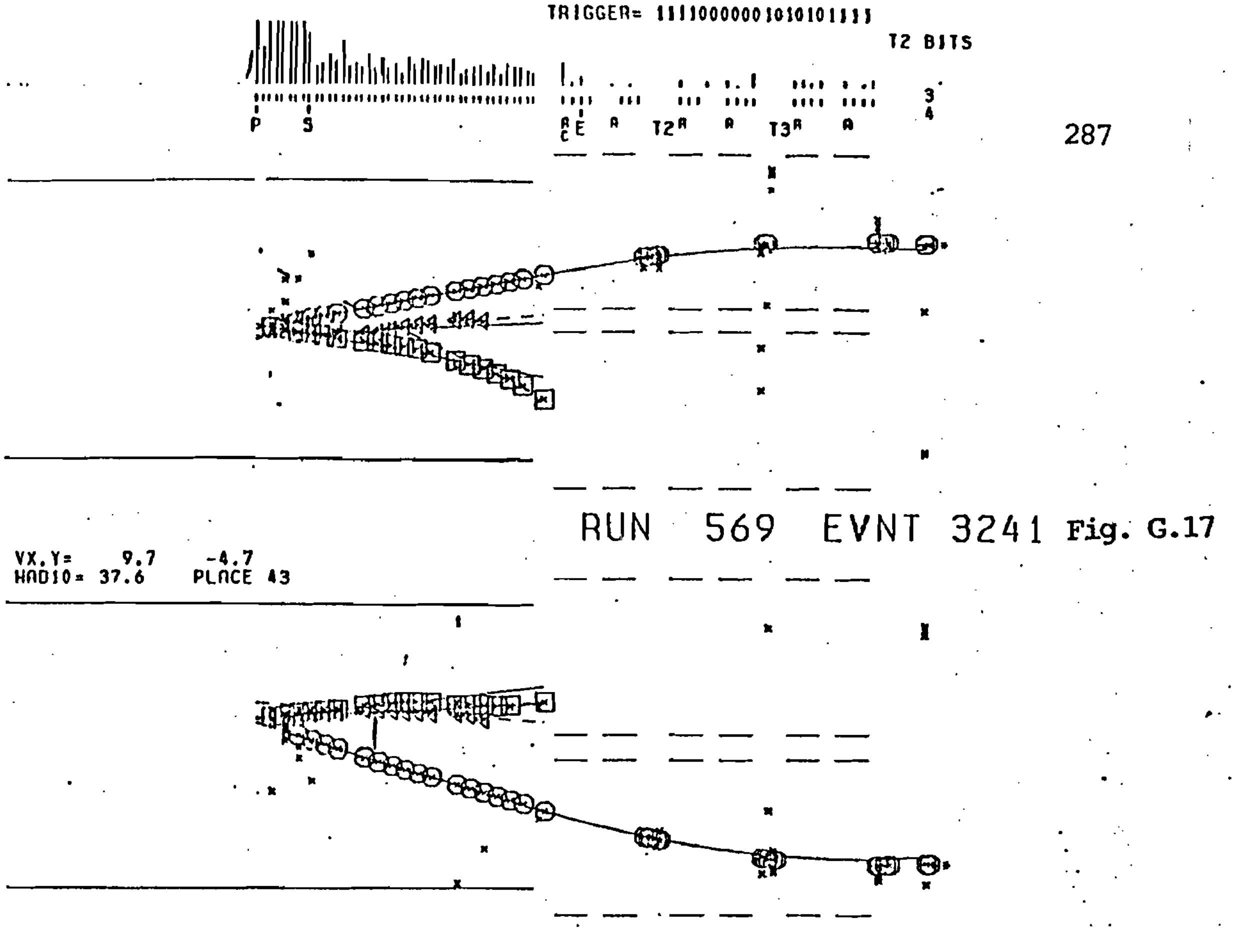

Fig. G.17

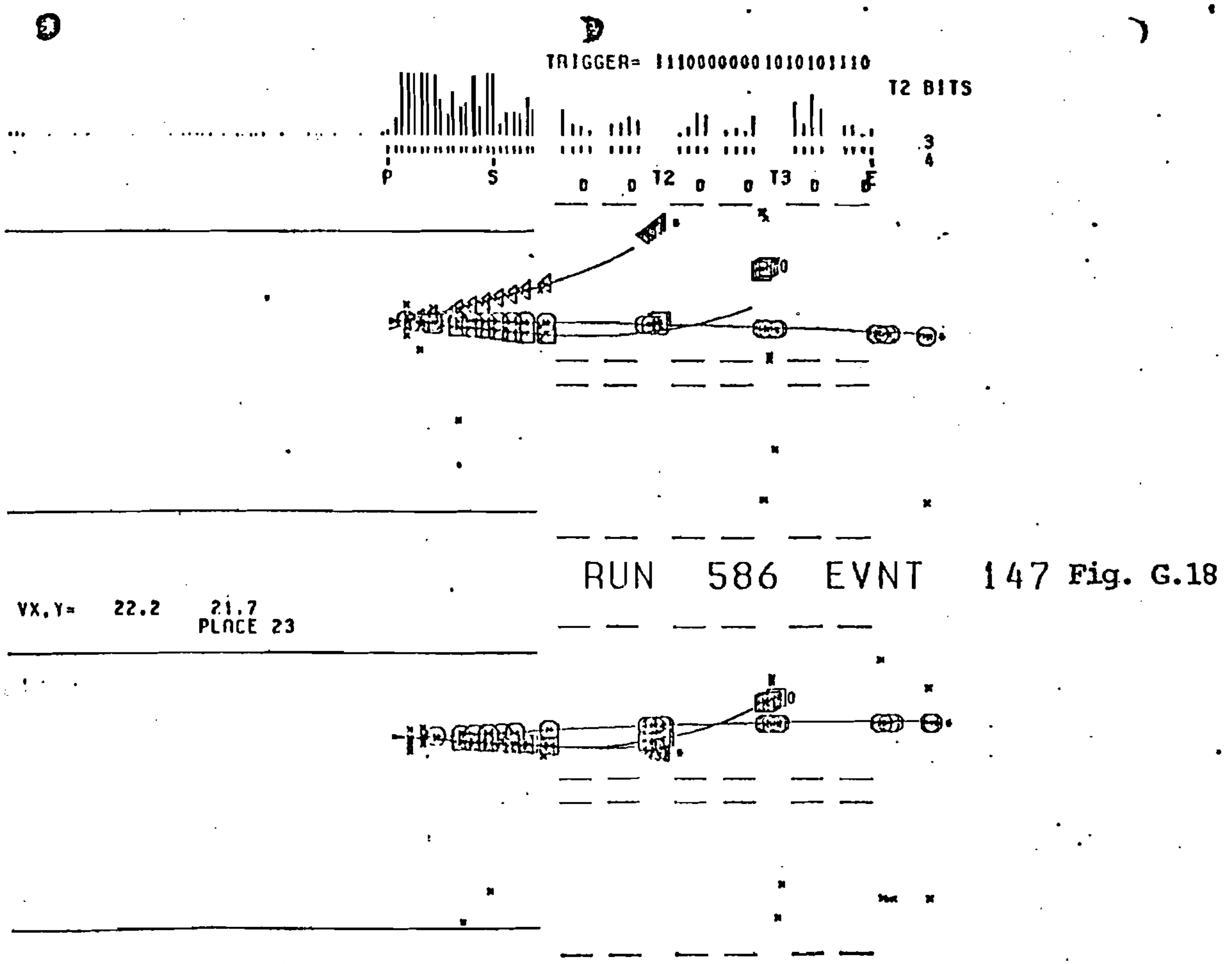

Fig. G.18

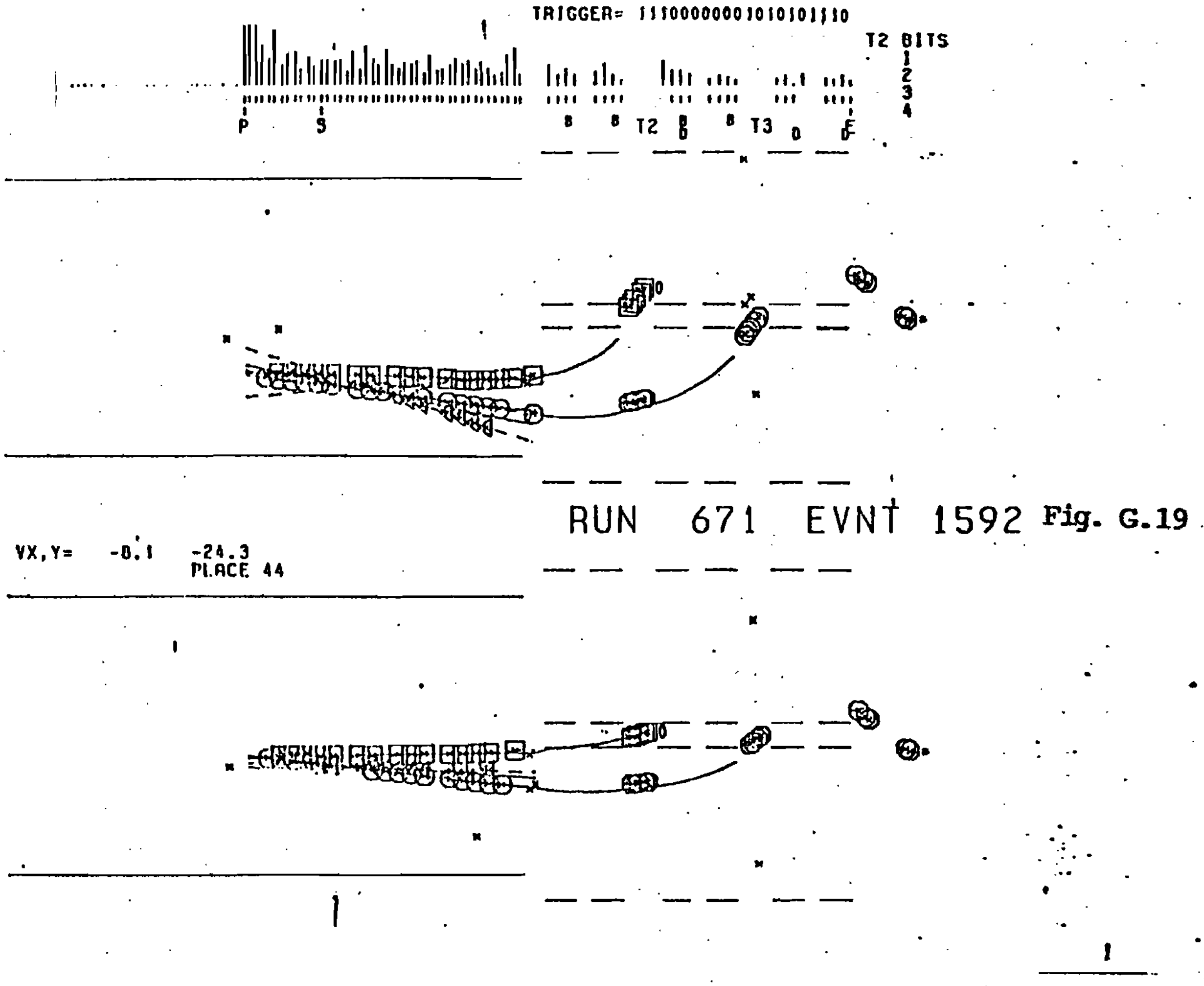

Fig. G.19

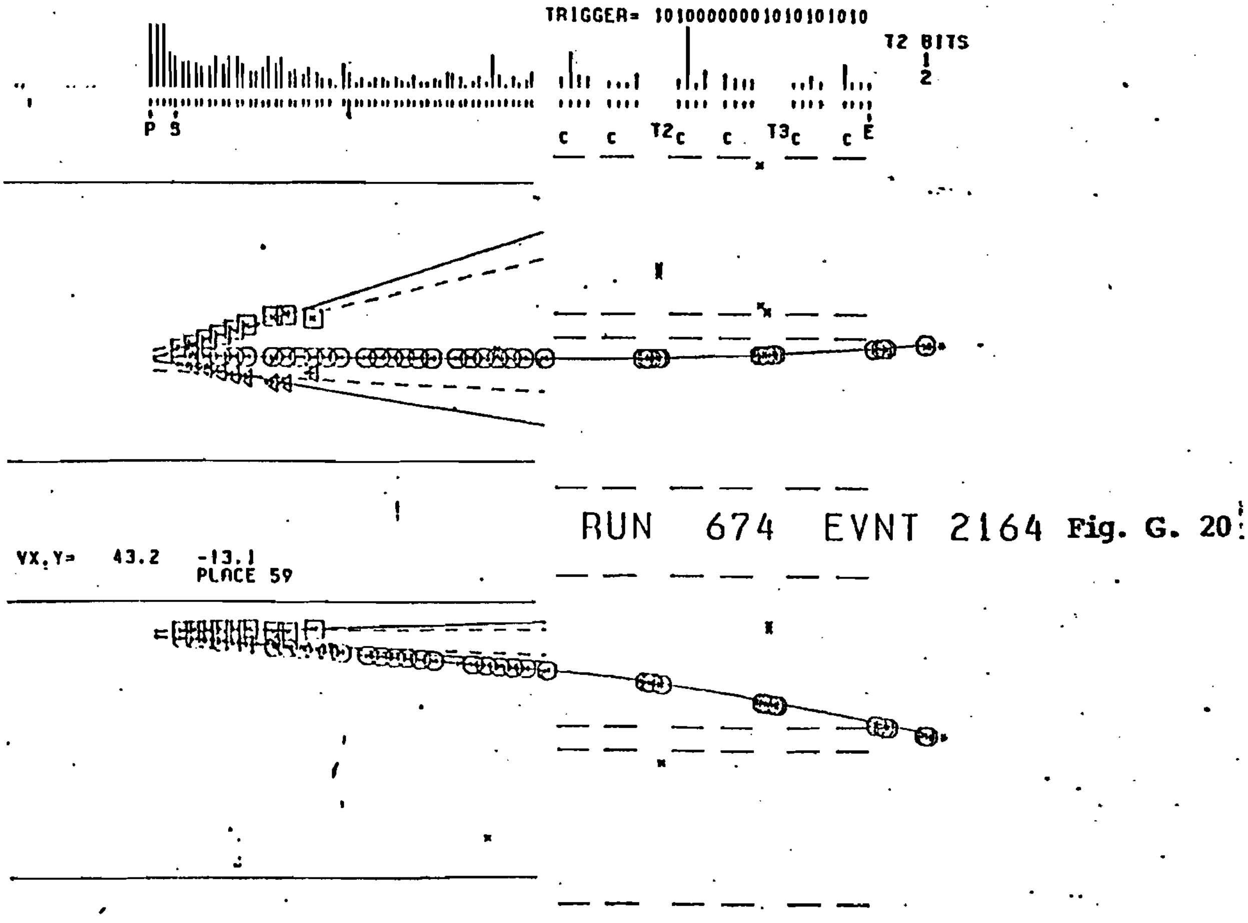

Fig. G. 20

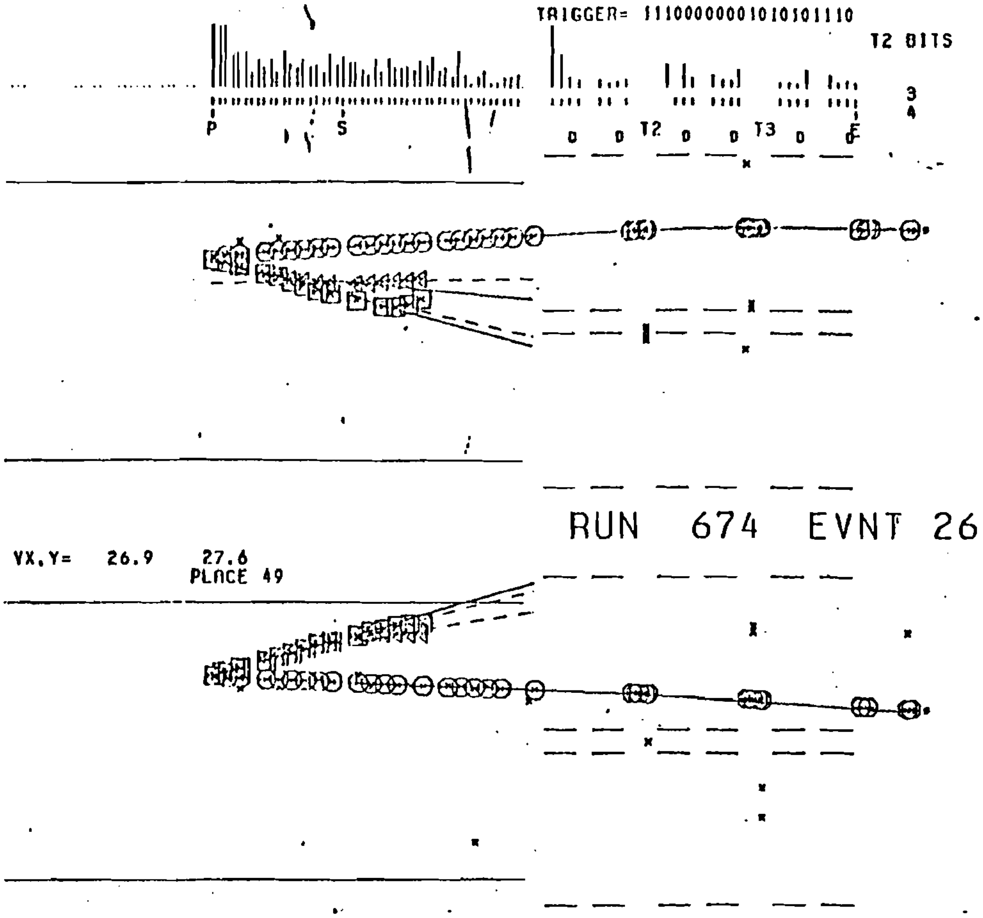

Fig. G.21

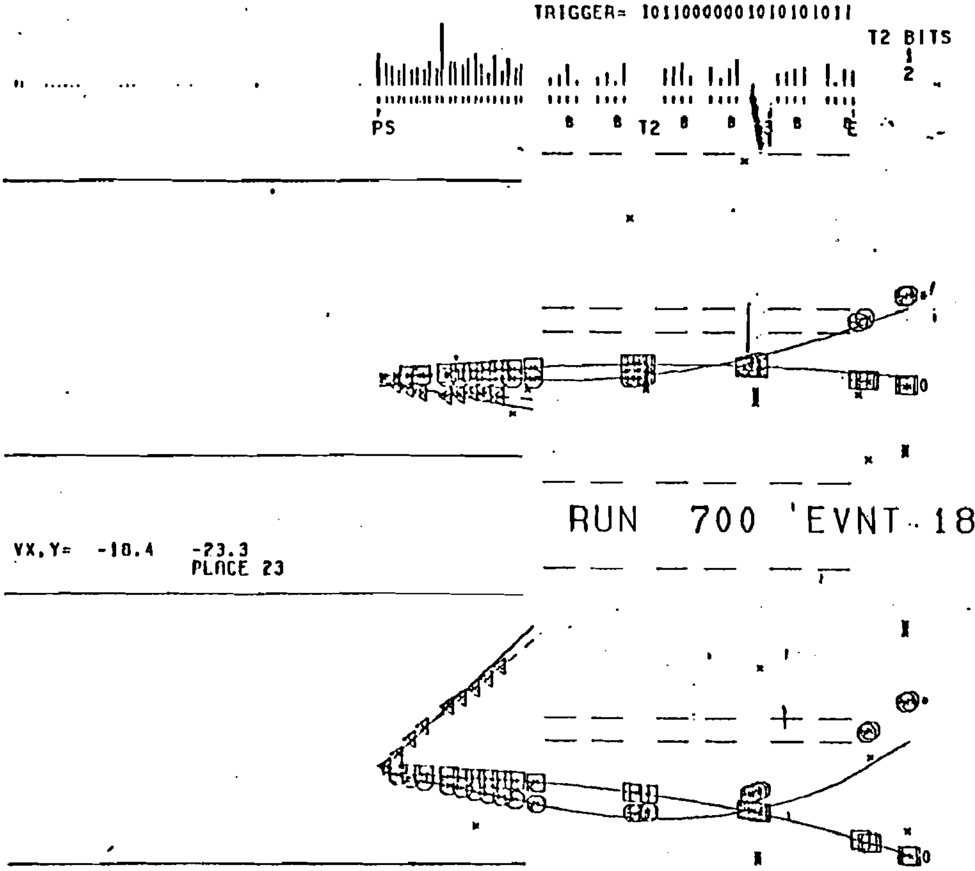

Fig. G.22

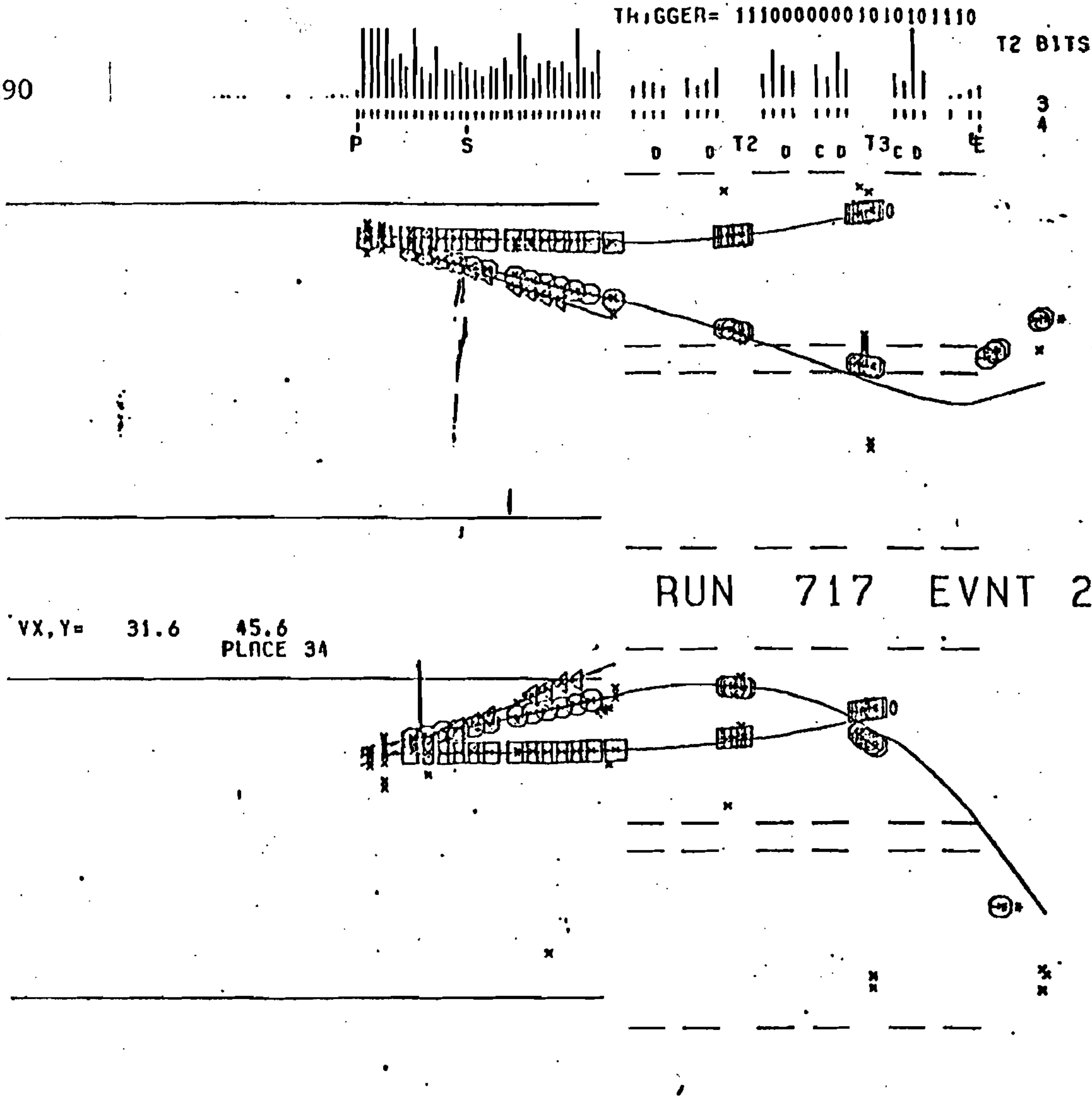
TRIGGER= 11100000001010101110
T2 BITS
3
4
P
S
D
D
T2
D
C D
T3
C D
E
RUN 717 EVNT 2289
VX,Y= 31.6 45.6
PLACE 34

Fig. G.23